Optical Transmission Through Sub-Wavelength Slits in Metals:
from Theory to Applications

THÈSE Nᴼ 4723 (2010)

PAR

Mickaël GUILLAUMÉE

EPFL

ÉCOLE POLYTECHNIQUE
FÉDÉRALE DE LAUSANNE

Suisse
2010

Résumé

Cette thèse traite des propriétés de transmission de la lumière à travers des fentes sub-longueur d'onde dans des films métalliques. On étudie la transmission à travers ces fentes d'un point de vue théorique et expérimental, ainsi que la possibilité de les utiliser pour différentes applications optiques.

La partie théorique de cette thèse étudie de façon approfondie la transmission à travers un réseau périodique de fentes sub-longueur d'onde. Un modèle analytique permettant de calculer la transmission de la lumière à travers un réseau de fente est développé. Ce modèle donne une expression analytique des relations de dispersion des modes responsables de la transmission élevée. Les modes provocant une transmission élevée présentent une nature hybride entre un mode de type Fabry-Pérot et un mode de type surface plasmon polariton. Cette étude donne une compréhension claire du comportement des différents modes dans le processus de transmission, ce qui est très important dans le but de modéliser des réseaux possédant des propriétés particulières et pouvant être utilisés pour diverses applications.

La transmission de la lumière est mesurée à travers des fentes uniques, des fentes avec des creux périodiques de chaque coté de la fente ainsi qu'avec des réseaux de fentes. Des structures type "fente-creux" recouvertes par une fine couche diélectrique ont également été fabriquées. Avec de telles structures, des modes guidés de polarisation transverse électrique peuvent être excités dans la couche diélectrique, ce qui permet d'augmenter grandement la transmission de la lumière polarisé TE à travers la fente par rapport à des structures type "fente-creux" conventionnelles, qui transmettent de façon résonantes uniquement la lumière polarisé transverse magnétique (TM). Les mesures sont comparées avec des calculs

théoriques afin de valider les différents outils de modélisation à disposition, ce qui s'avère nécessaire en vue d'utiliser ces structures pour des applications variées.

L'utilisation de fentes dans des films métalliques est ensuite étudiée pour différentes applications en prenant en compte les travaux expérimentaux et théoriques de cette thèse. Trois appareils optiques sont étudiés : des biocapteurs, des diodes électroluminescentes et des caméras. Les réseaux de fentes, dont la transmission optique est très sensible aux variations de l'indice de réfraction, peuvent être utilisés pour développer des capteurs compacts et portatifs. Notre étude théorique montre qu'une grande sensibilité à des changements d'indice de réfraction est obtenue dans le cas de réseaux suspendus.

Dans le cas des diodes électroluminescentes, des réseaux de fentes sont étudiés dans le but de fabriquer des contacts électriques transparents. L'étude réalisée montre que la transmission de la lumière peut être très élevée à travers un réseau de fente sur un substrat d'indice de réfraction élevé, caractéristique des diodes électroluminescentes. Grâce au couplage de la lumière par le réseau de fentes, la lumière peut même être extraite pour des angles d'incidence plus grands que l'angle critique. Les premiers calculs montrent que l'extraction de la lumière à travers un contact métallique avec un réseau de fente sur un substrat de GaP peut-être deux fois plus importante que pour une interface GaP-air planaire.

Enfin, des réseaux de fentes ainsi que des structures de type "fente-creux" ont été intégrées sur les pixels d'un capteur CMOS. Dans le cas d'un pixel avec un réseau de fentes, une extinction de polarisation de 200 est mesurée sur un gamme spectral de 200 nm. Cela signifie que des réseaux de fentes peuvent être utilisés comme micro-polariseurs dans le but d'effectuer de l'imagerie sensible à la polarisation. Dans le cas des pixels avec des structures de type "fente-creux", les mesures montrent que ce type de structure permet d'améliorer d'un facteur huit le signal mesuré sur le pixel. Ces structures peuvent être utilisées pour augmenter le rapport signal sur bruit du capteur.

Mots clés :

Optique, photonique, plasmonique, métal, réseau de diffraction, réseau de fente, cavité Fabry-Pérot, plasmon de surface, guide d'onde, transmission optique exaltée, biocapteur, diode électroluminescente, caméra, capteur CMOS.

Abstract

This thesis explores the properties of the transmission of light through subwavelength slits in metal films. Theoretical and experimental studies on the transmission through slits in metals are presented. In addition, the potential use of these slits for different applications is investigated.

The theoretical aspect concentrates on the study of the transmission of light through slit arrays. It is observed that high transmission is due to the coupling of two modes: one whose properties depend on the slit geometry and the other one whose properties depend on the grating periodicity. To determine the exact nature of these hybrid modes an analytical model is derived. The simplified model gives accurate analytical expressions for the transmission and also for the dispersion relations of the hybrid modes responsible for high transmission. The dispersion relations give a clear picture of the role played by the different resonances in the transmission process. We find that the high transmission modes are hybrid in nature between that of a Fabry-Pérot mode and a surface plasmon polariton mode. These hybrid modes have either symmetric or antisymmetric profiles. These findings are important as they clarify the nature of the modes responsible for high transmission, and therefore can be useful as a design tool for metal gratings for various applications.

The light transmission through single slits, slit and groove structures and slit arrays is optically characterized. Also, slit and groove structures covered by a thin dielectric layer are fabricated. With this type of structure, transverse electric (TE) polarized dielectric waveguide modes can be excited inside the dielectric film, which strongly increases the TE polarized transmission as compared to conventional slit and groove structures, which only gives high

transmission for transverse magnetic (TM) polarization. These structures demonstrate an efficient way to enhance light transmission through subwavelength apertures as both TE and TM polarization can be efficiently transmitted. The transmission measurements for the different types of structures are compared with theory. This gives an idea of the validity of the theoretical tools considered, which is necessary to address the potential of subwavelength slits in metals for applications.

Taking advantage of the theoretical and experimental work developed in this thesis, the use of slits in metals is considered for three different optical devices: biosensors, light emitting diodes and image sensors. In the case of biosensors, slit arrays whose optical transmission is highly sensitive to refractive index changes could be useful to design compact and portable sensors. Our work show that a high sensitivity to refractive index changes can be obtained in the case of suspended slit arrays. As an example, theoretically an adsorption of a 1.6 nm thick layer of bovine serum albumin on a slit array could provide a 3% intensity change.

Slit arrays are also investigated for light emitting diodes in order to obtain transparent metal contacts. It is shown that light transmission through slit arrays on a high refractive index substrate, characteristic of light emitting diode, can be very efficient. Light can be extracted even for angles of incident larger than the critical angle due to grating coupling. Preliminary calculations show that a metal contact with arrays of slit can give twice the extraction efficiency of a planar GaP-air interface.

Finally, slit arrays and slit and groove structures have been integrated as a post process onto pixels of image sensors. In the case of a pixel with a slit array, a polarization extinction ratio higher than 200 over a bandwidth of 200 nm is measured, which means that slit arrays can be used as very efficient micro-polarizers in view of polarization imaging. In the case of pixels with slit and groove structures, measurements show that the slit and groove structure could improve by a factor of eight the signal measured on the pixel. Such structure could be used to replace current optical systems or to improve device performances by increasing the signal to noise ratio and allowing polarization and colour selectivity.

Keywords:

Optic, photonic, plasmonic, metal, diffraction grating, slit array, Fabry-Pérot cavity, surface plasmon polariton (SPP), waveguide, enhanced optical transmission (EOT), biosensor, light emitting diode, image sensor, CMOS sensor.

Contents

Chapter 1
Introduction

Optical properties of metal-dielectric interfaces have been intensively studied since the beginning of the twentieth century. Metals have the ability to sustain coherent oscillations of free electrons that can interact with electromagnetic waves, leading to surface waves called surface plasmon polaritons. After a historical introduction, this chapter gives an overview of the state of the art of the research field studying surface plasmon polaritons called plasmonics. In the last section, the objective of this thesis is described and an outline of the manuscript is presented.

1.1. Historical review

Metals have been used for a long time for decorative applications. Romans were already using metal particles to colour glass windows and ceramic potteries. A prominent example dated to the fourth century AD is the Lycurgus cup displayed in the British museum and shown in Fig. 1.1. The scene on the cup depicts the legend of Lycurgus from Homer's Iliad. King Lycurgus, a man of violent temper, attacked Dionysos and one of his maenads, Ambrosia. Ambrosia called out to Mother Earth, who transformed her into a vine. She then coiled herself about the king, and held him captive. The cup shows this moment when Lycurgus is entrapped by the branches of the vine. It has been thought that the theme of this myth - the triumph of Dionysos over Lycurgus - might have been chosen to refer to a contemporary political event, the defeat of the emperor Licinius (reigned AD 308-24) by Constantine in AD 324. This cup, in addition to attracting interest from a historical point of view, is also famous for its remarkable optical properties. Whereas the cup appears green when illuminated from the outside (i.e. in reflection), a striking red colour is observed when the light source is placed inside the cup. This effect is caused by the presence of gold and silver nanoparticles embedded in the glass. At wavelengths corresponding to the green colour, the metal particles induce strong scattering, leading to the green colour in reflection, and absorption, giving rise to the red colour in transmission.
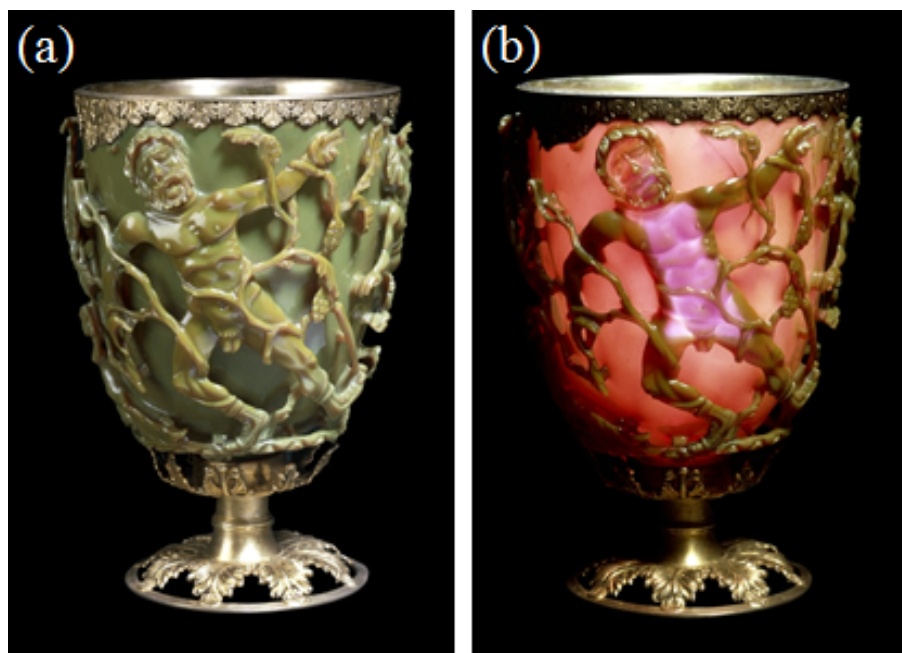
Figure 1.1.   The Lycurgus cup illuminated from (a) outside and (b) inside [1].

The explanation of these optical effects was made possible only centuries later. In 1856, Faraday presented a scientific paper reporting the colourful appearance of colloidal solutions of metal particles when illuminated with white light [2]. The first successful theoretical treatment of light scattering by a homogeneous sphere in a medium was achieved by Mie in 1908 [3]. His calculations show that the scattering efficiency of a particle has resonances at particular wavelengths depending on refractive indices of both the particle and the surrounding medium and also on the particle size. The resonances in the scattering efficiency of the metal particles are at the origin of the observed colours. These resonances are today seen as the coupling of light with a collective oscillation of free electrons in the metal called plasmons.

In the middle of the twentieth century, it was shown both theoretically and experimentally that when a metal is exposed to a beam of electrons, bulk [4-7] and surface [8,9] plasma oscillations can be produced. The first reported excitations of surface plasmon were however performed 50 years before on metal diffraction grating. At that time, Wood had observed rapid variations in the intensity of the diffracted orders of a metal grating but was not able to explain what he called anomalies [10]. It was not until 1965 that Hessel and Oliner recognized that one type of the anomalies observed by Wood was due to the excitation of surface plasmon modes [11].

Surface plasmons are solution of Maxwell's equations and are called surface plasmon polaritons (SPP's) to reflect the coupling of collective oscillation of free surface charges of the metal with electromagnetic waves. SPP's are surface waves propagating at metal-dielectric interfaces and have attracted interest due to their strongly confined electromagnetic field at the metal surface. New techniques based on attenuated-total-reflection (ATR) were proposed by Otto, Raether and Kretschmann around the 1970's to optically excite surface plasmons [12]. These techniques facilitated the study of surface plasmon, which in turn quickly led to a new class of sensors called surface plasmon resonance (SPR) sensors [13].

1.2. Recent developments

The considerable advances in nanotechnology made in recent years imply that metal structures can be fabricated at the nanometre scale. This enables surface plasmon properties to be tailored such that light can be controlled and manipulated at the nanoscale, which offers opportunities for new types of photonic devices. A brief overview of the recent development in the research field of plasmonic is given in the present section.

One important aspect of SPP modes is the possibility to confine and channel light with subwavelength structures. The strong mode confinement as compared to conventional optical waveguides could be particularly useful in view of waveguide miniaturization and high density integrated photonic circuits [14]. The SPP propagation length, which constitutes the main limitations of SPP based waveguides, can be increased in several ways, for example exciting the antisymmetric mode sustained by thin metal films. Light needs also to be confined laterally. To achieve this, different schemes have been proposed, such as metal stripes [15-18], grooves [19,20] and particle chains [21,22]. SPP-based optical elements for photonic circuits such as lenses, mirrors, beam splitters, multiplexers and resonators have also been demonstrated [23-28]. SPP-based elements are intrinsically two-dimensional elements, which make them particularly suited for highly integrated optical circuits.

The strong field confinement close to the metal surface means that SPP excitation strongly depends on the local dielectric environment. The binding of molecules on the metal surface induces a modification of the surrounding permittivity, which in turn leads to a change in the SPP coupling efficiency. This is the principle behind SPP-based sensing, which has been demonstrated with both metal films and particles [29]. SPP-based sensing is now a mature technology and commercial instruments have been developed [30].

The strong field enhancement induced locally by SPP excitation at rough metal surfaces or particles has been used in several spectroscopy techniques and particularly to enhance the Raman signal [29,31-34] and infrared absorption [35]. The localized SPP resonance of particles can induce heating of its surroundings. This local heating has been optimized and tuned to the infrared spectral range and employed to photothermally ablate cancer cells [36,37]. The advantage of photothermal therapies as compared to other techniques is that it can eliminate only the targeted affected tissues without destroying nearby healthy ones.

The unique properties of SPP modes have also been considered in many other areas among them super-resolution [38,39], negative refraction [40] or omnidirectional absorption

[41].

One topic of interest for this thesis is enhanced optical transmission through subwavelength apertures in metal films. There is no propagating mode inside subwavelength holes in a metal, and therefore only a small portion of the light is transmitted through them. However, it was observed by Ebbesen *et al.* [42] that the transmission is strongly enhanced at particular wavelengths when holes are placed in a periodic array similar to the one shown in Fig. 1.2(a). The normalized transmission, which is defined as the ratio between the light that illuminates an aperture to the one transmitted by this aperture, is shown in Fig. 1.2(c) for square arrays of $N \times N$ holes. A strong enhancement is observed in the case of hole arrays as compared to the case of a single hole, represented by the black solid line. For a sufficiently large array, the transmission can be greater than unity. This means that light transmitted by a hole can be greater than that impinging on it. The enhanced light transmission phenomenon through hole arrays has been explained by the excitation of SPP's on the film surface [43,44]. More generally, the excitation of surface modes of any type can enhance light transmission through subwavelength hole arrays, like spoof SPP's in the case of perfect metals [45] or dielectric waveguide surface modes in the case of transverse electric (TE) polarization [46].

The phenomenon of enhanced optical transmission has been heavily studied, both from a theoretical and an experimental view point [47,48]. One important aspect regarding enhanced optical transmission is the type of aperture considered [49,50]. The possibility to couple incident light with a propagating mode inside the aperture as is the case in slits for transverse magnetic (TM) polarized light can lead to a transmission of unity in a lossless systems [51].

It has also been shown that the transmission can be enhanced for a single aperture flanked by periodic corrugations [52,53]. An example of such structure is shown in Fig. 1.2(b). The periodic structure converts incident waves into SPP waves which propagate towards the single aperture. Light directly incident on the aperture and SPP's can constructively interfere, increasing the overall transmission, as observed in Fig. 1.2(d).
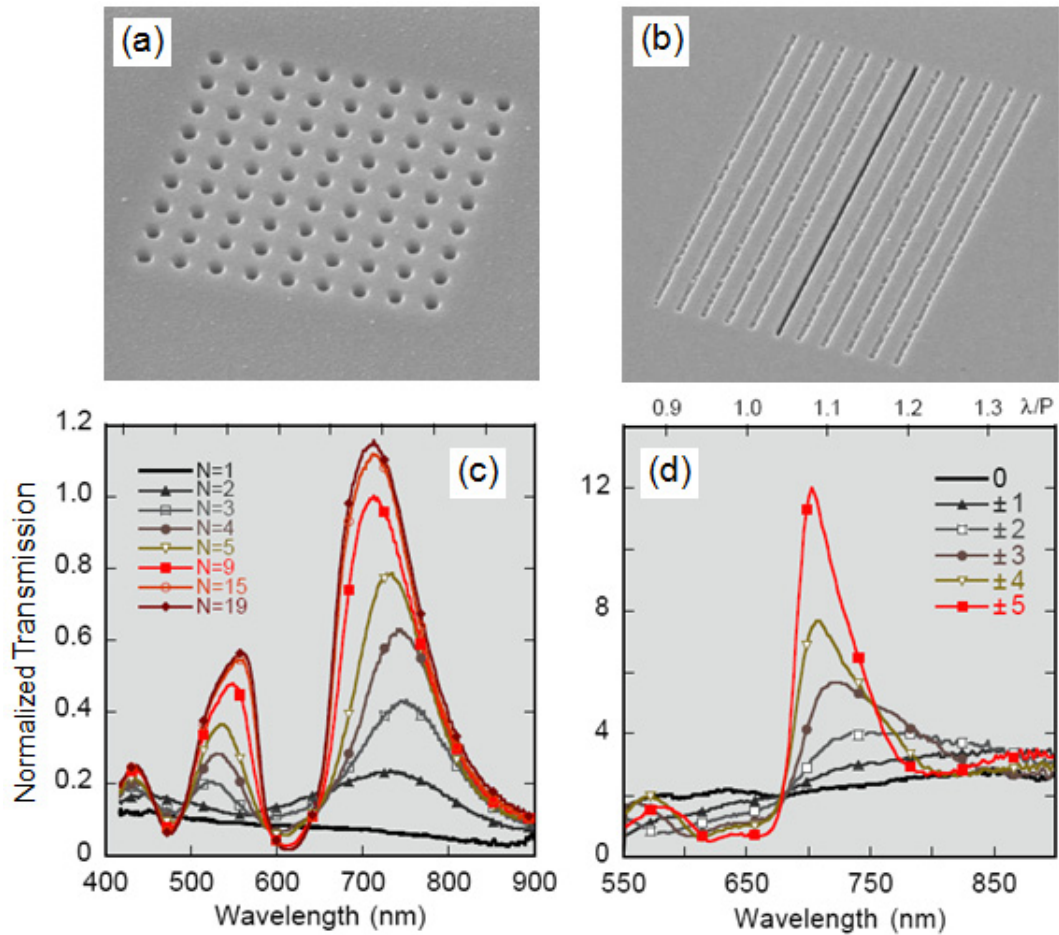
Figure 1.2. Scanning electron microscope (SEM) images of (a) an array of 9 × 9 holes (diameter 150 nm, periodicity 410 nm) in a silver film and (b) a single slit surrounded by 5 grooves (slit width 100 nm, period 650 nm). Panel (c) shows the corresponding transmission measurements of hole arrays for different hole numbers and (d) the transmission through slit and groove structures for different groove numbers. Adapted from [54].

1.3. Objective of the thesis

The objective of this thesis is to study theoretically and experimentally light transmission through nanostructured metal films and use these structures to enhance the properties of optical devices. As stated in Section 1.2, the transmission is considerably increased when propagating modes are sustained inside apertures like slits. The work of this thesis consequently concentrates on slits.

The properties of metals are discussed in Chapter 2 together with optical phenomena which will be used in the subsequent chapters. The use of slits to enhance optical devices efficiency requires a good understanding of the transmission process as well as adequate simulation tools. In view of this, Chapter 3 is dedicated to the description of the transmission mechanism through slits. The waveguide modes inside slits are derived and the notion of propagating and evanescent modes is introduced. It is shown that there is always a propagating mode inside slits for transverse magnetic (TM) polarization, no matter how narrow the slits are. This mode plays a major role in the high TM transmission through single slits, slit and groove structures and slit arrays. The transmission properties of slit arrays are then studied in details. A modal expansion method is used to calculate the transmission through slit arrays. Plotting the transmission for different geometrical parameters, it is observed that high transmission peaks are due to the excitation of hybrid modes. To facilitate the description of these hybrid modes, an analytical form of the modal expansion method is derived and the dispersion relations of the modes responsible for transmission are expressed. This theoretical study on slit arrays gives a clear picture of the transmission process through slit arrays.

Chapter 4 concentrates on transmission measurements through single slits, slit and groove structures and slit arrays. Sample fabrication and measurement process are both detailed. Transmission measurements are compared with theory. Finally, it is demonstrated experimentally that enhanced optical transmission through slit and groove structures can also occur for transverse electric (TE) polarisation when a thin dielectric layer is deposited above the grooves.

The use of slits in a metal film for optical devices is considered in Chapter 5 taking advantage of the work done in Chapter 3 and 4. Three different devices are considered: chemical/biological sensors, light emitting diodes and image sensors. In each case, the need for structured metal films is explained. Metal films structured with slits are designed, and

preliminary experimental results are reported. Limitations and perspectives are finally discussed.

Chapter 2

Optical properties of metals

In this chapter, the permittivity of metals is derived from classical theory. The basic characteristics of surface plasmon polaritons are then introduced, including the dispersion relation, confinement, propagation length, optical excitation and the effect of finite film thicknesses. Finally, important concepts for understanding the following chapters are introduced such as grating diffraction and Fabry-Pérot cavity.

2.1. Permittivity of metals

When an electromagnetic field is present in matter, the electric field **E** can perturb the electron motion and produce a distribution of charges. This leads to a dipole polarization per unit volume **P**:

$$\mathbf{P} = (\varepsilon - 1)\varepsilon_0 \mathbf{E}, \tag{2.1-1}$$

where ε and ε_0 are the permittivity of the material considered and of vacuum respectively. The permittivity determines the optical properties of a given medium and is linked to the refractive index denoted by *RIX* and defined as $RIX = \varepsilon^{1/2}$. In the case of anisotropic media, ε is written as a 3x3 matrix, and in the case of nonlinear media, ε is dependent on the electric field strength. In the present case, ε is considered as a scalar independent on **E**.

To compute the permittivity of a material, it is necessary to incorporate the atomic nature of matter. Hendrik Lorentz developed a very successful model in the late 1800's. His model assumes that all atoms (or molecules) in the medium are identical, each with active electrons responding to the external field. The atoms are uniformly distributed throughout space with n_e identical active electrons per volume. The polarization of the material is then

$$\mathbf{P} = n_e q_e \mathbf{x}, \tag{2.1-2}$$

where q_e denotes the electron charge and **x** the electron displacement from equilibrium. To determine **x**, each electron in the medium is treated as a simple harmonic oscillator: electrons are subject to an elastic restoring force that keeps each electron bound to its respective atom and to a damping force that dissipates energy and gives rise to absorption. The forces involved for an oscillator of mass m_e and charge q_e are then: (i) a driving force produce by **E**; (ii) a restoring force $K\mathbf{x}$ with K the spring constant; (iii) a damping force $m_e \gamma \dot{\mathbf{x}}$, γ being a damping constant. Applying Newton's second law:

$$q_e \mathbf{E} - m_e \gamma \dot{\mathbf{x}} - K\mathbf{x} = m_e \ddot{\mathbf{x}}. \tag{2.1-3}$$

Taking the electric field to be time harmonic with frequency ω, the solution to Eq. (2.1-3) is:

$$\mathbf{x} = \frac{(q_e / m_e)\mathbf{E}}{\omega_0^2 - \omega^2 - i\gamma\omega}. \tag{2.1-4}$$

From Eq. (2.1-1), (2.1-2) and (2.1-4), we obtain:

10

$$\varepsilon(\omega) = 1 + \frac{\omega_p{}^2}{\omega_0{}^2 - \omega^2 - i\gamma\omega}, \qquad (2.1\text{-}5)$$

where $\omega_0 = K/m_e$ and ω_p is the plasma frequency:

$$\omega_p = \left(\frac{q_e{}^2 n_e}{\varepsilon_0 m_e}\right)^{1/2}. \qquad (2.1\text{-}6)$$

In the case where the medium considered is a metal, electrons do not experience a restoring force and are free to move independent of atoms. The electrons in a conductor are a special case of Eq. (2.1-5) where the restoring "spring" constant K, and hence ω_0, is zero. The permittivity is then given by:

$$\varepsilon(\omega) = 1 - \frac{\omega_p{}^2}{\omega^2 + i\gamma\omega}, \qquad (2.1\text{-}7)$$

Neglecting damping, one sees that for $\omega < \omega_p$, $\varepsilon(\omega)$ is negative and for $\omega > \omega_p$, $\varepsilon(\omega)$ is positive. The light matter interaction for such material can then be strongly modified by changing the light frequency. Consider a wave propagating in such medium. The electric field amplitude E for a wave propagating in a direction y satisfying Maxwell's equations can be written in the following form:

$$E = E_0 \exp\left(i\varepsilon^{1/2} k_0 y\right), \qquad (2.1\text{-}8)$$

where E_0 is the electric field amplitude at $y = 0$, $k_0 = \omega/c = 2\pi/\lambda$ is the wavenumber in vacuum, c the speed of light, λ the wavelength and a time harmonic dependence of frequency ω is assumed.

For $\omega < \omega_p$, $\varepsilon^{1/2}$ is imaginary, thus the wave amplitude is exponentially decaying in the y direction. As the intensity is proportional to the square of the field amplitude, the intensity decays as $\exp(-2\varepsilon^{1/2} k_0 y)$ with $\alpha_{at} = 2\varepsilon^{1/2} k_0$ is the attenuation constant. This leads to the definition of the skin or penetration depth δ corresponding to the distance for which the intensity drops by a factor of e^{-1}, i.e.

$$\delta = \frac{1}{2\Im\left(\sqrt{\varepsilon}\right) k_0} \qquad (2.1\text{-}9)$$

For noble metals such as Au, Ag, Al or Cu, the skin depth is generally exceedingly small at visible wavelengths. For example, the skin depth for either gold or silver is between 10 to 20 nm in the visible-near infrared spectral range. Light incident on such metals does not

penetrate and is mainly reflected. This constitutes the basic optical property of a metal. As ε becomes more negative, the penetration into the metal is reduced.

At $\omega = \omega_p$, ε vanishes. The plasma oscillation originates from the long-range correlation of the electrons caused by Coulomb forces.

For $\omega > \omega_p$, $\varepsilon^{1/2}$ is real, leading to an oscillating field propagating in the y direction. The medium considered does not behave as a metal from an optical point of view and is transparent. This can be seen as the fact that the electrons cannot oscillates as fast as ω.

The model leading to Eq. (2.1-7) is known as the Drude model. To show the validity of this model, the experimental values of the real ($\Re$) and imaginary ($\Im$) parts of ε for gold are plotted in Fig. 2.1. These values, tabulated in Appendix 1, are obtained from the Sopra database [55]. If not mentioned, these values are the ones considered in the different calculations performed in this thesis. The permittivity values obtained from Eq. (2.1-7) are then represented by dashed lines with the parameters ω_p = 8.89 eV and γ = 0.07 eV [56]. Despite its simplicity, the Drude model gives a relatively good qualitative description of the dielectric function in metals. The deviations observed in Fig. 2.1 are mainly caused by interband transition in gold, which are not accounted for in the model presented here [57]. Whereas more refined models can be found [58,59], the Drude model is convenient for the insight it gives on the optical properties of metals.
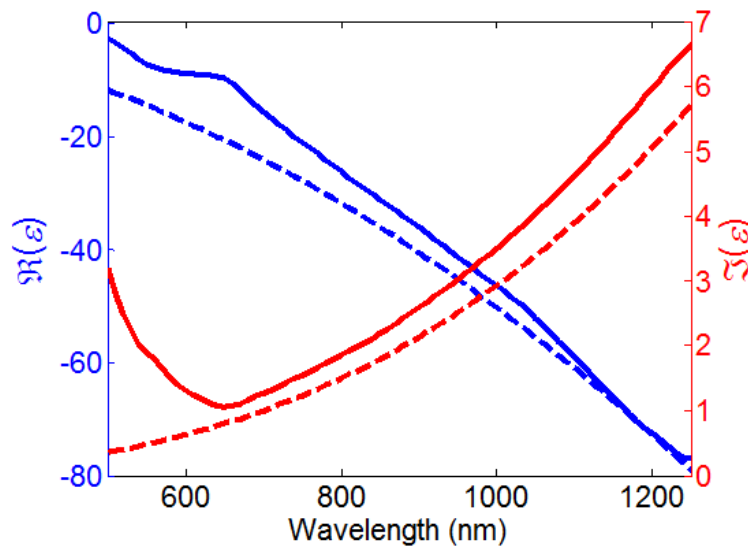
Figure 2.1.   Real and imaginary parts of the gold permittivity, calculated with the Drude model with parameters ω_p = 8.89 eV and γ = 0.07 eV (dashed line) and experimental data (solid line).

In the case where γ is much smaller than both ω and ω_p, which is the case for metals

like gold or silver in the visible, the real and imaginary parts of the permittivity can be approximated as [60]:

$$\Re(\varepsilon) \approx 1 - \frac{\omega_p^2}{\omega^2},$$ (2.1-10)

$$\Im(\varepsilon) \approx \frac{\gamma\omega_p^2}{2\omega^3},$$ (2.1-11)

This shows that the losses, through the damping term γ, are contained in the imaginary part of ε.

2.2. Surface plasmon polaritons

The derivation of the metal permittivity from the Drude model shows that optical properties are intrinsically linked to the oscillatory behaviour of electrons within the metal. Plasma oscillations can occur at a metal dielectric interface and are called surface plasmons. As these oscillations interact with light the oscillations are called surface plasmon polaritons (SPP's). From an electromagnetic point of view, SPP's can be seen as electromagnetic waves confined at a metal-dielectric interface which interact with collective oscillation of free surface charges of the metal [12], as shown in Fig. 2.2.
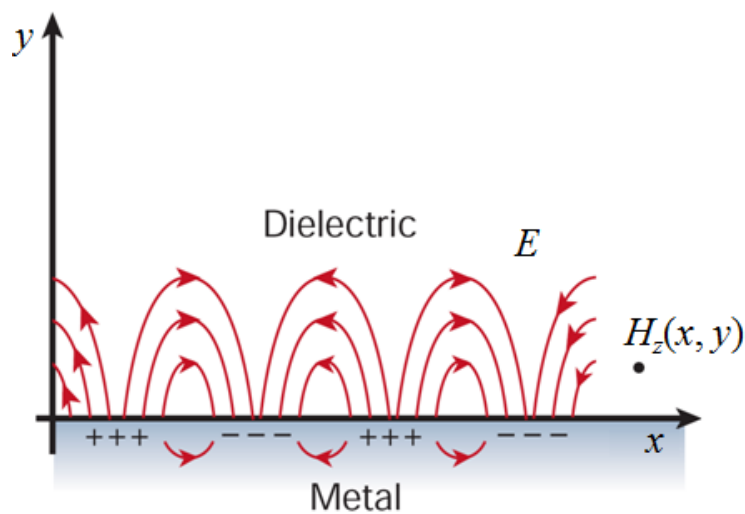
Figure 2.2.   Schematic of SPP's at the interface between a metal and a dielectric material showing the combined electromagnetic wave and surface charge oscillation character. Adapted from Ref. [14].

2.2.1.   Dispersion relation

The SPP dispersion relation is derived from Maxwell's equations: consider a metal medium of dielectric function ε_1 in the half space $y < 0$ and a dielectric medium of dielectric constant ε_2 in the half space $y > 0$ where ε_2 is assumed to be real; see Fig. 2.2. We are looking at a wave propagating at the metal-dielectric interface, i.e. along the x direction, with parallel wave vector β. In each medium, the wave amplitude decays exponential in the y direction. No confined modes are sustained by the metal film in the transverse electric (TE) case, i.e. when the electric field in the z direction. In the transverse magnetic (TM) case, the magnetic field is in the z direction and can be written:

14

$$H_{z1}(x,y) = A_1 \exp[i(\beta x - \chi y)] \text{ for } y < 0, \tag{2.2-1}$$

$$H_{z2}(x,y) = A_2 \exp[i(\beta x + \mu y)] \text{ for } y > 0, \tag{2.2-2}$$

with

$$\begin{aligned} \mu^2 &= \varepsilon_2 k_0{}^2 - \beta^2 \\ \chi^2 &= \varepsilon_1 k_0{}^2 - \beta^2 \end{aligned}, \tag{2.2-3}$$

where μ and χ are the transverse components of the wave vectors in the dielectric and metal respectively, A_1 and A_2 the amplitude of the field in the metal and the dielectric respectively. The tangential components of the electromagnetic fields should be continuous at the boundary. Therefore, at $y = 0$:

$$H_{z1}(x,0) = H_{z2}(x,0), \tag{2.2-4}$$

$$\frac{1}{\varepsilon_1} \frac{\partial}{\partial y} H_{z1}(x,0) = \frac{1}{\varepsilon_2} \frac{\partial}{\partial y} H_{z2}(x,0), \tag{2.2-5}$$

which give:

$$A_1 = A_2, \tag{2.2-6}$$

$$\varepsilon_1 \mu = -\varepsilon_2 \chi. \tag{2.2-7}$$

Equation (2.2-3) together with Eq. (2.2-7) then gives the following dispersion relation:

$$\beta = k_0 \left(\frac{\varepsilon_1 \varepsilon_2}{\varepsilon_1 + \varepsilon_2} \right)^{1/2}. \tag{2.2-8}$$

The dispersion curve obtained from Eq. (2.2-8) is plotted in Fig. 2.3 for a metal-air interface ($\varepsilon_2 = 1$) considering the Drude model. For simplicity, losses are neglected, i.e. $\gamma = 0$. The ordinate and abscissa axes are normalized by ω_p and $k_p = \omega_p/c$ respectively. The black solid line represents the light line ($\beta = \varepsilon_2{}^{1/2} k_0$) and the red area defines the light cone ($\beta < \varepsilon_2{}^{1/2} k_0$) inside which a wave is radiative and outside which it is evanescent. From Fig. 2.3, three different regimes are observed:

(i)   At low frequencies, the dispersion line is tangent to the light line with β larger than $\varepsilon_2{}^{1/2} k_0$. Inserting β in Eq. (2.2-1) and (2.2-2) shows that we are in presence of a wave propagating in the x direction, and the fact that $\beta > \varepsilon_2{}^{1/2} k_0$ implies that μ and χ are both imaginary, i.e. the wave exponentially decays in the y direction and is confined at the surface. The SPP wave vector increases monotonically from $\omega = 0$ to the asymptotic value:

$$\omega = \frac{\omega_p}{\sqrt{1+\varepsilon_2}} , \qquad\qquad (2.2\text{-}9)$$

which corresponds to the case $\varepsilon_1 = -\varepsilon_2$ represented by the black dashed line.

(ii)   For $\omega_p/(1+\varepsilon_2)^{1/2} < \omega < \omega_p$, $|\varepsilon_1| < |\varepsilon_2|$ and we see from Eq. (2.2-8) that β is imaginary, i.e. the wave does not propagates along the x axes. This shows that it is necessary to have $|\varepsilon_1| > |\varepsilon_2|$ for a metal dielectric interface to sustain SPP's.

(iii)   Above ω_p, $\varepsilon_1 > 0$ and the dispersion line is inside the light cone. This does not correspond to a surface wave. In fact, this line determines the locus of the Brewster angle. This is explained by the fact that Eq. (2.2-8) is not only the solution of Eq. (2.2-7) but also the solution of $\varepsilon_1\mu = \varepsilon_2\chi$, corresponding to the Brewster condition at which the reflection between two media is zero [61].
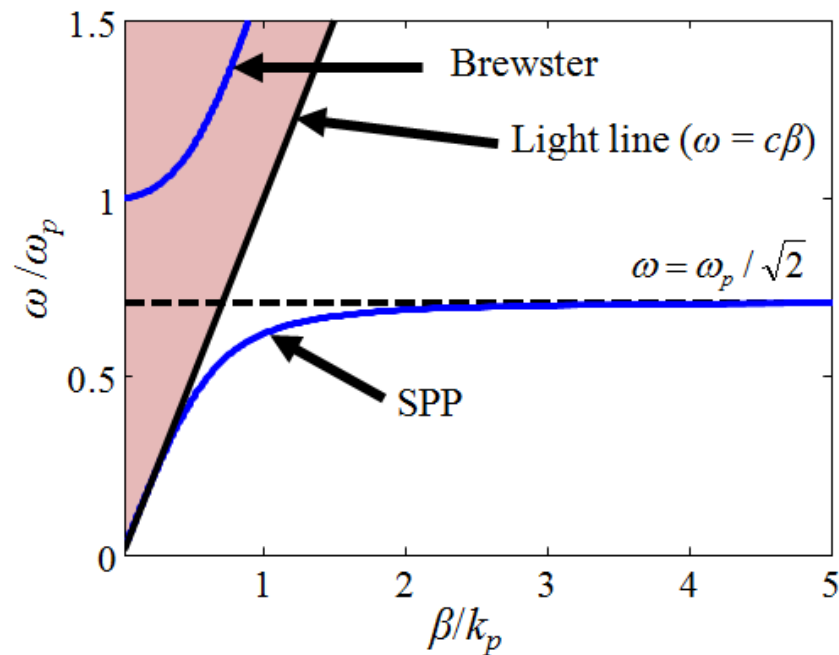
Figure 2.3.   Dispersion relation calculated from Eq. (2.2-8) for a metal-air interface considering the Drude model. The black solid line represents the light line and the red area defines the light cone.

To summarize, a condition for a metal-dielectric interface to sustain SPP's is $|\varepsilon_1| > |\varepsilon_2|$, with $\varepsilon_1 < 0$. This condition insures $\beta > \varepsilon_2^{1/2}k_0$, i.e. the wave considered is non-radiative, or in other terms bounded to the surface.

2.2.2.   SPP confinement and losses

Three different lengths characterizing SPPs are defined here. Two of them, the penetration depths of the mode into the dielectric and the metal, δ_d and δ_m respectively, characterize the strength of the light confinement. Whereas in other studies these depths are defined as the distance before which the field is reduced by e^{-1} [12,62], we prefer to be consistent with the definition of the skin depth defined in Eq. (2.1.9) considering the wave intensity. The penetration depths are then given by:

$$\delta_d = \frac{1}{2\Im(\mu)} \tag{2.2-10}$$

$$\delta_m = \frac{1}{2\Im(\chi)} \tag{2.2-11}$$

The remaining length scale defined here is the SPP propagation length δ_{SPP}, the distance the SPP wave travels along the surface before its intensity is diminished by e^{-1}:

$$\delta_{SPP} = \frac{1}{2\Im(\beta)} \tag{2.2-12}$$
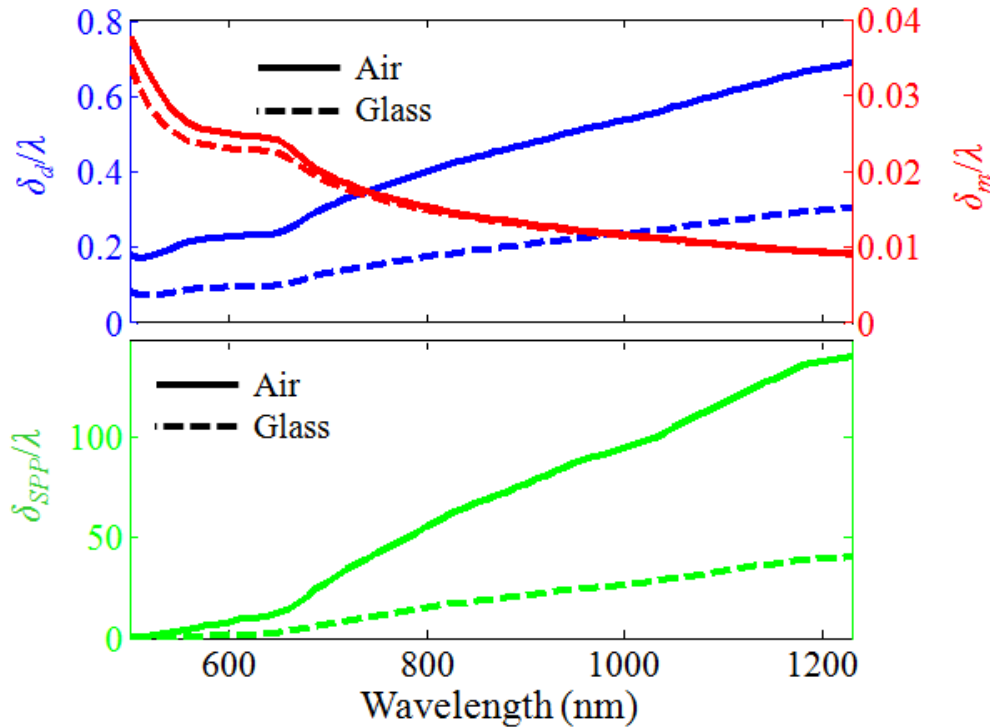
Figure 2.4.   Characteristics lengths of the SPP mode for a gold-air (solid lines) and a gold-glass (dashed lines) interfaces. The gold permittivity corresponds to the experimental values plotted in Fig. 2.1, and the glass dielectric constant is $\varepsilon_2 = 2.25$.

The three different lengths defined above are represented in Fig. 2.4 by solid and dashed lines for a gold-air and a gold-glass interface respectively. The gold permittivity corresponds to the experimental values plotted in Fig. 2.1, and the glass dielectric constant is $\varepsilon_2 = 2.25$. The lengths are normalized to the wavelength so that the effect of the dielectric constant can be observed. One sees that both the mode confinement on the air side ($\delta_d \approx \lambda/5$) and the field penetration inside the metal ($\delta_m \approx \lambda/25$) is highest at shorter wavelengths, where $\Re(\varepsilon_1)$ is the less negative. This is concomitant with a shorter SPP propagation. At longer wavelengths, the field extends further to the air ($\delta_d \approx \lambda$) and penetrates less inside the metal. The SPP mode is closer to an air mode, with low surface confinement. As a consequence, δ_{SPP} is larger as the mode is less affected by losses induced by the metal. In the case of glass, the increase of ε_2 as compared to air induces a higher mode confinement at the surface. This increases the mode losses and consequently decreases δ_{SPP}. From these calculations, one sees that the mode losses increase with mode confinement. Both mode confinement and losses are increased as $|\Re(\varepsilon_1)|$ approaches ε_2.

2.2.3. SPP excitation

In order to couple optical propagating waves to SPP waves, two requirements should be fulfilled:

(i)   The frequency of the incident and excited waves should be identical to satisfy energy conservation;

(ii)   The parallel wavevector of each wave must be equal to satisfy momentum conservation.

It was shown previously that for any frequency, the SPP dispersion relation gives $\beta > \varepsilon_2^{1/2}k_0$, i.e. the SPP wave vector is always larger than any longitudinal wave vector of propagating modes in air $k_{x,0}$ defined as:

$$k_{x,0} = \sqrt{\varepsilon_2}\, k_0 \sin\theta,$$ (2.2-13)

where θ is the angle of incidence. Thus it is not possible to excite SPP's at a flat metal-dielectric interface from a propagating mode in the dielectric. Specific coupling techniques are necessary to optically excite SPP waves. The most common techniques are described below.

2.2.3.1. Grating coupler

One way to couple light into SPP's is to structure the surface. Any sub-wavelength

irregularity on an otherwise flat surface scatters incident light into a continuum of wave vectors. In the case of a metal surface, some of these wave vectors will match the SPP one and coupling into SPP waves occurs.

Light coupling to SPP's can be enhanced placing the surface irregularities periodically, i.e. using a diffraction grating. The diffraction grating principle is depicted in Fig. 2.5. Here light can either be incident on or transmitted through the grating. From Huygens principle [59], each irregularity behaves as a new point source which generates a radial wave. These waves interfere and form new wave fronts, generating diffracted orders depending on their relative phase. This is represented in Fig. 2.5 by the straight red, purple, blue and green lines, which leads to the 0th, 1st, 2nd and 3rd diffracted order respectively. The parallel wave vector $k_{x,n}$ of each diffracted order is modified as compared to the one of the incident wave $k_{x,0}$, giving:

$$k_{x,n} = k_{x,0} + n\frac{2\pi}{p} \tag{2.2-14}$$

with n an integer related to the nth diffracted order and p the grating period.
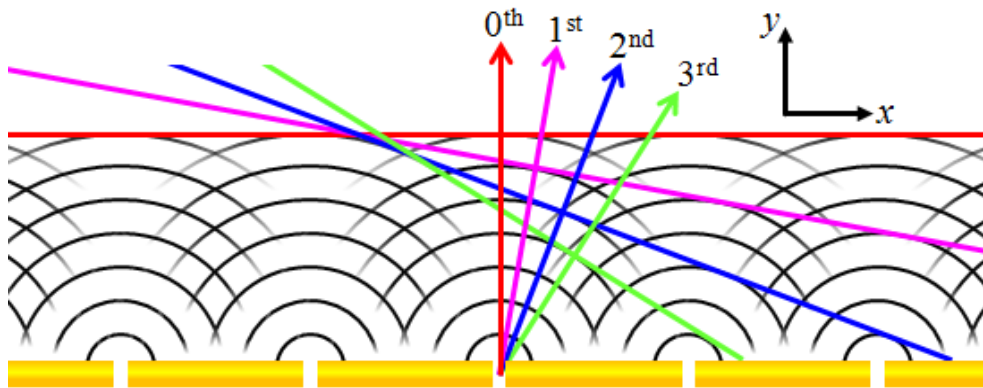
Figure 2.5.   Schematic of light diffraction by a grating leading to the formation a new wave fronts for $\lambda/(\varepsilon_2^{1/2}) = 5.6p$. The 0th, 1st, 2nd and 3rd diffracted order are represented by the straight red, purple, blue and green lines respectively.

From Eq. (2.2-14), one sees that $k_{x,n}$ can be greater than $\varepsilon_2^{1/2}k_0$. This means that wave with such wavevector are evanescent. An example of this is shown in Fig. 2.6: for light incident on the grating at the frequency and parallel wave vector represented by the purple dot, light is diffracted and the parallel wave vector is modified by $n2\pi/p$, as represented by the blue arrows. The different $k_{x,n}$ values defined by Eq. (2.2-14) and represented by green dots are allowed. Under the condition $\beta = k_{x,n}$, SPP excitation occurs. For normal incidence ($\theta = 0$),

the SPP coupling condition is given by:

$$\lambda = \frac{p}{n} \sqrt{\varepsilon_2} \sqrt{\frac{\varepsilon_1}{\varepsilon_1 + \varepsilon_2}} \qquad (2.2\text{-}15)$$
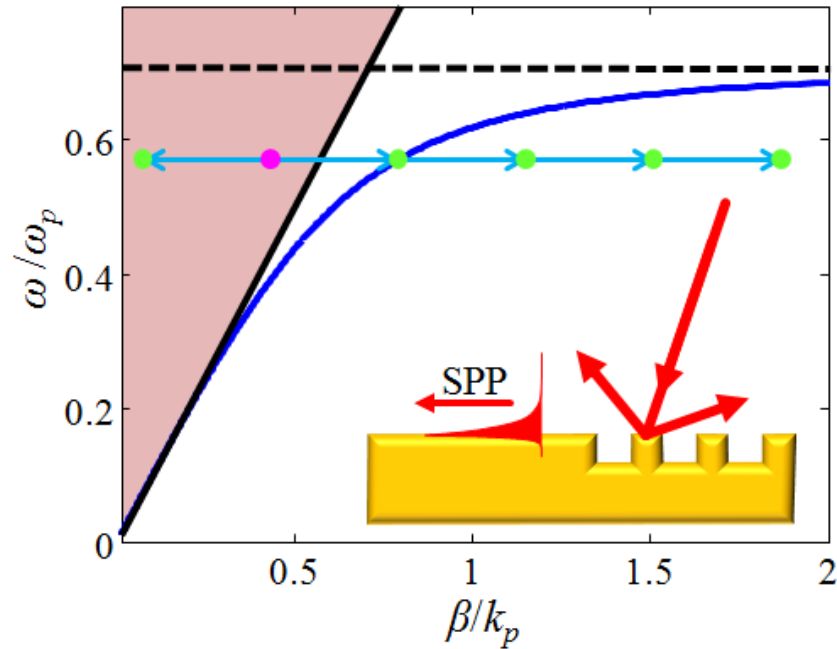
Figure 2.6.   Illustration of an SPP excitation with a grating. The figure is a close-up of the dispersion relation shown in Fig. 2.3. Waves diffracted by a grating can take discrete values, as represented by the green dots. The inset shows the experimental arrangement of the grating coupler.

2.2.3.2.   Attenuated total reflection

Techniques based on attenuated-total-reflection (ATR) to optically excite SPP waves were proposed by Otto, Raether and Kretschmann around 1970 [12]. Consider an SPP excitation at a metal-air interface. If the metal is illuminated through a glass prism of dielectric constant ε_2 such that $\varepsilon_2 > 1$, we see from Eq. (2.2-13) that $k_{x,0}$ is increased by $\varepsilon_2^{1/2}$ as compared to the air case. Consequently, the light cone is "increased" from k_0 to $\varepsilon_2^{1/2}k_0$, as shown in Fig. 2.7(a). With such increase of the wavevector of the incident light, it is then possible to excite SPP's at a metal-air interface.

Two configurations using a prism coupler are possible, see Fig. 2.7(b). The metal and the prism can be separated by an air space, as shown in the left part of Fig. 2.7(b). In this case, light totally internally reflected inside the prism leads to an evanescent field at the prism surface with $k_{x,0} = \varepsilon_2^{1/2}k_0\sin\theta$. If the metal interface is placed within this evanescent field, e.g.

less than a wavelength away, light can couple to SPP's at the condition $k_{x,0} = \beta$. In the second scheme, the metal film has a thickness smaller than the skin depth (cf. Section 2.1) and is deposited on the prism. Light tunnels evanescently through the metal with $k_{x,0} = \varepsilon_2^{1/2} k_0 \sin\theta$, and SPP coupling can occur at the air side of the metal film. In both cases, the SPP excitation is recognized as a minimum in the intensity reflected inside the prism.
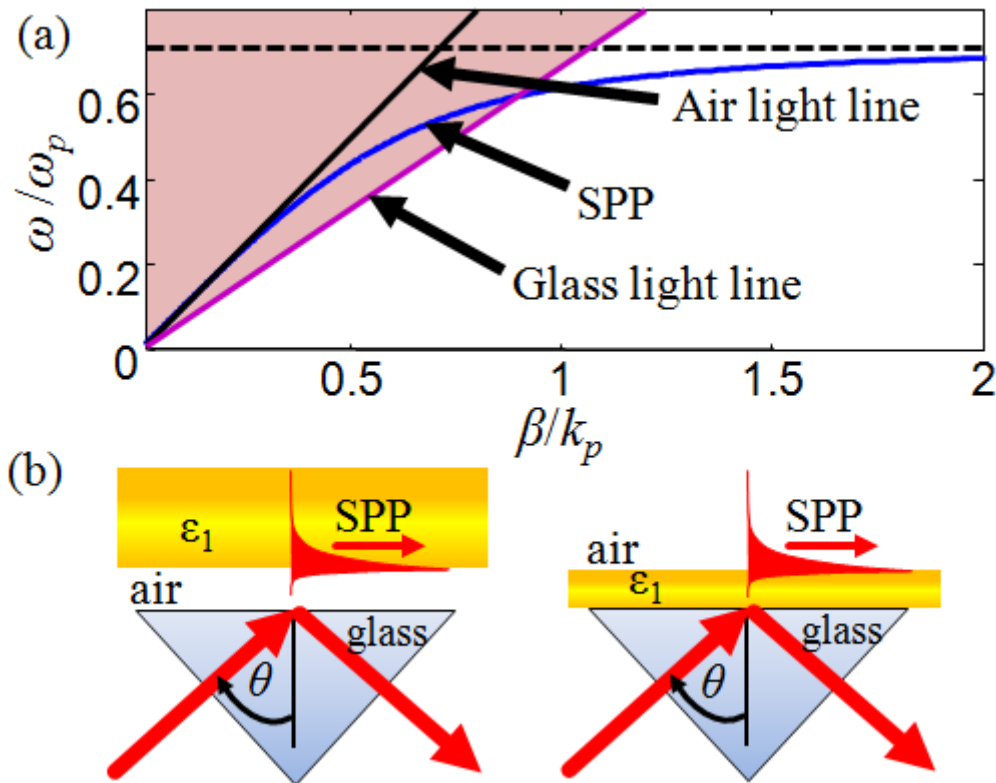
Figure 2.7.   SPP excitation from the ATR method. (a) Close-up of the dispersion relation shown in Fig. 2.3 with the air (black solid line) and glass (purple solid line) light lines. (b) Experimental arrangements of the Otto (left part) and Raether-Kretschmann (right part) configuration.

2.2.4.   SPP dispersion relation in the case of thin films: derivation from a Fabry-Pérot cavity

We saw that one way to optically couple SPP's is to use thin metal films. With such films, the SPP dispersion relation is modified as the two SPP's waves excited on both sides of the film can couple. The SPP dispersion relation in the case of thin films can be derived from Maxwell's equations together with the boundary conditions at each interface as done in Section 2.2.1. This approach will be used in Chapter 3 for the mode derivation of a metal

dielectric metal waveguide. Consequently, we prefer to consider here the resonance of the transmission through the thin film. This introduces the concept of Fabry-Pérot (FP) cavity, which is invoked several times in the next Chapters.
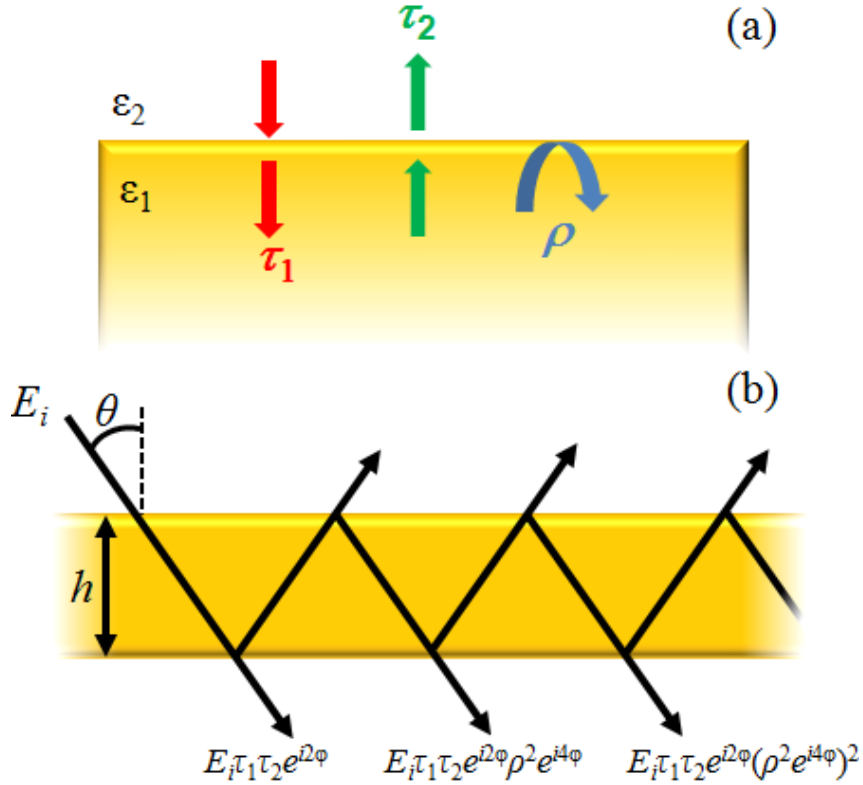
Figure 2.8.   (a) Schematic defining the reflection and transmission coefficient at a single interface. (b) Schematic of the FP cavity principle: a wave transmitted through a thin film experiences multiple reflections, leading to the interference between the transmitted waves.

Consider a film of permittivity ε_1 and thickness h surrounded by a medium of permittivity ε_2, as shown in Fig. 2.8. This medium is considered identical on both sides of the film for simplicity. A TM wave is incident on the film at an angle θ with field amplitude E_i. In the case of a propagating wave inside the film, multiple reflections occur as schemed in Fig. 2.8(b). The field amplitude transmitted E_t is then the sum of an infinite number of waves:

$$E_t = E_i \tau_1 \tau_2 e^{i2\varphi} \left[1 + \rho^2 e^{i4\varphi} + \left(\rho^2 e^{i4\varphi} \right)^2 + ... + \left(\rho^2 e^{i4\varphi} \right)^n + ... \right], \qquad (2.2\text{-}16)$$

where $2\varphi = h\chi$ corresponds to the phase accumulated by a wave after a single pass through the film, τ_1 and τ_2 are the transmission coefficients at the air metal and metal air interface respectively and ρ the reflection coefficient of a wave at the metal dielectric interface, see Fig.

2.8(a). The coefficients τ_1, τ_2 and ρ are obtained from Fresnel formulae [59]:

$$\tau_1 = \frac{2\varepsilon_1\mu}{\varepsilon_2\chi + \varepsilon_1\mu},$$
(2.2-17)

$$\tau_2 = \frac{2\varepsilon_2\chi}{\varepsilon_2\chi + \varepsilon_1\mu},$$
(2.2-18)

$$\rho = \frac{\varepsilon_2\chi - \varepsilon_1\mu}{\varepsilon_2\chi + \varepsilon_1\mu},$$
(2.2-19)

From Eq. (2.2-16), the transmission amplitude t of the thin film is:

$$t = \frac{E_i}{E_t} = \frac{\tau_1\tau_2 e^{i2\varphi}}{1 - \rho^2 e^{i4\varphi}}$$
(2.2-20)

and the transmission power is $T = |t|^2$. The transmission presents maxima at the minima of the determinant of Eq. (2.2-20), i.e. for the condition

$$\chi h + \arg(\rho) = \pi l$$
(2.2-21)

where l is an integer and $\arg(\rho)$ is the argument of ρ. Physically, this corresponds to the case where all waves are transmitted in phase through the film.

The FP equation allows us to derive the SPP modes of the thin film from the poles of t, corresponding to the zeros of the determinant of Eq. (2.2-20). Together with Eq. (2.2-19), this gives:

$$\left(\varepsilon_2\chi + \varepsilon_1\mu\right)^2 e^{-2\varphi} - \left(\varepsilon_2\chi - \varepsilon_1\mu\right)e^{2\varphi} = 0,$$
(2.2-22)

leading to the following dispersion relations:

$$\chi \tan\left(\chi\frac{h}{2}\right) = -i\frac{\varepsilon_1}{\varepsilon_2}\mu,$$
(2.2-23)

$$\chi \cot\left(\chi\frac{h}{2}\right) = i\frac{\varepsilon_1}{\varepsilon_2}\mu.$$
(2.2-24)

Solutions to Eq. (2.2-23) and (2.2-24) are represented by red and blue curve respectively in Fig. 2.9. The thickness considered is $k_p h = 1.35$. For $\omega_p = 8.89$ eV, as used in Fig. 2.1 to model gold permittivity, this corresponds to a metal thickness $h = 30$ nm. As compared to the "bulk" SPP curve (green line), the thin film leads to a splitting of the modes: a high frequency SPP mode ω^+ and a low frequency SPP mode ω^-. As shown schematically in Fig. 2.9, the ω^+

and the ω^- SPP mode presents an antisymmetric and symmetric field profile respectively. The antisymmetric mode is closer to an air mode. Consequently, it is less affected by the metal losses as compared to the symmetric mode. Therefore the antisymmetric mode has a longer propagation length, and has been called long-range SPP mode. Inversely, the symmetric mode has been named short range SPP mode.
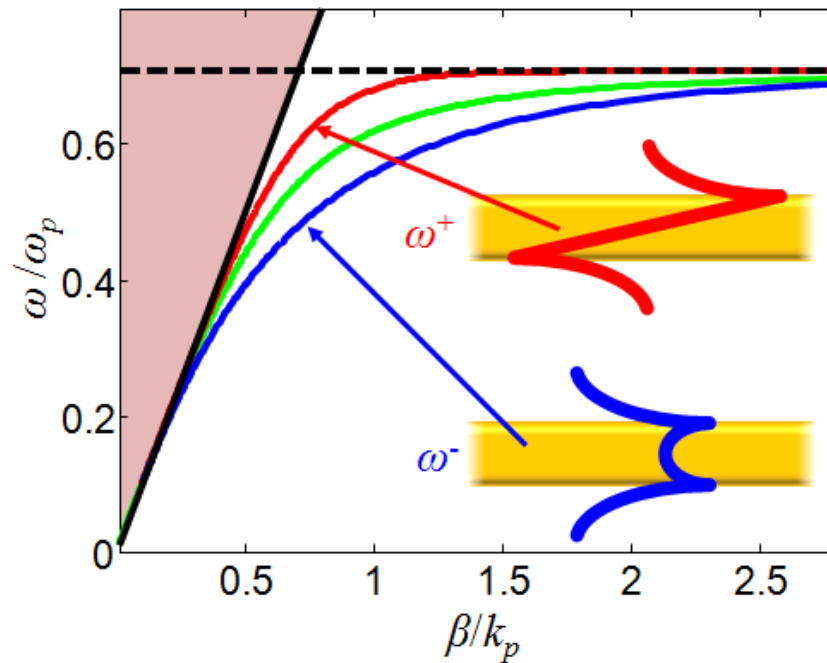
Figure 2.9.   Dispersion relation of SPP's in the case of a thin metal film with $k_ph = 1.35$, i.e. for $\omega_p = 8.89$ eV as in Fig. 2.1, $h = 30$ nm. The inset is a schematic of the field profile of the two different modes. The green line represents the unperturbed SPP mode.

We saw in Section 2.1 that inside a metal with $\varepsilon_1 < 0$, waves do not propagate and χ is complex. Consequently, the phenomenon of multiple reflections as schemed in Fig. 2.8 occurs by evanescent tunnelling through the metal and the coupling at the two surfaces will be exponentially decreased as h is increased.

Chapter 3

Theory of light transmission through subwavelength slits

In this chapter, the optical transmission through subwavelength slits are theoretically investigated. Section 3.1 deals with the case of a single slit. The waveguide modes of a slit are derived, and the conditions leading to enhanced optical transmission phenomenon through a single subwavelength slit are described. The transmission properties of slit arrays are then studied in details in Section 3.2. A modal expansion method is first used to calculate light transmission through slit arrays. It is observed that high transmission is due to hybrid modes. In order to have a better description of these hybrid modes, a simplified analytical form of the modal expansion method is derived and the dispersion relations of the hybrid modes are given. This work helps to assess the roles played by the different uncoupled modes in the transmission process.

3.1. The single slit case

3.1.1. Waveguiding properties of a single slit

The conditions of propagation inside an infinitely long slit in a metal film is now studied. A schematic of the system is represented in Fig. 3.1: a thin dielectric layer, of thickness w and permittivity ε_2 extending to infinity in the y and z directions is sandwiched between two semi-infinite metal regions of permittivity ε_1. Guided waves propagate along the y axis. The study can be separated into the two polarization direction TE and TM polarization, which correspond to the case where the electric field vector **E** and magnetic field vector **H** is transverse to the (x, y) plane respectively.
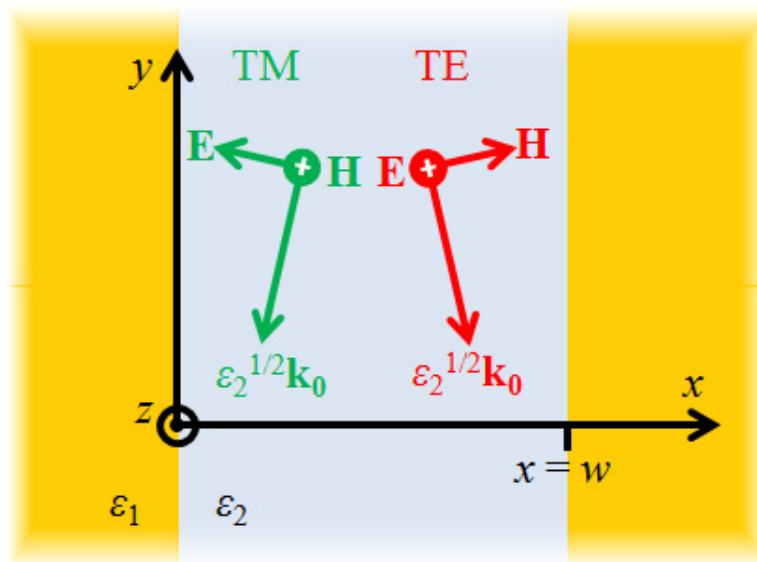
Figure 3.1.   Schematic of the structure studied and definitions used for the structure dimensions and incident field directions.

3.1.1.1. Derivation of the waveguide mode equation

To solve for the guided modes of the system schemed in Fig. 3.1, the method used for dielectric waveguides described in Ref. [63] is followed. The case $|\varepsilon_2| < |\varepsilon_1|$ with the real part of ε_1 being negative is considered. The amplitude $f_z(x, y)$ of the field along the z axis for a given mode and polarization, which should satisfy Maxwell's equations, can be written in the following form:

$$f_z(x, y) = X_m(x)\exp(-i\beta_m y), \tag{3.1-1}$$

where $X_m(x)$ is the field profile of the guided mode, with the subscript m an integer called mode number. β_m is the propagating constant (i.e. the y component of the wavevector) of the mth mode.

The wavefunction is taken as:

$$X_m(x) = \begin{cases} A\sin[\mu_m(x - w/2)] + B\cos[\mu_m(x - w/2)], & 0 < x < w \\ C\exp[i\chi_m(x - w/2)], & x > w \\ D\exp[-i\chi_m(x - w/2)], & x < 0 \end{cases}, \qquad (3.1\text{-}2)$$

where A, B, C and D are constants and μ_m and χ_m, the transverse components of the different wavevectors, are related to the propagating constant by:

$$\begin{aligned} \mu_m^{\;2} &= \varepsilon_2 k_0^{\;2} - \beta_m^{\;2} \\ \chi_m^{\;2} &= \varepsilon_1 k_0^{\;2} - \beta_m^{\;2} \end{aligned}, \qquad (3.1\text{-}3)$$

where $k_0 = 2\pi/\lambda$ is the wavenumber in vacuum.

Note that the imaginary part of χ_m needs to be positive in order to obtain an exponential decay of the field amplitude in the metal, i.e. for $x > w$ and $x < 0$. The tangential components of the electromagnetic fields need to be continuous at the interfaces, i.e.:

$$\begin{aligned} A\sin(\mu_m w/2) + B\cos(\mu_m w/2) &= C\exp(i\chi_m w/2) \\ \mu_m A\cos(\mu_m w/2) - \mu_m B\sin(\mu_m w/2) &= iq\chi_m C\exp(i\chi_m w/2) \\ -A\sin(\mu_m w/2) + B\cos(\mu_m w/2) &= D\exp(i\chi_m w/2) \\ \mu_m A\cos(\mu_m w/2) + \mu_m B\sin(\mu_m w/2) &= iq\chi_m D\exp(i\chi_m w/2) \end{aligned}, \qquad (3.1\text{-}4)$$

with

$$q = \begin{cases} 1 & \text{for TE polarization} \\ \varepsilon_2/\varepsilon_1 & \text{for TM polarization} \end{cases}. \qquad (3.1\text{-}5)$$

From Eq. (3.1-4), two sets of solutions are found. By setting $A = 0$ and $C = D$, symmetric modes correspond to the solutions of the following transcendental equation:

$$\mu_m \tan(\mu_m w/2) = -iq\chi_m. \qquad (3.1\text{-}6)$$

Similarly, with $B = 0$ and $C = -D$, the antisymmetric modes are found from the following equation:

$$\mu_m \cot(\mu_m w/2) = iq\chi_m. \qquad (3.1\text{-}7)$$

3.1.1.2. Graphic solution of the waveguide mode equation

The solutions of the transcendental equations (3.1-6) and (3.1-7) can be found graphically by plotting the equations in the complex plane. Replacing μ_m and χ_m with Eq. (3.1-3), equations (3.1-6) and (3.1-7) are rewritten respectively:

$$\sqrt{\left(\varepsilon_2 k_0^2 - \beta_m^2\right)}\tan\left(\sqrt{\left(\varepsilon_2 k_0^2 - \beta_m^2\right)}w/2\right) + iq\sqrt{\left(\varepsilon_1 k_0^2 - \beta_m^2\right)} = 0, \qquad (3.1\text{-}8)$$

$$\sqrt{\left(\varepsilon_2 k_0^2 - \beta_m^2\right)}\cot\left(\sqrt{\left(\varepsilon_2 k_0^2 - \beta_m^2\right)}w/2\right) - iq\sqrt{\left(\varepsilon_1 k_0^2 - \beta_m^2\right)} = 0. \qquad (3.1\text{-}9)$$

The left hand side of Eq. (3.1-8) and (3.1-9) are plotted in Fig. 3.2(a) and (b) respectively in function of the real ($\Re$) and imaginary ($\Im$) parts of β_m. A gold-air-gold waveguide is considered, with TM polarization, $\lambda = 1500$ nm and $w = \lambda/30$. The symmetric and antisymmetric solutions correspond to the zeros observed in Fig. 3.2(a) and (b) respectively.
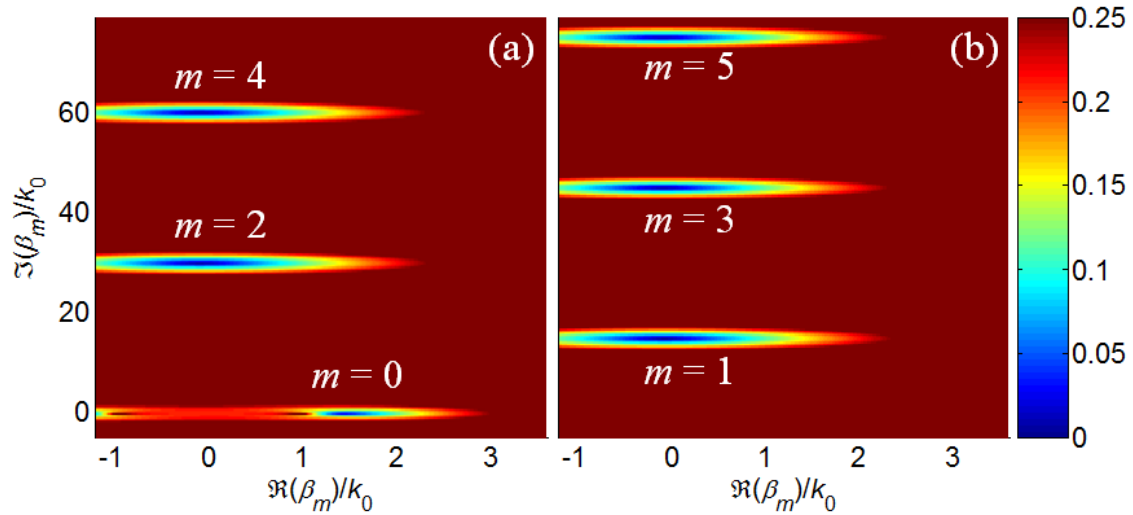
Figure 3.2.   Two dimensional plot of the left hand side of (a) Eq. (3.1-8) and (b) Eq. (3.1-9) as a function of complex β_m values for a gold-air-gold waveguide with $\lambda = 1500$ nm $w = 50$ nm and TM polarization. The axes of the graph are normalized to k_0.

3.1.1.3. Resolution of the propagation constants in the case of a perfect electric conductor

Even if it is possible to obtain graphically the propagation constants, it is advantageous to find the solutions directly. This is not straightforward for real metals. Here we proceed by firstly considering a perfectly electric conductor (PEC), i.e. $\varepsilon_1 \rightarrow -\infty$. Under this condition, Eq. (3.1-6) and (3.1-7) can be rewritten as a single equation:

$$\sin(\mu_m w) = 0 \quad \text{for TE polarization}$$
$$\cos(\mu_m w) = 0 \quad \text{for TM polarization} \qquad \text{(3.1-10)}$$

The solutions to Eq. (3.1-10) are $\mu_m = m\pi/w$, giving the following propagation constants:

$$\beta_m = \sqrt{\varepsilon_2 k_0^2 - (m\pi/w)^2} \ . \qquad \text{(3.1-11)}$$

Note that from the derivation of Eq. (3.1-10), the modes are symmetric for m even and antisymmetric for m odd in the TM polarization case, whereas the inverse applies for TE polarization.

The first β_m values are represented by blue dots in the complex plane in Fig. 3.3 for $w = \lambda/30$. One sees that in the TM polarization case (left graph), $\beta_0 = k_0$. The higher order modes have imaginary propagation constants (some of the blue dots are not seen as they are superimposed by the purple ones). Replacing β_m in Eq. (3.1-1), one sees that a real propagation constant corresponds to a wave propagating in the $-y$ direction and an imaginary propagation constant corresponds to a wave exponentially decaying in the $-y$ direction. This means that for TM polarization, only the $m = 0$ mode is a propagating mode for the slit considered in Fig. 3.3.

In the TE case, the $m = 0$ mode is not a solution because introducing $\mu_0 = 0$ in Eq. (3.1-2) gives $X_0(x) = 0$ (remember that $B = 0$ for antisymmetric modes). As seen in the right graph of Fig. 3.3, β_m is imaginary for all modes, i.e. all the modes are evanescent.

To obtain a propagating mode, β_m needs to be a real number. From Eq. (3.1-11), one sees that this condition is obtained for $\varepsilon_2 k_0^2 > (m\pi/w)^2$, i.e. for wavelength smaller than λ_c:

$$\lambda_c = \frac{2w\sqrt{\varepsilon_2}}{m} \ . \qquad \text{(3.1-12)}$$

This equation gives the cut-off wavelength of a slit in the PEC case. This is an important point regarding the understanding of light transmission through subwavelength slits. It shows that for TM polarization, polarization for which the $m = 0$ mode exits, the $m = 0$ mode is always a propagating one, no matter how narrow the slit is. This mode β_0 is called the fundamental slit mode. On the other hand, TE polarized light can propagates inside the slit only for wavelength smaller than $2w\varepsilon_2^{1/2}$ as the $m = 0$ mode is not a solution for TE polarization.

3.1.1.4. Determination of the propagation constants in the case of real metals

For real metals, the propagation constants β_m are determined starting from the values obtained for PEC as a first guess. The permittivity ε_1 is then increased from $-\infty$ to the values of the real metal. As an example, the propagation constants obtained for three different wavelengths and $w = \lambda/30$ in the case of gold are plotted in Fig. 3.3. As the wavelength is reduced, the metal permittivity increases. This is reflected in the shift of the positions of the propagation constants as compared to the PEC case. Figure 3.3 shows that starting with the PEC case helps finding the propagation constants of the different modes.
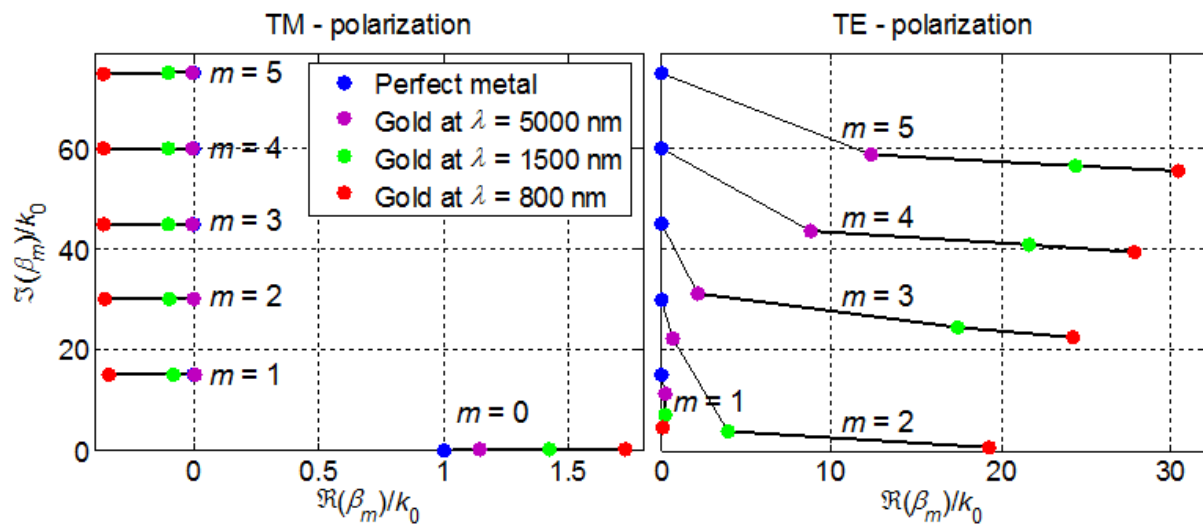
Figure 3.3.   Propagation constant β_m for a metal-air-metal waveguide with $w = \lambda/30$. The first β_m up to $m = 5$ are displayed on the graphs. The blue data are obtained using PEC whereas the purple, green and red data are obtained with a gold permittivity ε_1 of value $-930 + 191i$, $-90 + 10i$ and $-26 + 2i$ for 5000, 1500 and 800 nm wavelength respectively. The axes of the graph are normalized to k_0.

The cut-off wavelength in the TE case is red-shifted in the case of real metals as compared to PEC. Physically, this can be explained by the fact that the field penetrates further into the metal as the conductivity is reduced. As the metal conductivity is reduced, the imaginary part of β_1 is reduced, as shown in the right graph of Fig. 3.3. This corresponds to a slower exponential decay of the mode inside the slit.

From the propagation constants, the field profile of the different modes is known. The field profile of the fundamental slit mode for a metal-air-metal waveguide with $w = 100$ nm, $\lambda = 800$ nm and TM polarization is plotted in Fig. 3.4. In the PEC case, the field is constant along the slit width and does not penetrate inside the metal (blue curve). This is no longer the

case considering finite permittivity values, as shown by the red curve obtained for gold which is exponentially decaying in the metal.
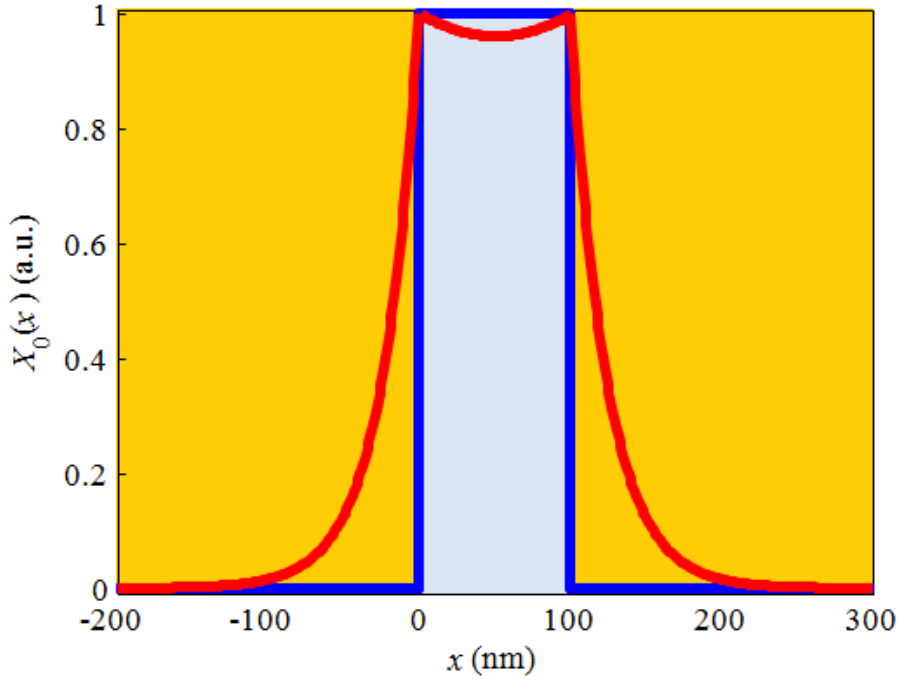
Figure 3.4.   Field amplitude $X_0(x)$ of the fundamental ($m = 0$) slit mode for a metal air metal waveguide with $w = 100$ nm, $\lambda = 800$ nm and TM polarization. The blue curve is obtained for a perfect electric conductor whereas the red curve is obtained for gold ($\varepsilon_1 = -26 + 2i$). The yellow and light blue areas correspond to media of permittivity ε_1 and ε_2 respectively.

3.1.1.5.   Surface wave characteristics of the fundamental TM slit mode

Observing the field profile of the TM fundamental mode in the real metal case, a similarity with SPP wave is observed. Indeed, the field is decaying exponentially away from metal dielectric interfaces, as is the case for SPP waves. The difference here is that the two SPP waves propagating at both interfaces can couple. Indeed, Eq. (3.1-6), which can be written as:

$$\mu_0 \tanh\left(i\,\mu_0 w/2\right) = q\chi_0, \tag{3.1-13}$$

reduces to:

$$\mu_0 = -q\chi_0, \tag{3.1-14}$$

in the case where $\Im\left(\mu_m w/2\right) \gg 1$ [64]. This corresponds to Eq. (2.2-7) in Chapter 2 giving the SPP dispersion relation. Consequently, the fundamental slit mode is intimately linked to

the existence of SPP's at metal dielectric interfaces. This can be seen in Fig. 3.5, where the field amplitude of the $m = 0$ slit mode is represented by the blue solid line. Here the slit is wide enough such that the amplitude is decaying down to zero in the middle of the slit. The mode profile corresponds to two weakly coupled SPP waves propagating at each metal dielectric interfaces. Note that below cut-off, the $m = 1$ slit mode also gives an SPP-like field profile except that this time it corresponds to an antisymmetric coupled SPP, as shown by the red dashed curve in Fig. 3.5. The surface-wave characteristics of both $m = 0$ and $m = 1$ TM waveguide modes leads to the unique property $\beta_m > \varepsilon_2^{1/2} k_0$ [65].
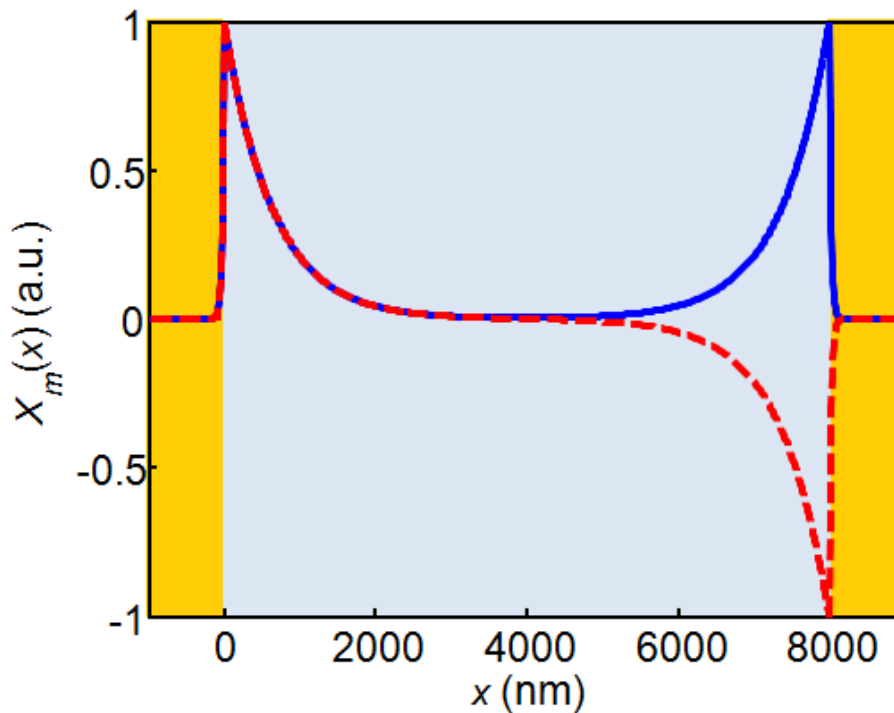
Figure 3.5.   Field amplitude $X_m(x)$ of $m = 0$ (blue curve) and $m = 1$ (red dashed curve) slit modes for a gold-air-gold waveguide with $\varepsilon_1 = -26 + 2i$, $w = 8000$ nm, $\lambda = 800$ nm and TM polarization. The yellow and light blue areas correspond to media of permittivity ε_1 and ε_2 respectively.

3.1.1.6.   Permittivity dependency on waveguide properties

Up to now, the waveguiding properties for metal-dielectric-metal waveguides have been discussed for $|\varepsilon_2| < |\varepsilon_1|$ with the real part of ε_1 negative only. However, Eq. (3.1-6) and (3.1-7) can be used for other values of ε_1 and ε_2 has it is shown in Ref. [63] where the same derivation is made for dielectric waveguides. It is then interesting to discuss the different guiding properties obtained depending on the values of ε_1 and ε_2 and considering subwavelength slits. The different possibilities are schemed in Fig. 3.6, together with their main guiding

properties.

In the case studied before, i.e. metal-dielectric-metal waveguides with $|\varepsilon_2| < |\varepsilon_1|$, we saw that the fundamental TM mode is a propagating mode, no matter how narrow the slit is. However, if $|\varepsilon_2| > |\varepsilon_1|$, this mode becomes an evanescent one. As we saw in the previous section, the fundamental slit mode can be seen as two coupled SPP waves. It was shown in Section 2.2.1 that in the case where $|\varepsilon_2| > |\varepsilon_1|$, β_0 is mainly imaginary and there is no SPP propagating along the surface. This explains why this mode becomes evanescent for such waveguide.
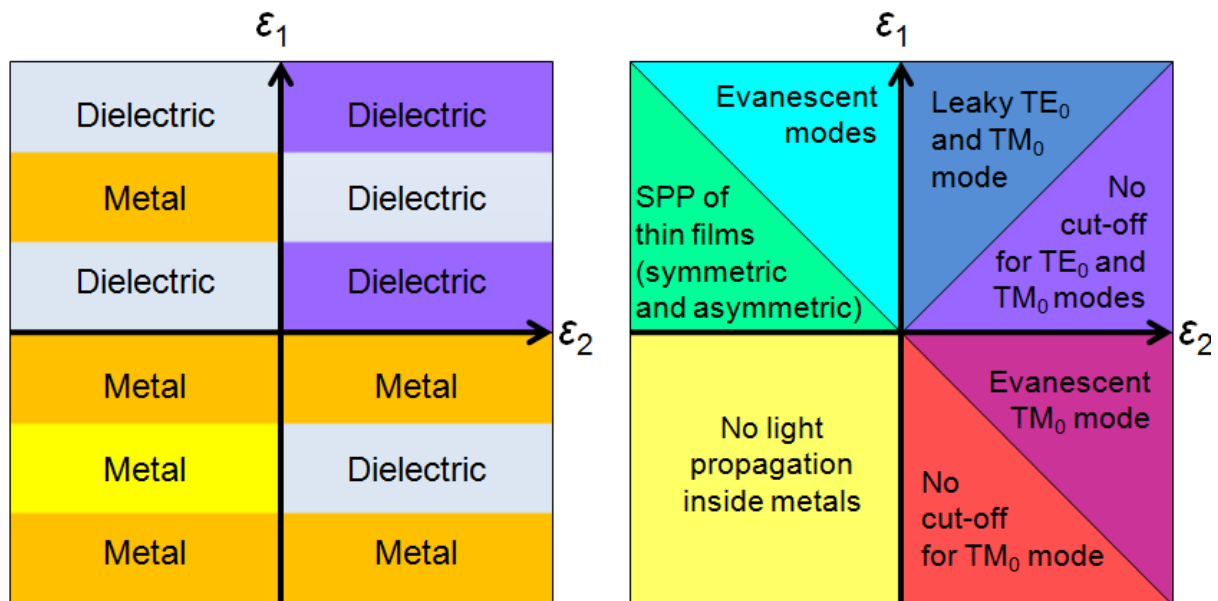
Figure 3.6.   Diagram representing the different configurations of a thin slab sandwiched between two semi-infinite media as schemed in Fig. 3.1 depending on the value taken by the permittivity of each media.

In the case of dielectric waveguides, a condition to obtain propagating modes is that $\beta_m > \varepsilon_1 k_0$, which implies that $\varepsilon_2 > \varepsilon_1 > 0$, see for example Ref. [63]. In this case, neither TE and TM modes has a cut-off wavelength. If $\varepsilon_1 > \varepsilon_2 > 0$, there is no confined modes inside the slit, these modes are leaky modes.

In the case of dielectric metal dielectric waveguides, i.e. for $\varepsilon_2 < 0$ and $\varepsilon_1 > 0$, the metal slab supports SPP modes confined at each metal dielectric interfaces for $|\varepsilon_1| < |\varepsilon_2|$. For thin enough metal slabs, the SPP modes from each interface couple together to form symmetric and antisymmetric SPP modes, as discussed in Chapter 1. Finally, if ε_1 and ε_2 are both negative, i.e. both media are metals, there is no propagating mode sustained by the system, as light does not propagates inside metals.

3.1.2. Light transmission through a subwavelength slit

Consider now a slit in a metal film of finite thickness h, as shown in Fig. 3.7(a), such that for the slit width and permittivity ε_2 considered, only the fundamental TM slit mode is a propagating mode inside the slit. The normalized transmission through such slit in a PEC is shown in Fig. 3.7(b) considering $h = 28.2$ mm and $w = 25$ μm. The normalized transmission defines the ratio between the light that illuminates an aperture to the one transmitted by this aperture, as will be discussed in more details in Chapter 4. Transmission peaks are observed, which are due to the fact that the slit is acting as an FP cavity [66]: light propagating inside the slit with propagation constant β_0 is reflected at the slit entrance and exit, i.e. at $y = \pm h/2$. Considering a symmetric structure, i.e. $\varepsilon_t = \varepsilon_b$, the transmission peaks for an FP cavity occur at the condition (cf. Chapter 1):

$$\beta_0 h + \arg(\rho) = \pi d , \tag{3.1-15}$$

where ρ is the reflection coefficient of β_0 at $y = \pm h/2$, i.e. the phase change upon reflection of the fundamental slit mode at $y = \pm h/2$. The coefficient ρ, obtained matching the tangential components of the electric and magnetic field at the slit apertures [67], increases as w is reduced [68]. As a consequence, the quality of the cavity is higher and normalized transmission increases with the λ/w ratio, as shown in Fig. 3.7(b). The resonant behaviour inside the slit leads to high transmission: the photon flux transmitted through the slit can be many times larger than the one impinging on the slit.

Figure 3.7.   (a) Schematic of the studied structure and definitions used for the structure dimensions and incident field directions. (b) Normalized transmission spectra calculated for a single slit in a PEC with $h = 28.2$ mm, $w = 25$ μm and $\varepsilon_2 = \varepsilon_t = \varepsilon_b = 1$ for normal incidence TM polarized light, taken from Ref. [68].

In the case where the slit modes is evanescent, e.g. in the TE case above cut-off, there is no FP mode, and the transmission scales with $\exp\left[-2\Im(\beta_0)h\right]$. Consequently, increasing the film thickness h drastically reduces the transmission. Note however that similar to the TM case, transmission resonances can occur in the TE case for slit widths wide enough to sustain a propagating TE mode.

3.1.3. Enhanced optical transmission through a subwavelength slit surrounded by periodic grooves

It is possible to enhance the transmission through a single subwavelength slit in a metal by adding periodic grooves on each side of the slit [52], see Fig. 3.8(a) for a schematic of the structure and the geometrical parameters considered. The basic principle is the following: TM polarized light incident on the groove array can couple to SPP's which propagate along the metal surface, leading to a concentration of the electromagnetic field above the slit. In the case of constructive interference between SPP's and light directly impinging on the slit, enhanced transmission is obtained.

Figure 3.8(b) shows the transmission through a single slit in a PEC with different number of grooves on each side, N_g. The black curve for $N_g = 0$ corresponds to the single slit case discussed in Section 3.1.2. The two transmission peaks at $\lambda \approx 400$ nm and $\lambda \approx 850$ nm are associated to the excitation of FP modes. As N_g increases, an additional transmission peak appears at a wavelength $\lambda \approx 560$ nm, i.e. slightly larger than the groove periodicity $p = 500$ nm. This transmission peak is attributed to diffractive coupling of incident light to SPP's. Such phenomenon allows light that does not directly impinge upon the slit to contribute to the transmission.

It should be noted that SPP's are invoked to explain the transmission peak observed at $\lambda \approx 560$ nm in Fig. 3.8(b). However, this figure is obtained considering the metal as a PEC, which does not sustain SPP's. A PEC surface, where grooves have been sculpted, does however support surface waves that "spoof" SPP's, as described in Ref. [45]. Consequently, it is more accurate to speak about surface waves or "spoof" SPP's in the case of PEC. In fact, any kinds of surface waves excited in the neighbourhood of the slit can lead to enhance optical transmission phenomenon. This has been shown by Nikitin *et al.*, who proposed to use a thin dielectric film on top of a slit and groove structure to couple incident TE polarized light to dielectric waveguide modes [69], thus enhancing the overall transmission. This is discussed in more details in Section 4.4.
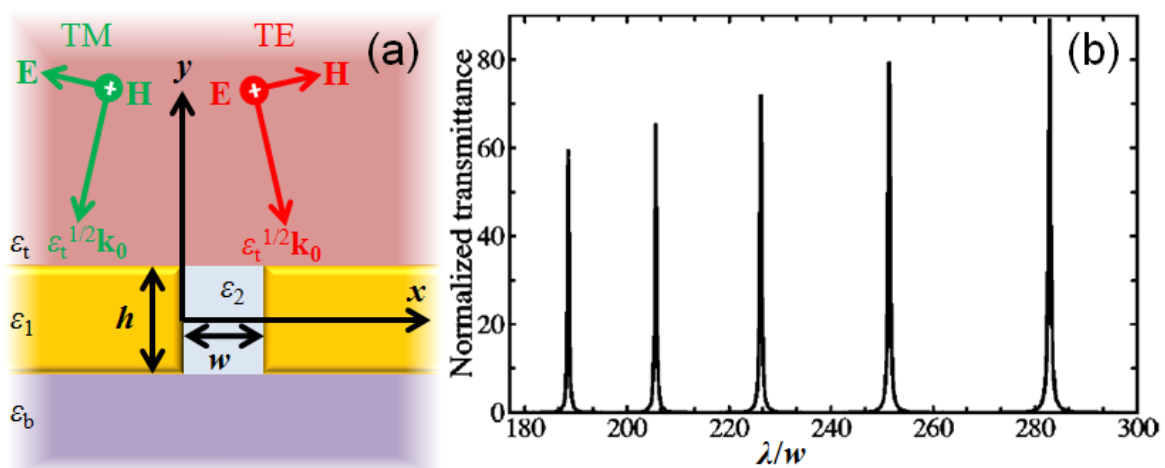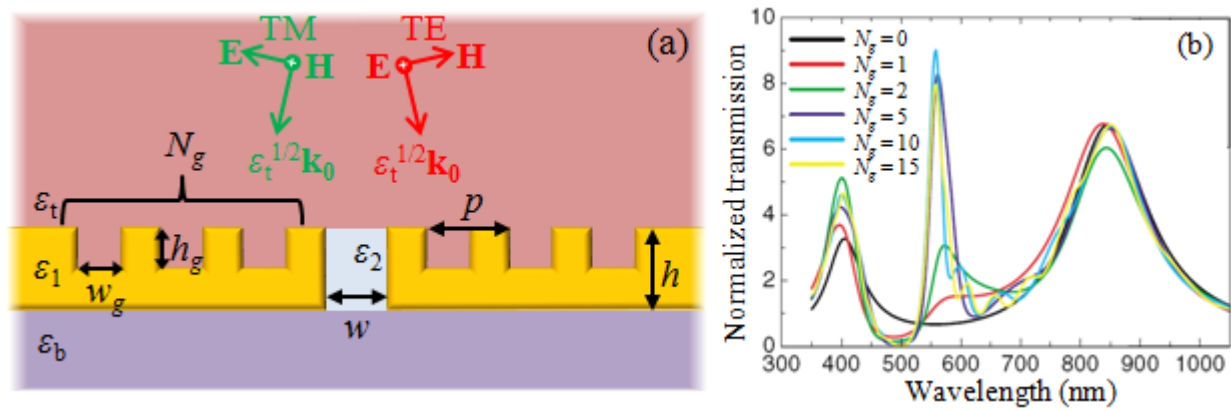
Figure 3.8.   Schematic of the slit and groove structure and definitions used for the structure's dimensions and incident field directions. (b) Transmission spectra calculated for a slit and groove structure in a PEC with $h = 350$ nm, $h_g = 100$ nm, $w = w_g = 40$ nm, $p = 500$ nm and $\varepsilon_2 = \varepsilon_t = \varepsilon_b = 1$ for normal incidence TM polarized light, adapted from Ref. [52].

It is possible to optimize the structure by varying the different geometrical parameters. García-Vidal *et al.* showed that the transmission can be boosted when the excitation of both FP and SPP modes coincide [52]. The FP and SPP modes can be tuned at a desired wavelength by changing the film thickness h and groove periodicity p respectively. Janssen *et al.* showed that the distance between the slit and the first groove plays an important role in the interference between light incident on the slit and SPP's [70]. They also showed that the transmission saturates after a fixed number of grooves; this number depends on the depth and width of the grooves. This is due to reciprocity principle: in the case of shallow grooves, both in-coupling of incident light to SPP's and out-coupling of SPP's to far field is lower than for deep grooves. Consequently, the number of grooves at which transmission saturates will be larger for shallow grooves than deeper ones.

Different variations of the structure shown in Fig. 3.8(a) have been studied like the so called bull's eye structure, which corresponds to the two dimensional equivalent of the slit and groove structure, i.e. a single hole surrounded by circular grooves. Also, one important modification is the addition of grooves at the output surface. Due to the presence of grooves, surface waves lanched at the slit exit are scattered into free space. These scattered waves then interfere with light radiated directly from the slit, leading to beaming of the transmitted radiation [71].

3.1.4. Conclusion

The mode equations of a slit in a metal film have been derived. The mode wavevectors are first determined in the case of a PEC. These wavevectors are then used as a first guess to find the mode wavevectors in the case of real metals in the complex plane. It is shown that irrespective of the slit width, the fundamental TM slit mode is always propagating. This mode, which corresponds to the coupling of two SPP modes propagating on each metal dielectric interface, leads to the enhanced light transmission phenomenon observed through a subwavelength slit. Light transmission can be further boosted by adding on each side of the slit periodic grooves which couple incident light into surface waves. Light transmission through a single slit is experimentally investigated in Chapter 4, and the use of enhanced transmission through a single slit for image sensors is studied in Chapter 5. The description of the single slit transmission properties is also useful for the understanding of the slit array case, which is now described.

3.2. Optical properties of slit arrays

The present section discusses the transmission characteristics of periodic slit arrays. Such arrays constitute a grating. As discussed in Section 2.2.3.1, a grating can excites SPP's under TM polarized light. We are interested in the effect of the SPP excitation on the optical properties of slit arrays and consequently focus on TM polarization as TE polarization does not excite SPP. For simplicity, the case where $\varepsilon_2 = \varepsilon_t = \varepsilon_b = 1$ is considered. For a complete derivation of the model for both polarizations, see Appendix 2.

In Section 3.2.1, a modal expansion method, based on the work of Lochbihler *et al.* [72], is used to calculate light transmission through slit arrays. Transmission peaks are observed close to two types of modes: one mode depends on the slit geometry and the other on the periodicity of the grating. Both modes couple together and form hybrid modes responsible for high transmission. In order to have a better description of these hybrid modes, a simplified analytical form is derived from the Lochbihler model in Section 3.2.2. The simplified model gives accurate analytical formula for the transmission and the dispersion relations of the hybrid modes. This is particularly helpful to interpret the role played by the different uncoupled modes in the transmission process, as described in Section 3.2.3.

3.2.1. Modal expansion method

3.2.1.1. Choice of the model

Several approaches can be used to calculate the transmission of light through periodic arrays of slits. Numerical methods such as Finite Difference Time Domain (FDTD) [73] have the advantage that they can handle objects of any shapes. FDTD is considered to be exact in case of infinitesimally small mesh size. However, such calculations are time consuming when the mesh size is much smaller than the entire computational domain. This is typically the case when SPP waves are involved. In order to get a good accuracy, the mesh size should be small enough (few nanometres) due to the high confinement of the field on the metallic surface. Another disadvantage of using FDTD is that the method provides a poor insight into the physics.

Rigorous modal theories expressing the field in terms of plane waves [74] have been developed to treat the diffraction properties of an array of slits for an arbitrary value of the permittivity. Contrary to FDTD, this technique is not as reliable in terms of shape of the structure, but provides a fast calculation treatment of the problem and gives a better physical

insight of the scattering properties of the system.

In the case of highly conductive structures, it is necessary to use a large number of plane waves to represent accurately the field inside the metal with rigorous methods. This can cause numerical instabilities [72]. It is possible to overcome this problem using the method described by Lochbihler *et al.* [72]. Instead of calculating the field inside the metal region, surface impedance boundary conditions (SIBC) are considered at metal dielectric interfaces. At these interfaces, SIBC assumes that the relation between the tangential components of electric ($\mathbf{E}_\parallel$) and magnetic ($\mathbf{H}_\parallel$) fields are given by:

$$\mathbf{E}_\parallel = Z\mathbf{n} \times \mathbf{H}_\parallel, \qquad\qquad (3.2\text{-}1)$$

with Z the surface impedance and $\mathbf{n}$ the vector normal to the interface pointing toward the free space region. For metals with dielectric function ε_1 such that $|\varepsilon_1| \gg 1$, the surface impedance can be approximated as $Z = \varepsilon_1^{-1/2}$. SIBC has been used successfully for gold gratings in the visible to infrared wavelength range [75,76]. Using SIBC does not allow the evanescent tunneling through the metal to be considered as the electromagnetic field is not calculated inside metal regions. Consequently, this model is limited to metal walls with thickness greater than the metal skin depth, as is the case in the present work.

3.2.1.2. Theoretical formalism

Here, we study the transmission of a plane wave through an infinite metal lamellar grating surrounded by air with period *p*, thickness *h* and slit width *w*, see Fig. 3.9. The incident wave propagates in a direction contained in the (x, y) plane and forms an angle θ with the *y* axis.
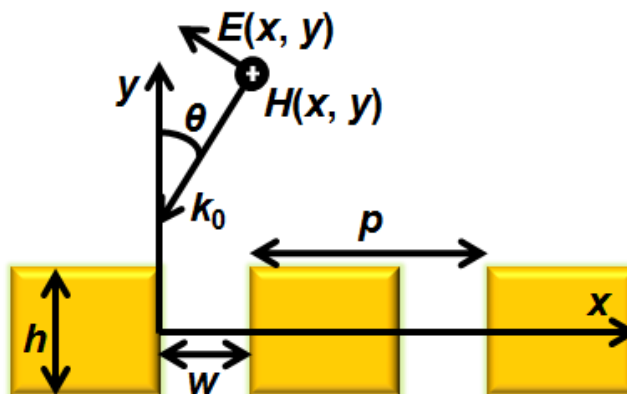
Figure 3.9.   Schematic of the studied structure and definitions used for the structure's dimensions and incident field directions. The structure repeats itself infinitely with period *p* in the *x* direction.

The magnetic field H_z above and below the grating is rigorously expressed as a Rayleigh expansion (or plane wave expansion):

$$H_z(x,y) = \exp\{i[k_{x,0}x - k_{y,0}(y - h/2)]\}$$

$$+ \sum_{n=-\infty}^{\infty} r_n \exp\{i[k_{x,n}x + k_{y,n}(y - h/2)]\} \quad \text{for } y \geq h/2, \quad (3.2\text{-}2)$$

$$H_z(x,y) = \sum_{n=-\infty}^{\infty} t_n \exp\{i[k_{x,n}x - k_{y,n}(y + h/2)]\} \text{ for } y \leq -h/2, \quad (3.2\text{-}3)$$

with $k_{x,n} = (2\pi/\lambda)\sin\theta + (2\pi/p)n$, n is an integer related to the nth diffracted order, $k_{y,n} = (k_0{}^2 - k_{x,n}{}^2)^{1/2}$, k_0 is the incident complex wave vector such that real(k_0) = $2\pi/\lambda$. r_n and t_n are respectively the amplitudes of the reflected and transmitted fields.

Inside the apertures, H_z is expressed as a sum of waveguide modes:

$$H_z(x,y) = \sum_{m=0}^{\infty} X_m(x)[a_m \exp(i\beta_m y) + b_m \exp(-i\beta_m y)] \text{ for } -h/2 \leq y \leq h/2, \quad (3.2\text{-}4)$$

where a_m and b_m are the amplitudes of backward and forward propagating waves inside the slit respectively and are related to the mode number m. Imposing SIBC conditions, the wave function of the mode is modified as compared to the rigorous case derived in Section 3.1.1: $X_m(x) = \cos(\mu_m x) + \sin(\mu_m x)\eta/\mu_m$ with $\eta = -ik_0/\varepsilon_1{}^{1/2}$. The terms μ_m and β_m are, as defined in Section 3.1, the transverse and longitudinal wavenumbers of the mth mode respectively. Under SIBC, the determination of μ_m and β_m is obtained considering a single isolated slit since proximity effects between slits are not considered, and the mode equation is given by $\tan(\mu_m w) = 2\,\eta\mu_m/(\mu_m{}^2 - \eta^2)$. A similar approach as that in Section 3.1.1.4 is used to find the solutions of the mode equation.

To satisfy the continuity of tangential components of electric and magnetic fields, the continuity of H_z and its normal derivative are considered. Matching H_z at $y = \pm h/2$, multiplying for any $m = j$ the resulting equations by $X_j(x)$ and integrating over the region $0 \leq x \leq w$ as done in Ref. [72], the following set of equations is obtained for any $m = j$:

$$I_j[a_j \exp(i\beta_j h/2) + b_j \exp(-i\beta_j h/2)] = \sum_{n=-\infty}^{\infty} (r_n + \delta_{n,0})K_{j,n}, \quad (3.2\text{-}5)$$

$$I_j[a_j \exp(-i\beta_j h/2) + b_j \exp(i\beta_j h/2)] = \sum_{n=-\infty}^{\infty} t_n K_{j,n}, \quad (3.2\text{-}6)$$

where the overlap integrals are defined by:

$$I_j = \int_0^w X_j(x)X_j(x)dx = \left[1+\left(\frac{\eta}{\mu_j}\right)^2\right]\frac{c}{2}+\frac{\eta}{\mu_j^2}, \qquad (3.2\text{-}7)$$

$$K_{j,n} = \int_0^w \exp(ik_{x,n}x)X_j(x)dx, \qquad (3.2\text{-}8)$$

In a similar way, the normal derivative of H_z are matched at $y = \pm h/2$ and for $0 \le x \le w$. Considering SIBC for metal-dielectric interfaces at $y = \pm h/2$ for $w \le x \le p$, the obtained equations are multiplied for any $n = q$ by $\exp(-ik_{x,q}x)$ and integrated over the region $0 \le x \le p$. This gives the following set of equations for any $n = q$:

$$ik_{y,q}(r_q - \delta_{q,0}) = i\sum_{m=0}^{\infty}\beta_m[a_m\exp(i\beta_m h/2)-b_m\exp(-i\beta_m h/2)]J_{q,m}$$

$$+\eta\sum_{n=-\infty}^{\infty}(r_n+\delta_{n,0})Q_{q,n}, \qquad (3.2\text{-}9)$$

$$ik_{y,q}t_q = -i\sum_{m=0}^{\infty}\beta_m[a_m\exp(-i\beta_m h/2)-b_m\exp(i\beta_m h/2)]J_{q,m}+\eta\sum_{n=-\infty}^{\infty}t_n Q_{q,n}, \quad (3.2\text{-}10)$$

where the overlap integrals are defined by:

$$J_{q,m} = 1/p\int_0^w \exp(-ik_{x,q}x)X_m(x)dx, \qquad (3.2\text{-}11)$$

$$Q_{q,n} = 1/p\int_0^w \exp[i(k_{x,n}-k_{x,q})x]dx. \qquad (3.2\text{-}12)$$

The calculation of the unknown coefficients r_n, t_n, a_m and b_m is then performed after truncation and writing Eq. (3.2-5), (3.2-6), (3.2-9), (3.2-10) into a matrix equation.

3.2.1.3. Accuracy of the model

In Fig. 3.10(a), the transmission spectrum of a gold grating obtained with the above method (red solid curve) is compared with a spectrum obtained with rigorous coupled wave analysis (RCWA, green dashed curve) [77]. The chosen parameters are $w = 50$ nm, $p = 1200$ nm, $h = 200$ nm and normal incidence. Visible to near infrared wavelengths are considered, a range where SPP excitation is observed for gold. Excellent agreement is observed, validating the use of the above method. The spectrum is also compared with FDTD in Fig. 3.10(b) and shows excellent agreement. The agreement is poorer at smaller wavelength, e.g. for $\lambda < 600$ nm. This is due to an increase of the real part of the gold permittivity in this wavelength range, where the SIBC approximation is less accurate.
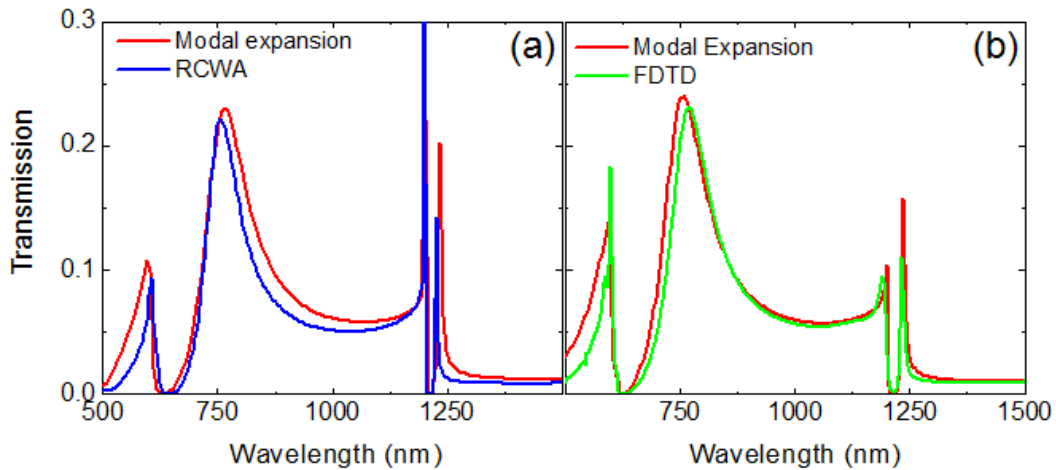
Figure 3.10.   Transmission spectra of a gold grating with $p = 1200$ nm, $w = 50$ nm, $h = 200$ nm and normal incidence. (a) Spectra calculated with the modal expansion method and RCWA where the permittivity of gold is taken from the Sopra database. (b) Spectra calculated with the modal expansion method and FDTD where the permittivity of gold is a fit of the Sopra database using a Drude model.

For completeness, it should be specified that in Fig. 3.10(a), the permittivity of gold is taken from the Sopra database [78]. This is not the case in Fig. 3.10(b), as an analytical model of dispersion is needed in the case of FDTD calculations [58]. The data used for the permittivity in Fig. 3.10(b) is consequently a fit of the Sopra database using a Drude model (cf. Section 2.1).

3.2.1.4.   Light transmission properties through slit arrays

Figure 3.11 shows the total transmission of a gold grating for $h = 600$ nm, $w = 50$ nm at normal incidence as a function of p and λ. Note that plotting the transmission as a function of $k_{x,0}$ and λ would lead to similar observations. It is however more convenient to plot the transmission in function of p and λ for an easier identification of the grating resonances, which appear close to $\lambda = p/n$.

Transmission peaks are observed with transmission above 0.6 in some cases. As observed in other studies [79-81], some of the transmission peaks are following the SPP dispersion relation, see for example the narrow transmission peak from $\lambda \approx p \approx 2250$ nm to $\lambda \approx p \approx 3000$ nm. These high transmission peaks have been consequently attributed to SPP excitation. Other high transmission peaks present "flat" bands, i.e. the transmission is almost independent of period, see for example at $\lambda \approx 1850$ nm for periods ranging from 500 to 1500 nm. These flat bands have been previously attributed to FP resonances inside slits [66,81,82], as it is observed in the case of a single slit discussed in Section 3.1.2. These resonances are

also called vertical SPP resonances [79] as the fundamental TM slit mode corresponds to the coupling of two coupled SPP (cf. Section 3.1.1). In fact, there is a continuous change from FP related peaks to SPP related peaks, as reported by several past studies [51,83,84]. The transmission peak related to FP-like resonance at $\lambda \approx 1850$ nm and $p = 500$ nm continuously evolves to an SPP-like peak on increasing p. This has been explained by Marquier *et al.* as coupled SPP-FP modes [84].
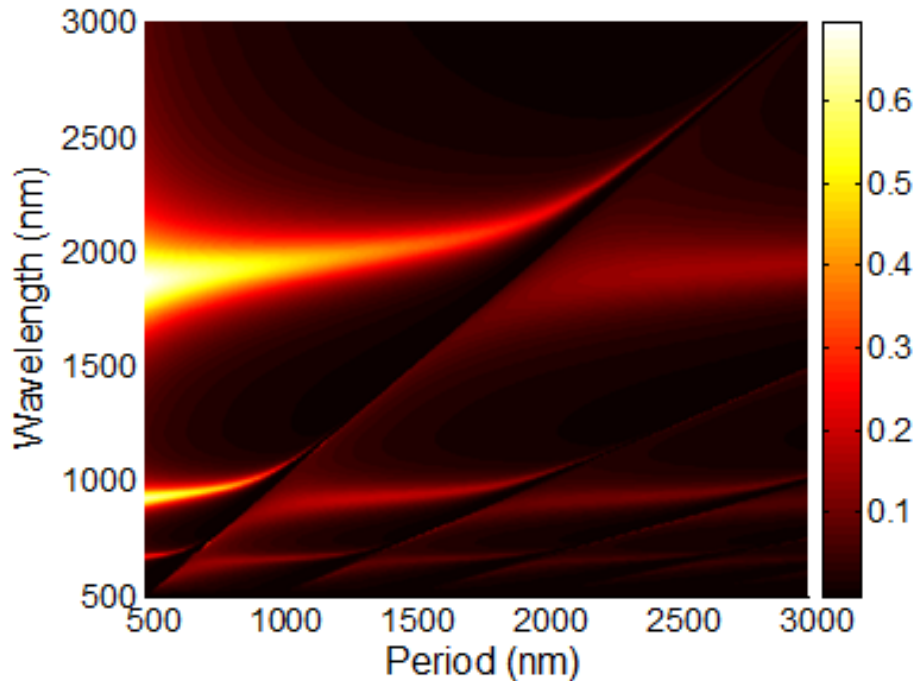
Figure 3.11.   Transmission of a gold grating for $w = 50$ nm, $h = 600$ at normal incidence as a function of p and λ obtained from the modal expansion method. The brighter the region, the larger is the transmission.

The exact role of SPP in the transmission process has been controversial. Several studies observed that the transmission at the SPP condition is close to zero [85,86]. Also, peaks observed in close proximity to the SPP condition were sometimes not attributed to SPP excitation but to the discontinuity observed when a diffracted order passes from evanescent to propagating [87,88], i.e. at the Rayleigh wavelength [89]. The nature of the coupled modes responsible for transmission peaks is unclear.

In order to give a clear picture of these modes, the model described above is reduced in a simplified form in the next section. It is then possible to extract the dispersion relations of the transmission resonances into simple equations. This clarifies some past controversy and offers a unifying picture of the transmission resonances.

3.2.2. Simplified model

3.2.2.1. Analytical formula for the transmission

Light transmission through slit arrays can be accurately written in a simple form considering narrow slits (i.e. $w < \lambda/10$). In this limit, several simplifications can be made:

(i) Only the fundamental slit mode β_0 is considered as it is the only propagating mode for narrow slits, the others being evanescent. This approximation has already been made to study light transmission through both slit arrays [51,82,85,88,90] and hole arrays [91].

(ii) The $Q_{q,n}$ matrix, which represents the overlap between plane waves, can be considered diagonal [92], i.e. $Q_{q,n} = \delta_{q,n}Q = \delta_{q,n}(p - w)/p$. This means that the plane waves do not mix via scattering from the slits.

With these two approximations, Eq. (3.2-9) and (3.2-10) can be rewritten as:

$$r_n = \beta_0\left(a_0 e^{i\varphi} - b_0 e^{-i\varphi}\right)J_{n,0}\alpha_n + \delta_{n,0}\left(k_{y,0} - i\eta Q\right)\alpha_0, \qquad (3.2\text{-}13)$$

$$t_n = -\beta_0\left(a_0 e^{-i\varphi} - b_0 e^{i\varphi}\right)J_{n,0}\alpha_n, \qquad (3.2\text{-}14)$$

with the notation $\alpha_n = (k_{y,n} + i\eta Q)^{-1}$ and $\varphi = \beta_0 h/2$. Substituting r_n and t_n of Eq. (3.2-13) and (3.2-14) into Eq. (3.2-5) and (3.2-6) gives:

$$I_0\left(a_0 e^{i\varphi} + b_0 e^{-i\varphi}\right) = \beta_0\left(a_0 e^{i\varphi} - b_0 e^{-i\varphi}\right)\sum_{n=-\infty}^{\infty} J_{n,0}K_{0,n}\alpha_n + 2K_{0,0}\alpha_0 k_{y,0}, \qquad (3.2\text{-}15)$$

$$I_0\left(a_0 e^{-i\varphi} + b_0 e^{i\varphi}\right) = -\beta_0\left(a_0 e^{-i\varphi} - b_0 e^{i\varphi}\right)\sum_{n=-\infty}^{\infty} J_{n,0}K_{0,n}\alpha_n. \qquad (3.2\text{-}16)$$

Equations (3.2-15) and (3.2-16) constitute two equation with two unknown: a_0 and b_0. These unknown can thus be expressed independently and inserted in Eq. (3.2-14), giving the transmission amplitude in the following analytical form:

$$t_n = \frac{J_{n,0}K_{0,0}\alpha_n\alpha_0 k_{y,0}N_{slit}}{\left[-i\sum_{n=-\infty}^{\infty} N_n \sin\varphi + N_{slit}\cos\varphi\right]\left[\sum_{n=-\infty}^{\infty} N_n \cos\varphi - iN_{slit}\sin\varphi\right]}, \qquad (3.2\text{-}17)$$

with the notations $N_n = J_{n,0}K_{0,n}\alpha_n$ and $N_{slit} = I_0/\beta_0$.

3.2.2.2. Accuracy of the model

In Fig. 3.12, the transmission from the simplified model (blue dashed curve) is compared with the complete modal expansion method (red solid curve). Both curves superimpose. This validates the assumption that for narrow slits ($w = 50$ nm), only the

fundamental mode inside the slit is relevant and $Q_{q,n}$ can be considered as diagonal. The fact that $Q_{q,n}$ is diagonal implies that the coupling within the different diffracted orders occurs via the slits. In the case of an evanescent mode inside the slit, light impinging on the array would not be diffracted, and the array would behave as a flat interface.
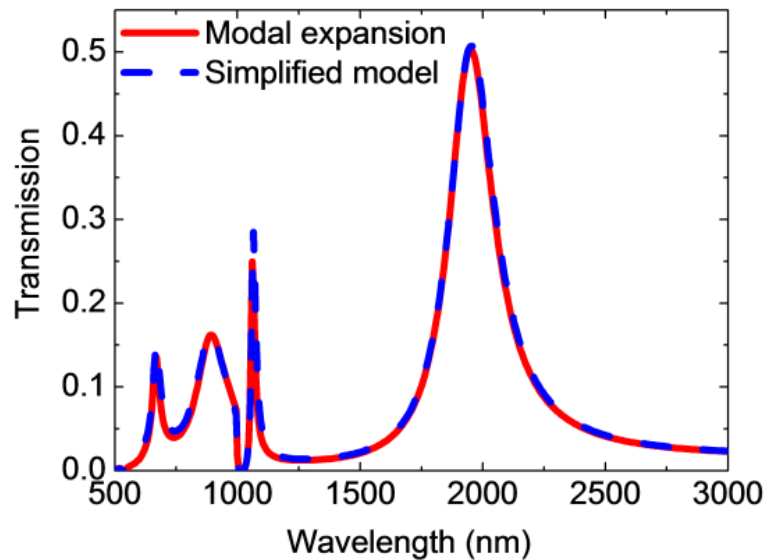
Figure 3.12.   Transmission spectra of a gold grating with $p = 1000$ nm, $w = 50$ nm, $h = 600$ nm and normal incidence obtained from different models: modal expansion method (solid curve) and the simplified model derived in the present study (dashed curve).

3.2.2.3.   Dispersion relation of transmission resonances

From the simplified model, the dispersion relations of the modes responsible for transmission can be obtained analytically. Resonant transmission is obtained by computing the poles of t_n in the complex frequency domain [79,88]. Poles of t_n correspond to zeros of the determinant in Eq. (3.2-17), which are obtained from the following two transcendental equations:

$$N_0 + \sum_{n \neq 0} N_n + iN_{slit} \cot \varphi = 0, \tag{3.2-18}$$

$$N_0 + \sum_{n \neq 0} N_n - iN_{slit} \tan \varphi = 0. \tag{3.2-19}$$

These equations are particularly interesting as the entire transmission problem is reduced to two sets of modes, giving the position of the transmission peaks. As an example, the above equations are used to calculate the peak positions of Fig. 3.11 obtained with the full model. The figure is reproduced a second time in Fig. 3.13(a) for convenience. In Fig.

3.13(b), blue dotted curves and red dashed curves are plotted from Eq. (3.2-18) and (3.2-19) respectively. The SPP dispersion relations are represented by the green solid curves. All transmission maxima observed in Fig. 3.13(a) match with the dispersion curves plotted in Fig. 3.13(b). This shows that the mode equations obtained from the simplified model accurately predict the peak transmission observed with the complete model in the limits considered (i.e. $w < \lambda/10$).
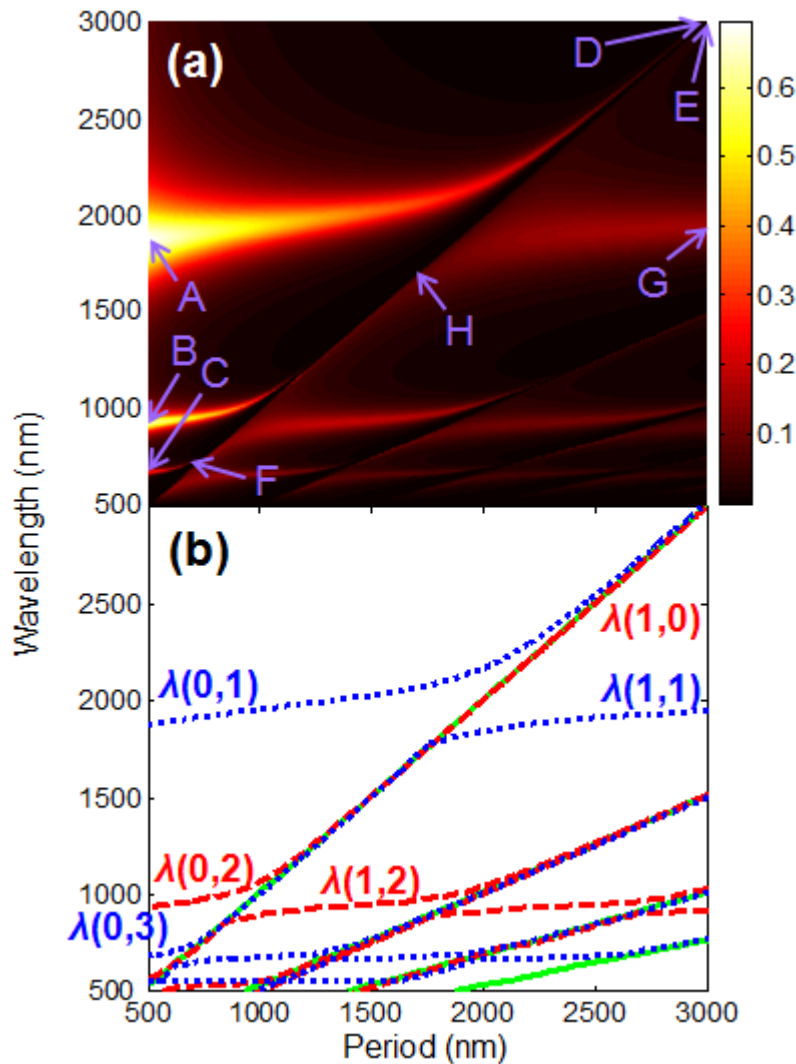
Figure 3.13.   (a) Transmission of a gold grating for $w = 50$ nm, $h = 600$ nm and normal incidence in function of p and λ obtained from the modal expansion method. The brighter the region, the larger is the transmission. The field amplitude or intensity is plotted in the next section for the points marked with capital letteres. (b) Dispersion relations of the transmission resonances obtained from the solutions of Eq. (3.2-18) (blue dotted curves) and Eq. (3.2-19) (red dashed curves) for the same set of parameters as in Fig. 3.13(a). The green solid curves correspond to the SPP dispersion relations.

Note that the dispersion relations predict transmission resonances that are not observed in Fig. 3.13(a), see for example at $\lambda \approx p \approx 2000$ nm where the red dashed line in Fig. 3.13(b) does not reflect into a transmission peak in Fig. 3.13(a). This point will be clarified in Section 3.2.4.

3.2.3. Description of the dispersion relation of the modes responsible for high transmission

The different uncoupled modes of the structure are contained in the dispersion relations previously derived. The role of these different uncoupled modes on the overall transmission process is investigated, giving a clear picture of the modes responsible for high transmission.

3.2.3.1. Periodicity related effects

We saw that due to the periodicity, the transmission properties of slit arrays are strongly modified from the single slit case. Resonances or anomalies related to the periodicity of the structure are expressed in the dispersion relations within the N_n terms, rewritten here for clarity:

$$N_n = J_{n,0} K_{0,n} \alpha_n = \frac{J_{n,0} K_{0,n}}{k_{y,n} + i\eta Q}. \tag{3.2-20}$$

N_n shows a discontinuity at $k_{y,n} = 0$, i.e. for $k_0 = k_{x,n}$. At this condition, $k_{y,n}$ abruptly changes from an imaginary to a real value as a diffracted order passes from evanescent to propagating. This corresponds to the Rayleigh wavelength $\lambda_{RW,n}$, which is expressed at normal incidence as:

$$\lambda_{RW,n} = \frac{p}{n}. \tag{3.2-21}$$

The term N_1 is plotted in Fig. 3.14 for a gold grating with $w = 50$ nm, $p = 1000$ nm and normal incidence. It shows that at $\lambda_{RW,1}$, N_1 is discontinuous, see the abrupt change in the phase of N_1, $\arg(N_1)$.

N_n terms are resonant at the poles of α_n, i.e. for $k_{y,n} + i\eta Q = 0$. Considering normal incidence, the resonance is found at:

$$\lambda_{SPP,n} = \frac{p}{n} \left(\frac{\varepsilon_1 - Q^2}{\varepsilon_1} \right)^{1/2}. \tag{3.2-22}$$

The resonance of N_1 is indeed observed in Fig. 3.14 at $\lambda_{SPP,1}$.

Note that if w tends toward zero, $Q = 1$ and Eq. (3.2-22) corresponds to the SPP

dispersion relation under SIBC [93] of a flat metal-air interface. For $Q \neq 1$, Eq. (3.2-22) is the dispersion relation of a "dressed" SPP, taking into account the perturbation of the slits.

$\lambda_{RW,n}$ and $\lambda_{SPP,n}$ appear each time as a pair because they both depend linearly on period and on incidence angle. $\lambda_{SPP,n}$ is red shifted as compared to $\lambda_{RW,n}$ and blue shifted as compared to a flat metal-air interface. In the case of a PEC, $\lambda_{RW,n} = \lambda_{SPP,n}$, i.e. both the resonance and the discontinuity due to the periodic structure appear under the same condition.
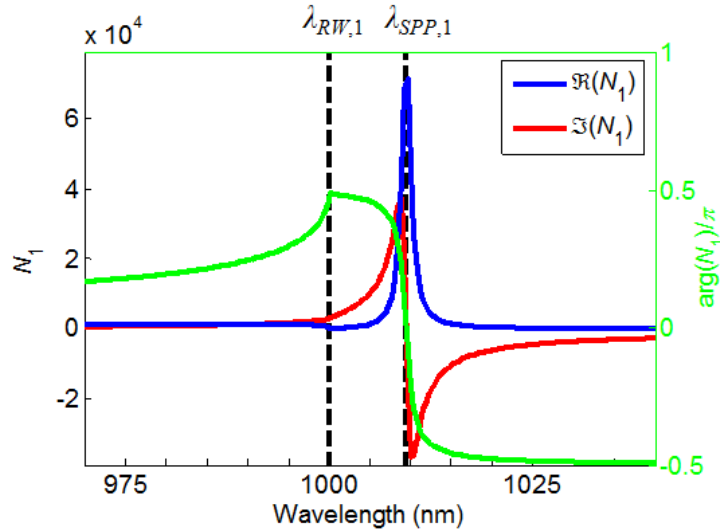
Figure 3.14. Phase (green curve), real (blue curve) and imaginary (red curve) part of the term N_1 for a gold grating with $w = 50$ nm, $p = 1000$ nm and normal incidence. $\lambda_{SPP,1}$ and $\lambda_{RW,1}$, calculated from Eq. (3.2-21) and (3.2-22) are represented by vertical dashed lines. The right hand axis corresponds to the phase of N_1.

3.2.3.2. High transmission far from SPP and RW conditions

Far from the pair $(\lambda_{SPP,n}, \lambda_{RW,n})$, $\sum_{n \neq 0} N_n$ is negligible and Eq. (3.2-18) and (3.2-19) can be respectively rewritten as:

$$\beta_0 \tan(\beta_0 h/2) = -iI_0/N_0 , \qquad (3.2\text{-}23)$$

$$\beta_0 \cot(\beta_0 h/2) = iI_0/N_0 . \qquad (3.2\text{-}24)$$

Note that the above equations are very similar to Eq. (3.1-6) – (3.1-7) describing the symmetric and antisymmetric modes of a slab waveguide respectively. The excitation of these modes will lead to FP resonances inside the slits. As N_0 is small as compared to the other terms, a FP condition occurs close to a wavelength $\lambda_{FP,l}$ at which either tangent or cotangent functions are resonant. This condition is expressed as:

$$\beta_0 h = \pi l , \qquad\qquad (3.2\text{-}25)$$

where l is an odd and even positive integer in Eq. (3.2-23) and Eq. (3.2-24) respectively. In analogy with waveguides, the integer l corresponds to the number of field maxima inside the slits. As tangent and cotangent are periodic functions whose period is $\beta_0 h = 2\pi$, a solution to Eq. (3.2-23) and (3.2-24) will be always found in an interval $(l - 1)\pi < \beta_0 h < (l + 1)\pi$.

From Eq. (3.2-25), high transmission is expected at $\lambda_{FP,1} \approx 1700$ nm, $\lambda_{FP,2} \approx 820$ nm and $\lambda_{FP,3} \approx 620$ nm for the slit parameters of Fig. 3.13. Indeed, broad transmission maxima are observed in Fig. 3.13(a) close to these three wavelengths regardless of period except in close proximity with the grating resonances. For example, for p ranging from 500 to 1500 nm, high transmission is observed close to $\lambda_{FP,1}$.
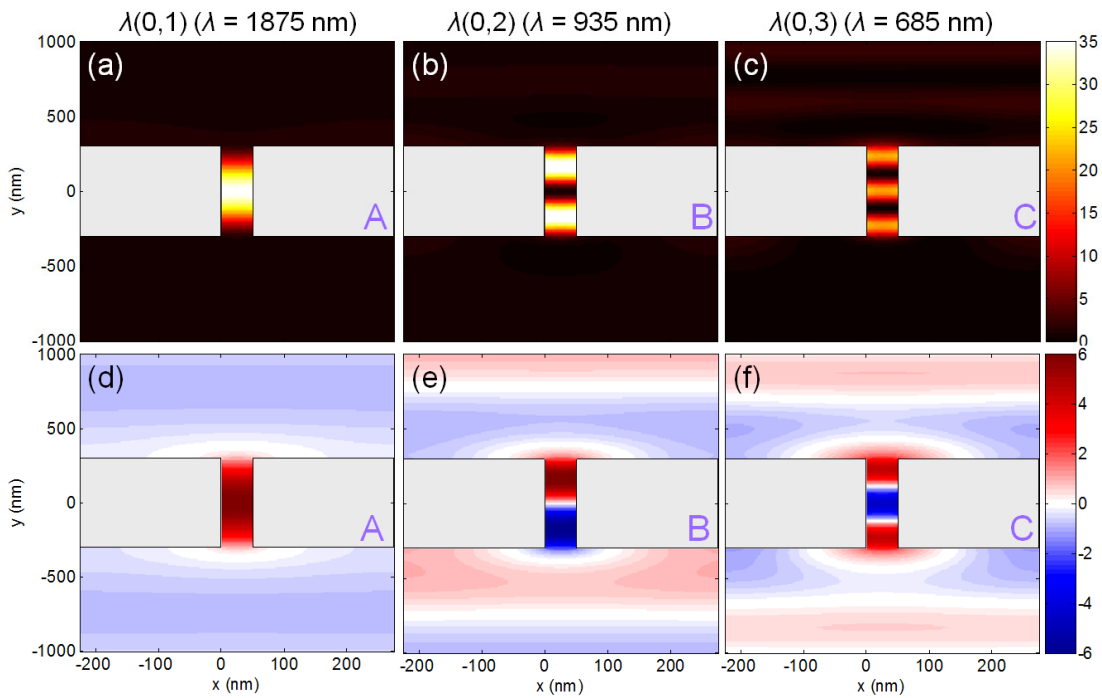
Figure 3.15.   Map of the field intensity (a) - (c) and of the field amplitude (d) – (f) plotted in the (x, y) plane over one grating period (p = 500 nm) in the x direction for different wavelengths. Letters A, B and C correspond to points in Fig. 3.13(a). Each figure is obtained from the simplified model. Grey rectangles represent the metal regions.

A map of the magnetic field intensity at points A, B and C of Fig. 3.13(a), which correspond to peak position close to $\lambda_{FP,l}$ with l = 1, 2 and 3 respectively, are shown in Fig. 3.15(a) - (c) for p = 500 nm. Each figure, obtained from the simplified model, is plotted in the (x, y) plane over one grating period in the x direction. Grey rectangles represent the metal

regions. In each case, the field is strongly localized inside the slit with l field maxima. This shows that the slit is acting as a FP cavity. When l field maxima are observed in the slit with l odd, the transmission peak position is predicted from Eq. (3.2-18), whereas it is obtained from Eq. (3.2-19) for l even. Plotting the field amplitude [Fig. 3.15(d) – (f)], one sees that the field is symmetric and antisymmetric with respect to the $y = 0$ axis for l odd and even respectively. Eq. (3.2-18) and Eq. (3.2-19) gives the dispersion relation of respectively symmetric and antisymmetric modes of the FP type.

3.2.3.3. High transmission near the SPP and RW conditions

For clarity, the different branches constituting the dispersion relation are labelled $\lambda(n,l)$, i.e. poles for which $\lambda_{SPP,n+1} < \lambda < \lambda_{SPP,n}$ and $\lambda_{FP,l+1} < \lambda < \lambda_{FP,l-1}$. Only the first six branches are labelled in Fig. 3.13(b) for clarity.
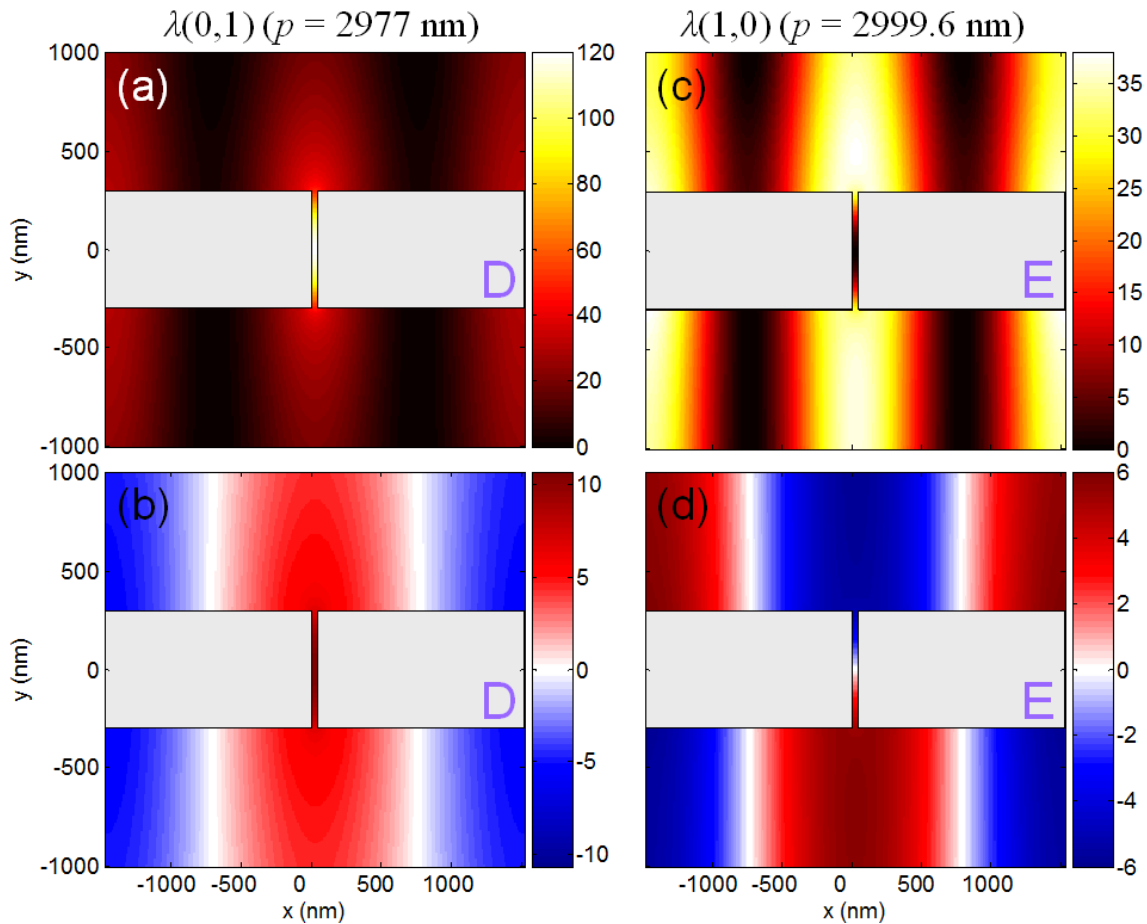
Figure 3.16. Map of the field intensity (a), (c) and of the field amplitude (b), (d) plotted as in Fig. 3.15 for $\lambda = 3000$ nm and two different periods. Letters D and E correspond to points in Fig. 3.13(a).

Focusing on the $\lambda(0,1)$ branch, the resonant transmission red-shifts as the period is increased. Mathematically, this is due to an increase of N_n as $\lambda_{SPP,1}$ is approached. The transmission resonance continuously evolves from a nearly flat dispersion FP-like resonance in the 500 - 1500 nm period range to an SPP-like one for periods ranging from 2000 to 3000 nm, where $\lambda(0,1)$ is tangential to $\lambda_{SPP,1}$. Whereas the field intensity is mainly confined inside the slit for the $\lambda(0,1)$ branch at small periods [see Fig. 3.15(a)], an intense field is present on the surface for larger periods, whilst a FP character remains inside the slit, see Fig. 3.16(a) for $\lambda = 3000$ nm and $p = 2977$ nm [point D in Fig. 3.13(a)]. Fig. 3.16(b) shows that the field amplitude along $\lambda(0,1)$ keeps a symmetric profile for large periods.

The $\lambda(0,2)$ branch is also red-shifted as the period is increased. It crosses $\lambda_{SPP,1}$ and merges to the $\lambda(1,0)$ branch which is close to $\lambda_{RW,1}$ for large periods. In Fig. 3.16(c), the field is no longer confined inside the slit for $p = 2999.6$ nm and $\lambda = 3000$ nm [point E in Fig. 3.13(a)] but it extends in the y direction above and below the grating. Plotting the field intensity on a large scale in Fig. 3.17 shows that the field is not tightly confined on the metal when the transmission mode is near λ_{RW}. As shown in Fig. 3.16(d), the field keeps the antisymmetric profile of the $\lambda(0,2)$ branch [cf. Fig. 3.15(e)].
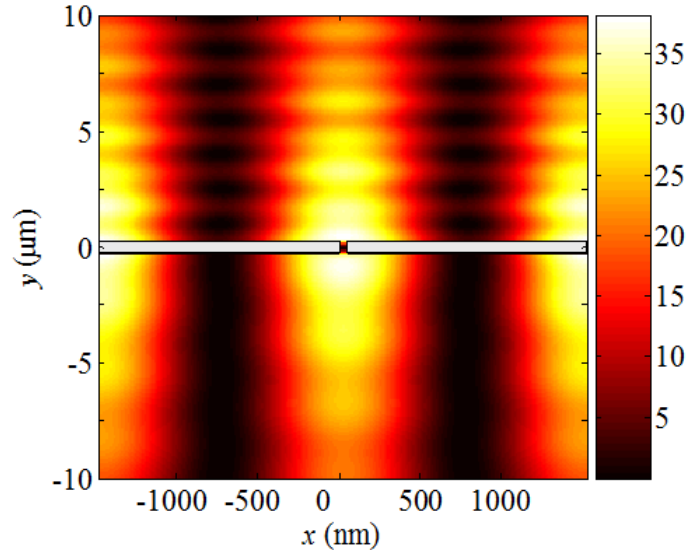
Figure 3.17. Map of the field intensity plotted for the structure considered in Fig. 3.16(c) but on a larger scale.

The transmission peak related to the $\lambda(1,0)$ mode is very narrow and not visible in Fig. 3.13(b) due to the figure resolution. To show that this mode effectively gives a transmission peak, a transmission spectra has been plotted in Fig. 3.18(a) for $\lambda = 3000$ nm and periods

close to the $\lambda(1,0)$ mode. A very narrow transmission peak labelled E is observed close to $\lambda_{RW,1}$ (represented by a vertical dashed line). The transmission peak related to the $\lambda(0,1)$ branch and labelled D is also observed. To clearly see the transmission peak of the $\lambda(1,0)$ mode, the interval between $\lambda_{RW,n}$ and $\lambda_{SPP,n}$ needs to be increased. This occurs when working at shorter wavelengths. The $\lambda(1,0)$ branch can be shifted to shorter periods (or wavelengths) by decreasing the film thickness. Transmission for $\lambda = 1300$ nm and $h = 200$ nm is shown in Fig. 3.18(b). A sharp transmission peak related to the $\lambda(1,0)$ branch is obtained tangent to $\lambda_{RW,1}$, whereas the low transmission for $p = 1290$ nm is attributed to $\lambda_{SPP,1}$ and the peak at $p = 1270$ nm to the $\lambda(0,1)$ mode.
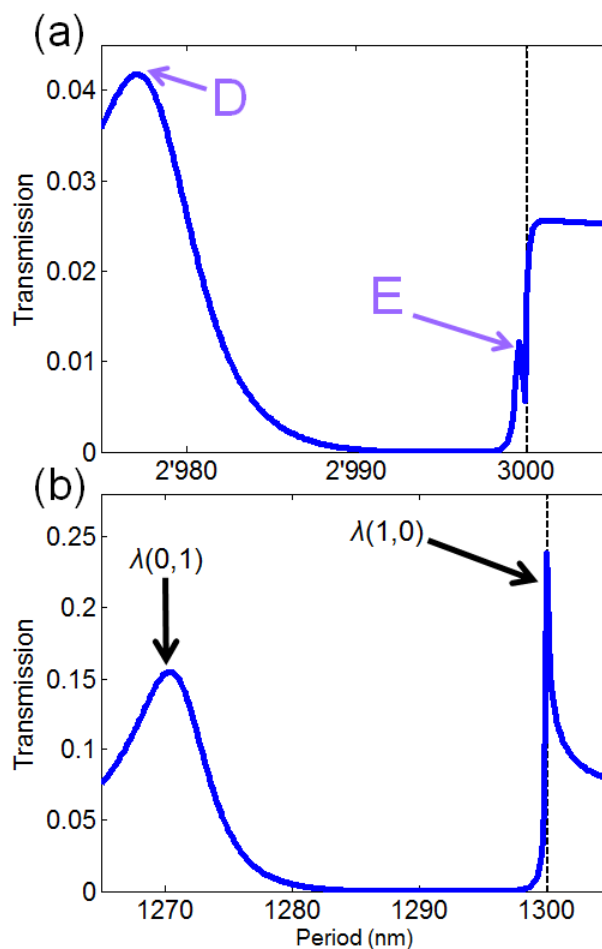
Figure 3.18. Transmission spectra of a gold grating at normal incidence and for (a) $\lambda = 3000$ nm, $w = 50$ nm, $h = 600$ nm (b) $\lambda = 1300$ nm, $w = 50$ nm, $h = 200$ nm obtained from the simplified model derived in the present study.

The higher order branches show a similar behaviour to the branches previously described. For example, one sees again in Fig. 3.13(b) a bending of the $\lambda(0,3)$ branch close to

$\lambda_{SPP,1}$ on increasing p. Observing the field intensity plotted in Fig. 3.19(a) for $p = 705$ nm and $\lambda = 745$ nm [point F in Fig. 3.13(a)] and comparing with Fig. 3.15(c), one sees that the two outer maxima of the FP cavity become less confined in the slit as p is increased along the $\lambda(0,3)$ branch. The $\lambda(0,3)$ branch crosses $\lambda_{SPP,1}$ at $\lambda_{FP,2}$ and finally merges into the $\lambda(1,1)$ one with only one single field maxima inside the slit, see Fig. 3.19(b) for $p = 3000$ nm and $\lambda = 1910$ nm [point G in Fig. 3.13(a)]. Also, the $\lambda(1,1)$ branch keeps the symmetric field profile of the $\lambda(0,3)$ one.
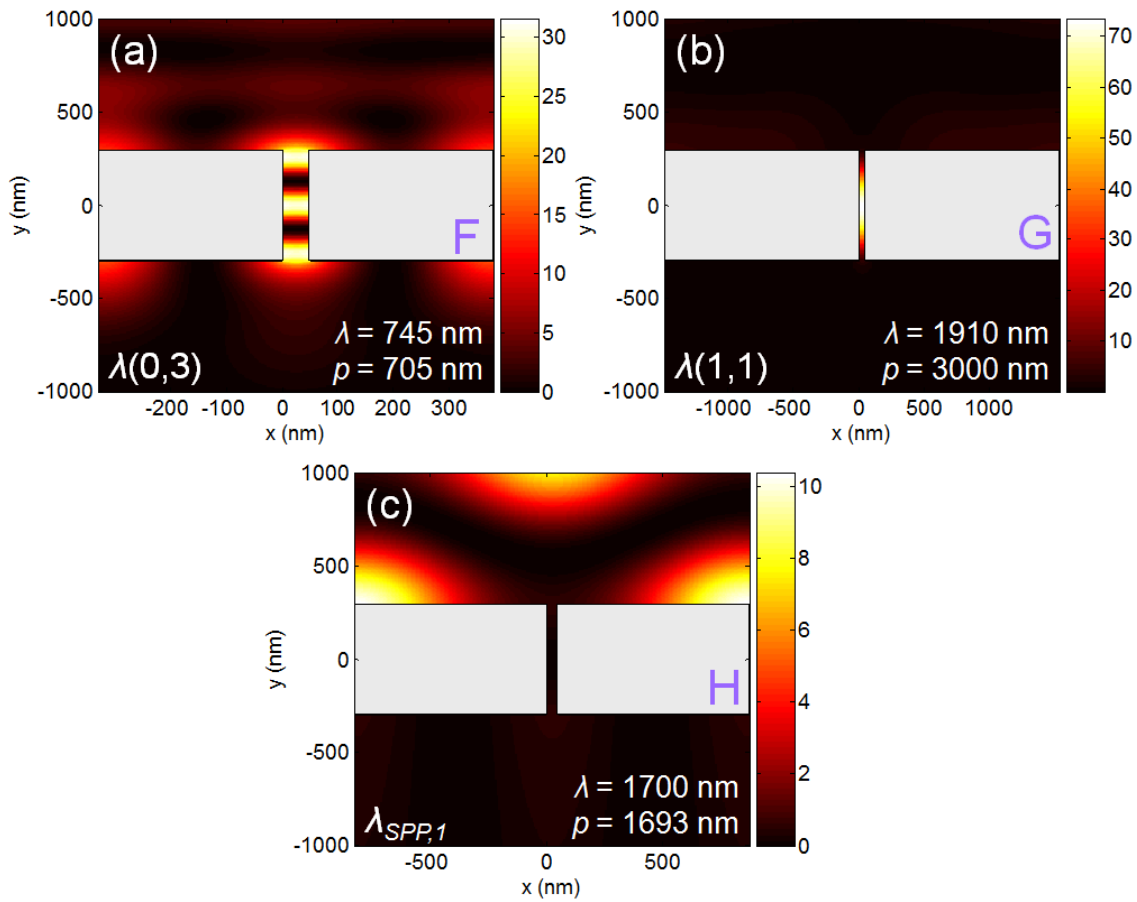
Figure 3.19. Map of the field intensity plotted as in Fig. 3.15 for different periods and wavelength. Letters F, G and H correspond to a set of parameters in Fig. 3.13(a).

It has been shown in Fig. 3.15 that far from the pair ($\lambda_{SPP,n}$, $\lambda_{RW,n}$), the transmission modes are similar to symmetric and antisymmetric waveguide modes. Near the pair ($\lambda_{SPP,n}$, $\lambda_{RW,n}$), the modes present similarities with the symmetric and antisymmetric SPP modes observed in thin metal films, see the schemes of Fig. 3.20. The field profile is represented twice, depending whether the field is in the middle of the slit ($x = w/2$) or in the middle of the metal region [$x = (p + w)/2$]. In the middle of the metal region, the field profile is very similar

to the thin metal film case. In both slit arrays and thin metal film, symmetric resonances are red-shifted as compared to $\lambda_{SPP,n}$, whereas the antisymmetric ones are blue-shifted. Also, the antisymmetric modes correspond to the long range SPP's, which give sharp resonances [see the $\lambda(1,0)$ mode in Fig. 3.18], whereas the symmetric modes correspond to the short range SPP's, presenting broader resonances [$\lambda(0,1)$ mode in Fig. 3.18] . The difference here as compared to a flat metal film is that SPP's are coupled on both sides of the film for any thickness due to the presence of slits. Finally, it can be said that Eq. (3.2-18) and Eq. (3.2-19) give the dispersion relation of respectively symmetric and antisymmetric hybrid "FP-SPP" modes.
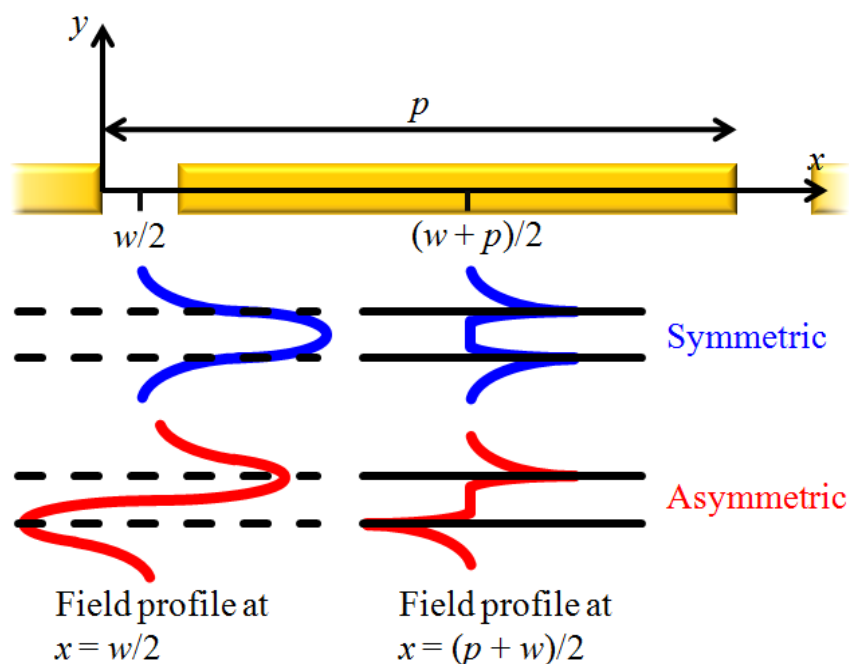
Figure 3.20.   Schematic of the field profile for a cross-section in the y direction in the case of the symmetric and antisymmetric hybrid FP-SPP modes. In both cases, the field profile is represented twice, depending whether the field is in the middle of the slit, i.e. at $x = w/2$ or in the middle of the metal region, i.e. at $x = (p + w)/2$.

3.2.4.   Role of SPP

Generalizing what has been observed before, $\lambda(n-1,l)$ branch crosses $\lambda_{SPP,n}$ before it merges with the $\lambda(n,l-2)$ branch. The crossing occurs when $\lambda = \lambda_{SPP,n} = \lambda_{FP,l-1}$. Mathematically, this crossing occurs when N_n is resonant at the same time as $\cot\varphi$ and $\tan\varphi$ for l odd and even respectively. At this point, the transmission is very low. As α_n is resonant at $\lambda_{SPP,n}$, t_n can be approximated at the SPP condition from Eq. (3.2-17) as:

$$t_n \approx -\frac{1}{\alpha_n} \frac{J_{n,0} K_{0,0} \alpha_0 k_{y,0} I_0 / \beta_0}{i(J_{n,0} K_{0,n})^2 \sin\varphi \cos\varphi} \approx 0. \tag{3.2-26}$$

Consequently, the transmission is always close to zero at $\lambda_{SPP,n}$, as observed in Fig. 3.13(a). This is in agreement with Cao *et al.* who already observed that the transmission is nearly zero at $\lambda_{SPP,n}$ [85]. It also explains why transmission peaks are not observed in transmission spectra when the dispersion relations predict transmission resonances that are too close to the SPP conditions. Lalanne *et al.* [88] investigated in a past study the zero observed at $\lambda_{SPP,n}$ in terms of reflected and transmitted intensities of single interfaces. They found that the reflected intensity of the fundamental mode is close to one at $\lambda_{SPP,n}$. This means that there is no coupling into or out of the slit at the dressed SPP resonance. Physically, this low transmission can be understood as the fact that at the SPP condition, the field is bounded at the metal interface but not above the slit, as seen from Fig. 3.19(c) at the crossing of the $\lambda(0,2)$ branch with $\lambda_{SPP,1}$ for $p = 1693$ nm and $\lambda = 1700$ nm. This inhibits light from coupling into the slit mode.

In their study, Cao *et al.* also observed that the phase of the reflection coefficient at the grating interface of the fundamental slit mode $\arg(\rho)$ is resonant at $\lambda_{RW,n}$, and concluded that transmission resonances close to $\lambda = p$ are pure diffraction effects. However, PEC was assumed to match the field at $y = \pm h/2$. We performed similar calculations considering both PEC and finite conductivity. The transmission and reflection coefficients of single interfaces are derived in Appendix 2. Figure 3.21(a) shows the phase as well as the real and imaginary part of ρ. The resonance is centred at the α_n poles, i.e. at $\lambda_{SPP,n}$. A discontinuity is observed at $\lambda_{RW,n}$, in the same way as in the case of N_n terms discussed in Section 3.2.3.1. Note that this is what is observed also in other studies which consider real metals [94]. In the PEC case, $\eta = 0$ and α_n is then resonant at $\lambda_{RW,n}$. Consequently, ρ is both resonant and discontinuous at $\lambda_{RW,n}$, as observed in Fig. 3.21(b). This explains why a resonance was observed at $\lambda_{RW,n}$ in Ref. [85]. The finite conductivity of real metals red-shifts the SPP resonance.

The findings of Section 3.2 brings consensus between the different explanations regarding transmission resonances known in the literature. A dressed SPP mode is defined. This mode is slightly blue-shifted as compared to the SPP condition of a flat metal-air interface due to the perturbations generated by the slits. The excitation of this mode leads to a very low transmission. The modes responsible for high transmission have been defined by considering the dispersion relation of the complete system. These modes can either present a FP or an SPP like profile, and can be considered as hybrid FP-SPP modes.
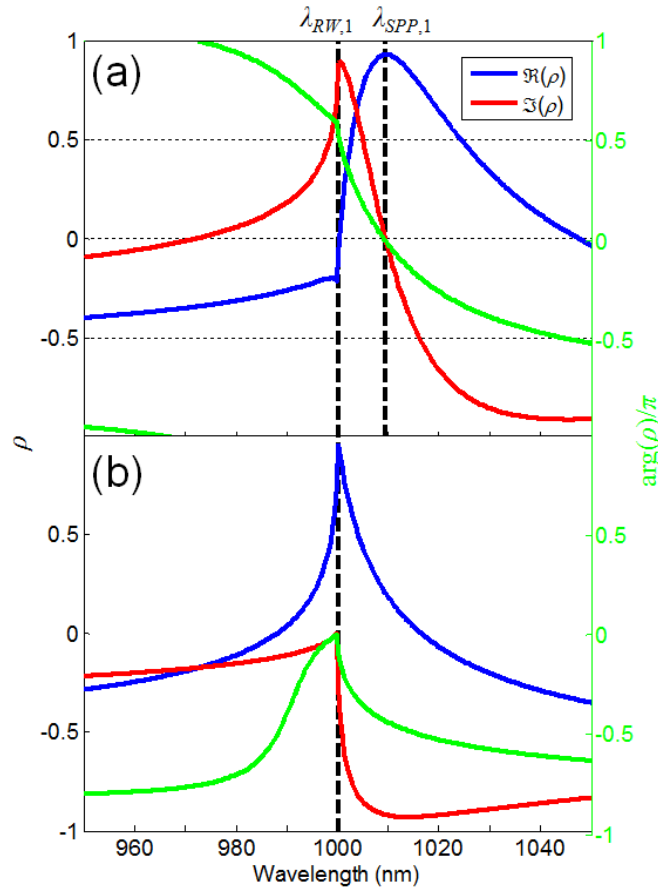
Figure 3.21.   Phase (green curve), real (blue curve) and imaginary (red curve) part of the reflection coefficient at the grating interface of the fundamental slit mode ρ for a grating with $w = 50$ nm, $p = 1000$ nm and normal incidence. The metal is considered as (a) gold; (b) a PEC. $\lambda_{SPP,1}$ and $\lambda_{RW,1}$, calculated from Eq. (3.2-21) and (3.2-22) are represented by vertical dashed lines. The right hand axis corresponds to the phase of ρ.

3.2.5.   Conclusion and outline

To conclude, a simplified version of the modal expansion method has been derived to study the TM light transmission through metal gratings with narrow slits and optically thick metal walls. The model gives an accurate analytical expression for the transmission and the dispersion relations of the modes responsible for high transmission. The dispersion relations accurately predict the position of the transmission peaks, and clarify the role played by the different modes of the grating in the transmission process. We find that high transmission occurs for the excitation of hybrid "SPP-FP" modes. Two types of modes are identified: symmetric and antisymmetric ones. These modes are very similar to the symmetric and antisymmetric modes of a waveguide unless they occur at wavelengths close to the uncoupled SPP condition, where these modes present similarities with the symmetric and antisymmetric

SPP modes of a thin metal film. These findings give a unifying picture regarding the transmission properties of metal gratings. Also, the observations made in the present chapter are helpful for the design of metal gratings for various applications. Some examples are given in the Chapter 5.

The model developed in this chapter is accurate for narrow slits, i.e. when the fundamental slit mode is the only propagating order. Increasing the slit width such that other slit modes become propagating will lead to additional transmission channels, resulting in more complex transmission mechanisms through the array.

The transmission through the metal is not considered in this chapter. This should be included in the calculation when the metal walls are thinner than the skin depth of the metal. For a thin film thickness h, SPP's at the top and bottom couple together and symmetric and antisymmetric SPP's need to be considered. As the metal thickness between the slits is decreased, symmetric and antisymmetric slit modes should appear due to neighbouring effects between the slits. Both cases would be very interesting to investigate, but a rigorous method is necessary.

As will be shown in Chapter 4 and 5 slit arrays are fabricated on substrates in most experimental studies. This implies that refractive indices above and below the array are different, as are $\lambda_{SPP,n}$ and $\lambda_{RW,n}$. Different refractive indices can be considered in the model described above but to fully illuminate the basic properties of light transmission through slit arrays, this was omitted.

Finally, this model and the dispersion relations of the modes giving high transmission might be extended to two dimensional hole arrays. This would give additional insight in their transmission properties. A starting point towards this can be the method described in Ref. [91]. Similar properties to the slit array case are expected for holes sustaining propagating modes.

Chapter 4

Metal structures on glass: fabrication, characterization and comparison with theory

The present chapter is dedicated to the measurement of the light transmission through the metal structures whose optical properties are described in Chapter 3: single slits, slit and grooves and slit arrays. After a description of the sample fabrication and the way transmission measurements are acquired, measurements of the different structures are reported and compared with theory. This validates the use of the design tools that we introduced before applying them in Chapter 5 to design metal structures for various applications.

4.1. Materials and methods

This chapter concentrates on the optical properties of gold structures on glass substrates. The first section describes the sample fabrication and the measurement procedure.

4.1.1. Sample Fabrication

The glass substrates are 150 μm thick optical microscope cover slips, which were cleaned with a commercially available soap (Hellmannex II, Hellma, Germany) and rinsed with deionised and purified water. Cleaned surfaces are necessary to remove any dirt or impurity present on the surface, which would result in an increased roughness of the metal film. Film roughness is a key issue in the quality of the sample. An increase in roughness leads to a limited SPP's propagation [12,95].

Gold is used in the experiments of the present work. As shown in Section 2.2.2, this metal presents large SPP propagation lengths at a gold-air interface for wavelengths above 600 nm. The SPP propagation length is approximately ten times the free space wavelength around 600 nm and can reach several hundred times the free space wavelength for near-infrared wavelengths. Gold is deposited on the glass substrate by sputtering. The film roughness was measured by atomic force microscopy (AFM). The root mean square roughness was lower than 1 nm. A thin (e.g. 5 or 10 nm) adhesion layer of titanium or chromium is often deposited between the glass substrate and the gold film to obtain a better adhesion of the layer. However, these metals present high losses and such layer significantly reduces the SPP propagation length. For this reason, no adhesion layer was used in our experiments.

Metal structures are milled in the gold film with focused ion beam (FIB). FIB milling relies on the impact of highly accelerated Ga^+ ions on the metal surface. The ion beam hits the sample surface and sputters a small amount of material, which leaves the surface. The ions are extracted from a liquid metal ion source accelerated by a high tension to an energy around 30 keV and focused by several electrostatic lenses. The intensity and beam width is adjusted using several diaphragms. FIB can modify the substrate properties by ion damage. In the case of crystalline substrates, the ion beam damages the lattice, creates an amorphous top layer and causes ion implantation [96,97], which in turn induces optical losses. Optical losses induced by FIB structuring on crystalline substrates will be discussed in Chapter 5. The effect of FIB damaging on glass substrates is investigated here. A 25×25 μm^2 square of depth 20 nm is

etched in a glass substrate. Transmission spectrum of the etched substrate is shown by the blue curve in Fig. 4.1. The transmission is reduced as compared to a glass substrate not being etched (red curve in Fig. 4.1). It shows that also in the case of amorphous substrates, FIB can induce optical losses. This will be of importance in the next section when comparing experimental data with theory. It should be noted that these losses are an experimental artefact and may be overcome by employing other fabrication techniques such as nanoimprint lithography and e-beam lithography. However, these techniques are less versatile than FIB for making exploratory structures.
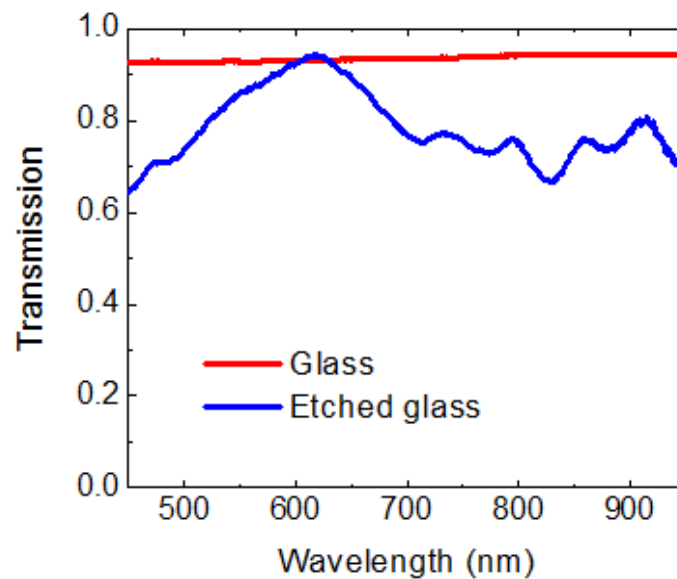
Figure 4.1   Transmission measured through a glass substrate before (red curve) and after (blue curve) FIB etching. The etched area is a 25×25 μm^2 square with 20 nm depth.

In the present chapter, three types of structures are fabricated and characterized: single isolated slits, slit and groove structures and slit arrays. The different structures are shown in Fig. 4.2 together with the definitions of the structure dimensions. If not specified, the length of the structures is $L = 10$ μm and each slit array is constituted of $N_{slit} = 10$ slits. Examples of slit array and slit and groove structures obtained by FIB are shown in Fig. 4.3(a) and 3.3(b) respectively. The optical properties of the various structures have been theoretically discussed in Chapter 3.

In addition to low roughness, gold films need to have small grain sizes with a narrow distribution to obtain the highest quality structure using FIB. The etching rate by FIB depends on the grain size. The presence of large grains induces irregularities in the structure. To illustrate this effect, Fig. 4.3 shows scanning electron microscope (SEM) images of slit arrays

etched in a gold film for two types of films. A gold film with small grains leads to a well defined and defect free structure, as observed in Fig. 4.3(a), whereas the presence of large grains as in Fig. 4.3(c) engenders irregularities in the structure.
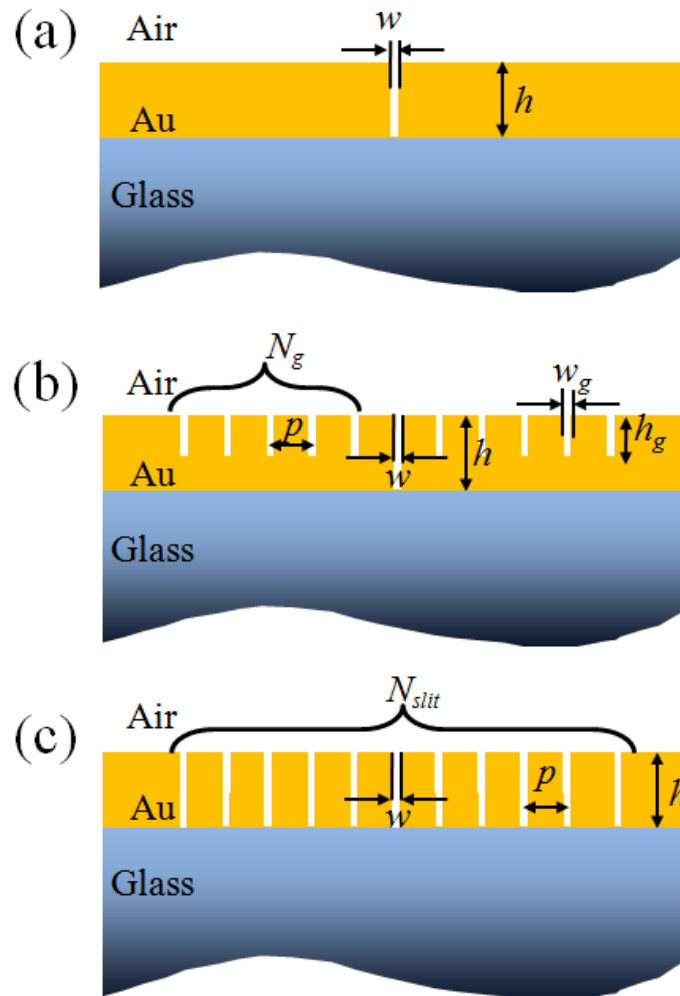
Figure 4.2.   Schematic of structures on glass substrate and definitions used for the structure dimensions. (a) single slit; (b) slit and groove structure; (c) slit array.

A cross-section of a slit and groove structure is shown in Fig. 4.3(d). The inset, which is a higher magnification of the slit with the first groove on its right, shows that the structure edges are rounded, and that the slit walls are tilted at an angle of $\approx 7°$ as compared to the vertical. The deviation in the structure dimensions depends on the feature sizes and aspect ratios. These structural imperfections need to be considered when comparing experiment with theory, which only accounts for vertical walls and sharp edges.
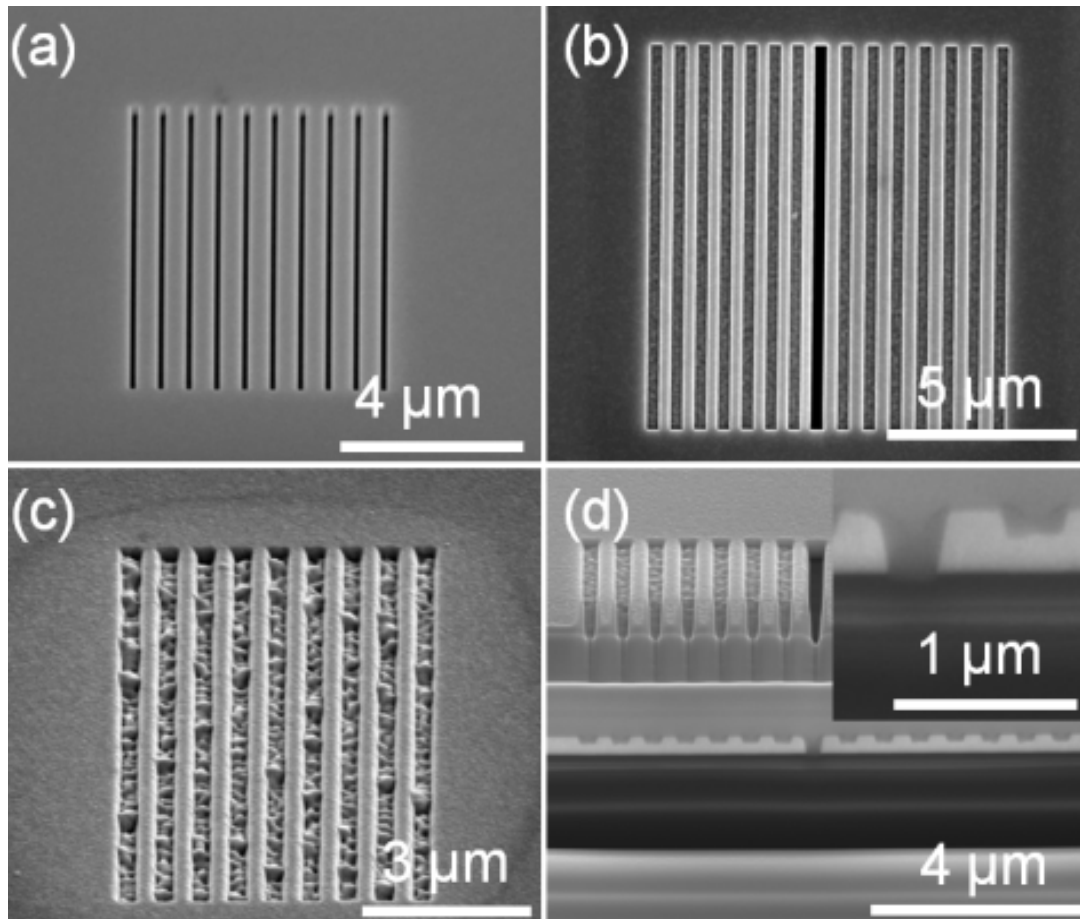
Figure 4.3.   SEM pictures of (a) a slit array with $p = 600$ nm $w = 150$ nm and $h = 285$ nm; (b) a slit and groove structure with $p = 638$ nm, $w = 311$ nm, $h = 420$ nm, $N_g = 7$, $w_g = 325$ and $h_g = 180$. A cross section of this structure is shown in (d). (c) A slit array etched in a gold film made of large grain sizes with $p = 638$ nm $w = 200$ nm and $h = 230$.

4.1.2.   Optical setup

An optical setup dedicated to the visible – near infrared spectral range (from 400 to 950 nm in the present case) is used to characterize the structures. It is composed of three parts: an inverted microscope (Zeiss Axiovert 135), a monochromator (SpectraPro 300i, Acton Research Corporation, USA) and a nitrogen cooled charge-coupled device (CCD) camera (LN/CCD-512SB with ST-130 controller, Princeton Instrument, USA). A schematic of the setup is shown in Fig. 4.4.
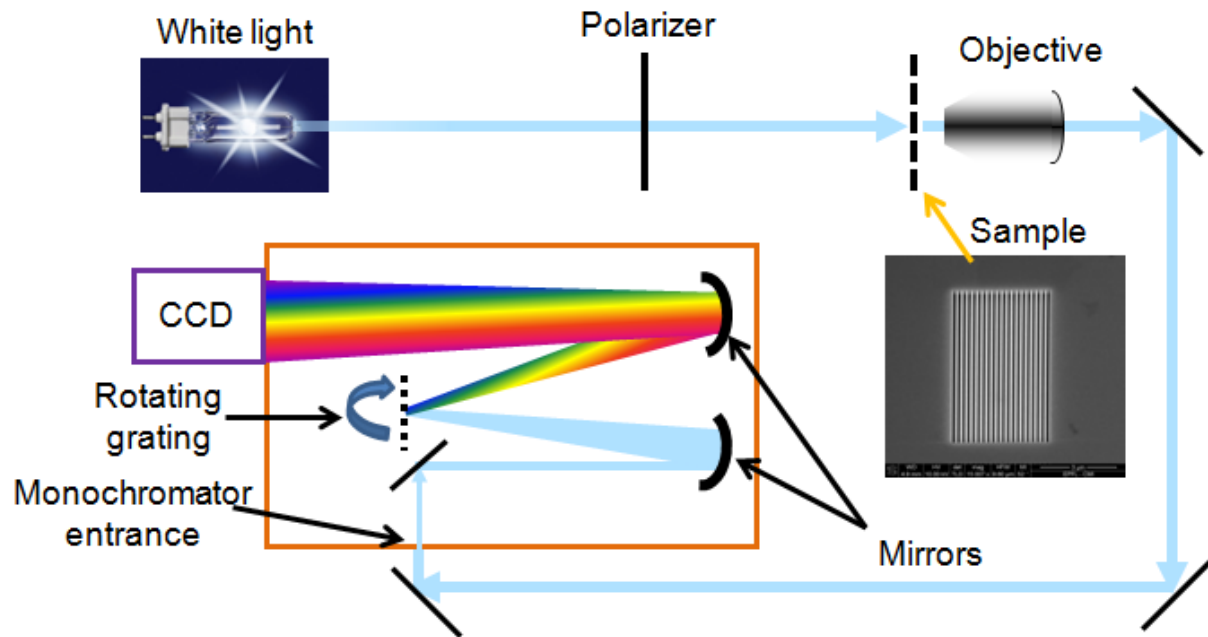
Figure 4.4. Schematic of the optical setup used to measure the light transmission through metal structures.

Structures are aligned on the optical axis of the microscope and illuminated with a halogen lamp. The incoming beam has a low numerical aperture (NA < 0.1). The halogen lamp provides unpolarized white light. The polarization state is controlled using a Glan laser prism (extinction ratio ER = 10^5) placed in a rotational mount and inserted between the lamp and the sample. Light transmitted through the structure is collected through a microscope objective and directed toward the entrance of the monochromator, where it forms an image of the structure. The entrance width determines the spectral resolution of the system. Light entering the monochomator is reflected on a grating and projected onto the CCD camera. If the position of the grating is such that the zero diffracted order is directed onto the CCD, an image of the monochromator entrance is formed on the CCD. This is what is observed in the left part of Fig. 4.5 where an image obtained in this configuration is shown for a slit and groove structure. The slit can be distinguished as well as the edges of the entrance of the monochromator. For clarity, a schematic of the image of the slit and the monochomator entrance is shown in the inset of Fig. 4.5. Rotating the grating such that a dispersive order is directed towards the CCD camera leads to Fig. 4.5(b), i.e. a two dimensional image with in abscissa the wavelength and in ordinate the position on the sample.
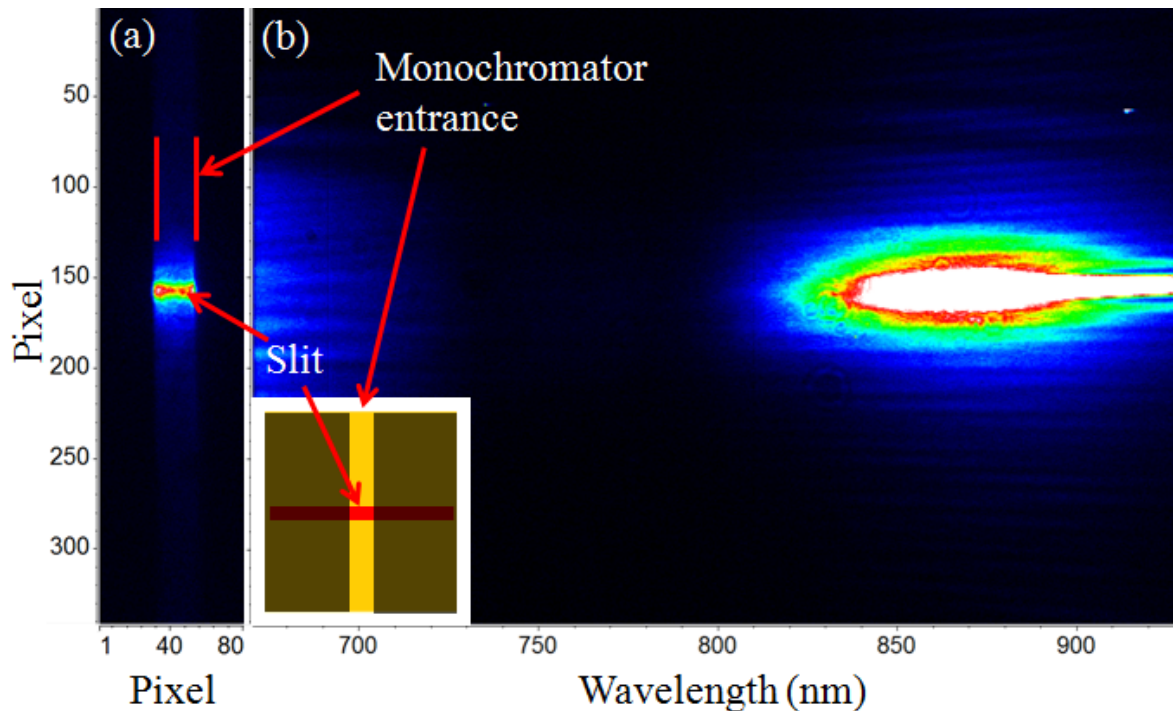
Figure 4.5.   Images of a slit and groove structure recorded by the CCD when the grating is placed such that (a) the zero diffracted order is directed onto the CCD, leading to a two dimensional spatial information; (b) a dispersive order is directed towards the CCD, which leads to an image with spectral information in abscise and spatial information in ordinate. The inset shows a schematic of the image of the slit and the monochomator entrance.

In the example of Fig. 4.5, the slit is centred and directed perpendicular to the monochromator entrance. In this configuration, the light transmitted by the slit is measured at its central portion. The structures used here are 10 µm long, which is sufficient to avoid any influence due to the edges in the measurement. Consequently, this configuration is close to the theoretical conditions used to design the structures, where infinitely long slits are assumed.

4.1.2.1.   Collection angle

Light transmitted through a single slit is scattered in all directions perpendicular to the slit axis. When the light is incident on the air side of the structure, transmitted light experiences refraction at the glass-air interface, see Fig. 4.6. At large scattered angles, light is not transmitted through the substrate due to total internal reflection and is consequently not measured. Also, the light is collected only within a finite collection angle θ_{col} in the experiment. The collection angle is governed by the NA of the microscope objective. If not

otherwise specified, the objective used in the measurements is a 40× power objective with NA = 0.6. With this NA, the collection angle is $\theta_{col} \approx 36.9°$. Considering a glass refractive index of 1.5, this gives $\theta_{col} \approx 23.6°$. In the case where light is isotropically scattered at the slit, which is valid for a PEC and $w << \lambda$, only 26% of the light is collected.
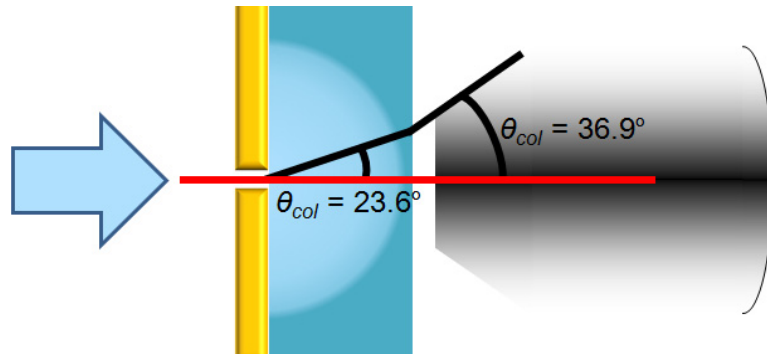
Figure 4.6.   Scheme representing the collection of the light transmitted through a slit on a glass substrate and a microscope objective of NA = 0.6.

In the case of a slit array, light is scattered within discrete orders. For wavelength higher than the first order Rayleigh wavelength $\lambda_{RW,1}$ (cf. Chapter 3), only the zero diffracted order is a propagating order. Consequently, in that case the total transmission is measured. The zero diffracted order is always collected, and higher orders n of diffraction are collected for $n\lambda/p <$ NA. For example, the first diffracted order for $p = 600$ nm will be collected with the 0.6 NA objective only for $\lambda < 360$ nm.

4.1.2.2.   Spectrum normalization

In order to normalize the transmission spectra of the structures, the following operation is performed for each pixel of the CCD:

$$T_{pixel} = \frac{P_{structure} - P_{noise}}{P_{reference} - P_{noise}}, \tag{4.1-1}$$

where $P_{structure}$ is the signal measured by the CCD when light is transmitted through a structure, $P_{reference}$ is the signal measured when light is transmitted through a glass substrate and P_{noise} the signal measured when the incoming beam is blocked.

Two different figures of merit are used to evaluate the transmission efficiency of the structures. For slit arrays, what is of interest is the absolute transmission T, i.e. the ratio between the power transmitted by the structure to the one incident on the entire structure. This corresponds to the values calculated for slit arrays in Chapter 3. If the number of slits can be

considered to be infinite, i.e. boundary effects can be neglected, T is directly obtained averaging T_{pixel} over several pixel lines. However, when a spectrum is measured for a finite array, light is scattered at the edge of the array. This results in light being detected over an area larger than the physical area of the slit array. This is shown in Fig 4.7 which shows the spectrum measured for a finite array of slits. The size of the slit arrays is marked by a dashed line. Light transmitted through the slit array clearly passes outside of the marked region. This can be seen particularly clearly at 940 nm where light is detected from pixel 50 to 70.
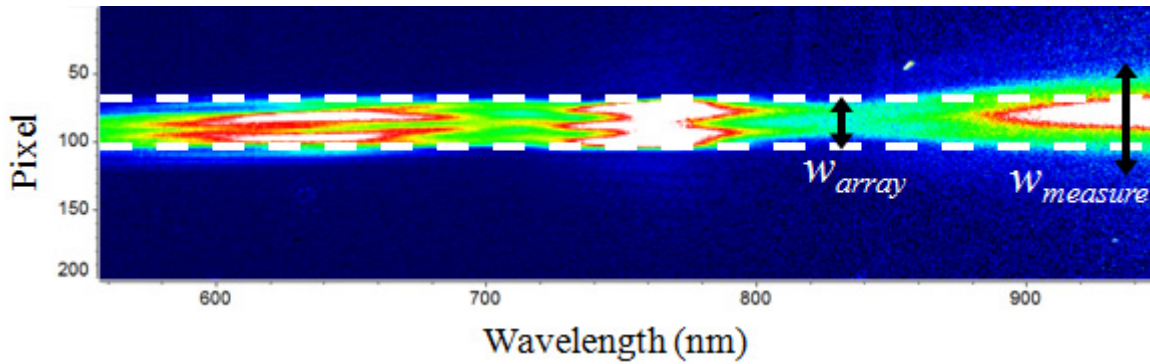
Figure 4.7.   Image of a slit array recorded by the CCD when the grating is placed such that a dispersive order is directed towards the CCD. The dashed lines represents the width of the array.

To overcome the influence of edge effects, it is necessary to average T_{pixel} over a number of pixel lines N_{pixel} larger than the one comprised inside the dashed line of Fig. 4.7. In other words, a width $w_{measure} = N_{pixel}S_{pixel}$ larger than $w_{array} = N_{slit}p$ needs to be considered, where S_{pixel} corresponds to the effective size of a pixel on the sample plane. In our setup, S_{pixel} = 145 nm. The absolute transmission is then:

$$T = \left\langle T_{pixel} \right\rangle \frac{w_{measure}}{w_{array}} . \qquad (4.1\text{-}2)$$

In the case of a single slit or slit and grooves, we are interested to the "funnelling" effect of the structure. A measure of the efficiency is the normalized transmission (NT), defined as the amount of light transmitted through the slit compared to the flux incident on the slit. The approach is similar to the one used in the case of slit array, averaging T_{pixel} over N_{pixel} lines. The normalized transmission is obtained as:

$$NT = \left\langle T_{pixel} \right\rangle \frac{w_{measure}}{w} . \qquad (4.1\text{-}3)$$

4.2. Transmission measurements through single slits

4.2.1. TM polarization

The transmission properties of a single slit have been described in the theoretical study of Chapter 3. It was shown that in the TM case, the fundamental mode is always a propagating one, which may lead to high transmission and FP resonances (cf. Section 3.1.2). TM transmission measurements of single slits in a 310 nm thick gold film are shown in Fig. 4.8(a) for widths of 100, 150 and 200 nm. For certain wavelengths, almost 25% of the light impinging on the aperture is transmitted within the collection angle of the setup. FP peaks are very broad due to the low reflection inside the aperture. The real part of the propagation constant for the fundamental TM mode $\Re(\beta_0)/k_0$ increases when the slit width is decreased, as shown in Fig. 4.9(a). This shifts the FP peak to longer wavelengths, which is barely observed in Fig. 4.8(a). Below 500 nm, the transmission decreases due to high losses of gold at short wavelengths [98]. This is confirmed in Fig. 4.9(a) observing for different slit widths the propagation constant of the fundamental TM mode. One sees that its imaginary part $\Im(\beta_0)/k_0$ increases below 500 nm, inducing losses and reducing the transmission.

4.2.2. TE polarization

In the TE case, the fundamental mode is evanescent for $\lambda > \lambda_c$, leading to low transmission. For real metals, λ_c is slightly larger than $\lambda = 2w$, which corresponds to the cut-off wavelength for PEC (cf. Chapter 3). The TE transmission, plotted in Fig. 4.8(b) on a logarithmic scale, decreases rapidly with increasing λ. This is characteristic of transmission below cut-off. Decreasing w also reduces the transmission, which is comparable to the instrumental noise for the 100 nm slit width. The values taken by the TE mode in Fig. 4.9(b) show that decreasing w increases $\Im(\beta_1)/k_0$, which means that the field amplitude decays more rapidly inside the slit for small slits.

The mode index calculated in the case of gold and $w = 100$ nm is compared with the PEC case in Fig. 4.9(b). The general trend with wavelength is similar, except at short wavelengths. This is due to two effects: (i) the cut-off wavelength is larger for gold than for PEC; (ii) at these wavelengths, the real part of the permittivity is less negative, and the mode penetration inside the metal is increased. As compared to TM modes, TE modes should be less sensitive to the PEC approximations with increasing slit width because TE modes are not confined on the metal surface but at the centre of the slit. This will be discussed in Section

68

4.4.2.2.

A single slit presents strong polarizations properties, as observed in Fig. 4.8(b), where TM transmission is higher than TE transmission for any w and λ. The extinction ratio (ER) of polarization, defined as the ratio between TM and TE transmission, strongly varies with slit width. The ER ranges from 2-3 to at least 500 for widths of 200nm and 100nm, respectively.
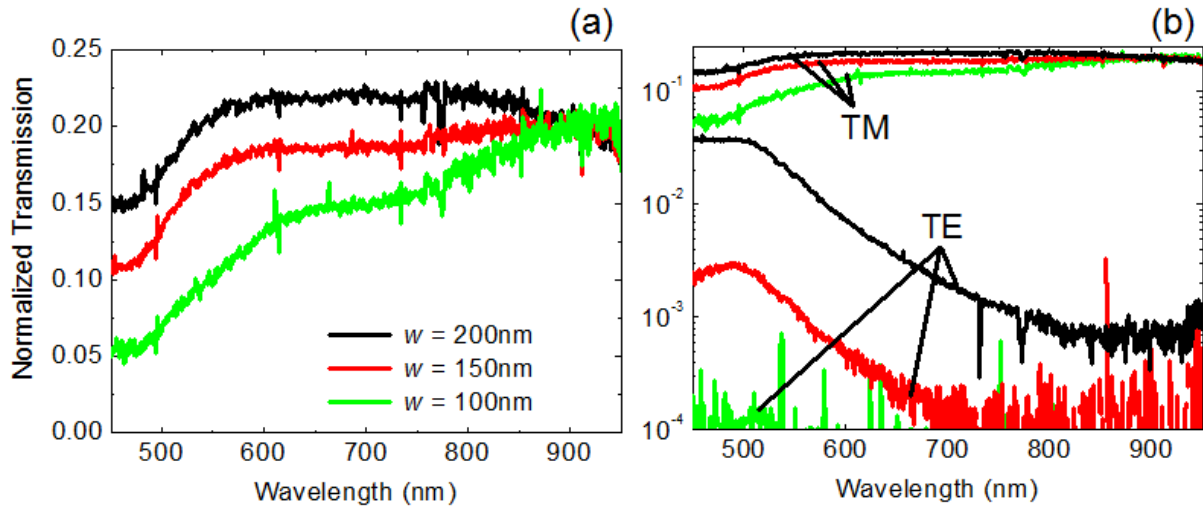
Figure 4.8.   Transmission spectra of single slits etched in a 310 nm thick gold film for widths of 100, 150 and 200 nm (a) for TM polarization (b) for TE and TM polarization plotted on a logarithmic scale.
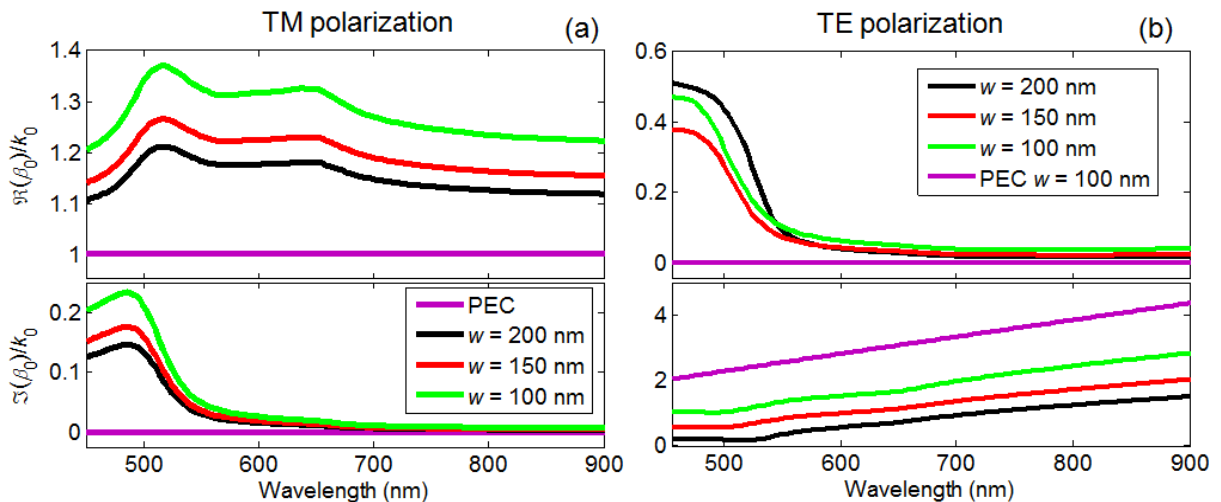
Figure 4.9.   Propagation constant (a) β_0 for TM polarization and (b) β_1 for TE polarization calculated in function of λ and w following the method of Section 3.1.1. The axes of the graph are normalized to k_0.

4.3. Enhanced optical transmission measured with slit and groove structures

The optical properties of slit and grooves structures on glass substrates are measured and compared with theory in the present section. The goal here is to validate the design tools used in order to apply them afterwards for photodetection, which is treated in Section 5.3.

4.3.1. TM transmission

As discussed in Chapter 3, placing periodic grooves around a single slit can boost TM transmission due to the excitation of SPP modes. Normalized transmission (NT) spectra are shown in Fig. 4.10(a) for slit and groove structures with periods ranging from 600 to 800 nm and the following set of parameters: $w = 100$ nm, $h = 180$ nm, $h_g = w_g = 100$ nm, $N_g = 5$ and TM polarization. High transmission induced by SPP excitation is expected at a wavelength λ larger than $\lambda_{SPP,n}$ [53,71]. As $\lambda_{SPP,n}$ scales with p, the transmission peak is red-shifted on increasing p. This is what is seen in Fig. 4.10(a), where the high transmission peak ($NT > 1$) measured at $\lambda \approx 765$ nm for $p = 600$ nm shifts to $\lambda \approx 910$ nm for $p = 800$ nm. When $NT > 1$, there is more light transmitted by the slit than the original flux impinging on the slit aperture, i.e. light is concentrated into the aperture.
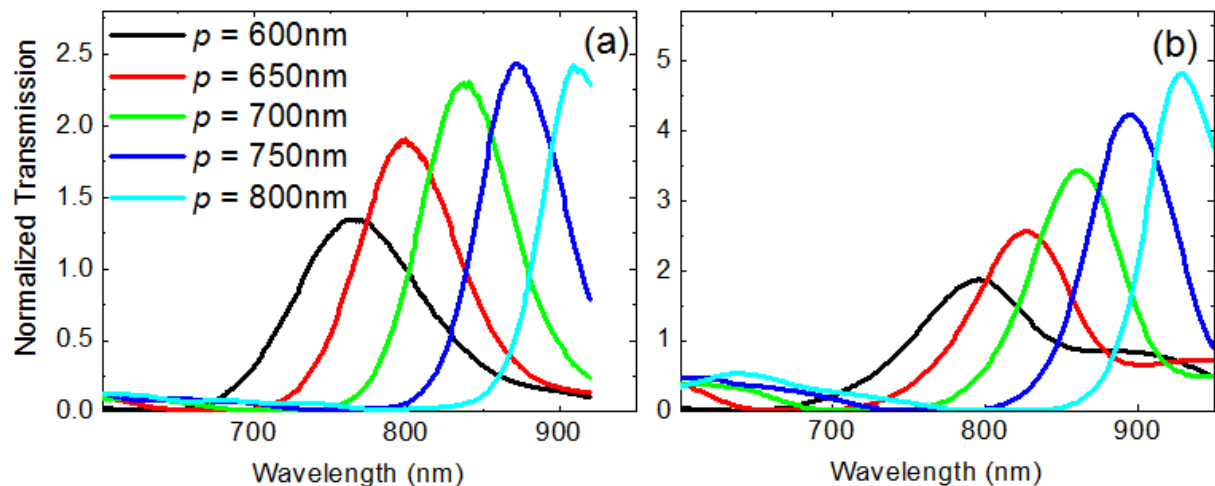
Figure 4.10   (a) Normalized transmission spectra measured for slit and groove structures with parameters $w = 100$ nm, $h = 180$ nm, $h_g = w_g = 100$ nm, $N_g = 5$ and TM polarization. (b) Corresponding theoretical calculations from the modal expansion method and considering $\theta_c \approx 23.6°$ as in the experiment [99].

4.3.2. Comparison between theory and experiment

The model used to calculate the optical transmission is based on a modal expansion method adapted to slit and grooves structures [93,100]. The code used has been developed by the groups of Prof. Luis Martín-Moreno from the Universidad de Zaragoza (UNIZAR) and Prof. Francisco J. García-Vidal from the Universidad Autónoma de Madrid (UAM) in Spain. The displayed data have been provided by Dr. Fernando de León-Pérez from UNIZAR. In this model, SIBC is considered at all interfaces except those of the lateral walls of both slit and grooves where a PEC was assumed. A constant refractive index of 1.5 is considered for the glass substrate.

The theoretical calculations of the spectra corresponding to the measurements of Fig. 4.10(a) are shown in Fig. 4.10(b). A collection angle $\theta_c \approx 23.6°$ has been considered, as is the case in the experiment (cf. Section 4.1.2). Good qualitative agreement between the theoretical and experimental results is observed. The spectral shift of the transmission peak to longer wavelengths with increasing 50 nm periods is approximately 35 nm for both theory and experiment. Moreover the linewidths of the peaks, which narrow toward longer wavelengths, are also in good agreement. The theoretical curves are slightly redshifted compared to the measured data, and the normalized transmission is slightly smaller in the experiment. These discrepancies can be caused by the approximations used in the model and also because several parameters of the experiment are not considered in theory: the finite size of the array, the non-zero NA of illumination, surface roughness or imperfection in the structure profile [cf. Fig. 4.3(d)]. The expected influence of these parameters is a smoothing of the spectral features.

Another possible factor that may explain these differences is the optical losses induced during FIB fabrication, as discussed in Section 4.1.1. Losses are concentrated in a thin layer below the etched area, where the ions penetrates. This effect is likely to be important in the transmission properties of the metal structures, as high field confinement occurs close to the structure.

4.3.3. Importance of the collection angle

To show the effect of the collection NA, light transmission through slit and groove structures with parameters $w = 100$ nm, $h = 240$ nm, $h_g = 80$, $w_g = 90$ nm, $N_g = 6$ and TM polarization is measured with two different objectives. Normalized transmission spectra measured with the 0.6 NA objective are shown in Fig. 4.11(a), whereas an oil immersion objective (NA = 1.25 and power 100×) was used for the spectra shown in Fig. 4.11(b). The

collection angle of this objective is $\theta_{col} \approx 56.4°$. Using such an objective doubles the intensity measured as compared to the 0.6 NA objective. The effect of the numerical aperture of collection is strongly dependant on the slit width. As the slit width is reduced, the emission pattern from the slit will become similar to the one of an emitting dipole, and the amount of light scattered at large angles increases.

Figure 4.11   Transmission spectra measured for slit and groove structures with parameters w = 100 nm, h = 240 nm, h_g = 80, w_g = 90 nm, N_g = 6 and TM polarization. (a) $\theta_{col} \approx$ 23.6° (b) $\theta_{col} \approx$ 56.4°.

4.3.4.   Polarization properties

The TE transmission through a slit is not expected to be modified by adding periodic grooves as there is no TE surface mode sustained at the metal-dielectric interface. This is what is observed in Fig. 4.12, where the TE transmission through a slit and groove structure is very similar to that of a single aperture. The transmission for TE is higher in Fig. 4.12 than in Fig. 4.8 obtained for a single slit. This is principally due to the fact that the film is thicker in the case of Fig. 4.8.

Transmission through a slit and groove structure involves two polarization dependent processes: (i) the excitation of SPP by the periodic grooves; (ii) the transmission through the slit. Consequently, these structures are highly polarization sensitive.
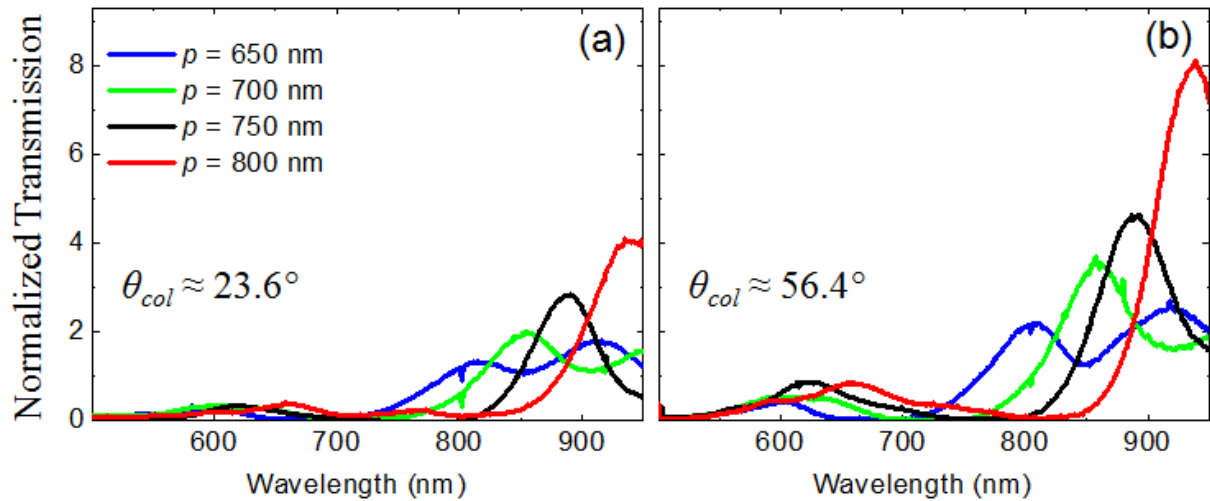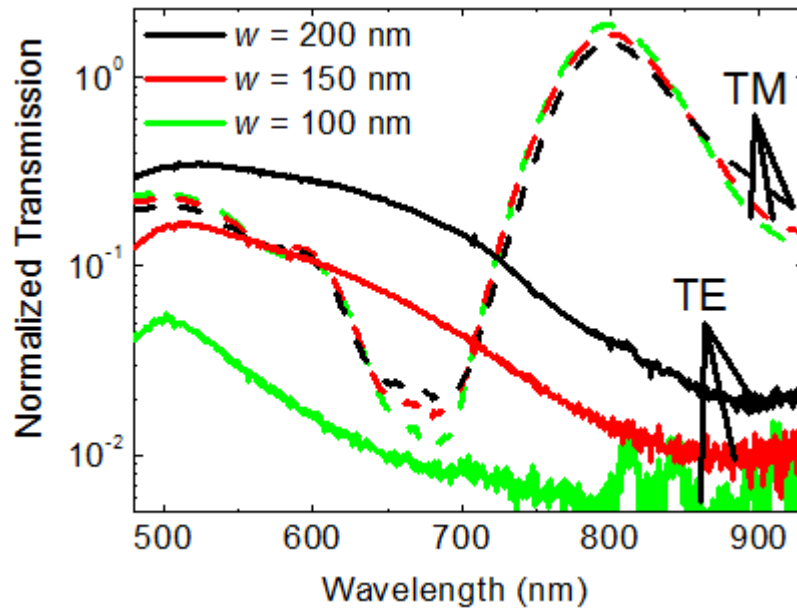
Figure 4.12　Normalized transmission spectra measured for slit and groove structures with parameters p = 650 nm, h = 180 nm, h_g = w_g = 100 nm, N_g = 5 for widths varying between 100 nm and 200 nm for TE and TM polarization plotted on a log scale.

4.4. Slit and groove structure with a thin dielectric top layer: towards unpolarized enhanced optical transmission

4.4.1. Introduction

The polarization sensitivity of slit and groove structures has been advantageously exploited in several studies, for example to filter polarization (cf. Section 5.3 and Ref. [99]) or to control the polarization state of optical devices [101]. Most of the TE polarized light is lost, which is a drawback in applications where high transmission is necessary, such as low noise [99] or high speed [102] photodetectors.

In order to increase the transmission of TE polarized light, it is first necessary to use a slit width such that it is above the cutoff width. Secondly, transmission can be increased by exciting TE surface waves, as is the case for enhanced TM transmission. This is made possible by adding a thin dielectric layer on top of the slit and groove structure. Such a layer permits TE polarized incident light to couple to dielectric waveguide modes. Light is then directed toward the slit which boosts TE polarized transmission. At the same time, TM polarized light can still be resonantly transmitted. This design was recently proposed and theoretically investigated in Ref. [69]. A scheme of this system is shown in Fig. 4.13(a). The goal of Section 4.4 is to validate this concept experimentally.
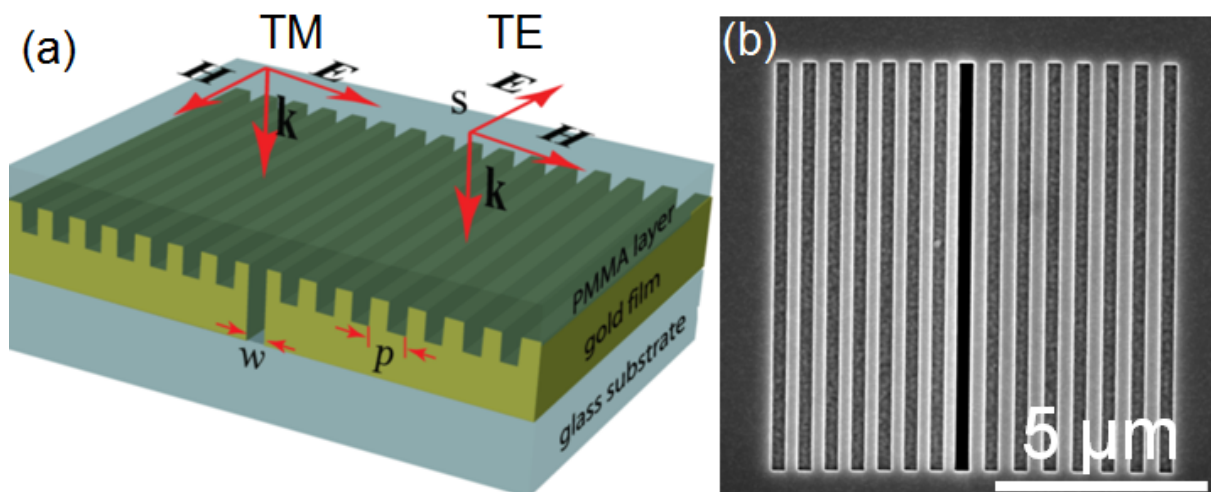
Figure 4.13   (a) Schematic of a slit and groove structure covered by a dielectric layer and definitions used for the structure dimensions. (b) SEM image of a slit and groove structure with $p = 638$ nm, $w = 311$ nm, $h = 420$ nm, $N_g = 7$, $w_g = 325$ and $h_g = 180$.

4.4.2. Transmission without dielectric layer

Transmission measurements through slit and groove structures are first performed without a dielectric layer. This helps afterwards to distinguish the effects induced by the addition of the dielectric layer.

4.4.2.1. Measurements

The slit and groove structures studied in Section 4.4 have in common the following geometrical parameters: $h = 420$ nm, $N_g = 7$, $w_g = 325$ and $h_g = 180$. Such a structure is shown in Fig. 4.13(b). Transmission spectra for $w = 311$ nm and various periods are plotted in Fig. 4.14. The high TM transmission peak induced by SPP excitation is red-shifted on increasing p, whereas the transmission is independent on p in the TE case, since no surface waves are resonantly excited. In Fig. 4.15, the slit width is varied and the period is fixed ($p = 638$ nm). Decreasing w reduces TE transmission. This is in accordance with what is observed for other slit and groove structures (cf. Section 4.3).
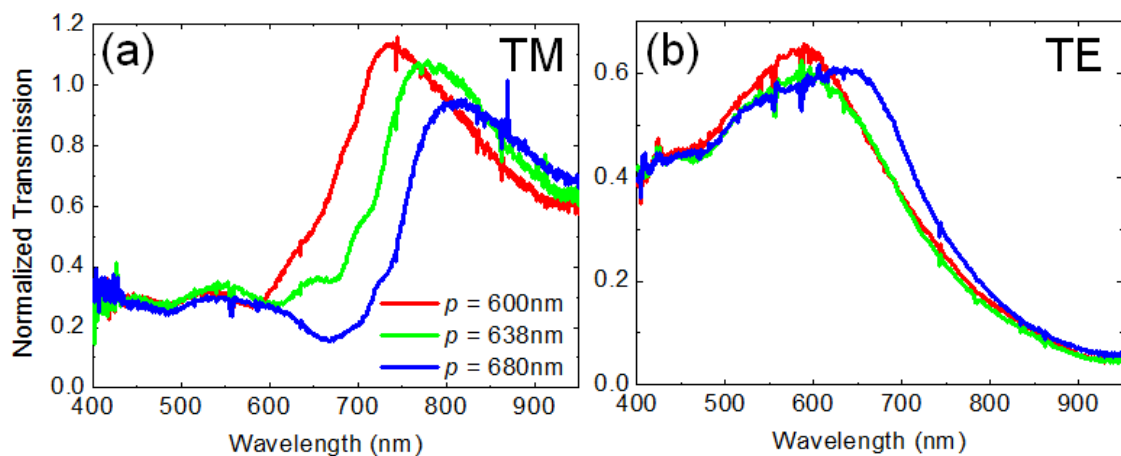
Figure 4.14   Normalized transmission spectra of slit and groove structures with $w = 311$ nm, $h = 420$ nm, $h_g = 180$ nm, $w_g = 325$ nm, $N_g = 7$ for periods varying between 600 to 680 nm and (a) TM and (b) TE polarization.

4.4.2.2. Agreement with theory

Measurements are compared with theoretical data provided by Dr. Alexey Yu. Nikitin from UNIZAR who used the model described in Ref. [69]. Gold is treated as a PEC and a fixed refractive index of 1.5 is considered for the glass substrate and later for the dielectric layer. The finite collection angle of the experiment has been taken into account in the calculations by restricting the integration interval of the propagating part of the transmitted angular spectra.
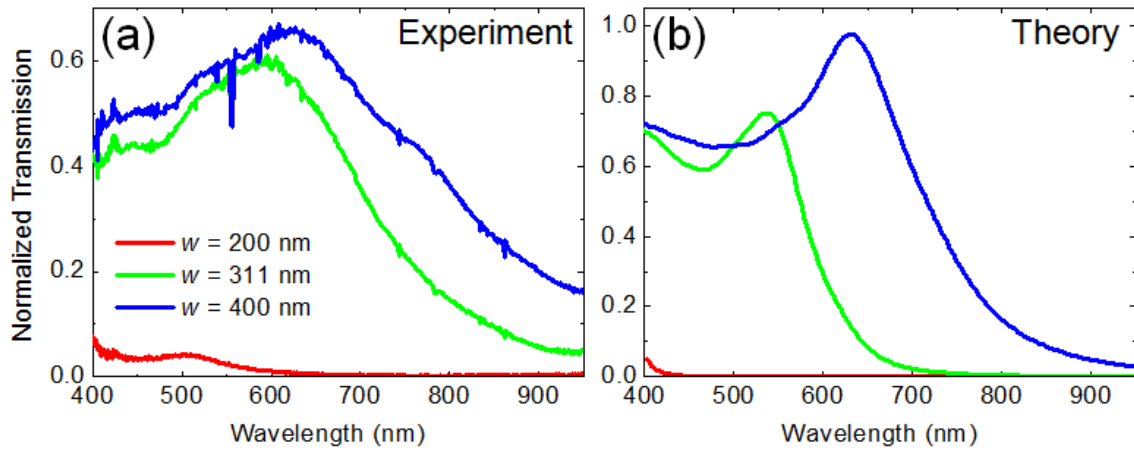
Figure 4.15   TE transmission spectra of slit and groove structures with $p = 638$ nm, $h = 420$ nm, $h_g = 180$ nm, $w_g = 325$ nm, $N_g = 7$ for slit widths varying between 200 to 400 nm. (a) Experiment. (b) Theory.
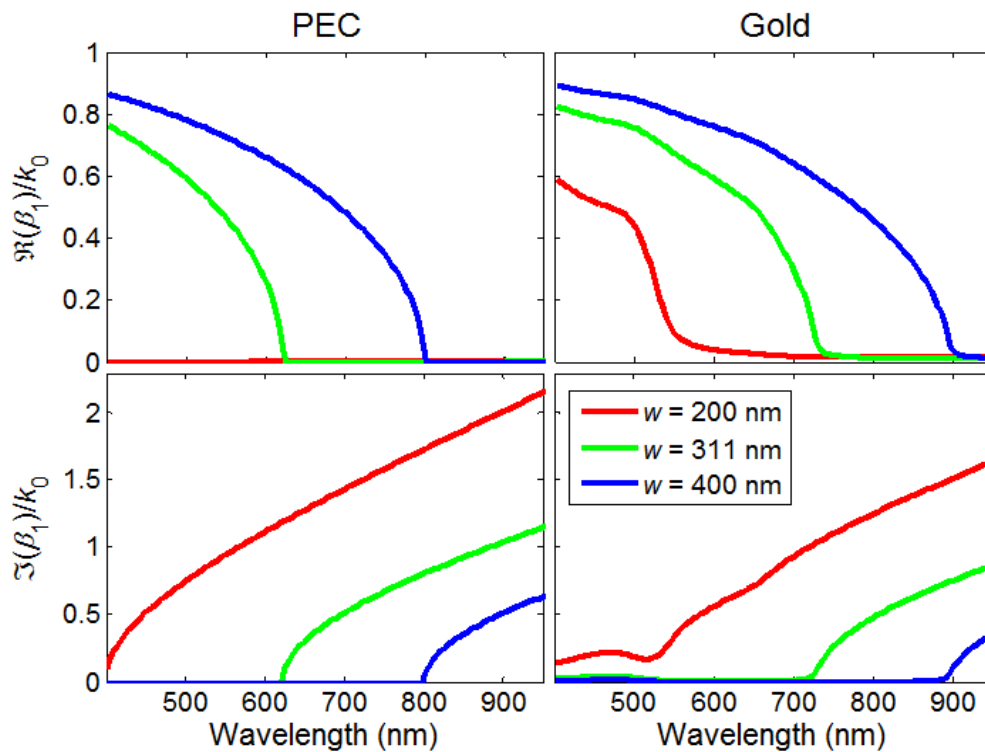
Figure 4.16   Propagation constant β_1 for TE polarization calculated in function of λ and w considering PEC (left part) and gold (right part). Data are calculated following the method of Section 3.1.1. The axes of the graph are normalized to k_0.

The measurements in Fig. 4.15(a) are in good agreement with the calculated spectra in Fig. 4.15(b), even if PEC is considered. Following the method of Chapter 3, the first TE mode is plotted for PEC and gold in Fig. 4.16. It is observed that for $w = 311$ nm and $w = 400$ nm, β_1 is very similar for both gold and PEC, validating the use of PEC for such structures. As

said in Section 4.2.2, TE modes are becoming less sensitive to the PEC approximations with increasing w because these modes are not confined on the metal surface. The PEC approximation provides a good semi-quantitative agreement with the experiment for TE polarization in the optical region. For TM polarization the results based on PEC approach are not reliable for wavelengths shorter than 600 nm, but the agreement improves with increasing wavelength as the real part of the permittivity is becoming more negative.

4.4.3.   Dielectric layer deposition

The slit and groove structures measured in the previous section have been covered by a dielectric layer with the following procedure. 100 mg of Poly(methyl methacrylate) (PMMA) was dissolved in 1 mL anisole (CH3OC6H5). The solution was spun onto the gold structure at a speed of 5300 revolutions per minute. This results in a PMMA layer of thickness $h_d = 250 \pm 10$ nm above the metallic structure. This corresponds to the thickness suggested in Ref. [69]. Both slit and grooves are completely filled with PMMA. The profile of the PMMA film on top of the structure was measured by AFM. Fig. 4.17 shows this profile for a line scan taken perpendicular to the slit and groove direction. A modulation $x_g < 30$ nm is measured on top of the grooves. This can be considered as optically flat ($x_g < \lambda/10$) as we consider a dielectric medium here. Above the slit, a modulation of height $x_s = 100 \pm 10$ nm has been measured. This gives $\lambda/5 < x_s < \lambda/10$ which should have little influence on the optical properties of the structure.
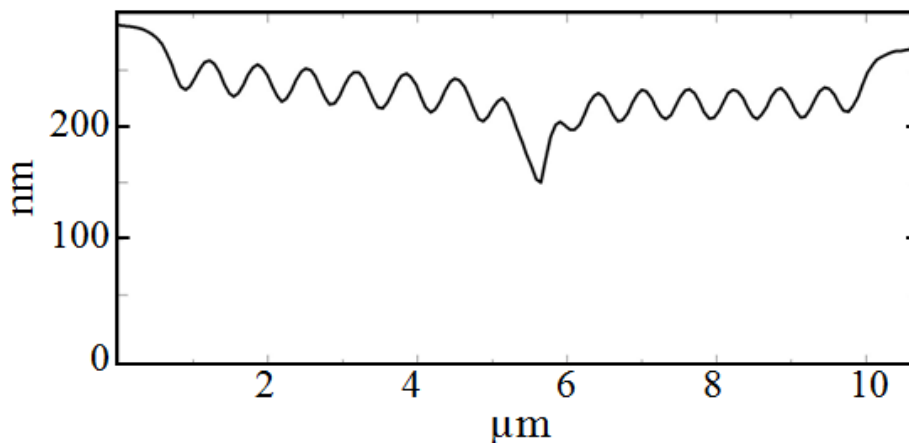
Figure 4.17   AFM measurement of the PMMA layer profile deposited above a slit and groove structure.

4.4.4.   Transmission measurements with PMMA layer

4.4.4.1.   TM transmission

The TM transmission through the structures covered by the PMMA layer is shown in Fig. 4.18. A red-shift of the transmission peak with increasing period is observed in Fig. 4.18(a), which is characteristic of the resonant transmission induced by surface wave excitation. $\lambda_{SPP,n}$ is red-shifted as compared to the air case due to the presence of the PMMA layer. Consequently, the transmission peaks observed in Fig. 4.14(a) are displaced to longer wavelength. In Fig. 4.18(a), these peaks are out of the wavelength range considered and therefore not observed. The peaks observed in Fig. 4.18 are attributed to the excitation of $\lambda_{SPP,2}$.
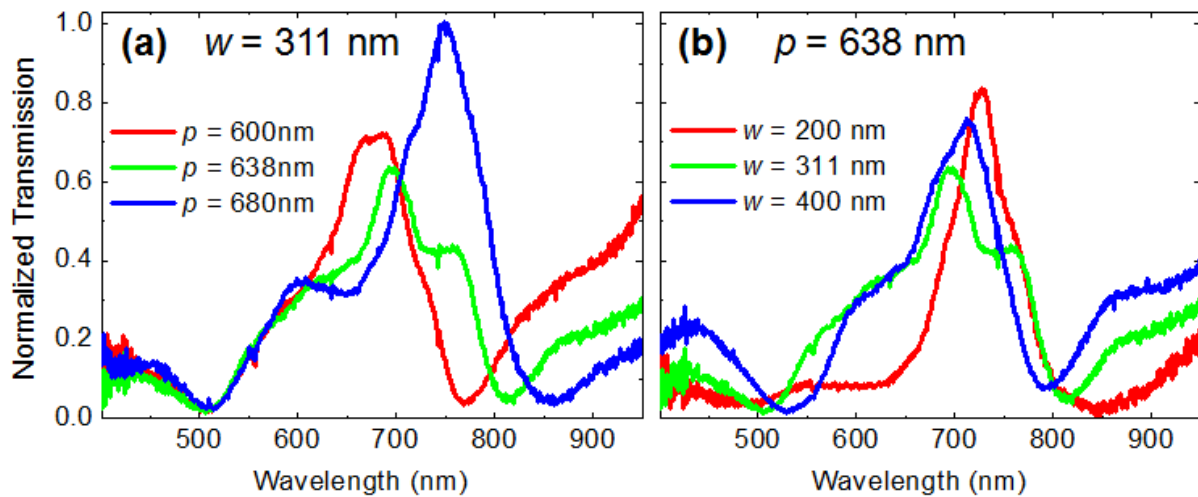
Figure 4.18   Normalized TM transmission spectra of slit and groove structures covered by a thin PMMA layer. The slit and groove dimensions are the same than for Fig. 4.14. In panels (a) $w = 311$ nm and p is varied. In panels (b) $p = 638$ nm and w is varied.

4.4.4.2.   TE transmission

Transmission spectra for TE polarization with the PMMA layer added on top of the structure are shown in Fig. 4.19. The dielectric layer modifies the transmission properties of the structure. Spectra are now dependent on periodicity. This indicates that the metallic grating allows incident light to resonantly couple into the dielectric layer. This coupling occurs at $\lambda_{w,n} = (p/n)q_w$, where q_w is the effective index of the waveguide mode. Only one TE polarized waveguide mode is supported in the 250 nm dielectric layer for the wavelength range considered, as show in Fig. 4.20.
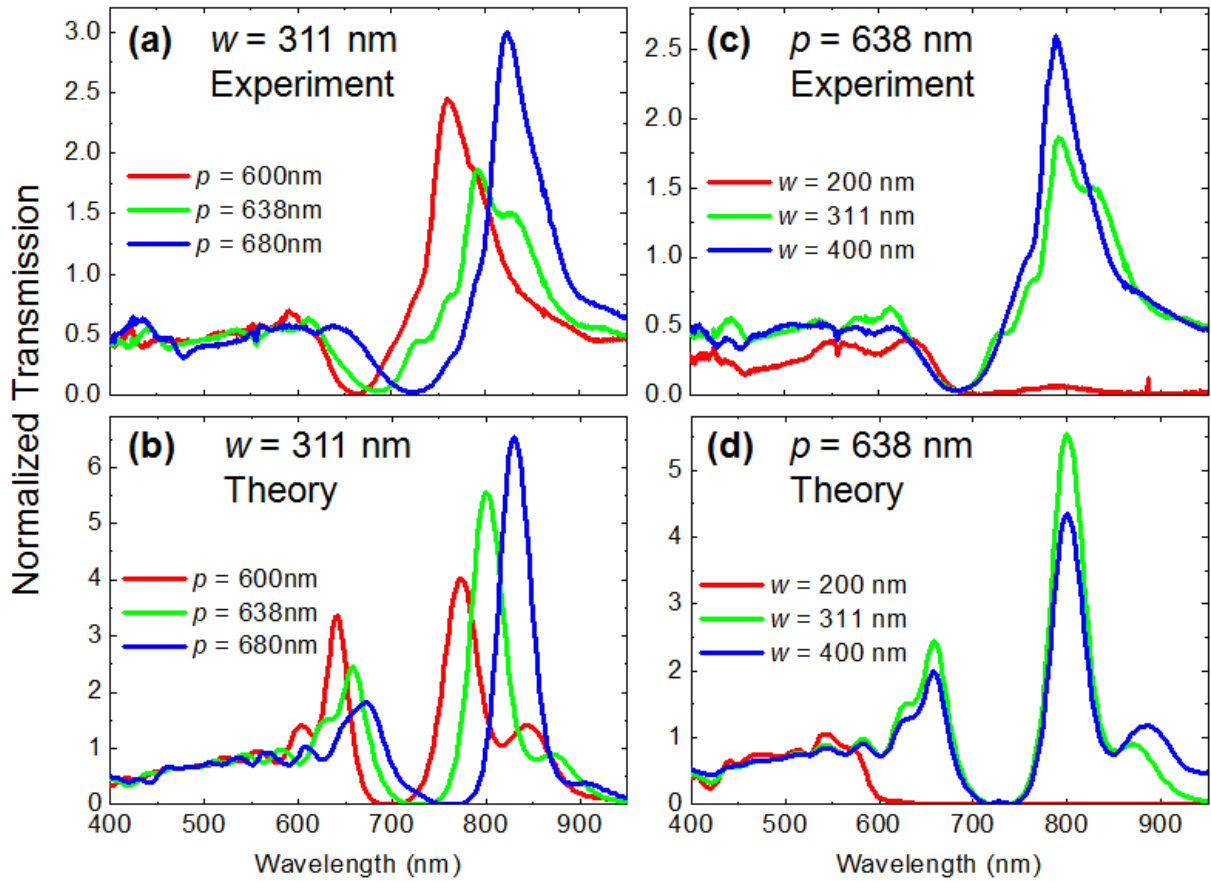
Figure 4.19   Normalized TE transmission spectra of slit and groove structures covered by a thin PMMA layer. The slit and groove dimensions are the same than for Fig. 4.14 and 4.15. Panels (a) and (c) show measurement spectra and panels (b) and (d) the corresponding calculations. In panels (a) and (b), $w = 311$ nm and p is varied. In panels (c) and (d), $p = 638$ nm and w is varied.
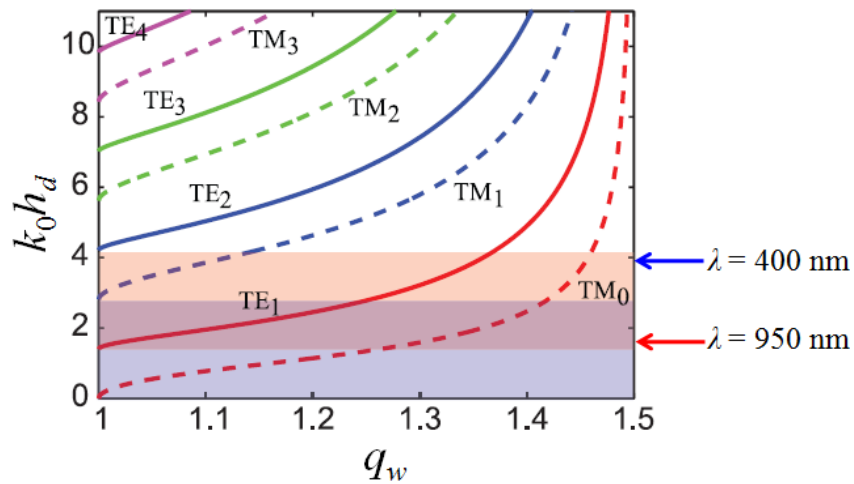
Figure 4.20   Dispersion curves of both TM (dashed lines) and TE (continuous lines) modes sustained in a dielectric film (refractive index 1.5) placed above a PEC. Highlighted regions represent single-mode regimes. Adapted from Ref. [69].

The highest transmission measured is $NT = 2.5$ for $p = 680$ nm at $\lambda \approx 825$ nm. This corresponds to a 25 fold increase as compared to the s-polarization case without PMMA layer. As discussed in the previous section, total transmission is higher than reported here as not all the light is collected due to the finite NA of the objective. Reducing the slit width such that $\lambda > \lambda_c$ drastically reduces light transmission, see Fig. 4.19(c). Even if the incident light is resonantly coupled into the waveguide mode, light is not transmitted by the single slit for $w = 200$ nm as the TE slit mode is evanescent and thus does not allow high transmission for a 420 nm thick film.

4.4.4.3.   Comparison between theory and experiment

General good agreement is observed between theory and experiment. An inconsistency is observed in the case of the structure with parameters $p = 638$ nm and $w = 311$ nm. This is most likely due to a large sample imperfection. Theory predicts twice the measured transmission, see Fig. 4.19(b) and 4.19(d). This quantitative discrepancy may be due to the reasons discussed in Section 4.3.2, imperfections in the PMMA layer flatness and PEC approximation in the calculations. On the other hand, peak positions in Fig. 4.19 are very accurately predicted theoretically. This is explained by the fact that $\lambda_{w,n}$, which governs peak positions, is weekly affected by sample imperfections and approximations made in calculation. Note that the field of the TE_1 polarized modes in the dielectric layer is not tightly bounded to the surface as in the TM_0 case, which correspond to the SPP mode. Therefore, approximating a real metal by a perfect one predicts more accurately the peak position for TE than for TM polarization.

4.5. Light transmission through slit arrays

4.5.1. TM polarization

As described in Chapter 3, periodic slit arrays support surface modes for TM polarized light which strongly modify the optical transmission properties as compared to a single slit. This is observed experimentally in Fig. 4.21(a), where transmission spectra have been measured for slit arrays with $w = 150$ nm, $h = 285$ nm and periods ranging from 350 nm to 600 nm. The minimum in transmission due to the excitation of SPP's at the gold glass interface observed at $\lambda \approx 620$ nm for $p = 350$ nm is continuously red-shifted as the period is increased. A broad hybrid FP-SPP transmission peak, observed at $\lambda \approx 900$ nm for $p = 350$ nm, is also red-shifted and is out of the spectral range considered in Fig. 4.21 for $p > 500$ nm.
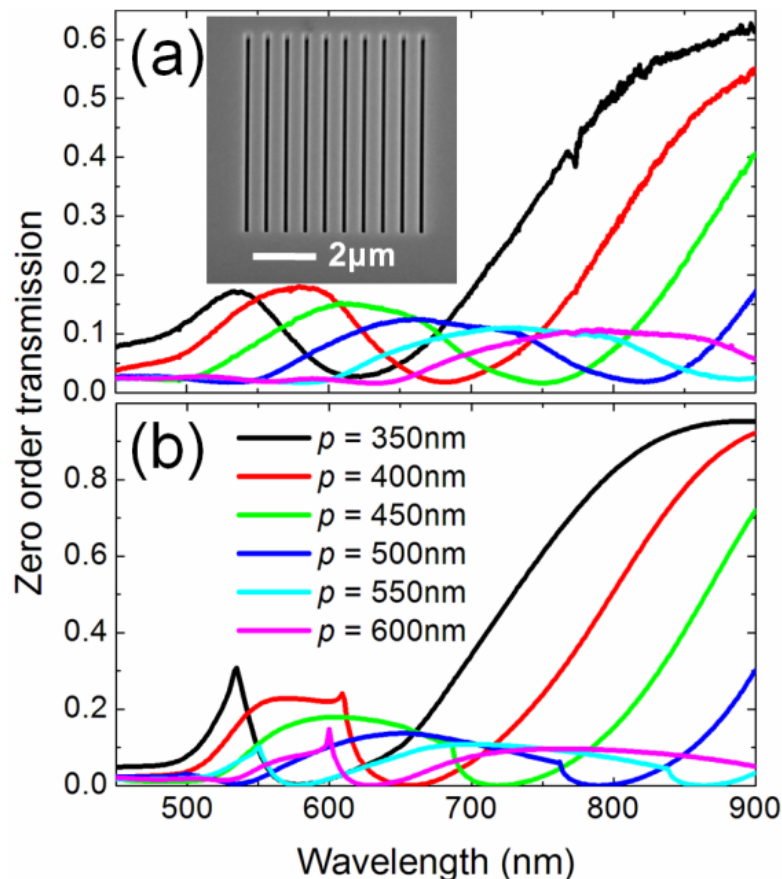
Figure 4.21   (a) Transmission measurements of slit arrays for TM polarization, $h = 285$ nm, $w = 150$ nm and period varying between 350 nm and 600 nm. (b) Corresponding calculations obtained from the modal expansion method. The inset in panel (a) is a SEM image of the slit array with $p = 600$ nm.

4.5.2.   Agreement with theory

Transmission spectra calculated with the modal expansion method (cf. Section 3.2.1) for the same slit array parameters as in Fig. 4.21(a) are shown in Fig. 4.21(b). The refractive index of the glass substrate is considered to be constant (1.525). Simulation and experiment are in good agreement. The peak positions are especially well reproduced. The differences are mainly in the amplitude and the sharpness of the transmission peaks. As in Section 3.2.1, FDTD and GSolver methods were also used and are in agreement with the model described in Chapter 3. The different experimental artefacts already mentioned in the case of slit and grooves (cf. Section 4.3.2) may explain the differences between theory and experiments.

Note that the agreement in terms of transmission amplitude is better here as compared to the slit and groove structures. This can be explained by the fact that PEC is assumed for the lateral walls of the metal in the case of slit and grooves, which underestimates the losses induced by the metal.

4.5.3.   TE polarization and extinction ratio

As in the case of slit and groove structures (cf. Section 4.3.4), the TE transmission through the slit arrays are very similar to that of a single aperture. This is observed in Fig. 4.22(a) for a slit array with parameters $p = 500$ nm, $h = 285$ nm and $w = 150$ nm. Varying the period modifies the total transmission magnitude due to a change in aperture number per area. The zero order transmission changes with p as the power is redistributed into the different diffracted orders.

The ER plotted in Fig. 4.22(b) for the same slit array as in Fig. 4.22(a) is higher than 100 in the 600-900nm range. It decreases at the SPP transmission minima, i.e. at $\lambda \approx 550$nm and $\lambda \approx 800$nm, as shown in Fig. 4.22(b).

Good agreement is again obtained between theory and experiment. The SPP minima are more pronounced in theory than in the experiment, see Fig. 4.22(a). This is due to the fact that the SPP excitation is a strong resonance which is in turn strongly affected by the various experimental parameters not considered in the calculations, see Section 4.3.2. This results to a higher ER in the experiment than in theory at the SPP dips.
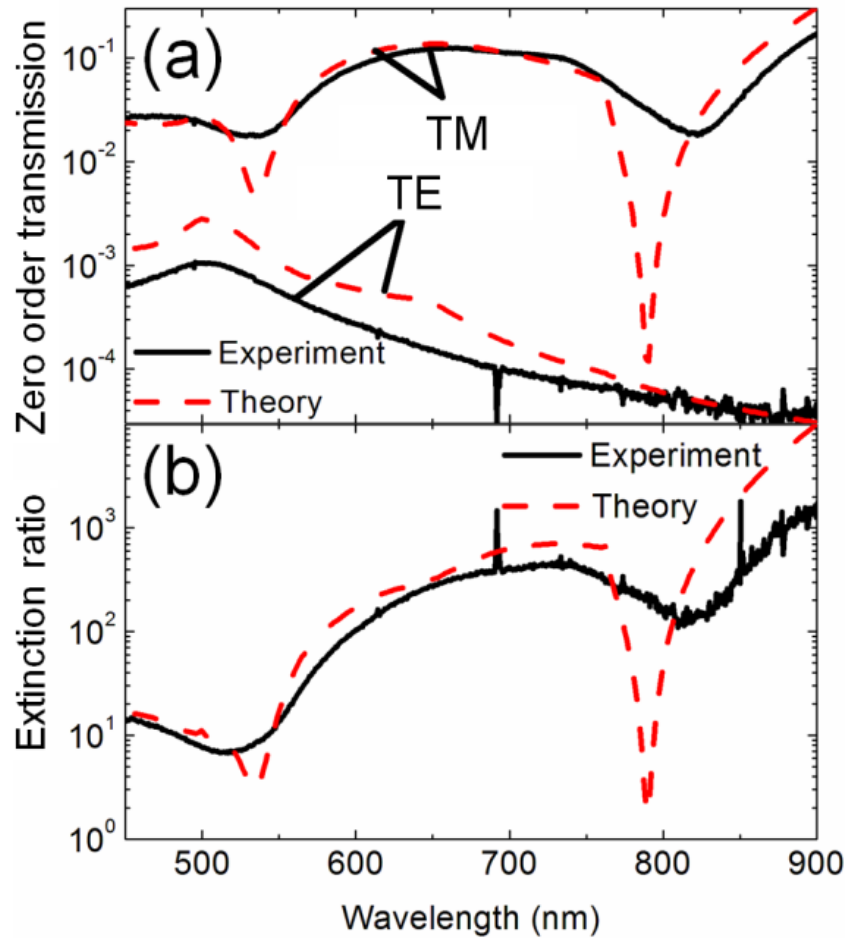
Figure 4.22   (a) TM and TE zero order transmission spectra (b) and the corresponding extinction ratio for $p = 500$ nm, $h = 285$ nm and $w = 150$ nm. Solid curves: experiment; dashed curves: calculation.

4.5.4.   Slit array imaging

A microscope image obtained in transmission is shown in Fig. 4.23(a) for different arrays of 20 slits in a 260 nm gold film. The arrays in the left and right column have a slit width of 100 and 150 nm respectively. The period is increased by 50 nm for each row, starting from $p = 300$ nm in the first row and ending to $p = 750$ nm in the last one. This image shows the different colours obtained depending on the different geometrical parameters of the array.
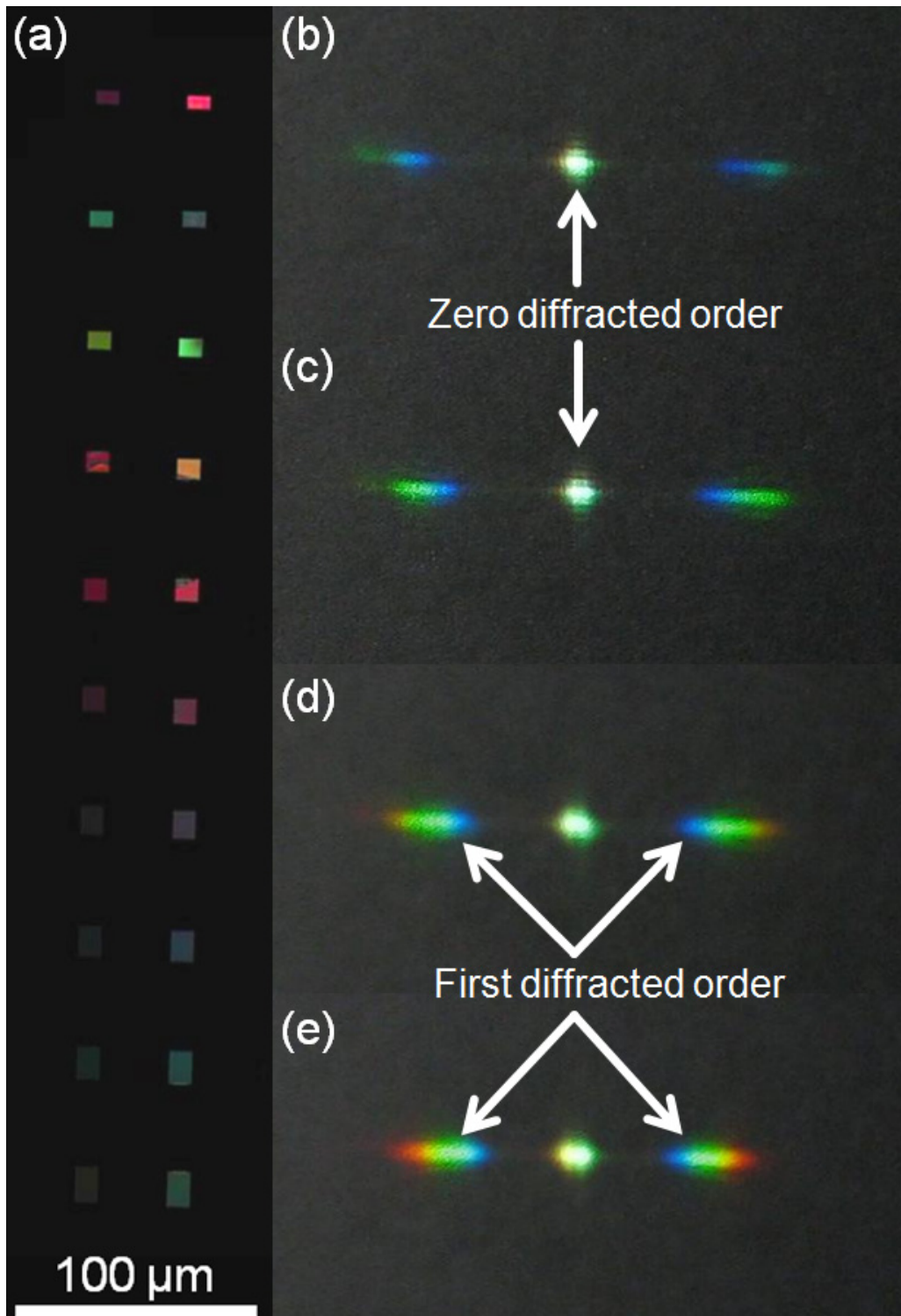
Figure 4.23   (a) A microscope image obtained in transmission for different arrays of 20 slits in a 260 nm gold film. The arrays in the left and right column have a slit width of 100 and 150 nm respectively. The period is increased by 50 nm for each row, starting from $p = 300$ nm in the first row is and ending to $p = 750$ nm in the last one. (b) – (e) Images taken in the Fourier plane showing the scattering pattern of slit arrays with period (b) 600 nm, (c) 650 nm, (d) 700 nm and (e) 750 nm.

Diffraction patterns of slit arrays ranging from 600 to 750 nm are shown in Fig. 4.23(b)-(e). To obtain these images, a supercontinuum white light source is used to provide an intense incoming beam. This beam has a low numerical aperture (NA < 0.1) and is TM polarised. A lens is placed at the back of the sample and images are taken in the Fourier plane. A schematic of this experiment is shown in Fig. 4.24. Each Fourier image shows a spot in the middle which is the zero diffracted order. On each side of this spot, two lines are observed, which correspond to the first diffracted orders. In Fig. 4.23(b), only blue and green colours are observed. As this image is obtained for p = 600 nm, the first diffracted order is not a propagating order for λ > 600 nm. That is the reason why there is no red colour observed. By increasing the period, we indeed see red colour in the first diffracted orders in Fig. 4.23(d) and (e).
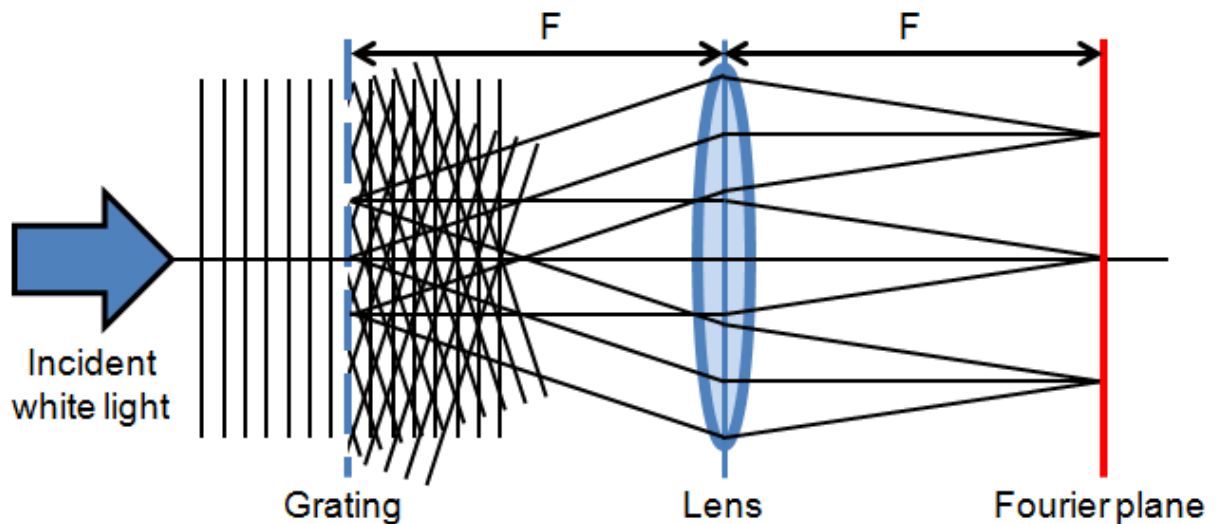
Figure 4.24   Schematic representing the acquisition principle of images in the Fourier plane. The lens has a focal length F.

4.6. Conclusion

The first part of this chapter is dedicated to the description of metal structure fabrication and characterization. Three types of structures have been considered: single slits, slit and grooves and slit arrays. The single slit is the basic building block of the two other structures: a single slit presents high TM transmission whereas TE transmission can be strongly reduced for narrow slit widths. Due to SPP's excitation, TM transmission is strongly modified for both slit arrays and slit and grooves as compared to the single slit case: the transmission can be either enhanced or decreased. On the other hand, TE transmission remains similar to the single slit case for both slit arrays and slit and grooves as there is no surface mode supported by the structure. The strong polarization properties measured for such structures can be advantageous, as is shown in Chapter 5.

To enhance TE transmission, it is first necessary that the slit allows TE polarized light to propagate. Next, a thin dielectric layer which sustains TE waveguide modes can be placed above either a slit array or a slit and groove structure. The slit and groove case under such configuration has been investigated, and extraordinary optical TE transmission has been experimentally demonstrated. This experiment illustrates the fact that different kinds of surface waves can be used to enhance transmission. It should be possible to transmit both polarizations at the same wavelength, thus increasing the overall transmission and removing polarization sensitivity. These findings could be used for devices where high throughput is necessary, such as low noise [99] or high speed photodetectors [102].

Finally, this chapter showed relatively good agreement between theory and experiment for the different structures. This is particularly important as it validates the theoretical tools used. These tools can afterwards be used to design structures for various applications. Examples of such applications are explored in Chapter 5.

Chapter 5

Applications

The phenomenon of enhanced optical transmission through metal structures can benefit several applications. For example, metal structures have been used to develop new nanolithography techniques [103,104], to control the emission of the light emitted from quantum cascade lasers [105,106], to improve the speed of photodetectors [102] and to design new chemical/biological sensors [107]. An extensive review regarding the potentials of the enhanced optical transmission process is found in Ref. [48]. In the present chapter, the use of nanostructured metals is investigated for three different optical devices:

(i)   chemical/biological sensors;

(ii)   light emitting diodes (LED's);

(iii)   image sensors.

For each we initially introduce the principle of each device is introduced. The potential of using nanostructured metals to improve the different devices is then explored both theoretically and experimentally. Finally, limitations and perspectives are discussed.

5.1. Surface plasmon resonance sensing

The excitation condition of SPP's at a metal-dielectric interface depends on the refractive indices of each medium (cf. Section 2.2). As the field is highly confined at the metal interface, SPP's are particularly sensitive to refractive index changes of the dielectric medium in close vicinity to the metal layer. Even a layer a few nanometres thick on the metal can modify the excitation of SPP modes. This effect is the basis of devices called surface plasmon resonance (SPR) sensors capable of detecting and quantifying chemical and biological compounds.
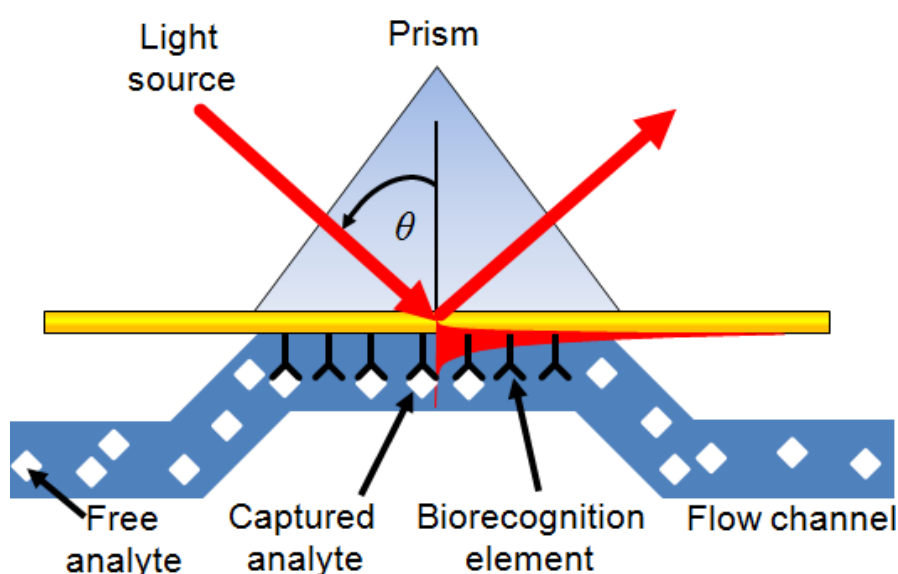
Figure 5.1.   Schematic of a SPR sensor

5.1.1. Principle

In most SPR sensors, SPP's are excited in Kretschmann configuration, see Fig. 5.1. Light is first coupled to a prism coated with a thin metal film. At the SPP condition, a minimum in the reflection spectrum is measured. The modification of the SPP condition induced by refractive index changes can be measured by three different approaches: (i) intensity changes measured near the resonance; (ii) angular analysis of the resonance position; (iii) spectral analysis of the resonance position.

SPR sensors can be prepared such that they are sensitive to a specific analyte. As shown in Fig. 5.1, biorecognition elements are immobilized on the metal surface. These biorecognition elements are able to interact with a specific analyte. Analyte molecules in a liquid in contact with the SPR sensor bind to the biorecognition elements, causing a refractive

index change close to the surface which is optically measured via the modification of the SPP excitation. The refractive index change is dependent on the concentration of analyte molecules at the sensor surface. Thus, it is possible to measure the concentration and the kinetics of biospecific interactions. The first demonstration of biosensing using SPR was reported by Liedberg *et al.* in 1983 [108]. They were able to detect antigen-antibody specific binding. Since this first demonstration, SPR sensors have been developed and the first commercial SPR biosensor was launched on the market in 1990 by BIAcore [30]. SPR biosensors have become a central tool for detection of chemical and biological species and for characterizing and quantifying biomolecular interactions [109].

There is an increasing demand for compact and portable sensors which allow on-site measurements. The use of prism couplers in conventional SPR sensors causes limitation in the miniaturization of the optics of the device. Recently, Brolo *et al.* proposed a new type of SPR sensors where light is coupled to SPP's with hole arrays [107]. Hole arrays present several properties which make them particularly suitable for miniaturized and multiplexed sensors, which can then be integrated in laboratory-on-chip devices [110]. Measurements can be performed in transmission as shown in Fig. 5.2. Also, the very small footprint of hole arrays together with microfluidic channels makes multiplexing and integrated devices possible.
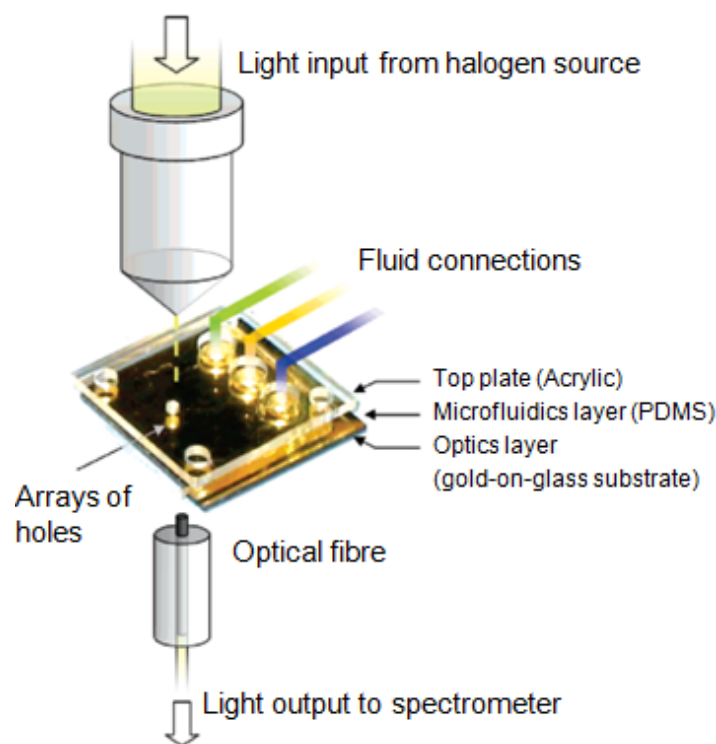
Figure 5.2. Scheme of the transmission mode optical setup and the fluidic connections employed for on-chip SPR sensors with hole arrays. Adapted from Ref. [110].

The sensor performance can be improved using slit arrays, as it potentially gives higher transmission than hole arrays. In the following section, the use of slit arrays is investigated for SPR sensing. The observations of the theoretical study on slit arrays of Chapter 3 are considered. This then gives design rules to obtain slit arrays with high sensitivity to refractive index changes. Finally, proof of concept is shown by measuring the transmission through slit arrays immersed in solutions of different refractive indices.

5.1.2. Design of slit arrays for chemical/biological sensing

The goal of this study is to design slit arrays that show high sensitivity to layers of molecules adsorbed on the metal surface of the array, see the schematic of Fig. 5.3. In a first attempt, the array is considered to be immersed in water. The water refractive index is denoted RIX_{water}. The adsorption of a layer of molecules is regarded as a an increase of RIX_{water} by ΔRIX. The sensitivity of the device can be evaluated in two different ways:

(i)   by considering spectral shifts induced by the increase of RIX_{water} by ΔRIX. These shifts are expressed in nanometers per refractive index unit (nm/RIU);

(ii)   by calculating ΔT, the change in transmission at a given wavelength as RIX_{water} is increased by ΔRIX.

Spectral shifts and transmission changes are linked, i.e. the larger the shift, the stronger the transmission will be modified at a given wavelength. Also, a shift of sharp spectral features should give rise to high transmission changes.
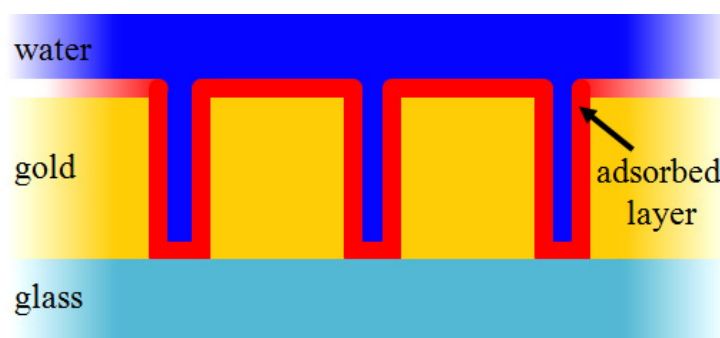
Figure 5.3.   Schematic of a slit array on a glass substrate immersed in water and coated with an adsorbed layer.

5.1.2.1.   Sensitivity of slit arrays to refractive index changes

The transmission of light through slit arrays in a gold film on a glass substrate and immersed in water is calculated with the modal expansion method. The zero order

transmission for the parameters p = 500 nm and w = 100 nm is plotted in Fig. 5.4(a) as a function of h and λ. The refractive indices of glass and water are 1.5 and 1.333 respectively. Two lines with zero transmission, represented by the dotted lines, are observed. These lines correspond to the two SPP modes excited at each interface. There are also two lines of high transmission. Following the notations of Chapter 3, these high transmission lines correspond to the $\lambda(0,1)$ and $\lambda(0,2)$ modes, as labeled in Fig. 5.4(a). The refractive index of the substrate is larger than that of water. As a consequence, the $\lambda(0,1)$ mode is not tangent to the gold-water SPP but tangent to the gold-glass SPP as the film thickness is decreased. The $\lambda(0,2)$ mode crosses the gold-glass SPP as the film thickness is decreased and becomes tangent to the gold-water SPP.

Figure 5.4.   (a) Zero order transmission of slit arrays on a glass substrate immersed in water with p = 500 nm and w = 100 nm. (b) Absolute intensity change as the water refractive index is changed from 1.333 to 1.334. Panel (c) and (d) are obtained as for panel (a) and (b) except that the period is varied and h = 265 nm.

The zero order transmission is then calculated increasing the water refractive index by ΔRIX = 0.001 and the absolute intensity change $|\Delta T|$ is plotted in Fig. 5.4(b). High intensity

changes are observed at the $\lambda(0,1)$ and $\lambda(0,2)$ modes and at the horizontal line corresponding to the Rayleigh wavelength in water. The largest change occurs at the $\lambda(0,2)$ mode for $h \approx 165$ nm and $\lambda \approx 760$ nm which corresponds to a narrow transmission peak. Fig. 5.4(c) and Fig. 5.4(d) are obtained in a similar way to that of Fig. 5.4(c) and Fig. 5.4(d) respectively except that the film thickness is fixed to $h = 165$ nm and the period is varied. Again, high intensity changes are observed for the $\lambda(0,1)$ and $\lambda(0,2)$ modes and at the Rayleigh wavelength in water. The highest intensity change is observed at the $\lambda(0,2)$ mode for $p \approx 500$ nm and $\lambda \approx 760$ nm.

Figure 5.4 shows that the highest intensity change is observed for the narrowest transmission peak related to the $\lambda(0,2)$ mode. A narrow transmission peak related to the $\lambda(0,1)$ mode is also obtained as the film thickness is decreased in Fig. 5.4(a) or the period increased in Fig. 5.4(c). However, this narrow peak does not give a higher intensity change than the broad peak obtained for thicker films. To investigate this behaviour, the spectral position of the minima and maxima are plotted in Fig. 5.5 as a function of the refractive index of the medium in which the slit array is immersed. This is shown for two different arrays with the following parameters: $p = 500$ nm, $w = 100$ nm and $h = 125$ nm and 265 nm in panel (a) and (b) respectively.

Figure 5.5.   Position of the spectral minima and maxima in function of the refractive index of the immersing medium; calculated for slit arrays on a glass substrate with parameters $p = 500$ nm, $w = 100$ nm and (a) $h = 125$ nm and (b) $h = 265$ nm. The number above each line corresponds to the wavelength shift in nm/RIU.

The results of Section 3.2 are used to interpret the observations of Fig. 5.5. The spectral position of the first order gold-water SPP and Rayleigh wavelength in water are given by $\lambda_{SPP} = p\mathrm{RIX}_{water}[\varepsilon_1/(\varepsilon_1 + \mathrm{RIX}_{water}^2)]^{1/2}$ and $\lambda_{RW} = p\mathrm{RIX}_{water}$ respectively, these give spectral shifts of ≈ 475 and 500 nm/RIU respectively. This is in agreement with what is observed in Fig. 5.5. In

the case of the $\lambda(0,1)$ and $\lambda(0,2)$ modes, the transmission peak position far from SPP excitation can be approximated by Eq. 2.2-25 which can be reformulated to $\lambda(0,l) = 2h\mathrm{RIX}_{\mathrm{eff}}/l$ where $\mathrm{RIX}_{\mathrm{eff}} = \beta_0/k_0$ is the effective index of the slit mode. Consequently, the spectral shift of the $\lambda(0,1)$ and $\lambda(0,2)$ modes for a refractive change of unity are approximately $2h$ and h respectively. These values constitute a rough approximation and strong deviations are expected close to the SPP excitation.

The spectral shift of the $\lambda(0,2)$ mode has been calculated for $h = 265$ nm, where the largest intensity change is observed in Fig. 5.4. The $\lambda(0,2)$ mode gives a shift of 185 nm/RIU. This is lower than expected from the previous design rules because the $\lambda(0,2)$ mode is bounded by the gold-glass SPP mode. For the $\lambda(0,1)$ mode, the spectral shift for $h = 125$ nm is 255 nm/RIU. As the gold thickness is increased to 265 nm, the shift is increased to 605 nm/RIU. This increase in spectral shift with h is in agreement with the rules derived in the previous paragraph. For both thicknesses, the intensity change observed in Fig. 5.4 is nearly the same because an increase of the spectral shift is compensated by a peak width increase.

It is observed that for both the $\lambda(0,1)$ and $\lambda(0,2)$ modes, sharp transmission peaks are obtained close to the SPP modes. These peaks show only small spectral shifts upon refractive index change, which is not concomitant with having the highest transmission changes. A way to improve the spectral shift of these peaks is to bind the modes to the gold-water SPP mode. This would ensure at least a spectral shift of 475 nm/RIU. To achieve this, the substrate should have a lower refractive index than water or should be removed, i.e. the slit array needs to be suspended.

The zero order transmission for arrays without substrates is shown in Fig. 5.6(a) for $p = 500$ nm and $w = 100$ nm. As the film thickness is decreased, the $\lambda(0,1)$ mode is displaced close to the gold-water SPP and becomes sharper. As in Fig. 5.4, the absolute intensity change as the water refractive index is changed by $\Delta\mathrm{RIX} = 0.001$ is plotted in Fig. 5.6(b). It shows that the intensity change is increased as the transmission peak related to the $\lambda(0,1)$ mode narrows. The spectral shift with refractive index of the $\lambda(0,1)$ mode is plotted in Fig. 5.6(c) for a slit array with parameters $p = 500$ nm, $h = 125$ nm and $w = 100$ nm. The spectral shift of the $\lambda(0,1)$ mode is twice as large as in the case of a glass substrate. This explains the large intensity change observed in Fig. 5.6.
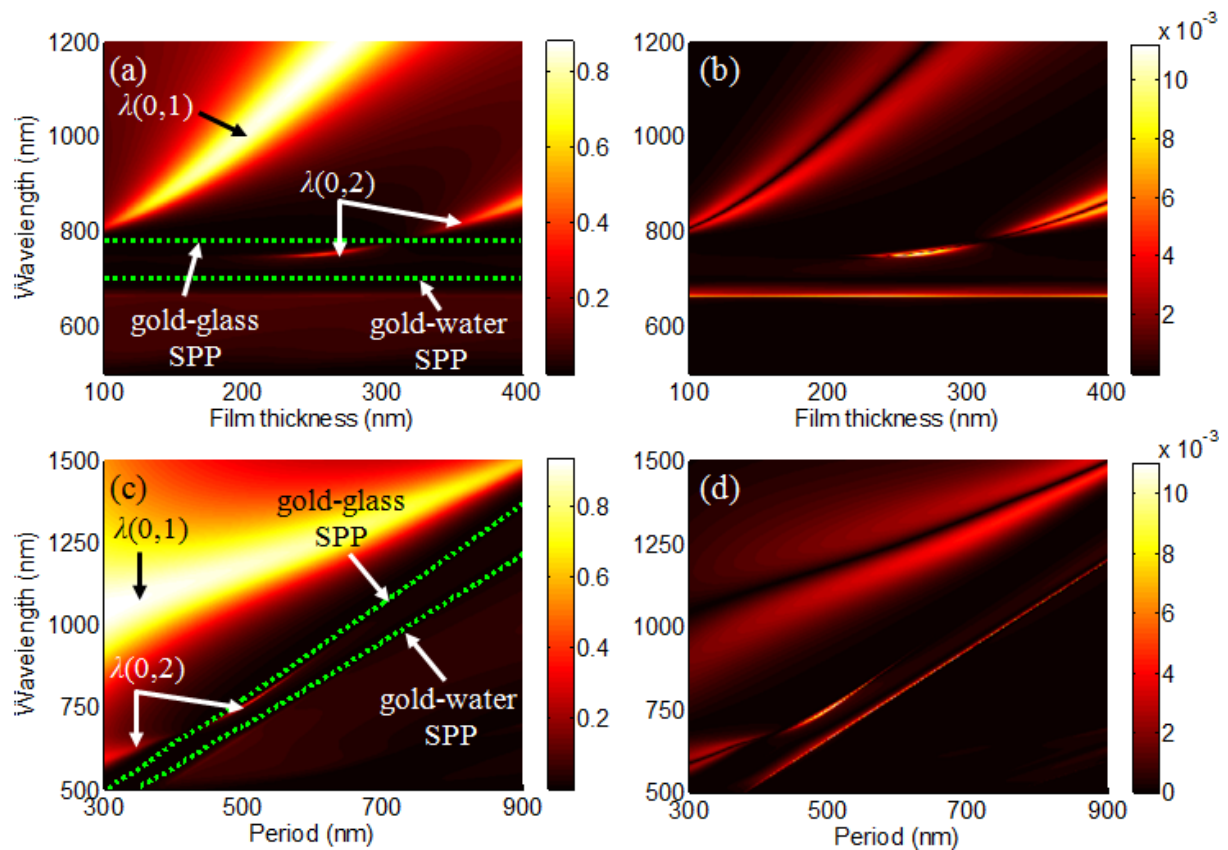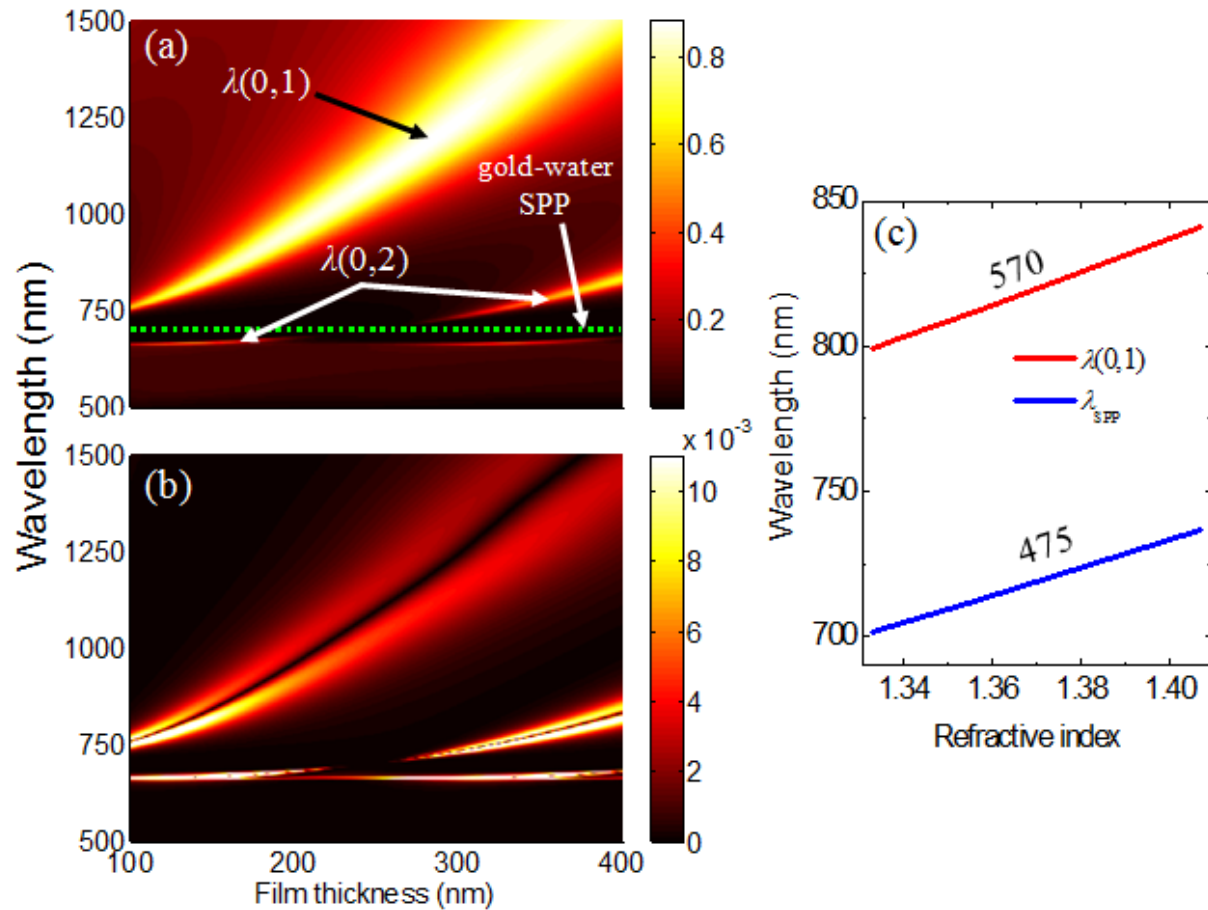
Figure 5.6.   (a) Zero order transmission of slit arrays without substrate immersed in water for p = 500 nm and w = 100 nm. (b) Absolute inten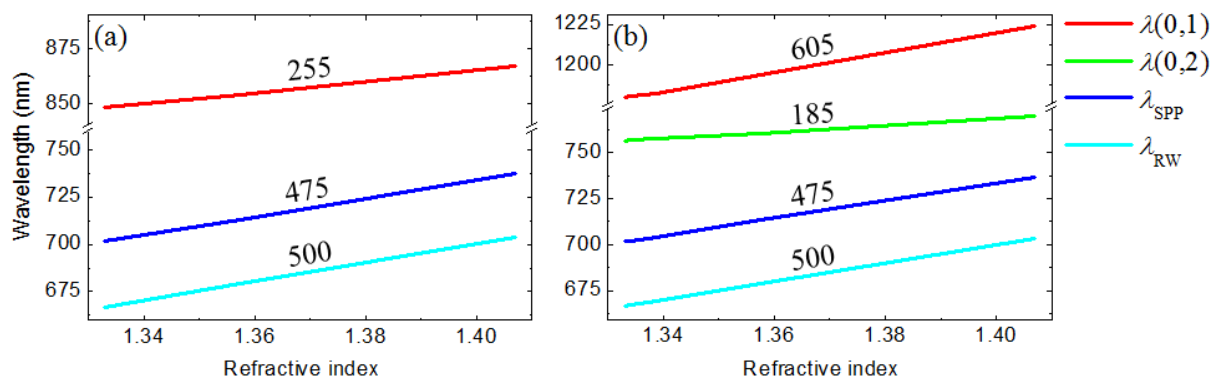sity change as the water refractive index is changed from 1.333 to 1.334. (c) Position of the spectral minima and maxima in function of the refractive index of the immersing medium; calculated for slit arrays with parameters p = 500 nm, h = 125 nm and w = 100 nm.

5.1.2.2.   Sensitivity of slit arrays to adsorbing layer of molecules

It is now necessary to verify that the previous considerations apply to the detection of a thin adsorbing layer. Both the slit array with a glass substrate in Fig. 5.4 and Fig. 5.5 and the optimized suspended array in Fig. 5.6 are considered. As a proof of principle, a bovine serum albumin (BSA) layer of thickness h_{BSA} = 1.6 nm and refractive index RIX_{BSA} = 1.465 is considered as the absorbed layer. These values are typical of the data reported in other work, see e.g. Ref. [111].

Calculations performed with RCWA are plotted in Fig. 5.7(a) and (b) for both an array on a glass substrate and a suspended array. The zero order transmission without BSA, denoted T_0(water), is represented by a solid blue line and the one calculated with an adsorbing BSA layer, denoted T_0(BSA), is given by a red dashed line. For both the slit array on glass and the

suspended array, it is not possible on such a scale to observe a modification in the spectrum due to the presence of BSA.

In order to observe spectral modifications, the intensity change between $T_0(BSA)$ and $T_0(water)$ is plotted in Fig. 5.7(b). It shows that the presence of the BSA layer induces an intensity changes as in the case where the refractive index is modified. The suspended array gives the highest intensity change. At the transmission peak corresponding to the $\lambda(0,1)$ mode, the transmission is modified by 3% due to the BSA adsorbing layer.
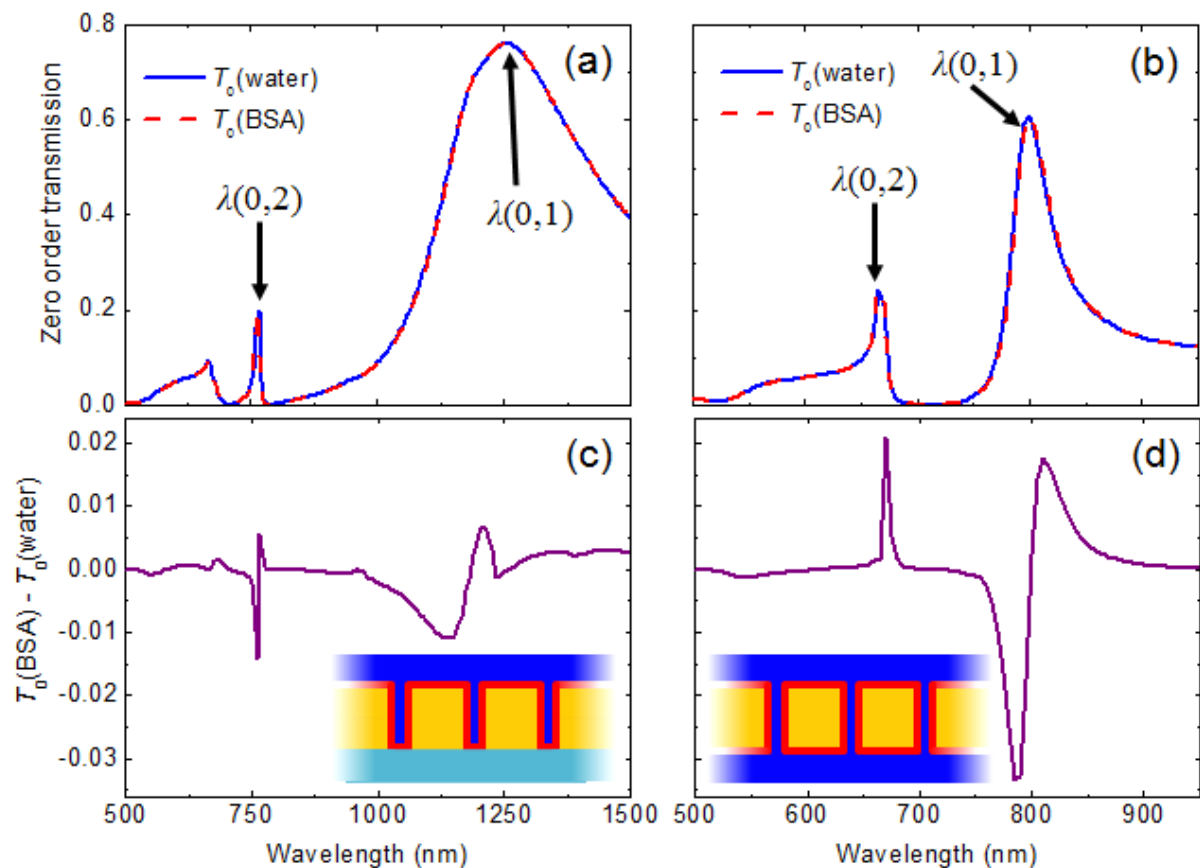
Figure 5.7. Zero order transmission calculated for (a) the slit array on a glass substrate and parameters $w = 100$, $h = 265$ nm and $p = 500$ (b) and the suspended slit array with $w = 100$, $h = 125$ nm and $p = 500$. The red dashed curves and blue solid curves are $T_0(BSA)$ and $T_0(water)$ respectively. Parts (c) and (d) show the corresponding difference between $T_0(BSA)$ and $T_0(water)$. The insets in parts (c) and (d) show the configuration used.

5.1.3. Experimental measurement of refractive index changes

As a proof of the presented modelling, the transmission spectra of slit arrays on a glass substrate immersed in different aqueous solutions are measured. Due to the presence of a fluidic channel used to immerse the array, it was not possible to take a reference spectrum

such that the different spectra could be normalized accurately. Consequently, the spectra displayed in Fig. 5.8(a) are not normalized and their amplitude cannot be compared with theoretical spectra. This is not important as spectral shifts between the different spectra are the information of importance in this study.

The transmitted intensity measured through such array with parameters $p = 500$ nm, $h = 285$ nm and $w = 100$ nm is shown in Fig. 5.8(a) by the black curve. The two transmission minima observed at $\lambda \approx 700$ nm and $\lambda \approx 825$ nm correspond to the gold-water SPP and to the gold-glass SPP respectively. The transmission peak observed at $\lambda \approx 760$ nm corresponds to the $\lambda(0,2)$ mode.
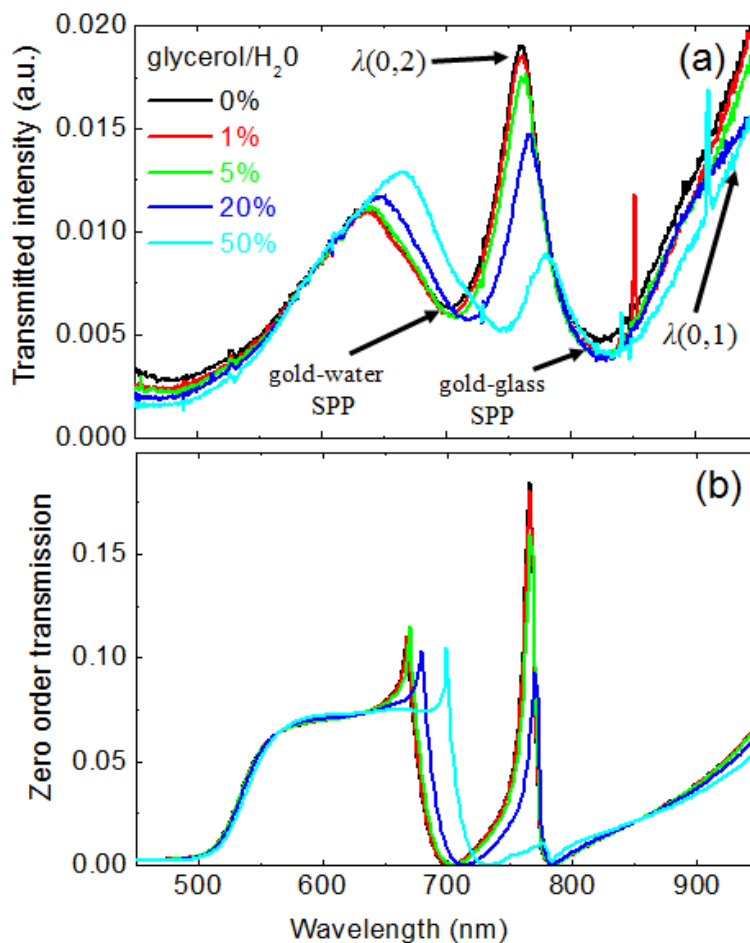
Figure 5.8.   (a) Zero order transmission spectra of slit arrays on a glass substrate immersed in different water-glycerol mixtures. The array parameters are $h = 285$ nm, $p = 500$ nm and $w = 100$ nm. (b) Corresponding calculations.

The refractive index of the solution immersing the slit array is modified by changing the volume percentage of glycerol in water. As the amount of glycerol is increased, the refractive

index increases. The transmission measurements for different concentrations of glycerol are shown in Fig. 5.8(a). As the amount of glycerol is increased, the transmission minimum corresponding to the gold-water/glycerol SPP is shifted towards longer wavelengths. The transmission peak observed at $\lambda \approx 760$ nm is also shifted to larger wavelengths. The gold-glass SPP position remains fixed. The displacement of the spectral features are in good agreement with the one observed in theory, as shown in Fig. 5.8(b) calculated for a water/glycerol mixture. Refractive indices were taken from Ref. [112].

The measured transmission minima and peak positions are plotted in Fig. 5.9 as a function of the refractive index of the water-glycerol mixture. The slope for the transmission minima follows the one of a flat SPP mode at the gold-water/glycerol mixture with a change of around 500 nm per refractive index unit. The slope of the transmission maximum is only of 300 nm per refractive index unit. This lower sensitivity is due to the fact that the transmission peak is bound by the gold-glass SPP, as previously observed theoretically. This is in accordance with experiments reported by Lee *et al.* [113].
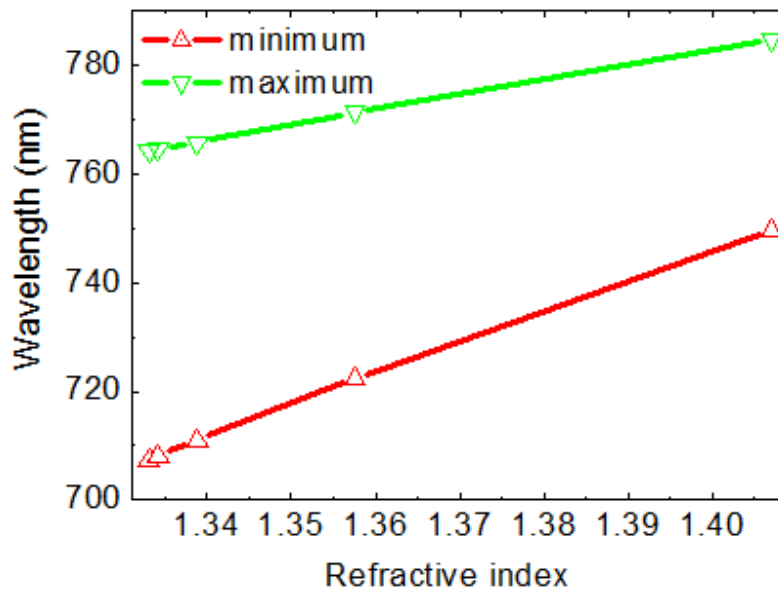
Figure 5.9.   Transmission minimum and maximum of the spectrum shown in Fig. 5.8(a) for the different refractive indices considered.

5.1.4. Conclusion and outline

The detection of refractive index changes with slit arrays has been studied in Section 5.1. Applying simple design rules, the sensitivity of slit arrays to refractive index changes is optimized. It is shown that a suspended slit array gives a better sensitivity to refractive index

changes as compared to arrays on glass substrates. The detection of a monolayer adsorbed on a slit array is theoretically investigated. A 1.6 nm thick BSA layer adsorbed on the slit array can induce a 3% absolute transmission change. As a proof of principle of the modelling, transmission spectra through slit arrays immersed in solutions with different refractive index have been measured. Good agreement with theory is observed.

Future experimental work should be dedicated to the detection of adsorbed layers on the slit arrays. The main challenge of the present design resides in the fabrication of suspended membranes. One example of suspended membranes used for SPR sensors has recently been demonstrated in Ref. [114]. More generally, the use of slit arrays in view of compact and portable sensors presents several limitations. As the measurements are performed in transmission, these types of sensors are limited to transparent materials and solutions. Also, expensive technologies such as FIB are currently used to fabricate slit arrays. To make biosensors based on slit arrays competitive, up-scalable fabrication techniques are necessary to reduce the cost of these devices. A recent work at CSEM has shown the possibility to fabricate hole arrays with an inexpensive lithography process based on self-assembled polystyrene spheres [115].

5.2. Light extraction of Light Emitting Diodes (LEDs)

An LED is a semiconductor light source. LEDs have been used since the late 1960s as status indicator on circuit boards and numeric displays. They were mainly restricted to these applications because the light output was not large enough to illuminate an area. With the improvement in LEDs technology, today's LEDs are 1000 times more efficient than in the 1960's and are considered as the future of lighting [116,117]. The main advantages of LEDs as compared to other light sources are their high efficiency, long lifetime, robustness and small size. The use of LEDs could save enormous amount of energy and money: it is estimated that by 2025, solid state lighting based on LEDs could reduce the global amount of electricity used for lighting by 50% [117]. To achieve this goal, it is necessary to continue to improve LEDs efficiency.

After a description of the LEDs principle and characteristics, the problem of light extraction is introduced. A theoretical study investigates the possibility of using slit arrays to improve light extraction efficiency, and preliminary experimental results are reported.

5.2.1. LEDs principle and characteristics

An LED, whose architecture is schemed in Fig. 5.10(a), is comprised of a semiconductor material doped with impurities in order to form a p-n junction. Upon application of a forward bias voltage at the contacts, electron and holes are injected as minority carriers across the p-n junction and recombine, see Fig. 5.10(b). Recombination leads to generation of photons whose wavelength depends on the band gap of the semiconductor materials forming the junction.

The efficiency of LEDs is stated by the external quantum efficiency (η_{ext}). It corresponds to the ratio of the photon flux at the output of the device to the injected electron flux. The external quantum efficiency is the product of three factors:

(i)   The injection efficiency (η_{inj}), defined as the ratio of the electron flux injected into the active region to the electron flux injected in the device

(ii)   The radiative efficiency (η_{rad}), i.e. the fraction of electron/hole pairs leading to radiative recombination.

(iii)   The extraction efficiency (η_{extr}), i.e. the ratio between the photon flux extracted from the device to the photon flux generated inside the device.

The internal quantum efficiency, which accounts for losses due to injection and non-

99

radiative recombination, is then defined as $\eta_{int} = \eta_{inj}\eta_{rad}$. In modern devices, internal quantum efficiency can be close to 100% [118]. The external quantum efficiency, which is then defined as $\eta_{ext} = \eta_{int}\eta_{extr}$, is consequently essentially limited by the extraction efficiency.
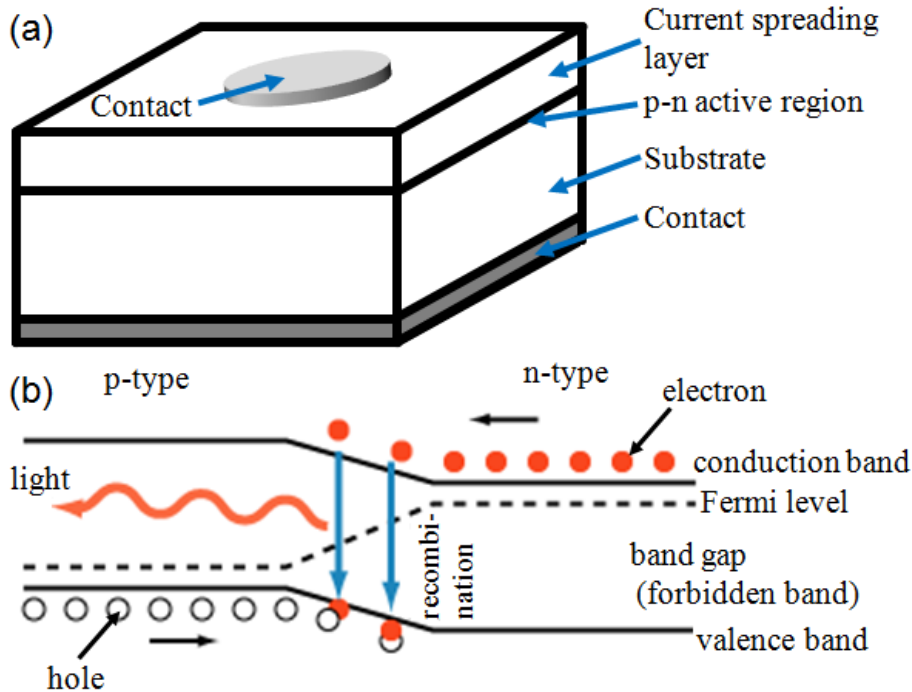
Figure 5.10.   Schematic of (a) an LED architecture; (b) a p-n junction under forward bias [119].

5.2.2.   Light extraction problem

The extraction efficiency depends on the optical properties of the device, its layer structure and its geometry. Three factors leads to extraction limitations: (i) re-absorption in the semiconductor; (ii) shadowing of the emission due to the top contact in the case of top surface emitting devices; (iii) internal reflection at the semiconductor-air interface. Re-absorption can be minimized by using a material with a bandgap energy larger than the energy of emitted photons, or by modifying the thicknesses of semiconductors. Thus, we focus on the last two limitations.

5.2.2.1.   Contact shadowing

The extraction efficiency can be significantly reduced due to shadowing of the emission by the top contact, from which charge carriers are introduced into the device. As an example, Fig. 5.11 shows a SEM image of an LED emitting facet. A large fraction of the facet is covered by metals, thus strongly affecting the efficiency of the device. Reducing the contact area leads to a reduction in current spreading. Transparent oxides such as indium tin oxide

and zinc oxide are currently investigated as a way to reduce contact shadowing.
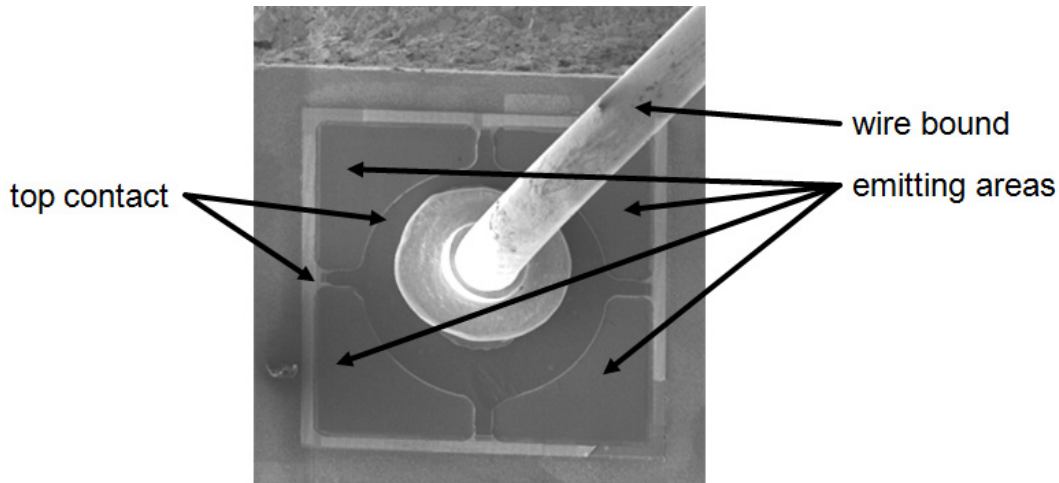
Figure 5.11.   SEM image of the emitting facet of an LED.

Hole arrays in metal films have been proposed as transparent contacts in organic LEDs [120]. The transmission through hole arrays is driven by the excitation of SPP's at the metal-dielectric interface. In the case of inorganic LEDs, hole arrays are not appropriate because the high refractive index of the semiconductor induces a SPP mode with large losses, as discussed in Section 2.2.2. On the other hand, high transmission through slit arrays can be obtained from the excitation of modes with a strong FP-like profile, as discussed in Section 3.2. These modes would hardly be affected by the metal-semiconductor interface. Consequently, slit arrays have the potential to increase light extraction by transforming the metal contact into a transparent contact. Although slit arrays are intrinsically polarization sensitive, this may not be a drawback for the LED market which uses polarization defined devices.

5.2.2.2.   Internal reflection

Total internal reflection (TIR) at the seminconductor-air interface strongly limits the extraction efficiency due to the high refractive index contrast between semiconductor (RIX$_{int}$) and air (RIX$_{ext}$). TIR is a direct consequence of conservation of momentum, as already discussed in Section 2.2.3: in the case of a homogeneous interface, the parallel wavevector k_x must remain the same in both regions, as schemed in Fig. 5.12(a). With the notation of Fig. 5.12, conservation of momentum is applied, giving:

$$k_{int} \sin \theta_{int} = k_{ext} \sin \theta_{ext},$$ (5.2-1)

which is a reformulation of Snell's law:

$$\mathrm{RIX}_{\mathrm{int}}\ \sin\theta_{\mathrm{int}} = \mathrm{RIX}_{\mathrm{ext}}\ \sin\theta_{\mathrm{ext}},\qquad(5.2\text{-}2)$$
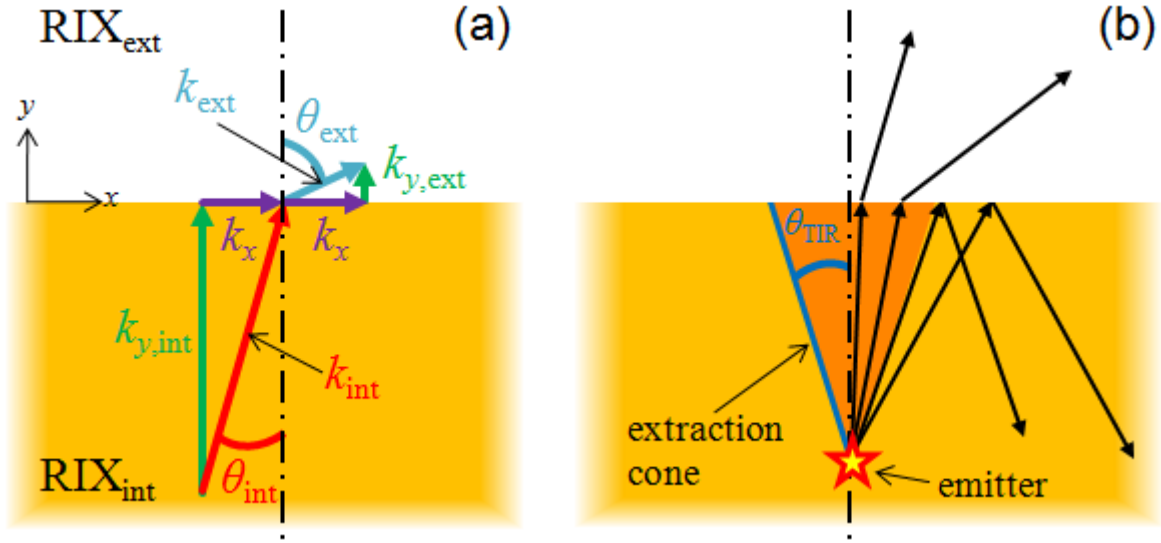
Figure 5.12.   Transmission and reflection at a semiconductor – air interface.

Considering $\mathrm{RIX}_{\mathrm{int}} > \mathrm{RIX}_{\mathrm{ext}}$, there is an angle θ_{TIR} called the critical angle above which $k_x >$ k_{ext}. Under this condition, $k_{y,\mathrm{ext}}$ is imaginary, i.e. the wave does not propagate in the external medium and is exponentially decaying, as discussed in Section 2.2.1. As a consequence, light with incident angle $\theta_{\mathrm{int}} > \theta_{\mathrm{TIR}}$ experiences TIR at the seminconductor air interface, as schemed in Fig. 5.12(b). From Snell's law, this angle is given by:

$$\theta_{\mathrm{TIR}} = \arcsin\!\left(\frac{\mathrm{RIX}_{\mathrm{ext}}}{\mathrm{RIX}_{\mathrm{int}}}\right).\qquad(5.2\text{-}3)$$

The corresponding solid angle Ω_{TIR} is:

$$\Omega_{\mathrm{TIR}} = 2\pi\left(1 - \cos\theta_{\mathrm{TIR}}\right).\qquad(5.2\text{-}4)$$

As an example, consider Gallium Phosphide (GaP) whose refractive index is 3.3 at 650 nm, this gives $\theta_{\mathrm{TIR}} \approx 17.6°$ and $\Omega_{\mathrm{TIR}}/4\pi \approx 0.02$. Assuming an isotropic internal emission, the fraction of the light that can be extracted through one single out-coupling surface is obtained by:

$$\gamma_{\mathrm{trans}} = \frac{\displaystyle\int_{\Omega} T(\theta_{\mathrm{int}},\varphi_{\mathrm{int}})\,d\Omega}{4\pi} = \frac{\displaystyle\int_{\theta=0}^{\pi/2}\int_{\varphi=0}^{2\pi} T(\theta_{\mathrm{int}},\varphi_{\mathrm{int}})\sin\theta_{\mathrm{int}}\,d\theta_{\mathrm{int}}\,d\varphi_{\mathrm{int}}}{4\pi},\qquad(5.2\text{-}5)$$

where φ_{int} is the azimuth angle as shown in Fig. 5.20 and T is the power transmission through

the interface calculated from Fresnel formulae [59]. For the previous example $\gamma_{trans} = 0.016$, i.e. 1.6% of the light generated by the LED is extracted.

Several approaches have been introduced in order to circumvent this problem. The number of extraction facets can be increased, which increases the light extraction accordingly. LEDs can be encapsulated in hemispherical domes to reduce the mismatch in refractive index and also improve emission directionality [121]. The device geometry can be modified such that a photon that is reflected internally at the semiconductor air interface has chances to modify its direction and eventually be reflected into one of the escape cones. For example, external quantum efficiencies above 50% have been reported with the truncated-inverted pyramidal configuration shown in Fig. 5.13 [122]. The main challenge here is to reduce the mean free path such that the probability that the photon get absorbed due to internal losses stays low.
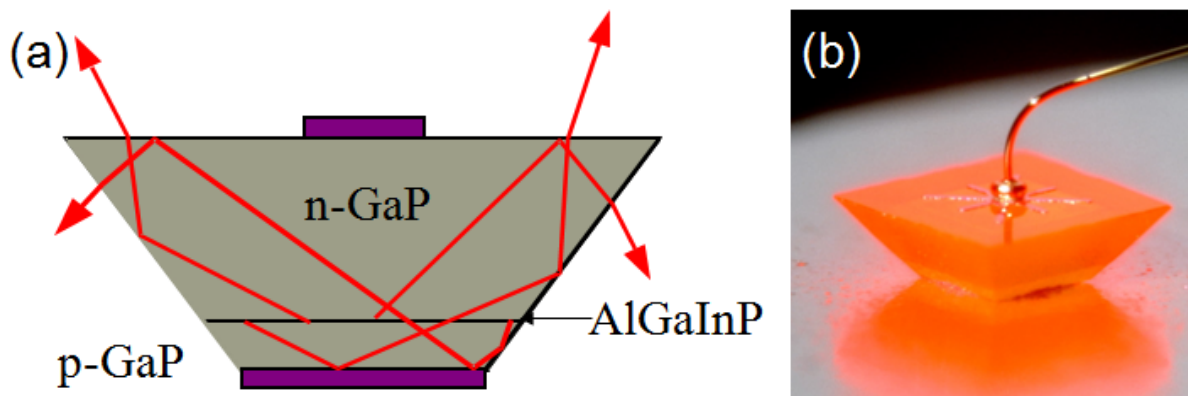
Figure 5.13.   Geometry of the truncated-inverted-pyramid LED: (a) schematic cross section showing means by which photons are redirected by total internal reflection; (b) image of a TIP LED under forward bias. Adapted from Ref. [122].

Alternatively, the spontaneous emission pattern can be modified placing the active region inside an optical cavity [123]. Due to a modification of the optical mode density, the emission is no longer isotropic and a larger fraction of the light is emitted inside the extraction cone, thus increasing the extraction efficiency and its directionality. These types of LEDs are called resonant cavity LED (RCLED) or microcavity LED (MCLED). Another way to modify spontaneous emission is to place a metal layer close to the active region [124,125]. A large part of the emission can then be coupled into the SPP mode, and light can afterwards be reemitted into free space by structuring periodically the metal. Following such a scheme organic LEDs have been proposed as an SPP's source [126,127].

Without modifying the spontaneous emission, it is possible to transmit light generated beyond critical angle. One way to achieve this is to roughen the out-coupling surface [128]. Also, photonic crystals have been used to extract by coherent scattering the light internally trapped [129]. Hole arrays in a metal film have been suggested by Drezet *et al.* as a way to extract light beyond the critical angle [130]. However, the absolute transmission of hole arrays stays relatively low for the reasons mentioned in Section 5.2.2.1.

5.2.3. Theoretical study

In the next section, slit arrays are investigated as a way to reduce contact shadowing by obtaining high transmission through a slit array in a metal film. The possibility to extract light beyond the critical angle with slit arrays is then investigated.

5.2.3.1. Light transmission through slit arrays on GaP substrate

We concentrate here on designing gold slit arrays on a GaP substrate giving the highest possible transmission. The target wavelength is 650 nm, which correspond to the wavelength emitted by a AlGaAsP based LED, and $RIX_{ext} = 1$. The Refractive index of GaP, tabulated in Appendix 1, is taken from the Sopra database [55].

It was shown many years ago that for loss-less resonant structures, reflection can be zero when only one order of diffraction is propagating [131]. As a consequence, the transmission through loss-less slit arrays can be unity [84], no matter how high the substrate refractive index is. Examples of unity transmission are shown in Fig. 5.14(a) for slit arrays in loss-less gold on a GaP substrate with refractive index 3.3. The array parameters are $p = 240$ and $w = 100$ and the light is impinging on the array at normal incidence from the air side. Figure 5.14(b) shows the reflection coefficients ρ_{air} and ρ_{GaP} of the fundamental slit mode at the air and GaP interface respectively. It shows that when the two reflection coefficients are equal, the transmission is unity when the correct metal film thickness is chosen. Considering the slit array as an FP cavity as in Appendix 3, the film thickness can be selected such that

$$\arg(\rho_{air}\rho_{air}) + 2\beta_0 h = 2\pi l \, . \tag{5.2-6}$$

It is shown in Fig. 5.14(c) that as the condition given by Eq. (5.2-6) is reached, unity transmission is obtained.
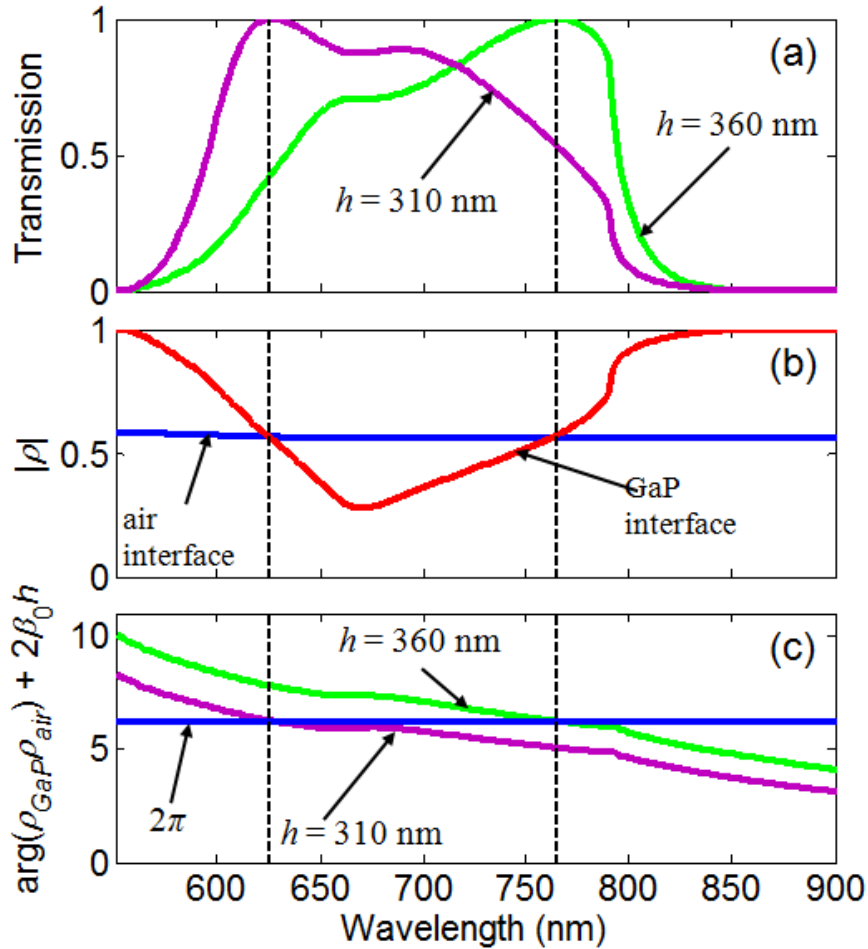
Figure 5.14.   (a) Total transmission T of a loss-less gold grating on a GaP substrate for $w = 50$ nm and $p = 240$ and normal incidence from air obtained from the modal expansion method. The purple and green curves are obtained for $h = 310$ and 360 nm respectively. (b) Corresponding reflection coefficients of the fundamental slit mode at the air and GaP interface respectively. (c) Plot of $\arg(\rho_{air}\rho_{GaP}) + 2\beta_0 h$ which shows that maximum transmission is reached as $\arg(\rho_{air}\rho_{GaP}) + 2\beta_0 h = 2\pi l$. The purple and green curves are obtained for $h = 310$ and 360 nm respectively and the blue curve indicate the value 2π.

When the metal losses are included, the maximum transmission is decreased. We have seen in Section 3.2 that high transmission is obtained for hybrid FP-SPP modes. As the SPP modes at the gold-GaP induce high losses, it is preferable to consider hybrid modes with a strong FP-like behaviour. The total transmission T and zero order transmission T_0 of a gold grating on a GaP substrate are shown in Fig. 5.15(a) and Fig. 5.15(b) respectively for $w = 100$ nm, $\lambda = 650$ and normal incidence from air as a function of p and h. High transmission is observed around three thicknesses: 100, 350 and 600 nm. These high transmission lines, which correspond to hybrid FP-SPP modes, are intersected by vertical lines of low transmission which correspond to the excitation of SPP modes. This is typical of what was

previously shown in Chapter 3. This calculation shows that transmissions higher than 80% are possible. To obtain such performance, the film thickness needs to be controlled very accurately.
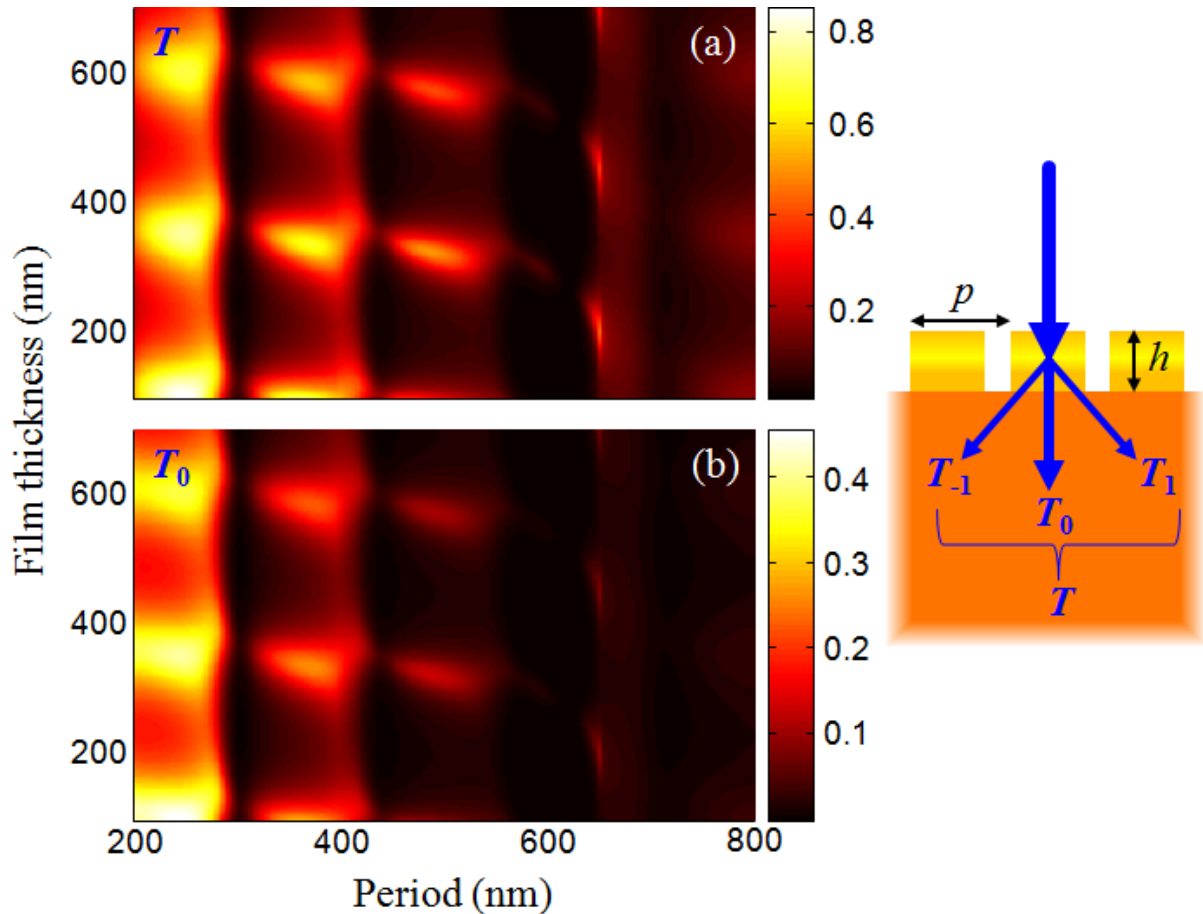
Figure 5.15. (a) Total transmission T and (b) zero order transmission of a gold grating on a GaP substrate for $w = 100$ nm, $\lambda = 650$ and normal incidence from air in function of p and h obtained from the modal expansion method. The brighter the region, the larger is the transmission. The schematic on the right side shows which side light is incident on the grating.

Light incident from air is considered in Fig. 5.15 because T_0 is identical in both directions due to reversibility. Moreover, we see in Fig. 5.15 that high values of T and T_0 are obtained at the same conditions. As T_0 is the only propagating transmitted order when light is incident from GaP for $p < \lambda$, extraction from GaP is at maximum when T is maximized for light incident from air. In addition, the difference between T and T_0 corresponds to diffraction at higher angles, which gives the possibility to transmit light beyond the light cone, as will be shown in Section 5.2.3.3.

5.2.3.2. Accuracy of the model

The modal expansion method used considers the surface impedance $Z = \varepsilon_1^{-1/2}$ at metal dielectric interfaces. The accuracy of such approximation decreases as the condition $|\varepsilon_1| >> |\varepsilon_2|$ is reduced. In the present case $|\varepsilon_1| \approx |\varepsilon_2|$, so SIBC is no longer accurate. This will mainly affect the properties of the gold-GaP interface. The position of the transmission maxima are strongly linked to Fabry-Pérot resonances, which depend on the slit mode and the film thickness. Consequently, the modal expansion method should still give reasonable results regarding the transmission peak position. The accuracy of the model in the case of GaP substrates has been checked with RCWA, see Fig. 5.16. Whereas the transmission minima induced by SPP's excitation are not accurately predicted, high transmission is observed nearly at the same position in both cases. Consequently, the model expansion method, which is faster, should be used to scan the different parameters of slit arrays. However, for fine adjustments, RCWA should be used to obtain an exact value of the transmission.
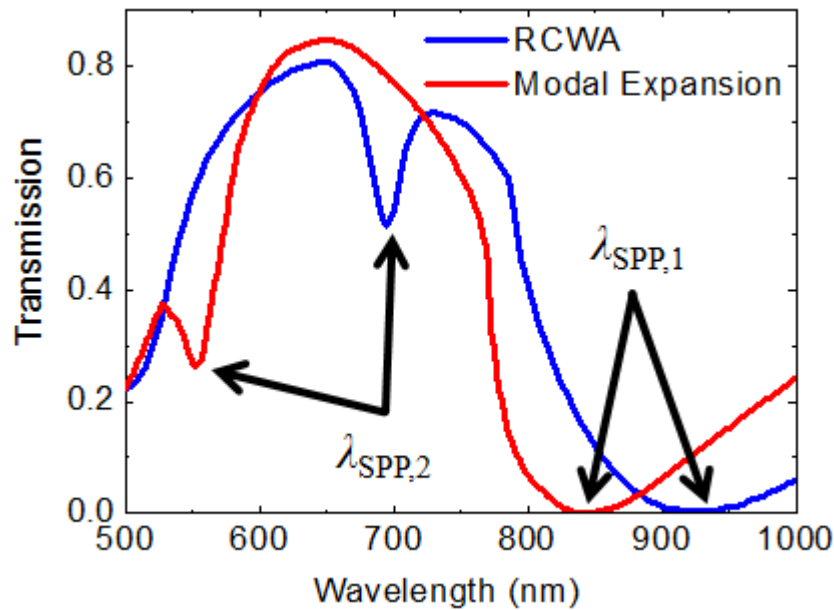
Figure 5.16.   Total transmission of a gold grating on a GaP substrate for $w = 100$ nm, $p = 240$ nm and $h = 100$ nm.

The transmission minima induced by $\lambda_{SPP,2}$ does not fall down to zero as for $\lambda_{SPP,1}$ and other calculations and measurements previously reported. For the parameters of Fig. 5.16, $|\varepsilon_1| \approx |\varepsilon_2|$ at $\lambda_{SPP,2}$. This gives a mode with high losses. Consequently, the resonance is poor and light transmission is not completely cancelled. For $|\varepsilon_1| < |\varepsilon_2|$ the mode is no longer a propagating SPP mode, see Section 2.2.1.

5.2.3.3.   Extraction beyond the light cone with slit arrays

The possibility to extract light beyond the critical angle using slit arrays is now considered. We saw in Section 5.2.2.2 that due to conservation of the parallel wavevector, light transmission at a planar GaP air interface is forbidden for incidence angle $\theta_{int} > \theta_{TIR}$. However, in the presence of a slit array, the parallel momentum is modified and takes the discrete values (cf. Section 2.2.3.1):

$$k_{x,n} = \mathrm{RIX}_{int} \frac{2\pi}{\lambda} \sin \theta_{int} + \frac{2\pi}{p} n . \qquad (5.2\text{-}7)$$
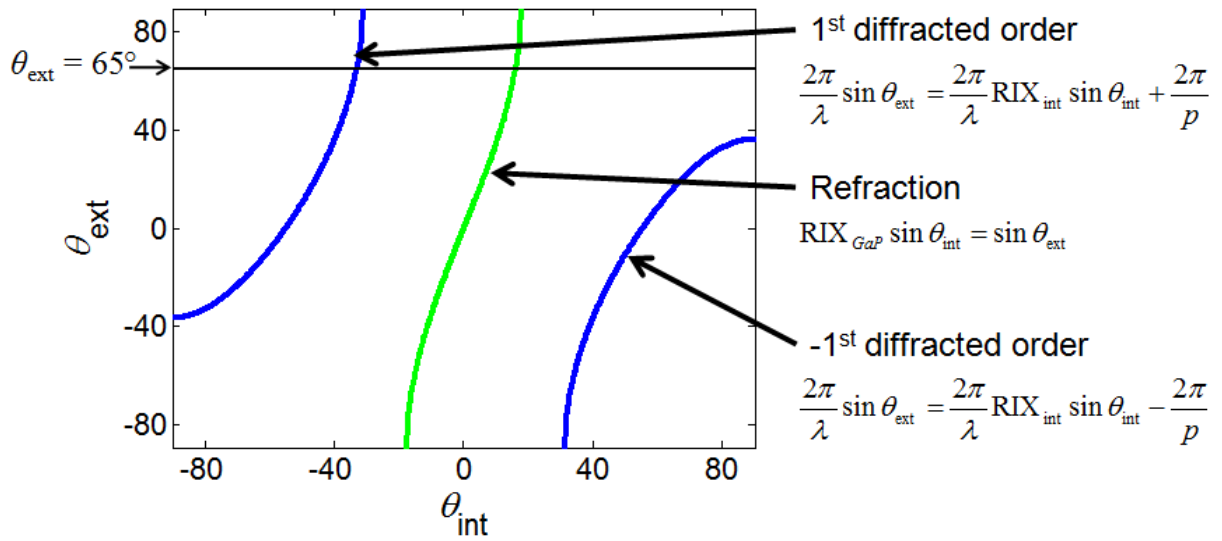
Figure 5.17.   Angle of transmission in air θ_{ext} plotted as a function of the incident angle in GaP θ_{int} for a slit array on a GaP substrate with $p = 240$ nm, $\lambda = 650$ nm and $\mathrm{RIX}_{int} = 3.3$.
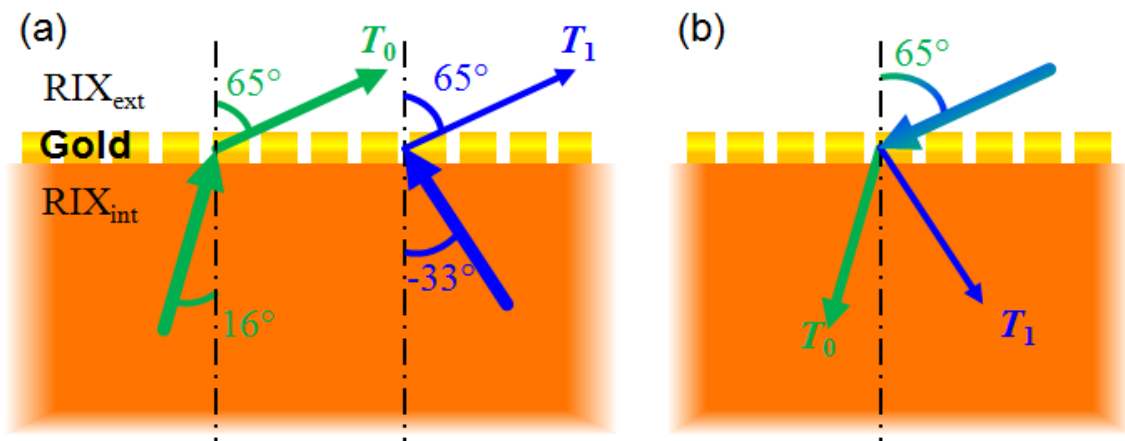
Figure 5.18.   Schematic of the transmission mechanism through a gold grating with a GaP substrate. The parameters considered are $p = 240$ nm, $\lambda = 650$ nm and $\mathrm{RIX}_{int} = 3.3$.

The angle θ_{ext} is plotted Fig. 5.17 as a function of the internal angle θ_{int} for $p = 240$nm, a

period for which high transmission was observed in Fig. 5.15. In addition to light extraction at angles lower than the critical angle, new channels are opened due to the grating coupling. Thus, it is possible to transmit light even if $\theta_{int} > \theta_{TIR}$. For example, light is transmitted in air at an angle $\theta_{ext} = 65°$ (represented as the horizontal black line in Fig. 5.17) for two different incident angles: (i) at $\theta_{int} = 16°$, due to refraction, (ii) at $\theta_{int} = -33°$, due to additional momentum provided by the grating. A schematic of these two different transmission channels are shown in Fig. 5.18.

The light transmitted from GaP with and without a metal grating is plotted in a polar diagram in Fig. 5.19 as a function of θ_{int}. The azimuth angle φ_{int} is kept to zero. A schematic of the polar and azimuth angles is shown in Fig. 5.20 for clarity. The array parameters are $w = 100$ nm, $p = 240$ nm and $h = 100$ nm. Transmission from GaP is higher without a metal grating close to $\theta_{int} = 0°$ but light is transmitted only at small angles. Placing a metal grating on the GaP, light can be transmitted for $\theta_{int} > \theta_{TIR}$ due to the grating coupling, as indicated by the two lobes observed at high angle in Fig. 5.19. The areas inside the transmission lines look roughly similar on both cases and the grating does not seem to provide higher extraction. But light transmitted for large incident angle from GaP gives a larger contribution to the extracted power when considered in terms of solid angles. To show this, it is necessary to calculate the light extraction efficiency.
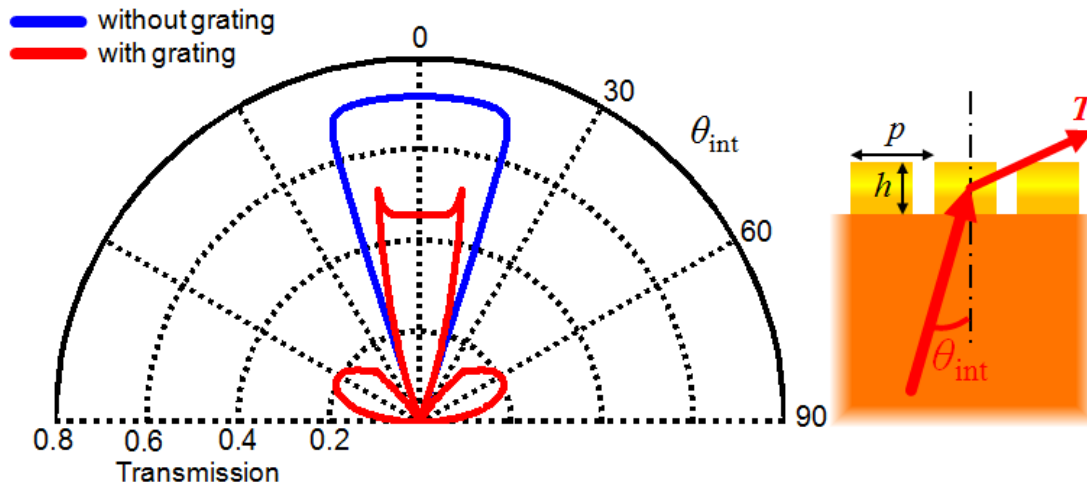
Figure 5.19. Total transmission of light incident from GaP as a function of θ_{int}. Blue curve: GaP – air interface; red curve: with a gold grating having the parameters $w = 100$ nm, $p = 240$ nm, $h = 100$ nm and $\lambda = 650$ nm. The graph on the right side shows from which side light is incident on the grating.
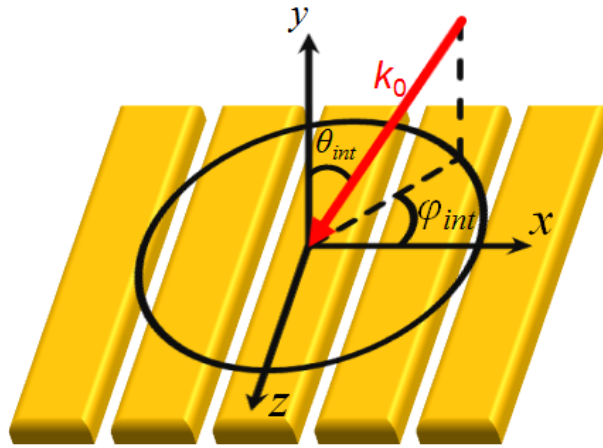
Figure 5.20.   Schematic representing the polar and azimuth angle denoted θ_{int} and φ_{int} respectively.

Assuming an isotropic emitter inside GaP, the fraction of the light extracted from GaP can be calculated from Eq. (5.2-5). The transmission through the slit array on a GaP substrate with light incident from GaP is first calculated for $\varphi_{int} = 0$ from the modal expansion method. The transmission $T(\theta_{int},\varphi_{int})$ is then approximated assuming Malus law, i.e.

$$T(\theta_{int}, \varphi_{int}) = T(\theta_{int}, 0)\cos^2 \varphi_{int}.$$
(5.2-8)

The light extraction for grating with different film thicknesses, $p = 240$ nm and $w = 100$ nm is shown in Fig. 5.21(a). It is observed that as the film thickness is changed, the light extraction smoothly oscillates. Such a smooth oscillation is not observed as the period of the array is changed when the film thickness is fixed to 100 nm; see Fig. 5.21(b). This is due to the fact that both p and θ_{int} modify wavevectors, inducing a complex band diagram, whereas this is not the case as the film thickness is modified; see Fig. 5.21(c) and Fig. 5.21(d).

In Fig. 5.21, the highest light extraction is observed in the case of a grating with $p = 260$ nm, $w = 100$ nm, $h = 100$ nm, a grating for which 4.1% of the light is extracted. This has to be compared with the 1.6% extracted for a planar interface, i.e. extraction is improved by more than a factor of 2.

Such a structure could considerably reduce the shadowing effect caused by the top contact. Also, the use of a backside mirror would allow photons not extracted at the first instance to have other chances to be extracted. This result is a proof of principal that a metal contact with arrays of slits can give extraction efficiency beyond what can be extracted through a planar GaP-air interface.
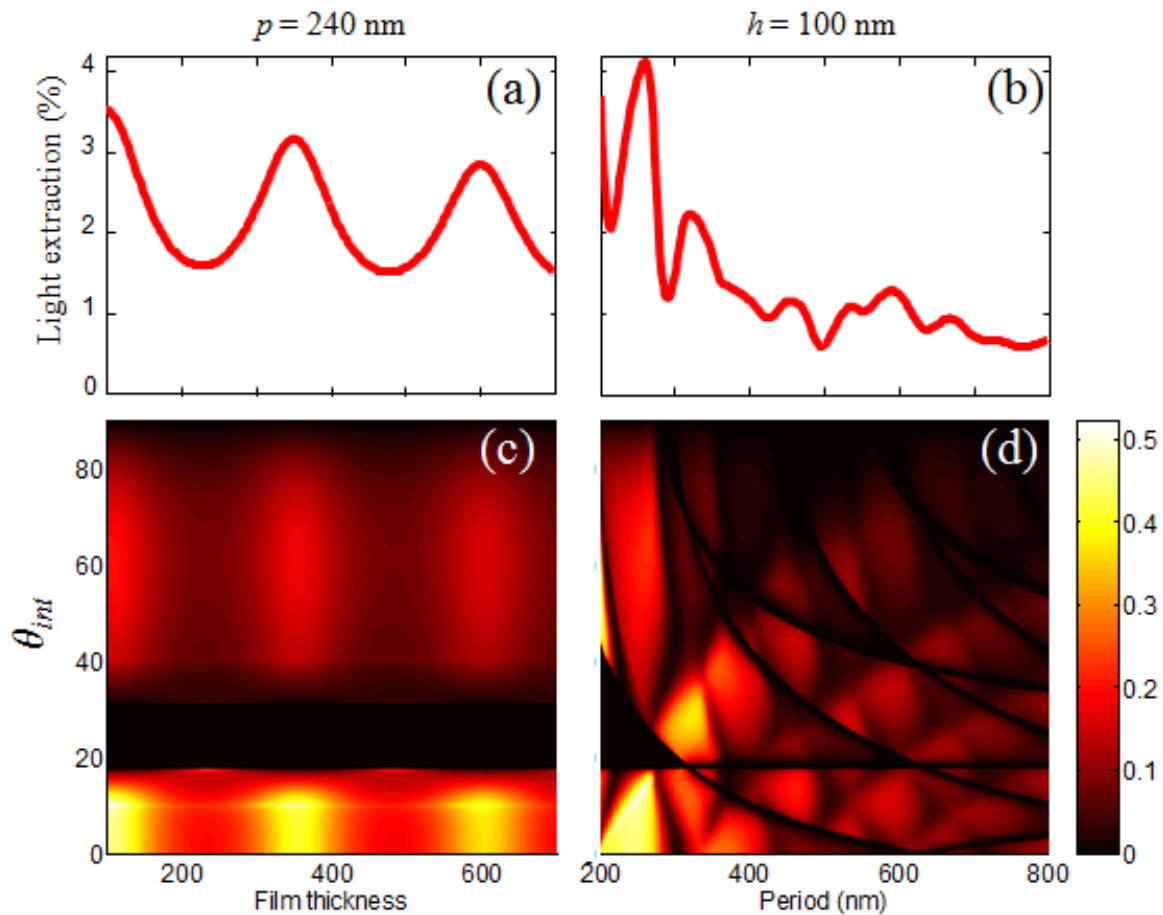
Figure 5.21. Light Extraction from GaP with a gold grating on the GaP surface (a) as a function of h and for $p = 240$ nm (b) as a function of p and for $h = 100$ nm. In both cases, $w = 100$ nm and $\lambda = 650$ nm. Pannel (c) and (d) are the corresponding total transmission T in function of θ_{int}.

5.2.4. Transmission measurements through slit arrays on GaP substrates

In order to validate experimentally the fact that the structures previously designed can be useful to improve LEDs light extraction, slit arrays on GaP substrates were fabricated using FIB. Measurements with the corresponding calculations obtained with RCWA are shown in Fig. 5.22. The measurements show transmission which are 50% lower than expected from theory, except at the SPP minimum. Different structural parameters have been modified, but the same trend was always observed.

Three possible parameters, not accounted for in theory, have been investigated to explain the low transmission measured:

(i)   Finite size effects:

(ii)   Structure profile;

(iii)   Damaging of the GaP substrate by FIB.

Point (i) has been considered experimentally by measuring slit arrays with different slit numbers. Transmission measurements are shown in Fig. 5.22. There is nearly no difference in changing the slit number. Thus, structure size does not dramatically decrease transmission.
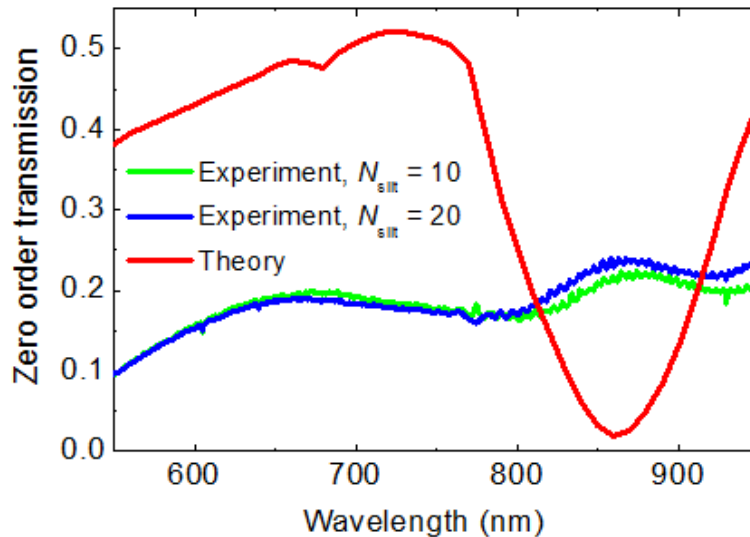
Figure 5.22.   Zero order transmission of gold gratings on a GaP substrate for $h = 200$ nm, $p = 240$ nm and $w = 140$ nm measured for $N_{slit} = 10$ (green curve), $N_{slit} = 20$ (blue curve). The red curve is the corresponding spectrum obtained with RCWA.

Point (ii) has been investigated by first measuring the slit profile. Figure 5.23(a) is a SEM picture showing the cross section etched by FIB of a slit array. As already shown in Section 4.1.1, the slit walls are tilted at an angle θ_{slit}. The true profile was then considered in the calculations using RCWA. As can be seen in Fig. 5.23(b), changing the angle slightly modifies the transmission, but not significantly enough to be the reason of the transmission drop measured.

Finally, damaging effects on the GaP substrate caused by FIB fabrication was investigated. As previously done in Section 4.1.1 for glass, a 25×25 μm^2 square of depth 20 nm is etched in a GaP substrate by FIB. Transmission spectrum of the etched substrate is shown by the blue curve in Fig. 5.24. The transmission is strongly decreased after FIB etching. For $\lambda = 650$ nm, the transmission is decreased by 40%. These optical losses are due to lattice damages, the creation of an amorphous top layer and ion implantation, typical in crystalline substrates [96,97]. This surely affects the optical properties of slit arrays.

Especially, the losses are the highest just below the array, where the substrate has been slightly etched, see Fig. 5.23(a). Damaging of the GaP substrate by FIB is consequently considered to be the main factor responsible to the low transmission measured through slit arrays.
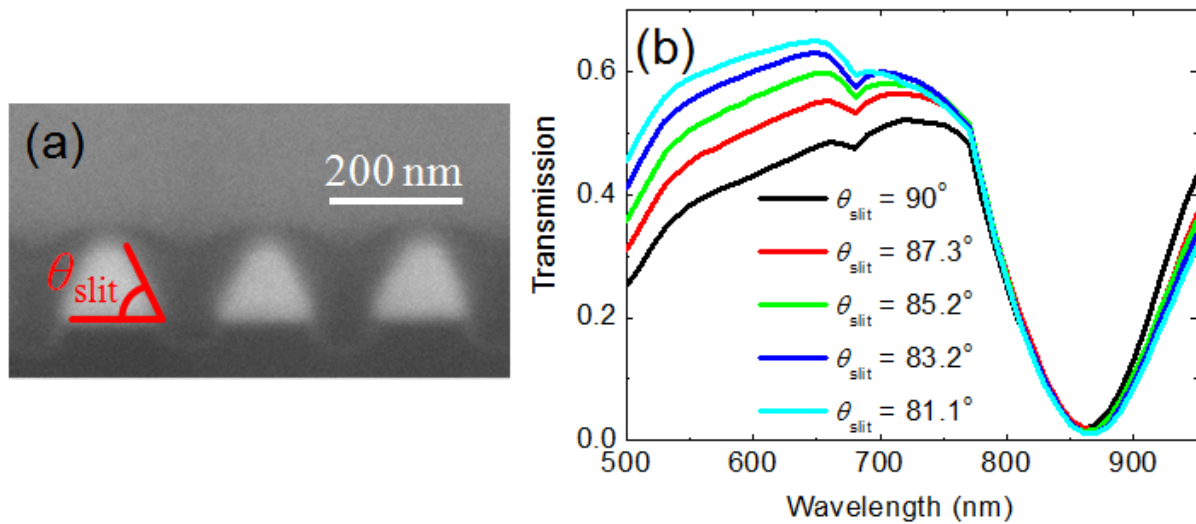
Figure 5.23. (a) Cross-section of a slit array imaged by SEM and definition of the tilted angle θ_{slit} accounted for the calculations. (b) Transmission of a slit array on a GaP substrate for h = 200 nm, p = 240 nm, w = 140 nm at the bottom of the slit, normal incidence from air and varying the angle θ_{slit}.
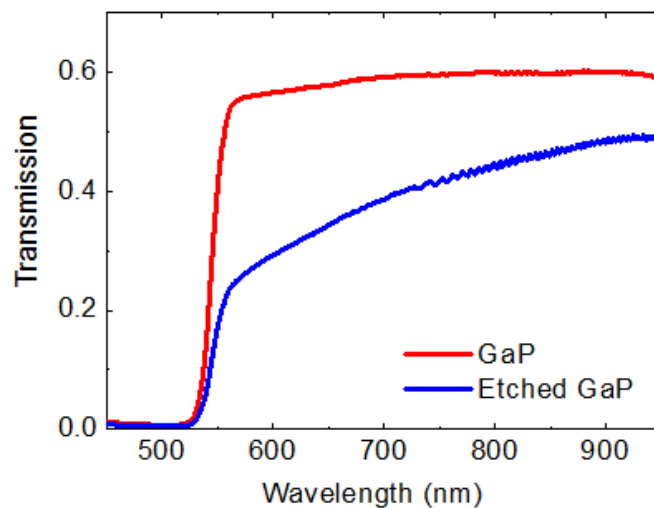
Figure 5.24. Transmission measured through a GaP substrate before and after FIB etching. The etched area is a 25×25 μm^2 square with 20 nm depth.

5.2.5. Limitations and perspectives

Section 5.2 shows that gold slit arrays have the potential to improve light extraction from LEDs reducing contact shadowing effects, thus improving the overall efficiency of LEDs, i.e. their external quantum efficiency. Light transmission through a slit array on a GaP substrate can be as high as 80% at normal incidence. It is also shown that due to grating coupling, light can be extracted beyond the critical angle. Preliminary calculations show that a metal contact with arrays of slit can give twice the extraction efficiency of a planar GaP-air interface. This result has been obtained without optimizing the transmission at large angles, which should be considered in future work. Although slit arrays are intrinsically polarization sensitive, this may not be a drawback for the LED market which uses polarization defined devices.

Preliminary experimental results where slit arrays on GaP have been fabricated by FIB show that it is necessary to modify the fabrication technology used. FIB fabrication damages the substrate, which induces high optical losses. Electron beam photolithography is currently being investigated at CSEM as an alternative technique of fabrication.

5.3. Image sensors

Image sensors are devices which convert an optical image into an electrical signal. This conversion is typically done from the absorption of incident photons by a semiconductor material, leading to the generation of charge carriers which in turn create a photocurrent. The frequency range covered by the sensor depends on the semiconductor used to absorb the incident radiation. We are interested here in visible to near infrared applications such as iris recognition, which usually takes place between 700 − 900 nm [132]. Silicon based vision sensors give high efficiency in this frequency range due to the intrinsic properties of silicon and seem to be the most suited candidate. Another reason to use silicon sensors is the maturity of silicon technology.

The main types of image sensors are either complementary metal-oxide-semiconductor (CMOS) sensors or charge-coupled device (CCD). The architecture of both devices is very similar: pixels comprised of a metal-oxide-semiconductor (MOS) capacitor are placed in an array. The main difference between CMOS and CCD devices is the way charges are transferred. In the CCD case, charges are transferred sequentially to a common output structure which converts the charges into a voltage. In a CMOS sensor, charge to voltage conversion takes place at the pixel level [133]. For a long time, CCD sensors were used for high performance applications whereas CMOS cameras, suffering from low sensitivity and high noise, were restricted to applications where low cost is desired, such as mobile phone camera or webcams. However, with the development of CMOS technology, CMOS sensors have reached almost the performance of CCD chips [134]. As CMOS sensors are fabricated within classical micro-electronic techniques, the costs of production are reduced compared to CCD devices. For this reason, we concentrate here on CMOS sensors.

The use of image sensors is not restricted only to record conventional two-dimensional black and white or colour images. Current research uses image sensors for distance measurements, 3-dimensional imaging, motion detection, object recognition and many other applications. Sensor performances such as dynamic range, resolution and speed are constantly improving, and sensitivity down to a single photon has been reached [135]. We intend, in this section, to use metal structures to enhance image sensor properties. After a description of the objectives, the integration and characterization of slit arrays and slit and groove structures on pixels is presented.

5.3.1. Objectives

The present study considers the use of metal structures in three domains of image sensing:

(i)   colour imaging;

(ii)   polarization imaging;

(iii)   signal to noise ratio improvement.

5.3.1.1.   Colour imaging

In conventional colour imaging, a colour filter array called Bayer filter is placed above the pixel array of the image sensors. This filter array consists of an arrangement of red, green and blue filters as shown in Fig. 5.25(a). The colour filters are made of colour dyes which absorb over certain wavelength range. Each pixel records one of the three basic colour ranges, see Fig. 5.25(b). The full-colour image is obtained by an algorithm interpolating a set of complete red, green, and blue values for each point.
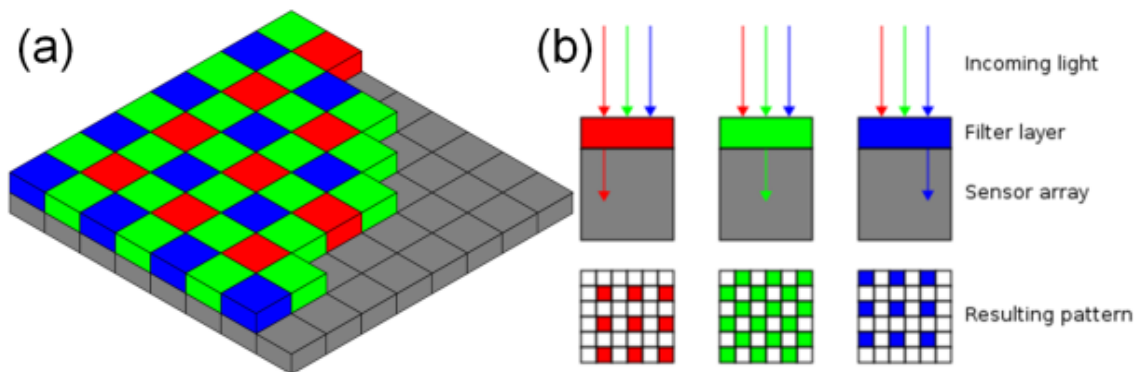
Figure 5.25.   Schematic representation of (a) the Bayer filter and (b) its basic principle, where on each pixel a different wavelength range or colour is collected. Image from Ref. [136].

Metal structures such as slit arrays and slit and grooves give high transmission at a specific wavelength which can be tuned by changing the structure geometrical parameters. These structures have consequently the potential to be used as colour filters. The advantage, as compared to conventional Bayer filters, is that metal filters do not suffer from photo-degradation. Moreover, the filter fabrication could directly be integrated into CMOS process, removing a fabrication step and thus reducing cost.

5.3.1.2.   Polarization imaging

The previous section showed how colour information can be extracted through filters on

116

individual pixels. Achieving this for polarization would provide information such as shape and object properties [137]. Polarization imaging can also improve biomedical imaging contrast due to the birefringence of biological tissue [138]. Information on the polarization state is usually obtained by mechanically rotating a polarizer in front of a camera. Movable components can be avoided on integrating micro-polarizers on each individual pixel, allowing to acquire polarization information at the pixel level [139]. Similar to the Bayer configuration, a smart arrangement of pixels allows the reconstruction of the polarization state [140], as shown in the schematic in Fig. 5.26. As slit arrays and slit and groove structures are polarization sensitive, the use of these metal structures to fabricate polarization sensitive pixels is investigated.
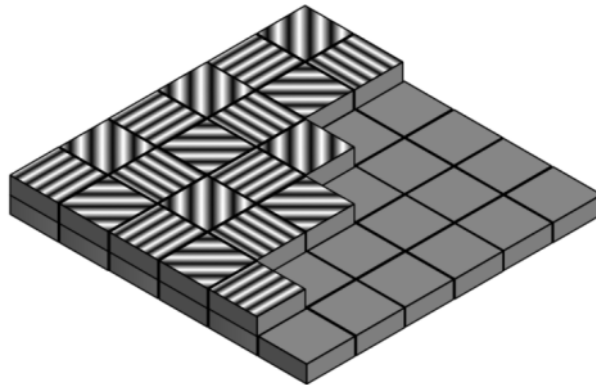
Figure 5.26.   Schematic representation of an array of micro-polarizers placed above an array of pixels used for polarization imaging, in analogy with the Bayer filter used for colour imaging.

5.3.1.3.   Signal to noise ratio improvement

In a CMOS sensor, charges are converted into a voltage at the pixel level. This requires extra circuitry in each pixel. Consequently, the photosensitive surface is smaller than the total pixel surface and part of the impinging light is lost. As CMOS technology is scaling down, the filling factor of photosensitive surface decreases, thus reducing the amount of detected light which in turn reduces the signal to noise ratio of the detector. This is a serious drawback in low light applications such as night vision or iris recognition. In order to effectively decrease "dead" pixel region areas, microlenses have been used at the surface of the image sensor to focus the incident light on the semiconductor's photosensitive area [141], as shown in Fig. 5.27.

In a recent study, Ishi *et. al.* [102] used a bull's eye structure above the photosensitive area of a photodiode. Their goal was to increase the speed of photodetectors. The response

time of a detector scales with the active area size. Reducing the active area of a detector will then increase its speed, but in turn reduce the output of the photodiode. The bull's eye structure overcomes this limitation as it concentrates the light into the reduced photosensitive area. A schematic of their plasmonic photodetector is represented in Fig. 5.28.
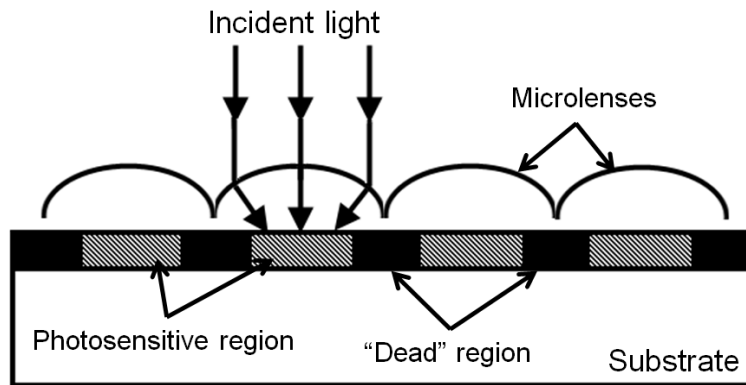
Figure 5.27.   Schematic illustration of the use of microlenses to effectively increase photosensitive region. Adapted from Ref. [141]
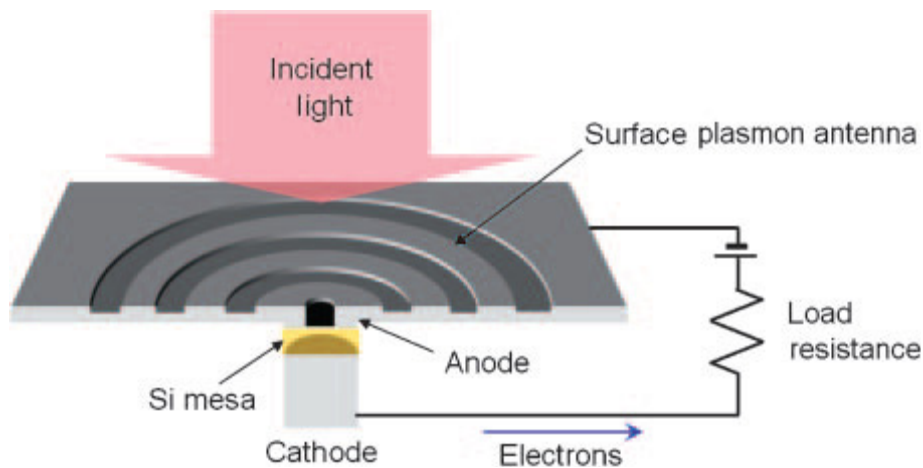
Figure 5.28.   Schematic cross sectional view of a photodiode with a bull's eye structure above the photosensitive area. Image from Ref. [102].

Here we address the possibility to improve the signal to noise ratio of image sensors with slit and groove structures. Using metal structures would provide several advantages over microlenses:

(i)   The fabrication of the metal structures could be directly integrated within the CMOS process;

(ii)   The use of a metal structure provides spectral filtering in addition to light harvesting. Consequently, in the case of colour imaging the plasmonic structure can replace both

lenses and colour filters.

(iii)   Plasmonic structures are not diffraction limited as is the case for lenses. Light can then be concentrated in sub-wavelength volumes.

5.3.2. Materials and method

To investigate the integration of metal structures on photodetectors, the CMOS-fabricated VisionSensor (ViSi) detector was used [142]. This sensor consists of an array of 50×50 μm^2 pixels, each pixel having a photosensitive area of 14×14 μm^2, see Fig. 5.29(a). In the CMOS process used, the photosensitive area is covered by a 5.5 μm thick silicon oxide (SiO_x) layer. Figure 5.29(b) is a image obtained by atomic force microscopy (AFM). The surface profile shows that the top of the photosensitive region is sunken below the electronic circuitry to a depth of around 1.2 μm.

The image sensor was covered by a gold film as a post process by sputtering. Slit arrays and slit and groove structures were then milled above the photosensitive areas using FIB technique. Slit and groove structures fabricated on top of the photosensitive areas of the two lower pixels are shown in the optical image in Fig. 5.29(c).

Due to the presence of the 5.5 μm thick SiO_x layer, refractive index below the metal structures is the same as for the experiments done in Chapter 4 on glass substrate. Thus, the transmission properties are expected to be similar. The thickness of the SiO_x layer and the size of the photosensitive region define the collection angle θ_{col}. see Fig. 5.29(d). In the case of a slit placed at the centre of the photosensitive area as in Fig. 5.29(d), $\theta_{col} = 52°$.

A schematic of the optical setup used to characterize the pixels with metal structures is shown in Fig. 5.30. A supercontinuum light source is coupled to a monochromator using two lenses. At the output of the monochromator, quasimonochromatic ($\Delta\lambda < 2$ nm) light is obtained. Two Glan laser prisms and a quarter wave plate are used to control the polarization state of the beam, which is then focused on an individual pixel of the photodetector with a numerical aperture smaller than 0.1. In order to record the spectrum of a given pixel, the incident wavelength is scanned by rotating the grating inside the monochromator, while the optical power P measured on the pixel of interest is recorded.
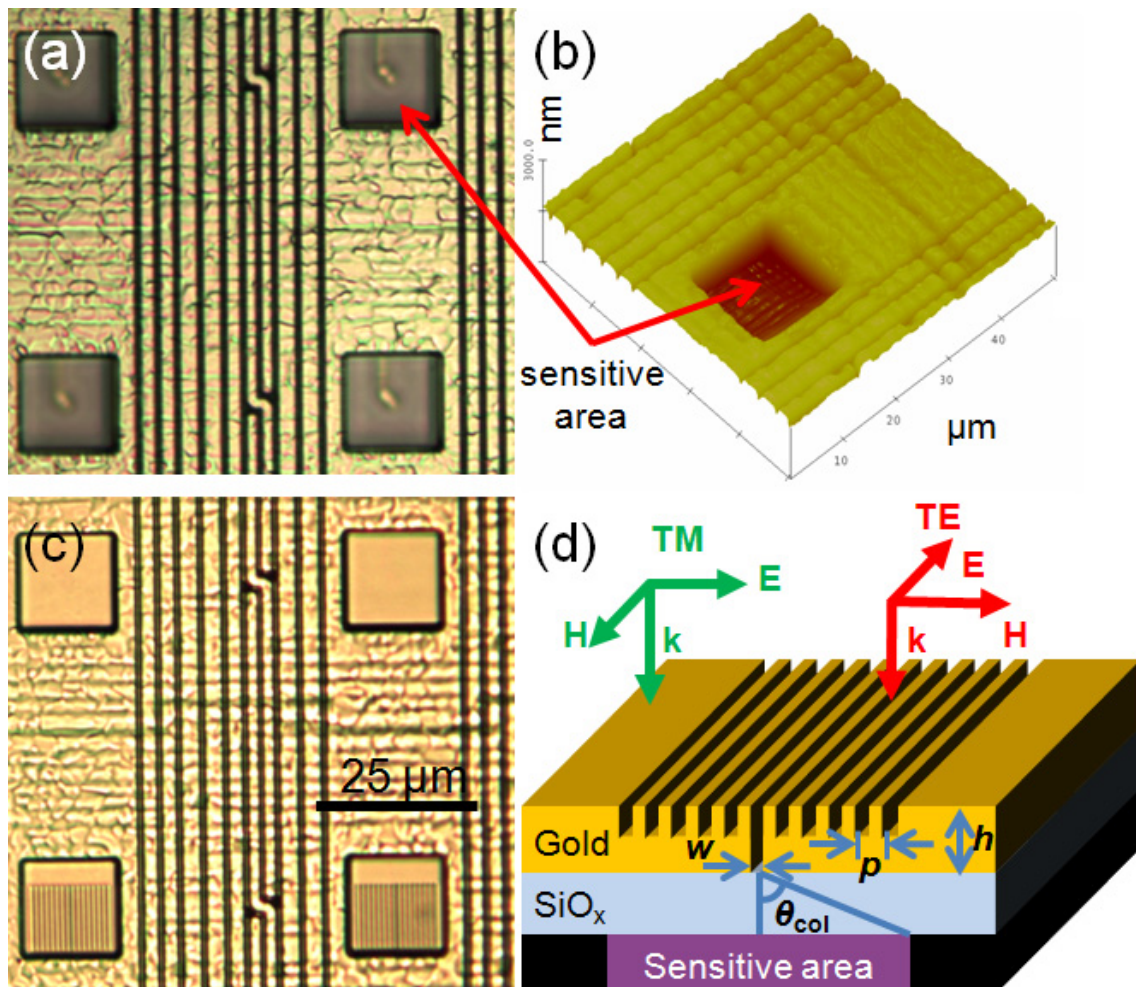
Figure 5.29. Optical image of 4 pixels (a) before (c) and after gold deposition. In panel (c), slit and groove structures have been fabricated above the photosensitive area of the two lower pixels. (b) A three dimensional image obtained by AFM showing the surface profile of a pixel. (d) Schematic cross sectional view of a slit and groove structure integrated on top of the photosensitive area of a vision sensor pixel and definitions used in this work.
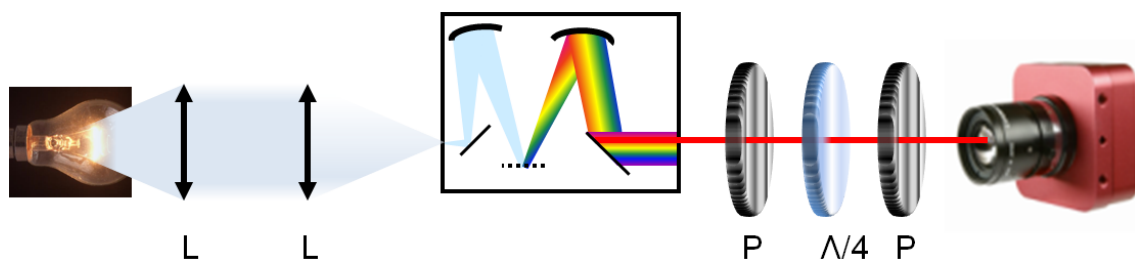
Figure 5.30. Schematic of the optical setup used for the characterization of the "plasmonic" pixels. L, P and $\Lambda/4$ are lenses (focal length of 150 nm), polarizers and a quarter wave plate, respectively. The incident white light represented by a bulb is a supercontinuum light source.

In order to normalize the spectrum recorded for a pixel with a metal structure, the power measured for a pixel without any layer of gold above the photosensitive region denoted P_0 is taken as a reference. In the case of a slit array, the transmission is

$$T = \frac{P}{P_0} * \frac{A_0}{LN_{slit}p}, \tag{5.3-1}$$

with A_0 the area of the photosensitive region and p, L and N_{slit} the periodicity, slit length and number of slits in the array, as defined in Section 4.1.1. In the case of a slit and groove structure, the normalized transmission NT is

$$NT = \frac{P}{P_0} * \frac{A_0}{wL}. \tag{5.3-2}$$

Considering the size of the photosensitive area constrained to the slit size because of the surrounding electronics, the highest signal to noise ratio will be given by the highest possible NT. For $NT > 1$, the signal to noise ratio of the pixel is then increased by a factor NT. In the case where there is no constraint in the size of the photosensitive area, a maximal NT is not necessarily synonymous of signal to noise ratio improvement [143]. It is then necessary to consider the total transmission of the slit and groove structure

$$T = \frac{P}{P_0} = NT \frac{wL}{A_0}. \tag{5.3-3}$$

As the noise of the detector is proportional to the square root of the size of the photosensitive area [63], the figure of merit

$$F = T\sqrt{\frac{A_0}{wL}} = NT\sqrt{\frac{wL}{A_0}}, \tag{5.3-4}$$

characterizes the signal to noise ratio improvement induced by the slit and groove structure.

5.3.3. Slit arrays on image sensors

The integration of slit arrays on image sensors is considered here. Arrays of slits have been etched to a 340 nm thick gold film deposited above the photosensitive area of pixels. The array contains $N_{slit} = 20$ of width $w = 150$ nm and length 10 µm. The spectrum measured for a pixel with a slit array of period $p = 400$ nm and TM incident light is shown by the red curve in the top graph of Fig. 5.31. Strong oscillations are observed in the spectrum. This is due to the oxide layer present above the photosensitive area which acts as a FP cavity: light bounces backward and forward several times inside the oxide layer, as shown in Fig. 5.32.

Such oscillations are also present in the reference spectrum (i.e. for a pixel without metal); see the red curve in the bottom graph of Fig. 5.31. The oscillations are amplified in the case of the slit array due to the higher reflection at the Au-SiO_x interface, and they undergo a π phase shift at the Au-SiO_x interface compared to the reference. The transmission peaks observed previously for slit arrays cannot be exploited for colour imaging purposes unless the slit array is placed closer to the photosensitive area, which would avoid FP fringes.
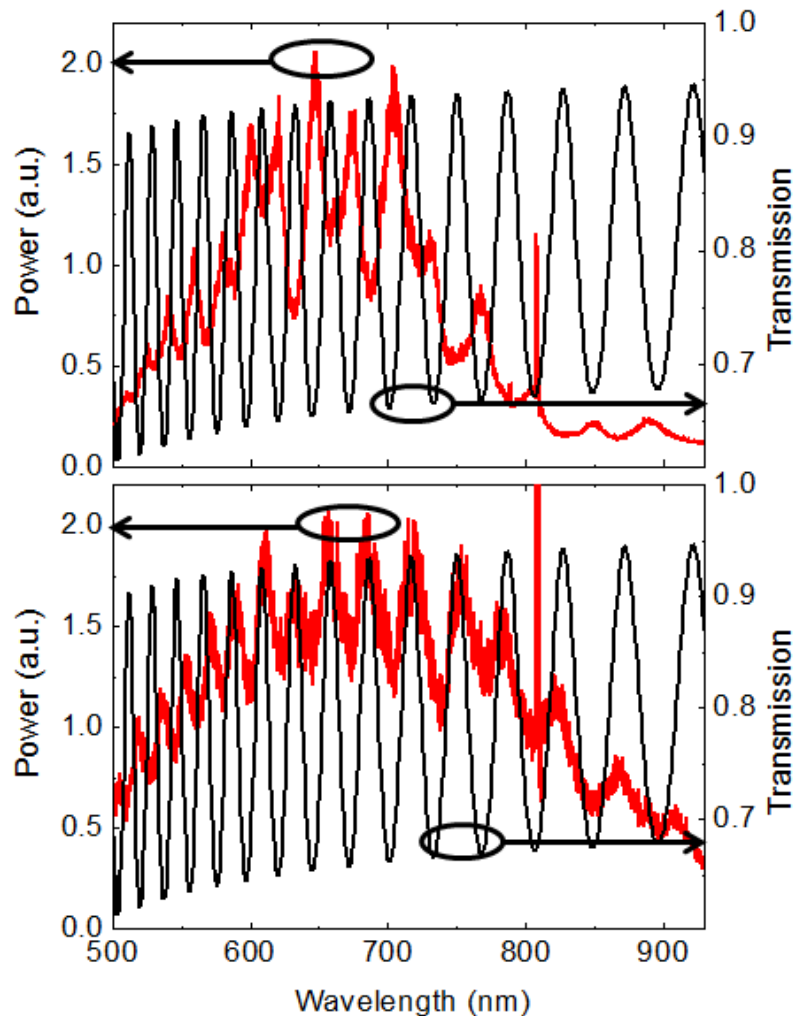
Figure 5.31.   Optical power measured for a pixel without any layer of gold above the photosensitive region (red curve, top graph) and for a pixel with an array of 20 slits with $h = 340$ nm, $w = 150$ nm and $p = 400$ nm obtained for TM polarization (red curve, bottom graph). The black curves in both graph correspond to the light transmission of a 5.375 μm thick SiO_x layer on a silicon wafer.
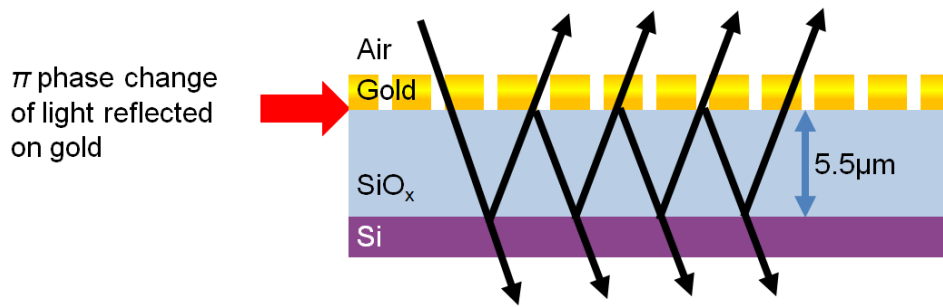
Figure 5.32. Schematic of the FP fringes generation in the oxide layer present above the photosensitive area of the pixel.

It is possible to reproduce the position and spacing of these oscillations by calculating with Fresnel formulae the transmission of a 5.375 µm thick SiO_x layer on a silicon wafer, see the black curves in Fig. 5.31. A refractive index of 1.5 is considered for the SiO_x layer, whereas the dielectric constant of Si is taken from the Sopra database [55]. The oscillations of the black and red curves match in the case of the reference spectrum, whereas the one measured for the pixel with a slit array is out of phase with the reference.

It was shown in Section 4.5 that slit arrays on glass substrate can provide strong extinction ratio of polarization. For example, an array with geometrical parameters $p = 500$ nm, $h = 285$ nm and $w = 150$ nm gives both an excellent polarization extinction ratio and a good transmission from the visible to near-infrared spectrum while having dimensions suitable for CMOS manufacturing.

A slit array with $p = 500$ nm and $w = 150$ nm was etched into a 340 nm thick gold film deposited on the pixels. Results are shown in Fig. 5.33. The power measured for a pixel with the slit array is almost the same as for a pixel without metal for TM polarization, whereas it is three orders of magnitude lower for TE polarization, as shown in Fig. 5.33(a). Again, FP fringes observed for pixels without metal are amplified by the presence of the array. However the oscillations are not detrimental for polarization imaging since the TE polarization stays low, and the ER is higher than 200 from 650 to 850 nm, see Fig. 5.33(b). The higher ER obtained here than the one measured on glass is due to the thicker metal film which lowers the s-polarized transmission. These measurements demonstrate the possibility to integrate efficient micro-polarizers on CMOS detectors for the visible spectrum. These polarizers could be integrated directly within CMOS process, due to their planarity and dimensions.
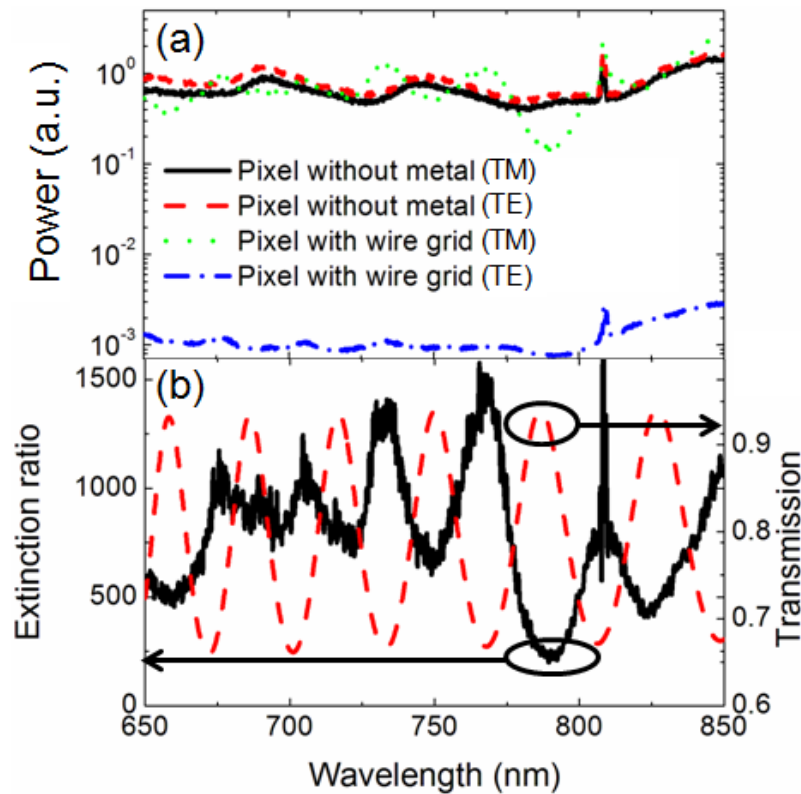
Figure 5.33. (a) Optical power measured for TM and TE polarization on a pixel of a CMOS sensor without metal (black solid line and red dashed line, respectively) and with a wire grid with $p = 500$ nm, $h = 340$ nm and $w = 150$ nm (green dotted line and blue dashed dotted line respectively). (b) Corresponding extinction ratio (black solid line) and calculated transmission of a 5.375 μm thick SiO_x layer on a silicon wafer.

5.3.4. Slit and groove structures on image sensors

This section considers the integration of slit and groove structures on image sensors. The TM normalized transmission spectra measured on pixels with slit and groove structures for different periods ranging from 600 to 800nm are shown in Fig. 5.34(a). Following the notations of Chapter 4, the structure parameters are $w = 100$ nm $h = 180$ nm, $N_g = 5$ and $h_g = w_g = 100$ nm.

As compared to the slit array case, the FP fringes due to the SiO_x layer are nearly absent for slit and groove structures. This difference can be explained by the different scattering patterns of the structures: whereas in the case of slit and groove structures light is scattered in all directions, several discrete diffracted orders appear for slit arrays, see the schematic of Fig. 5.35. Only the 0th diffracted order is detected for the slit arrays of our experiment. Consequently, the light bounces backward and forward several times in the same direction resulting in FP fringes.

Figure 5.34. (a) Normalized transmission of slit and groove structures for TM polarization with N_g = 5, w = 100 nm, h = 180 nm and periods varying from 600 to 800 nm measured on the pixel of a CMOS sensor. (b) Corresponding calculations obtained from the modal expansion method for a collection angle θ_c = 52°.
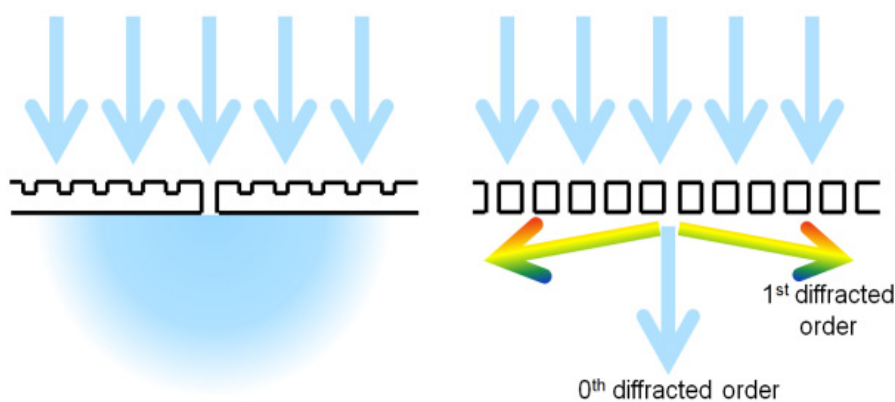
Figure 5.35. Schematic representing the scattering behaviour of a slit and groove structure (left hand side) and a slit array (right hand side). The arrows on the top indicate the incoming light.

125

The experimental results obtained with the image sensor are noisier than the ones measured on glass substrates. This is intrinsically linked to the method used to record the optical signal in the detector used in this study. Instead of integrating photocurrents for a fixed duration, photocurrents are integrated until a given reference voltage is reached. This prevents saturation and gives a large dynamical range [142] but also gives a noise which scales inversely proportional to the signal. This explains why the signal is noisier for the highest transmission in the measurements of Fig. 5.34.

As for slit and groove structures on glass, a transmission peak is observed which shifts to longer wavelength with increasing p. The normalized transmission is greater than 8 for periods of 700 and 750 nm. This means that for a photosensitive area the size of the slit, the signal would be increased by a factor of more than 8 due to the metal structure. These measurements have been compared with the modal expansion method described in Ref. [93,100], see Fig. 5.34(b). A collection angle $\theta_{col} = 52°$ has been considered which corresponds to the effective collection angle of the pixel. The experimental spectra show good agreements with the calculated ones in terms of the redshift of the transmission peak with increasing period and the peak widths. The agreement in terms of amplitude is surprisingly good considering the fact that spectra measured for slit and groove structures on glass show a transmission 50% lower than expected theoretically. This could be partly explained by the fact that in the case of a pixel without a metal layer above the photosensitive region, a high reflection occurs at the Si-SiO$_x$ interface (cf. Fig. 5.32) and part of the light is not absorbed. In the case of a slit and groove structure, light transmitted through the slit and reflected at the Si-SiO$_x$ interface is efficiently reflected by the gold layer and has several "chances" to get absorbed due to multiple reflections between the metal layer and the silicon.

The influence of the slit width w has also been investigated, see Fig. 5.36. For the three different periods considered, increasing w from 100 to 200 nm only decreases slightly the normalized transmission. This means that nearly twice as much of light is detected for $w = 200$ nm as compared to $w = 100$ nm. This effect can be explained by the increased losses of the slit mode as the slit width is reduced. Considering the figure of merit defined by Eq. (5.3-4), these results show that a slit width of 200 nm lead to a signal to noise ratio increase of $\sqrt{2}$ as compared to a slit of 100 nm.
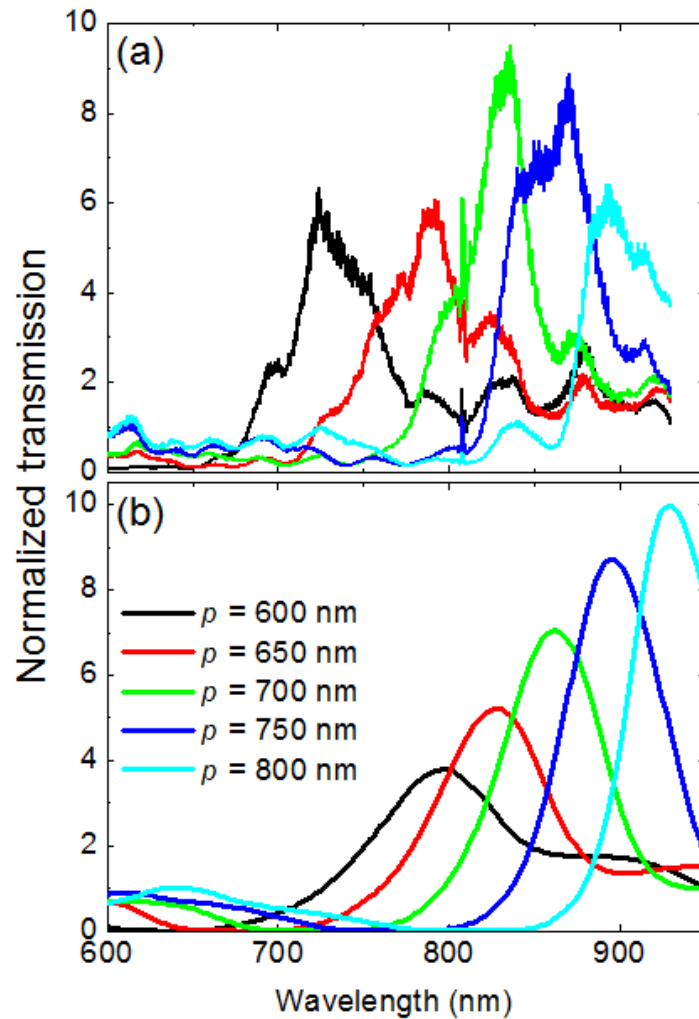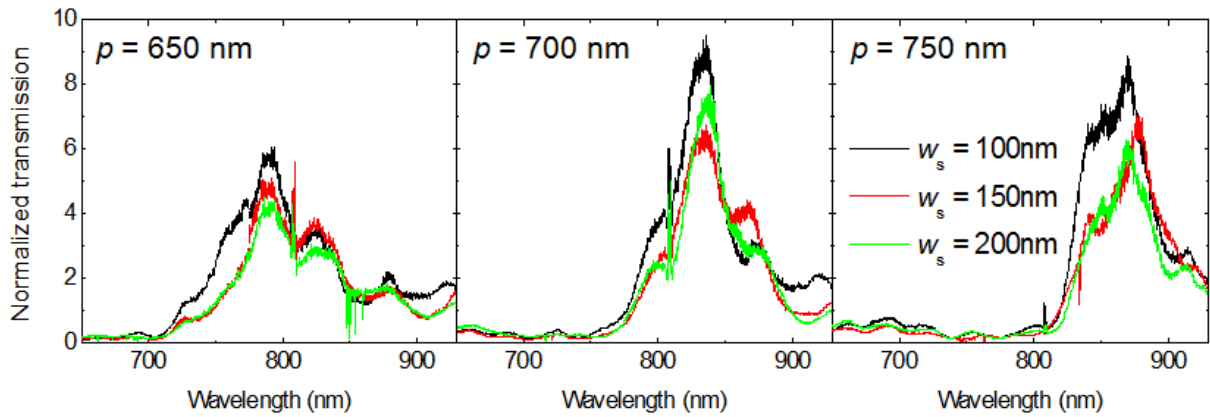
Figure 5.36.   Normalized transmission of slit and groove structures for TM polarization with $N_g = 5$ and $h = 180$ nm measured on the pixel of a CMOS sensor for different slit width and for period $p = 650$ nm (left), $p = 700$ nm (middle) and $p = 750$ nm (right).

These different results demonstrate the possibility to use slit and groove structures to improve signal to noise ratio of CMOS sensors. Placing the photosensitive area in the near field of the slit aperture would increase further the signal and would permit to reduce the size of the photosensitive area below the diffraction limit. Also, high transmission can be tuned at a desired wavelength changing the array periodicity. This could be used for colour imaging.
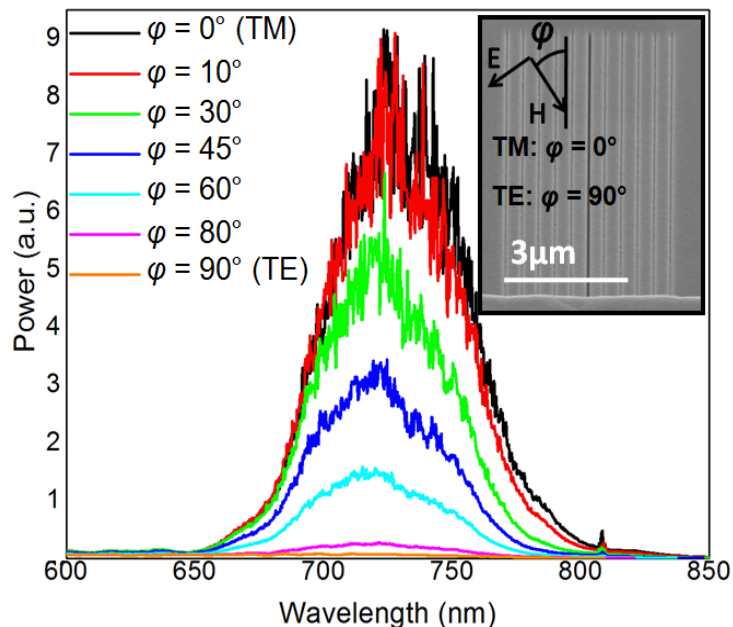
Figure 5.37.   Optical power measured for a pixel with a slit and groove structure with parameters $N_g = 5$, $w = 100$ nm, $h = 180$ nm and $p = 600$ nm for different polarization states. The inset, which is a SEM picture of the slit and groove structure, defines the polarization angle φ.

Finally, the polarization sensitivity of pixels with slit and groove structures has been measured. In Fig. 5.37, the optical power measured for a pixel with a slit and groove structure with parameters $N_g = 5$, $w = 100$ nm, $h = 180$ nm and $p = 600$ nm is shown for different polarization states. The measured power is strongly reduced by changing the angle φ defined by the angle between the grooves direction and the incident light magnetic field, see the inset in Fig. 5.37. This shows that slit and groove structures can also be used as micro-polarizers integrated in pixels for polarization imaging purposes.

5.3.5.   Outline and perspective

Section 5.3 showed that subwavelength slits in metals can be advantageously used for different vision applications. Metal slit arrays integrated above the photosensitive region of pixels can be used as very efficient micro-polarizers. It should also be possible to use slit arrays to replace conventional dye-based Bayer filters for colour imaging, but the 5.5 μm thick SiO$_x$ layer present above the photosensitive region needs to be removed. It was shown that slit and groove structures could improve by a factor of eight the signal measured on a sensor. This factor is not at the fundamental limit. Several theoretical studies have shown that higher enhanced transmission can be achieved with improved designs, see for example Ref. [70]. Also, slit and groove structures can be used for both colour and polarization imaging. Non-polarization sensitive structures can be made by making bull's eye structures.

Image sensor designers keep exploring new solutions to continuously improve the performance of vision sensors. An emerging way to improve the signal to noise ratio of photodetectors is the back side illumination (BSI) configuration. In conventional front side illumination (FSI) architectures, light travels to the photo-sensitive area through the front side of the pixel, see the left side of Fig. 5.38. This requires the light to first pass through transistors, dielectric layers and metal circuitry, which can block or deflect it into neighboring pixels, causing a reduced fill factor and additional problems such as cross talk between pixels. Instead of illuminating a CMOS image sensor from the top (front) side of the silicon die, BSI collects photons from the backside of the pixel area. By eliminating obstacles such as metals and dielectric layers, BSI helps to stop the loss of photons and maximizes the area over which photons are collected. The BSI architecture still needs colour filters and microlenses, which means that metal structures such as the one considered in Section 5.3 can still be valuable for this emerging technology.
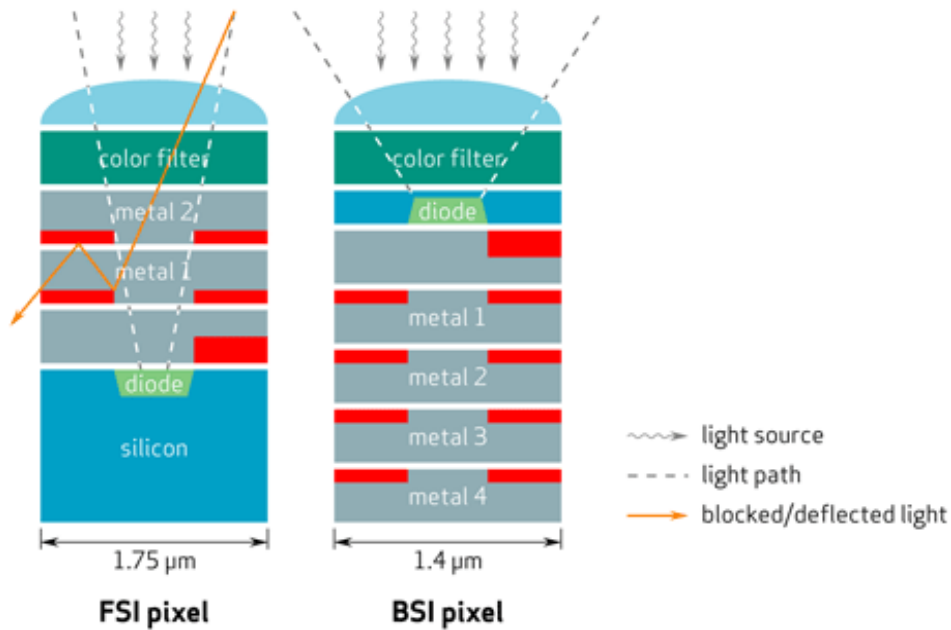
Figure 5.38. Schematic cross sectional view of a pixel in the FSI (left part) and BSI (right part) configurations. Image from Ref. [144].
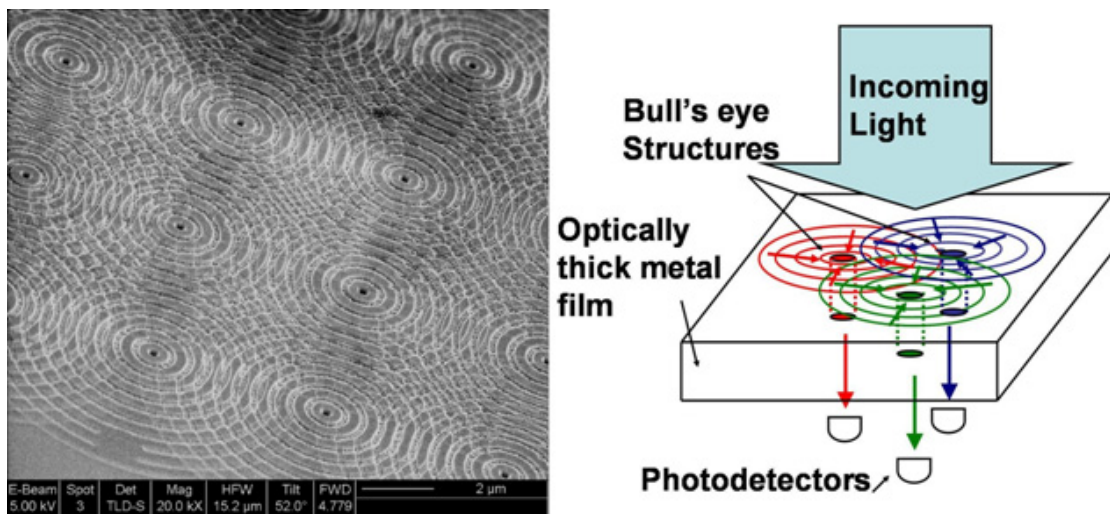
Figure 5.39. Schematic cross sectional view of a pixel in the FSI (left part) and BSI (right part) configuration. Image from Ref. [145,146].

In the classical colour imaging approach exposed in Section 5.3.1.1, a pixel is sensitive to only one colour or frequency range, while photons with other frequencies impinging on that pixel are lost. This leads to inefficient use of the incoming light. There exist several ways to collect different colours on each pixel. For example, the Foveon X3 sensor uses three layers of pixels, each layer capturing a particular colour [147]. Metal structures have also been suggested by Laux *et al.* as a way to improve spectral imaging [145]. The concept is to

overlap bull's eye as illustrated in the left part of Fig. 5.39. With such a system, each bull's eye structure will collect light over a certain frequency range and be able to redirect it to its central aperture even from the region where it overlaps with other collectors, as schemed in the right part of Fig. 5.39. This is an elegant way of sorting photons by colours. As the transmission through a bull's eye is relatively low, Laux *et al.* also proposed to overlap slit and grooves structures in a similar way. This new design contains then also polarization information.

Finally, the integration of plasmonic "photon sorters" into BSI image sensor could lead to a competitive device. Despite several limitations such as transmission efficiency, metal structures presents unique properties that could be certainly used in image sensing applications.

Chapter 6

Conclusion & outlook

This thesis presented a theoretical and experimental investigation of the optical properties of subwavelength slits in metal films. The results include theoretical work, the fabrication of samples and optical characterization as well as several studies investigating the potential use of slits in metals for different applications.

The theoretical study carried out in Chapter 3 gives a unified picture on the phenomenon of TM light transmission through subwavelength slit arrays in metal films. To achieve this, an analytical model is derived from the modal expansion method described by Lochbihler *et al.* [72]. The analytical model is very accurate for narrow slits and optically thick metal walls. This model enables a dressed surface plasmon polariton (SPP) mode to be defined. The difference of this mode as compared to an SPP mode on a flat metal-dielectric interface is that the perturbation induced by the slits is considered. The transmission is very low when this dressed mode is excited. In addition, the dispersion relations of the modes responsible for high transmission are derived. The main transmission modes are Fabry-Pérot (FP) like resonances which become hybrid FP-SPP modes as the wavelength of the resonance approaches the dressed SPP resonance. The FP-SPP modes are analogous to symmetric and antisymmetric modes of a waveguide except for wavelengths close to the dressed SPP mode. In that case, strong dispersion of the hybrid "SPP-FP" modes is observed and the field profile of these modes presents similarities with the symmetric and antisymmetric SPP modes of a

thin metal film. The good understanding of the behaviour of the different modes provided by this study is particularly useful for designing slit arrays with specific optical characteristics needed in different applications.

These results open several new routes which could be investigated further. The analytical model could be extended to the case of subwavelength hole arrays in a future work. The reflection/transmission coefficients at each interface of the hole array would then be known analytically. This would be particularly useful in order to increase the transmission through the holes which stays relatively low due to the evanescent nature of the modes inside the holes. One way to improve the transmission would be to design an anti-reflection coating on the array.

Before addressing the potential of slits in metals for various applications, the light transmission through single slits, slit and grooves and slit arrays was investigated in Chapter 4. In addition to the enhanced TM optical transmission phenomenon expected for conventional slit and groove structures, measurements of slit and groove structures covered by a thin dielectric layer show that TE transmission can also be boosted by exciting TE waveguide modes sustained in the thin dielectric layer.

For each of the structures considered in Chapter 4, a comparison is made with theory in order to give an idea of the validity of the different models. In most cases good agreement between theory and experiment is observed, especially for the position of the different spectral features. There are, however, deviations in the transmission amplitude, which is in general lower than expected from theory. This can be explained not only by sample imperfections, but also by metal losses which are neglected in the case of the model used for single slits and slit and groove structures.

Finally, this work investigates the use of slits in metals for three different optical devices: biosensors, light emitting diodes (LEDs) and image sensors. In the case of biosensing, slit arrays with high sensitivity to refractive index changes are considered with the goal to fabricate compact and portable sensors. Based on the theoretical study of Chapter 3, calculations show that the sensitivity of slit arrays on glass substrates is limited by the higher refractive index of glass as compared to water. The device sensitivity can be increased removing the substrate, i.e. using membranes. Such membranes should provide a 3% intensity change as a 1.6 nm thick bovine serum albumin layer is adsorbed on the array. Measurements of slit arrays on glass substrates immersed in solutions of different refractive indices corroborate our theoretical work. The fabrication of membranes and the detection of adsorbed layer of molecules still need to be studied and is foreseen in a future work.

Slit arrays have been investigated as transparent electrical contacts for LEDs. Theoretical calculations show that normal incidence transmission can be as high as 80% for hybrid FP-SPP modes that are far from the dressed SPP mode. In addition, light can be transmitted for angles of incidence larger than the critical angle due to grating coupling. Preliminary calculations show that the light extraction efficiency through a slit array could be twice the one of a planar GaP-air interface. Preliminary experimental work has been done, where slit arrays have been fabricated on GaP substrate by FIB. Unfortunately, FIB fabrication induces significant optical losses due to amorphization of GaP. Electron beam photolithography is currently investigated at CSEM as an alternative technique of fabrication. With these fabricated arrays, it should be verified whether light transmission is as high as theoretically predicted before fabricating such arrays on LEDs and validate the possibility to improve LEDs efficiency with slit arrays.

Finally, slit arrays and slit and groove structures have been integrated on the pixels of CMOS sensors as a post process. A polarization extinction ratio higher than 200 over a bandwidth of 200 nm is measured on a pixel with a slit array integrated onto it. As the structure dimensions of the array are suitable for CMOS manufacturing, this is an important result in view of direct integration above pixels of efficient and low cost micro-polarizers within CMOS process. In addition to polarization selectivity, slit and groove structures integrated on CMOS pixels can also provide spectral selectivity and light transmission enhancement. Whereas the spectral sensitivity could be used for colour imaging, the light transmission enhancement could be used to increase the signal to noise ratio of image sensors. However to obtain such goal, light transmission efficiency needs to be further increased, and the design of the slit and groove structure needs to be considered at the same time as the design of the complete architecture of the sensor.

The results obtained in the case of the slit and groove structures covered by a thin dielectric layer could be further improved by matching enhanced optical transmission for both polarizations at the same wavelength. This would be particularly useful in optical devices where high throughput is necessary such as low noise or high speed photodetectors. This work could also be extended to structure like bull's eyes in order to improve their transmission efficiency.

Finally, the different results of this thesis could be extended to longer wavelengths, where optical losses induced by metals are low. This should improve further structure's performances.

Appendix A
Refractive indices of gold and gallium phosphide

Table A.1.   Refractive indices of gold and gallium phosphide used in this thesis, taken from Sopra database [55].

Wavelength (nm)	$\Re(RIX_{gold})$	$\Im(RIX_{gold})$	Wavelength (nm)	$\Re(RIX_{GaP})$
400	1.6579	1.956	500	3.5752
450	1.5085	1.8789	510	3.5465
500	0.85123	1.8867	520	3.5275
550	0.35043	2.714	530	3.5082
600	0.22026	3	540	3.4671
650	0.16779	3.1378	550	3.4495
700	0.1605	3.9636	560	3.4264
750	0.16915	4.5939	570	3.4114
800	0.1814	5.1268	580	3.3808
850	0.19632	5.5883	590	3.3601
900	0.21532	6.0064	600	3.3528
950	0.23453	6.4381	610	3.3385

Wavelength (nm)	$\Re\left(RIX_{gold}\right)$	$\Im\left(RIX_{gold}\right)$	Wavelength (nm)	$\Re\left(RIX_{GaP}\right)$
1000	0.25683	6.8154	620	3.3246
1050	0.27891	7.2251	630	3.3177
1100	0.30009	7.6836	640	3.3016
1150	0.32366	8.1318	650	3.2915
1200	0.34998	8.5228	660	3.2799
1250	0.37794	8.7681	670	3.2691
1300	0.4072	8.7585	680	3.2704
1350	0.43731	8.7652	690	3.2489
1400	0.46755	8.8897	700	3.2463
1450	0.49783	9.1569	710	3.2499
1500	0.52843	9.4784	720	3.242
1550	0.55911	9.8112	730	3.2319
1600	0.58939	10.125	740	3.2221
1650	0.61966	10.438	750	3.2199
1700	0.65111	10.752	760	3.2203
1750	0.68263	11.067	770	3.216
1800	0.71485	11.375	780	3.2009
1850	0.74761	11.68	790	3.1828
1900	0.78036	11.985	800	3.1791
1950	0.81489	12.29	810	3.187
2000	0.84972	12.595	820	3.1851
2050	0.88456	12.9	830	3.1786
2100	0.92067	13.205	840	3.1711
2150	0.9574	13.509	850	3.1639
2200	0.99413	13.814	860	3.1602
2250	1.0309	14.118	870	3.16
2300	1.0687	14.419	880	3.1536
2350	1.1066	14.72	890	3.1472
2400	1.1445	15.021	900	3.1408

Appendix B
Modal expansion derivation

The modal expansion method to calculate the optical properties of metal grating is derived here for both TE and TM polarization and in the general case where the permittivity can take any value above and below the grating and inside the slits, see Fig. B.1 for a scheme of the structure and its different parameters. The electric field vector $\mathbf{E}$ and magnetic field vector $\mathbf{H}$ corresponds to the field $f_z(x,y)$ for TE and TM polarization respectively.
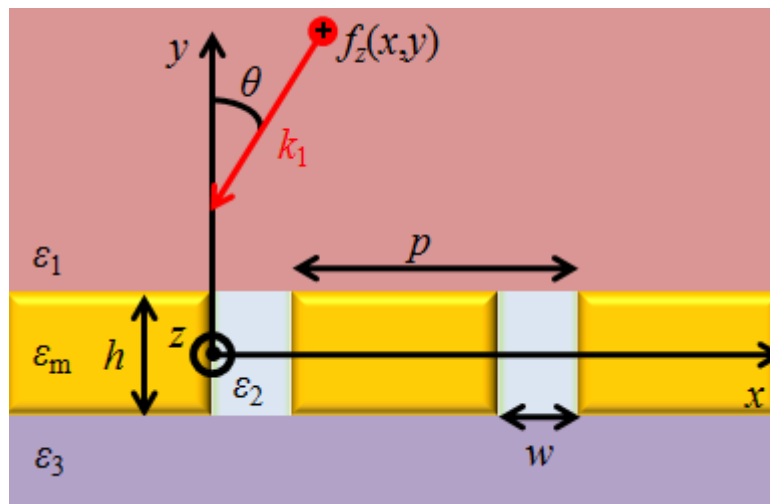
Figure B.1.   Schematic of the studied structure and definitions used for the structure's dimensions and incident field directions. The structure repeats itself infinitely with period p in the x direction.

If not mentioned, the same terminology as in Section 3.2 is considered. The field above and below the grating is expressed as a Rayleigh (or plane wave) expansion:

$$f_z(x,y) = \exp\{i[k_{x,0}x - k_{y1,0}(y - h/2)]\}$$

$$+ \sum_{n=-\infty}^{\infty} r_n \exp\{i[k_{x,n}x + k_{y1,n}(y - h/2)]\} \quad \text{for } y \geq h/2, \quad \text{(B-1)}$$

$$f_z(x,y) = \sum_{n=-\infty}^{\infty} t_n \exp\{i[k_{x,n}x - k_{y3,n}(y + h/2)]\} \quad \text{for } y \leq -h/2, \quad \text{(B-2)}$$

where $k_{x,n} = \sqrt{\varepsilon_1}k_0\sin\theta + n(2\pi/p)$, $k_{yi,n} = (\varepsilon_i k_0^2 - k_{x,n}^2)^{1/2}$, $k_0 = 2\pi/\lambda$ and i corresponds to the ith region. Inside the apertures, the field is expressed as a sum of waveguide modes:

$$f_z(x,y) = \sum_{m=0}^{\infty} X_m(x)[a_m \exp(i\beta_m y) + b_m \exp(-i\beta_m y)] \quad \text{for } -h/2 \leq y \leq h/2. \quad \text{(B-3)}$$

where

$$X_m(x) = \begin{cases} \cos(\mu_m x) + \sin(\mu_m x)\eta_2/\mu_m & \text{for TM polarization} \\ \eta\cos(\mu_m x) + \sin(\mu_m x)/\mu_m & \text{for TE polarization} \end{cases}, \quad \text{(B-4)}$$

$$\begin{cases} \eta_i = -i\varepsilon_i k_0/\sqrt{\varepsilon_m} & \text{for TM polarization} \\ \eta = i/(k_0\sqrt{\varepsilon_m}) & \text{for TE polarization} \end{cases}, \quad \text{(B-5)}$$

where i corresponds to the ith region. The mode equation is given by:

$$\tan(\mu_m w) = \begin{cases} 2\eta\mu_m/(\mu_m^2 - \eta^2) & \text{for TM polarization} \\ 2\eta\mu_m/[(\mu_m\eta)^2 - 1] & \text{for TE polarization} \end{cases}. \quad \text{(B-6)}$$

The continuity of the tangential components of the fields described above is then imposed at each interface. The equations obtained below are obtained following the procedure described by Lochbihler and Depine in Ref. [72]. For TM polarization, the following set of equations is obtained:

$$I_j[a_j \exp(i\beta_j h/2) + b_j \exp(-i\beta_j h/2)] = \sum_{n=-\infty}^{\infty} (r_n + \delta_{n,0})K_{j,n}, \quad \text{(B-7a)}$$

$$I_j[a_j \exp(-i\beta_j h/2) + b_j \exp(i\beta_j h/2)] = \sum_{n=-\infty}^{\infty} t_n K_{j,n}, \quad \text{(B-8a)}$$

$$ik_{y1,q}\left(r_q - \delta_{q,0}\right) = i\frac{\varepsilon_1}{\varepsilon_2}\sum_{m=0}^{\infty}\beta_m\left[a_m\exp(i\beta_m h/2) - b_m\exp(-i\beta_m h/2)\right]J_{q,m}$$

$$+\eta_1\sum_{n=-\infty}^{\infty}\left(r_n + \delta_{n,0}\right)Q_{q,n}\,,\tag{B-9a}$$

$$ik_{y3,q}t_q = -i\frac{\varepsilon_3}{\varepsilon_2}\sum_{m=0}^{\infty}\beta_m\left[a_m\exp(-i\beta_m h/2) - b_m\exp(i\beta_m h/2)\right]J_{q,m} + \eta_3\sum_{n=-\infty}^{\infty}t_n Q_{q,n}\,,\tag{B-10a}$$

whereas the equations obtained for TE polarization are:

$$I_j\beta_j\left[a_j\exp(i\beta_j h/2) - b_j\exp(-i\beta_j h/2)\right] = \sum_{n=-\infty}^{\infty}k_{y1,n}\left(r_n + \delta_{n,0}\right)K_{j,n}\,,\tag{B-7b}$$

$$I_j\beta_j\left[a_j\exp(-i\beta_j h/2) - b_j\exp(i\beta_j h/2)\right] = -\sum_{n=-\infty}^{\infty}k_{y3,n}t_n K_{j,n}\,,\tag{B-8b}$$

$$r_q - \delta_{q,0} = \sum_{m=0}^{\infty}\left[a_m\exp(i\beta_m h/2) + b_m\exp(-i\beta_m h/2)\right]J_{q,m}$$

$$+i\eta\sum_{n=-\infty}^{\infty}k_{y1,n}\left(r_n - \delta_{n,0}\right)Q_{q,n}\,,\tag{B-9b}$$

$$t_q = \sum_{m=0}^{\infty}\left[a_m\exp(-i\beta_m h/2) + b_m\exp(i\beta_m h/2)\right]J_{q,m} + i\eta\sum_{n=-\infty}^{\infty}k_{y3,n}t_n Q_{q,n}\,.\tag{B-10b}$$

where the overlap integrals are defined by:

$$I_j = \int_0^w X_j(x)X_j(x)dx = \begin{cases}\left[1 + \left(\eta_2/\mu_j\right)^2\right]w/2 + \eta_2/\left(\mu_j^2\right) & \text{for TM polarization}\\\left[\eta^2 + \left(1/\mu_j\right)^2\right]w/2 + \eta/\left(\mu_j^2\right) & \text{for TE polarization}\end{cases}\,,\tag{B-11}$$

$$K_{j,n} = \int_0^w \exp(ik_{x,n}x)X_j(x)dx\,,\tag{B-12}$$

$$J_{q,m} = 1/p\int_0^w \exp(-ik_{x,q}x)X_m(x)dx\,,\tag{B-13}$$

$$Q_{q,n} = 1/p\int_0^w \exp\left[i\left(k_{x,n} - k_{x,q}\right)x\right]dx\,.\tag{B-14}$$

The calculation of the unknown coefficients r_n, t_n, a_m and b_m is then performed after truncation and writing Eq. (B-7), (B-8), (B-9), (B-10) into a matrix equation. As an example, the matrix equation is written for TM:

$$M\Psi = \Omega. \tag{B-15}$$

where

$$\Psi = \begin{pmatrix} a_0 \\ \vdots \\ a_m \\ b_0 \\ \vdots \\ b_m \\ r_{-n} \\ \vdots \\ r_n \\ t_{-n} \\ \vdots \\ t_n \end{pmatrix} \quad \text{and} \quad \Omega = \begin{pmatrix} -K_{0,0} \\ \vdots \\ -K_{m,0} \\ 0 \\ \vdots \\ 0 \\ k_{y1,-n}\delta_{-n,0} - i\eta_1 Q_{-n,0} \\ \vdots \\ k_{y1,n}\delta_{n,0} - i\eta_1 Q_{n,0} \\ 0 \\ \vdots \\ 0 \end{pmatrix} \tag{B-16}$$

and the matrix M is shown in the following page due to space reasons.

$$
\left(
\begin{array}{cccccccccc}
-I_0 e^{i\beta_0 h/2} & 0 & -I_0 e^{-i\beta_0 h/2} & 0 & K_{j,-n} & \cdots & K_{j,n} & 0 & \cdots & 0 \\
& \ddots & & \ddots & \vdots & \ddots & \vdots & \vdots & \ddots & \vdots \\
0 & -I_m e^{i\beta_m h/2} & 0 & -I_0 e^{-i\beta_j h/2} & K_{j,-n} & \cdots & K_{j,n} & 0 & \cdots & 0 \\
-I_0 e^{-i\beta_0 h/2} & 0 & -I_0 e^{i\beta_0 h/2} & 0 & 0 & \cdots & 0 & K_{j,-n} & \cdots & K_{j,-n} \\
& \ddots & & \ddots & \vdots & \ddots & \vdots & \vdots & \ddots & \vdots \\
0 & -I_m e^{-i\beta_m h/2} & 0 & -I_m e^{i\beta_m h/2} & 0 & \cdots & 0 & K_{j,n} & \cdots & K_{j,n} \\
-\dfrac{\varepsilon_1}{\varepsilon_2}\beta_0 J_{-n,0} e^{i\beta_0 h/2} & \cdots & -\dfrac{\varepsilon_1}{\varepsilon_2}\beta_m J_{-n,m} e^{i\beta_m h/2} & \dfrac{\varepsilon_1}{\varepsilon_2}\beta_0 J_{-n,0} e^{-i\beta_0 h/2} & \cdots & \dfrac{\varepsilon_1}{\varepsilon_2}\beta_m J_{-n,m} e^{-i\beta_m h/2} & k_{y1,-n}+i\eta_1 Q_{-n,-n} & \cdots & i\eta_1 Q_{-n,n} & 0 & \cdots & 0 \\
\vdots & \ddots & \vdots & \vdots & \ddots & \vdots & \vdots & \ddots & \vdots & \vdots & \ddots & \vdots \\
-\dfrac{\varepsilon_1}{\varepsilon_2}\beta_0 J_{n,0} e^{i\beta_0 h/2} & \cdots & -\dfrac{\varepsilon_1}{\varepsilon_2}\beta_m J_{n,m} e^{i\beta_m h/2} & \dfrac{\varepsilon_1}{\varepsilon_2}\beta_0 J_{n,0} e^{-i\beta_0 h/2} & \cdots & \dfrac{\varepsilon_1}{\varepsilon_2}\beta_m J_{n,m} e^{-i\beta_m h/2} & i\eta_1 Q_{n,-n} & \cdots & k_{y1,n}+i\eta_1 Q_{n,n} & 0 & \cdots & 0 \\
\dfrac{\varepsilon_3}{\varepsilon_2}\beta_0 J_{-n,0} e^{-i\beta_0 h/2} & \cdots & \dfrac{\varepsilon_3}{\varepsilon_2}\beta_m J_{-n,m} e^{-i\beta_m h/2} & -\dfrac{\varepsilon_3}{\varepsilon_2}\beta_0 J_{-n,0} e^{i\beta_0 h/2} & \cdots & -\dfrac{\varepsilon_3}{\varepsilon_2}\beta_m J_{-n,m} e^{i\beta_m h/2} & 0 & \cdots & 0 & k_{y3,-n}+i\eta_3 Q_{-n,-n} & \cdots & i\eta_3 Q_{-n,n} \\
\vdots & \ddots & \vdots & \vdots & \ddots & \vdots & \vdots & \ddots & \vdots & \vdots & \ddots & \vdots \\
\dfrac{\varepsilon_3}{\varepsilon_2}\beta_0 J_{n,0} e^{i\beta_0 h/2} & \cdots & \dfrac{\varepsilon_3}{\varepsilon_2}\beta_m J_{n,m} e^{-i\beta_m h/2} & -\dfrac{\varepsilon_3}{\varepsilon_2}\beta_0 J_{n,0} e^{i\beta_0 h/2} & \cdots & -\dfrac{\varepsilon_3}{\varepsilon_2}\beta_m J_{n,m} e^{i\beta_m h/2} & 0 & \cdots & 0 & i\eta_3 Q_{n,-n} & \cdots & k_{y3,n}+i\eta_3 Q_{n,n}
\end{array}
\right)
$$

Figure B.2.   The Matrix M in Eq. (B-15)

Appendix C

Analytical formulas for the transmission and reflection coefficients of single interfaces in slit arrays

The simplifications made in Section 3.2.2.1 can be used to express the transmission and reflection coefficients of each interface, see the schematic diagram of Fig. C.1 for a symmetric structure (i.e. $\varepsilon_t = \varepsilon_b$).
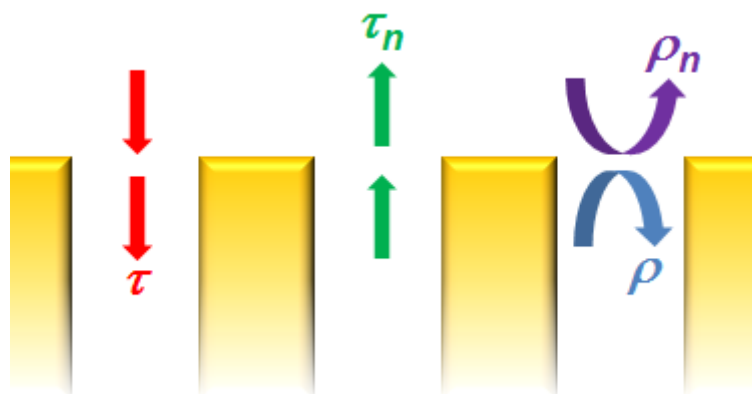
Figure C.1.   Isolated single interface of a slit array with the definition of the transmission and reflection coefficients.

The quantities τ and τ_n are the transmission coefficients of the incident light into the fundamental slit mode and the fundamental slit mode into the transmitted diffracted order n respectively. ρ and ρ_n are the reflection coefficients of respectively the fundamental slit mode and the incident light into the reflected order n.

A procedure analogous to the one used in Ref. [148] is followed to determine the reflection and transmission coefficients. Setting $a_0 = 0$ and $b_0 e^{-\varphi} = \tau$, Eq. (3.2-15) leads to:

$$\tau = \frac{2K_{0,0}\alpha_0 k_{y,0}/\beta_0}{\sum\limits_{n=-\infty}^{\infty} N_n + N_{slit}}.$$ (C-1)

Similarly with $a_0 e^{-\varphi} = \rho$ and $b_0 e^{\varphi} = 1$, Eq. (3.2-16) gives:

$$\rho = \frac{\sum\limits_{n=-\infty}^{\infty} N_n - N_{slit}}{\sum\limits_{n=-\infty}^{\infty} N_n + N_{slit}}.$$ (C-2)

Note the similarity between the two above equations and the one giving the Fresnel transmission and reflection coefficient of single interfaces (cf. Section 2.2.4). In the present case of a symmetric structure, and for a grating of height h, r_n and t_n are expressed as a typical FP equations for a three layer system (cf. Section 2.2.4):

$$r_n = \rho_n + \frac{\rho\tau\tau_n e^{i4\varphi}}{1-\rho^2 e^{i4\varphi}},$$ (C-3)

$$t_n = \frac{\tau\tau_n e^{i2\varphi}}{1-\rho^2 e^{i4\varphi}},$$ (C-4)

and the coefficients a_0 and b_0 can be similarly obtained as:

$$a_0 = \frac{\tau\rho e^{i3\varphi}}{1-\rho^2 e^{i4\varphi}},$$ (C-5)

$$b_0 = \frac{\tau e^{i\varphi}}{1-\rho^2 e^{i4\varphi}}.$$ (C-6)

Replacing r_n, t_n, a_0 and b_0 in Eq. (3.2-13) and (3.2-14) leads to:

$$\tau_n = \frac{2I_0 J_{n,0}\alpha_n}{\sum\limits_{n=-\infty}^{\infty} N_n + N_{slit}},$$ (C-7)

$$\rho_n = \delta_{n,0}\left(k_{y,0} - i\eta Q\right)\alpha_0 - \frac{2J_{n,0}\alpha_n K_{0,0}\alpha_0 k_{y,0}}{\sum\limits_{n=-\infty}^{\infty} N_n + N_{slit}}.$$ (C-8)

Equation (3.2-17) is obtained replacing in Eq. (C-4) the coefficients of single interfaces. This derivation emphasize that a slit array can be considered as a FP cavity. Whereas in conventional FP cavities the optical properties are determined from the reflection/transmission coefficients at each interface, effective reflection/transmission coefficients are defined here at the slit extremities. These coefficients have the particularity to be dependent on the array periodicity.

References

1. http://www.britishmuseum.org/, 2010.

2. M. Faraday, "The Bakerian lecture: experimental relations of gold (and other metals) to light," Philosophical Transactions of the Royal Society of London **147,** 145-181 (1857).

3. G. Mie, "Beiträge zur Optik trüber Medien, speziell kolloidaler Metallösungen," Annalen der Physik **330,** 377-445 (2006).

4. D. Bohm and D. Pines, "A collective description of electron interactions. I. Magnetic interactions," Physical Review **82,** 625-634 (1951).

5. D. Pines and D. Bohm, "A collective description of electron interactions: II. Collective vs individual particle aspects of the interactions," Physical Review **85,** 338-353 (1952).

6. D. Bohm and D. Pines, "A collective description of electron interactions: III. Coulomb interactions in a degenerate electron gas," Physical Review **92,** 609-625 (1953).

7. D. Pines, "A collective description of electron interactions: IV. electron interaction in metals," Physical Review **92,** 626-636 (1953).

8. C. J. Powell and J. B. Swan, "Effect of oxidation on the characteristic loss spectra of aluminum and magnesium," Physical Review **118,** 640-643 (1960).

9. R. H. Ritchie, "Plasma losses by fast electrons in thin films," Physical Review **106,** 874-881 (1957).

10. R. W. Wood, "On a Remarkable Case of Uneven Distribution of Light in a Diffraction Grating Spectrum," Proceedings of the Physical Society of London **18,** 269-275 (1902).

11. A. Hessel and A. A. Oliner, "A new theory of Wood's anomalies on optical gratings," Applied Optics. **4,** 1275-1297 (1965).

12. H. Raether, *Surface Plasmons on Smooth and Rough Surfaces and on Gratings, Vol. 111 of Springer Tracts in Modern Physics* (Springer-Verlag, Berlin, 1988).

13. B. Liedberg, C. Nylander, and I. Lunström, "Surface plasmon resonance for gas detection and biosensing," Sensors and Actuators **4,** 299-304 (1983).

14. W. L. Barnes, Alain Dereux, and T. W. Ebbesen, "Surface plasmon subwavelength optics," Nature **424,** 824-830 (2003).

15. P. Berini, "Plasmon-polariton waves guided by thin lossy metal films of finite width: Bound modes of symmetric structures," Physical Review B **61,** 10484-10503 (2000).

16. B. Lamprecht, J. R. Krenn, G. Schider, H. Ditlbacher, M. Salerno, N. Felidj, A. Leitner, F. R. Aussenegg, and J. C. Weeber, "Surface plasmon propagation in microscale metal stripes," Applied physics letters **79,** 51 (2001).

17. J. C. Weeber, J. R. Krenn, A. Dereux, B. Lamprecht, Y. Lacroute, and J. P. Goudonnet, "Near-field observation of surface plasmon polariton propagation on thin metal stripes," Physical Review B **64,** 45411 (2001).

18. J. C. Weeber, Y. Lacroute, and A. Dereux, "Optical near-field distributions of surface plasmon waveguide modes," Physical Review B **68,** 115401 (2003).

19. S. I. Bozhevolnyi, V. S. Volkov, E. Devaux, and T. W. Ebbesen, "Channel plasmon-polariton guiding by subwavelength metal grooves," Physical Review Letters. **95,** 46802 (2005).

20. I. V. Novikov and A. A. Maradudin, "Channel polaritons," Physical Review B **66,** 35403 (2002).

21. M. Quinten, A. Leitner, J. R. Krenn, and F. R. Aussenegg, "Electromagnetic energy transport via linear chains of silver nanoparticles," Optics Letters **23,** 1331-1333 (1998).

22. S. A. Maier, P. G. Kik, H. A. Atwater, S. Meltzer, E. Harel, B. E. Koel, and A. A. G. Requicha, "Local detection of electromagnetic energy transport below the diffraction limit in metal nanoparticle plasmon waveguides," Nature Materials **2,** 229-232 (2003).

23. H. Ditlbacher, A. Hohenau, D. Wagner, U. Kreibig, M. Rogers, F. Hofer, F. R. Aussenegg, and J. R. Krenn, "Silver nanowires as surface plasmon resonators," Physical Review Letters. **95,** 257403 (2005).

24. M. U. Gonzalez, J. C. Weeber, A. L. Baudrion, A. Dereux, A. L. Stepanov, J. R. Krenn, E. Devaux, and T. W. Ebbesen, "Design, near-field characterization, and modeling of 45° surface-plasmon Bragg mirrors," Physical Review B **73,** 155416 (2006).

25. A. Hohenau, J. R. Krenn, A. L. Stepanov, A. Drezet, H. Ditlbacher, B. Steinberger, A. Leitner, and F. R. Aussenegg, "Dielectric optical elements for surface plasmons," Optics Letters **30,** 893-895 (2005).

26. A. Drezet, D. Koller, A. Hohenau, A. Leitner, F. R. Aussenegg, and J. R. Krenn, "Plasmonic crystal demultiplexer and multiports," Nano letters **7,** 1697-1700 (2007).

References

27. S. I. Bozhevolnyi, V. S. Volkov, E. Devaux, J. Y. Laluet, and T. W. Ebbesen, "Channel plasmon subwavelength waveguide components including interferometers and ring resonators," Nature **440,** 508-511 (2006).

28. H. Ditlbacher, J. R. Krenn, G. Schider, A. Leitner, and F. R. Aussenegg, "Two-dimensional optics with surface plasmon polaritons," Applied physics letters **81,** 1762 (2002).

29. K. A. Willets and R. P. Van Duyne, "Localized surface plasmon resonance spectroscopy and sensing," *Annual* Review of Physical Chemistry **58,**267-297 (2007).

30. http://www.biacore.com/lifesciences/index.html, 2010.

31. C. E. Talley, J. B. Jackson, C. Oubre, N. K. Grady, C. W. Hollars, S. M. Lane, T. R. Huser, P. Nordlander, and N. J. Halas, "Surface-enhanced Raman scattering from individual Au nanoparticles and nanoparticle dimer substrates," Nano letters **5,** 1569-1574 (2005).

32. M. G. Albrecht and J. A. Creighton, "Anomalously intense Raman spectra of pyridine at a silver electrode," Journal of the American Chemical Society **99,** 5215-5217 (1977).

33. D. L. Jeanmaire and R. P. Van Duyne, "Surface raman spectroelectrochemistry:: Part I. Heterocyclic, aromatic, and aliphatic amines adsorbed on the anodized silver electrode," Journal of electroanalytical chemistry **84,** 1-20 (1977).

34. S. Lal, S. Link, and N. J. Halas, "Nano-optics from sensing to waveguiding," Nature Photonics **1,** 641-648 (2007).

35. F. Le, D. W. Brandl, Y. A. Urzhumov, H. Wang, J. Kundu, N. J. Halas, J. Aizpurua, and P. Nordlander, "Metallic nanoparticle arrays: A common substrate for both surface-enhanced Raman scattering and surface-enhanced infrared absorption," ACS nano **2,** 707-718 (2008).

36. A. M. Gobin, M. H. Lee, N. J. Halas, W. D. James, R. A. Drezek, and J. L. West, "Near-infrared resonant nanoshells for combined optical imaging and photothermal cancer therapy," Nano letters**7,** 1929-1934 (2007).

37. L. R. Hirsch, R. J. Stafford, J. A. Bankson, S. R. Sershen, B. Rivera, R. E. Price, J. D. Hazle, N. J. Halas, and J. L. West, "Nanoshell-mediated near-infrared thermal therapy of tumors under magnetic resonance guidance," Proceedings of the National Academy of Sciences of the United States of America **100,** 13549 (2003).

38. N. Fang, H. Lee, C. Sun, and X. Zhang, "Sub-diffraction-limited optical imaging with a silver superlens," Science **308,** 534 (2005).

39. J. B. Pendry, "Negative refraction makes a perfect lens," Physical Review Letters. **85,** 3966-3969 (2000).

40. H. J. Lezec, J. A. Dionne, and H. A. Atwater, "Negative refraction at visible frequencies," Science **316,** 430 (2007).

41. T. V. Teperik, F. J. Garcia de Abajo, A. G. Borisov, M. Abdelsalam, P. N. Bartlett, Y.

Sugawara, and J. J. Baumberg, "Omnidirectional absorption in nanostructured metal surfaces," Nature Photonics **2,** 299-301 (2008).

42. T. W. Ebbesen, H. J. Lezec, H. F. Ghaemi, T. Thio, and P. A. Wolff, "Extraordinary optical transmission through sub-wavelength hole arrays," Nature **391,** 667-669 (1998).

43. E. Popov, M. Neviere, S. Enoch, and R. Reinisch, "Theory of light transmission through subwavelength periodic hole arrays," Physical Review B **62,** 16100-16108 (2000).

44. L. Martin-Moreno, F. J. Garcia-Vidal, H. J. Lezec, K. M. Pellerin, T. Thio, J. B. Pendry, and T. W. Ebbesen, "Theory of extraordinary optical transmission through subwavelength hole arrays," Physical Review Letters. **86,** 1114-1117 (2001).

45. J. B. Pendry, L. Martin-Moreno, and F. J. Garcia-Vidal, "Mimicking surface plasmons with structured surfaces," Science **305,** 847-848 (2004).

46. E. Moreno, L. Martin-Moreno, and F. J. Garcia-Vidal, "Extraordinary optical transmission without plasmons: the s-polarization case," Journal of Optics A: Pure and Applied Optics **8,** 94 (2006).

47. F. J. G. de Abajo, "Colloquium: Light scattering by particle and hole arrays," Reviews of Modern Physics **79,** 1267 (2007).

48. C. Genet and T. W. Ebbesen, "Light in tiny holes," Nature **445,** 39-46 (2007).

49. A. Degiron and T. W. Ebbesen, "The role of localized surface plasmon modes in the enhanced transmission of periodic subwavelength apertures," Journal of Optics A: Pure and Applied Optics **7,** S90-S96 (2005).

50. K. L. Van der Molen, K. J. Klein Koerkamp, S. Enoch, F. B. Segerink, N. F. Van Hulst, and L. Kuipers, "Role of shape and localized resonances in extraordinary transmission through periodic arrays of subwavelength holes: Experiment and theory," Physical Review B **72,** 45421 (2005).

51. F. J. Garcia-Vidal and L. Martin-Moreno, "Transmission and focusing of light in one-dimensional periodically nanostructured metals," Physical Review B **66,** 155412 (2002).

52. F. J. Garcia-Vidal, H. J. Lezec, T. W. Ebbesen, and L. Martin-Moreno, "Multiple paths to enhance optical transmission through a single subwavelength slit," Physical Review Letters. **90,** 213901 (2003).

53. D. E. Grupp, H. J. Lezec, T. Thio, and T. W. Ebbesen, "Beyond the Bethe limit: Tunable enhanced light transmission through a single sub-wavelength aperture," Advanced Materials **11,** 860 (1999).

54. H. Lezec and T. Thio, "Diffracted evanescent wave model for enhanced and suppressed optical transmission through subwavelength hole arrays," Optics Express. **12,** 3629-3651 (2004).

55. Data may be retrieved at http://www.sspectra.com/sopra.html, 2010.

References

56. E. J. Zeman and G. C. Schatz, "An accurate electromagnetic theory study of surface enhancement factors for Ag, Au, Cu, Li, Na, Al, Ga, in, Zn, and Cd," Journal of physical chemistry **91,** 634-643 (1987).

57. C. F. Bohren and D. R. Huffman, "Absorption and scattering of light by small particles," New York (1983).

58. A. Vial, A. S. Grimault, D. Macias, D. Barchiesi, and M. L. La Chapelle, "Improved analytical fit of gold dispersion: Application to the modeling of extinction spectra with a finite-difference time-domain method," Physical Review B **71,** 85416 (2005).

59. E. Hecht, "The propagation of light" in *Optics*, Addison Wesley Longman, ed. (Addison Wesley Longman, 1998).

60. Born, M. and Wolf, E. Principles of Optics, seventh (expanded) ed. 1999. Cambridge University Press, Cambridge.

61. H. A. Macleod, "Thin Film Optical Filters," Bristol, UK (1986).

62. W. L. Barnes, "Surface plasmon polariton length scales: a route to sub-wavelength optics," Journal of Optics A: Pure and Applied Optics **8,** S87-S93 (2006).

63. A. Yariv, *Optical electronics in modern communications* (Oxford University Press, USA, 2007).

64. S. Collin, F. Pardo, and J. L. Pelouard, "Waveguiding in nanoscale metallic apertures," Science **305,** 847 (2004).

65. M. J. Adams, *An introduction to optical waveguides* (Wiley New York, 1981).

66. Y. Takakura, "Optical Resonance in a Narrow Slit in a Thick Metallic Screen," Physical Review Letters. **86,** 5601-5603 (2001).

67. R. Gordon, "Light in a subwavelength slit in a metal: Propagation and reflection," Physical Review B **73,** 153405 (2006).

68. J. Bravo-Abad, L. Martin-Moreno, and F. J. Garcia-Vidal, "Transmission properties of a single metallic slit: from the subwavelength regime to the geometrical-optics limit," Physical Review E **69,** 26601 (2004).

69. A. Yu. Nikitin, F. J. Garcia-Vidal, and L. Martin-Moreno, "Enhanced optical transmission, beaming and focusing through a subwavelength slit under excitation of dielectric waveguide modes," Journal of Optics A: Pure and Applied Optics **11,** 125702 (2009).

70. O. T. A. Janssen, H. P. Urbach, and G. W. 't Hooft, "Giant optical transmission of a subwavelength slit optimized using the magnetic field phase," Physical Review Letters. **99,** 43902 (2007).

71. H. J. Lezec, A. Degiron, E. Devaux, R. A. Linke, L. Martin-Moreno, F. J. Garcia-Vidal, and T. W. Ebbesen, "Beaming light from a subwavelength aperture," Science **297,** 820-822 (2002).

References

72. H. Lochbihler and R. A. Depine, "Highly conducting wire gratings in the resonance region," Applied Optics. **32,** 3459-19 (1993).

73. Several codes are commercially available. During the present thesis, Omnisim from Photon Design has been used. More informations can be found at http://www.photond.com/products/omnisim.htm, 2010.

74. L. C. Botten, M. S. Craig, R. C. McPhedran, J. L. Adams, and J. R. Andrewartha, "The finitely conducting lamellar diffraction grating," Journal of Modern Optics **28,** 1087-1102 (1981).

75. R. A. Depine, "Perfectly conducting diffraction grating formalisms extended to good conductors via the surface impedance boundary condition," Applied Optics. **26,** 2348-2354 (1987).

76. M. Guillaumée, L. A. Dunbar, C. Santschi, E. Grenet, R. Eckert, O. J. F. Martin, and R. P. Stanley, "Polarization sensitive silicon photodiodes using nanostructured metallic grids," Applied Physics Letters **94,** 193503 (2009).

77. The commercially available software GSolver has been used. More informations can be found at http://www.gsolver.com/, 2010.

78. Data may be retrieved at http://www.sopra-sa.com, 2008.

79. S. Collin, F. Pardo, R. Teissier, and J. L. Pelouard, "Strong discontinuities in the complex photonic band structure of transmission metallic gratings," Physical Review B **63,** 33107 (2001).

80. E. Popov, M. Neviere, S. Enoch, and R. Reinisch, "Theory of light transmission through subwavelength periodic hole arrays," Physical Review B **62,** 16100-16108 (2000).

81. J. A. Porto, F. J. Garcia-Vidal, and J. B. Pendry, "Transmission resonances on metallic gratings with very narrow slits," Physical Review Letters. **83,** 2845-2848 (1999).

82. S. Astilean, P. Lalanne, and M. Palamaru, "Light transmission through metallic channels much smaller than the wavelength," Optics Communications **175,** 265-273 (2000).

83. D. Crouse and P. Keshavareddy, "Role of optical and surface plasmon modes in enhanced transmission and applications," Optics Express. **13,** 7760-7771 (2005).

84. F. Marquier, J. J. Greffet, S. Collin, F. Pardo, and J. L. Pelouard, "Resonant transmission through a metallic film due to coupled modes," Optics Express. **209,** 17 (2002).

85. Q. Cao and P. Lalanne, "Negative role of surface plasmons in the transmission of metallic gratings with very narrow slits," Physical Review Letters. **88,** 57403 (2002).

86. Y. Xie, A. Zakharian, J. Moloney, and M. Mansuripur, "Transmission of light through a periodic array of slits in a thick metallic film," Optics Express. **13,** 4485-4491 (2005).

87. N. Garcia and M. Nieto-Vesperinas, "Theory of electromagnetic wave transmission through metallic gratings of subwavelength slits," Journal of Optics A: Pure and Applied

Optics **9,** 490-495 (2007).

88. P. Lalanne, C. Sauvan, J. P. Hugonin, J. C. Rodier, and P. Chavel, "Perturbative approach for surface plasmon effects on flat interfaces periodically corrugated by subwavelength apertures," Physical Review B **68,** 125404 (2003).

89. Rayleigh, Lord. On the dynamical theory of gratings. 79, 399-416. 1907. London, Proceedings of the Royal Society

90. C. C. Chen, "Transmission of microwave through perforated flat plates of finite thickness," IEEE Transactions on Microwave Theory and Techniques **21,** 1-6 (1973).

91. L. Martin-Moreno and F. J. Garcia-Vidal, "Minimal model for optical transmission through holey metal films," Journal of Physics, Condensed Matter **20,** (2008).

92. K. G. Lee and Q. H. Park, "Coupling of surface plasmon polaritons and light in metallic nanoslits," Physical Review Letters. **95,** 103902 (2005).

93. F. Leon-Perez, G. Brucoli, F. J. Garcia-Vidal, and L. Martin-Moreno, "Theory on the scattering of light and surface plasmon polaritons by arrays of holes and dimples in a metal film," New Journal of Physics **10,** 105017 (2008).

94. B. Sturman, E. Podivilov, and M. Gorkunov, "Theory of extraordinary light transmission through arrays of subwavelength slits," Physical Review B **77,** 75106 (2008).

95. A. Hoffmann, Z. Lenkefi, and Z. Szentirmay, "Effect of roughness on surface plasmon scattering in gold films," Journal of Physics: Condensed Matter **10,** 5503-5513 (1998).

96. S. Rubanov and P. R. Munroe, "FIB-induced damage in silicon," Journal of Microscopy **214,** 213-221 (2004).

97. J. Schrauwen, D. Van Thourhout, and R. Baets, "Focused-ion-beam fabricated vertical fiber couplers on silicon-on-insulator waveguides," Applied physics letters **89,** 141102 (2006).

98. Y. Pang, C. Genet, and T. W. Ebbesen, "Optical transmission through subwavelength slit apertures in metallic films," Optics Communications **280,** 10-15 (2007).

99. L. A. Dunbar, M. Guillaumée, F. Leon-Perez, C. Santschi, E. Grenet, R. Eckert, F. Lopez-Tejeira, F. J. Garcia-Vidal, L. Martin-Moreno, and R. P. Stanley, "Enhanced transmission from a single subwavelength slit aperture surrounded by grooves on a standard detector," Applied physics letters **95,** 011113 (2009).

100. F. Lopez-Tejeira, F. J. Garcia-Vidal, and L. Martin-Moreno, "Scattering of surface plasmons by one-dimensional periodic nanoindented surfaces," Physical Review B **72,** 161405 (2005).

101. N. Yu, Q. J. Wang, C. Pfl³gl, L. Diehl, F. Capasso, T. Edamura, S. Furuta, M. Yamanishi, and H. Kan, "Semiconductor lasers with integrated plasmonic polarizers," Applied Physics Letters **94,** 151101 (2009).

102. T. Ishi, J. Fujikata, K Makita, T. Babat, and K Ohashi, "Si nano-photodiode with a surface plasmon antenna," Japanese Journal of Applied Physics **44,** L364-L366 (2005).

103. D. B. Shao and S. C. Chen, "Surface-plasmon-assisted nanoscale photolithography by polarized light," Applied physics letters **86,** 253107 (2005).

104. W. Srituravanich, L. Pan, Y. Wang, C. Sun, D. B. Bogy, and X. Zhang, "Flying plasmonic lens in the near field for high-speed nanolithography," Nature Nanotechnology **3,** 733-737 (2008).

105. N. Yu, J. Fan, Q. J. Wang, C. Pfl³gl, L. Diehl, T. Edamura, M. Yamanishi, H. Kan, and F. Capasso, "Small-divergence semiconductor lasers by plasmonic collimation," Nature Photonics **2,** 564-570 (2008).

106. N. Yu, R. Blanchard, J. Fan, F. Capasso, T. Edamura, M. Yamanishi, and H. Kan, "Small divergence edge-emitting semiconductor lasers with two-dimensional plasmonic collimators," Applied physics letters **93,** 181101 (2008).

107. A. G. Brolo, R. Gordon, B. Leathem, and K. L. Kavanaghs, "Surface plasmon sensor based on the enhanced light transmission through arrays of nanoholes in gold films," Langmuir **20,** 4813-4815 (2004).

108. B. Liedberg, C. Nylander, and I. Lunstr÷m, "Surface plasmon resonance for gas detection and biosensing* 1," Sensors and Actuators **4,** 299-304 (1983).

109. J. Homola, S. S. Yee, and G. Gauglitz, "Surface plasmon resonance sensors: review," Sensors & Actuators: B. Chemical **54,** 3-15 (1999).

110. A. De Leebeeck, L. K. S. Kumar, V. de Lange, D. Sinton, R. Gordon, and A. G. Brolo, "On-chip surface-based detection with nanohole arrays," Analytical Chemistry **79,** 4094-4100 (2007).

111. R. Seitz, R. Brings, and R. Geiger, "Protein adsorption on solidûliquid interfaces monitored by laser-ellipsometry," Applied Surface Science **252,** 154-157 (2005).

112. http://www.dow.com/glycerine/resources/table12_020.htm, 2010.

113. K. L. Lee, W. S. Wang, and P. K. Wei, "Comparisons of Surface Plasmon Sensitivities in Periodic Gold Nanostructures," Plasmonics **3,** 119-125 (2008).

114. A. A. Yanik, M. Huang, A. Artar, T. Y. Chang, and H. Altug, "Integrated nanoplasmonic-nanofluidic biosensors with targeted delivery of analytes," Applied physics letters **96,** 021101 (2010).

115. Klein M.J.K, M. Guillaumée, Wenger B., L. A. Dunbar, Brugger J., Heinzelmann H., and Pugin R., "Inexpensive and fast wafer-scale fabrication of nanohole arrays in thin gold films for plasmonics," Nanotechnology (under review) (2010).

116. http://www.electrooptics.com/features/junjul06/junjul06leds.html, "LED there be light", 2010.

117. http://lighting.sandia.gov/lightingdocs/OIDA_SSL_Roadmap_Summary_2002.pdf, "The

promise of solid state lighting for general illumination", 2010.

118. Joray, R. *Microcavity light emitting diodes in the visible red and near infrared wavelength range*, Ph.D. thesis, Swiss Federal Institute of Technology, Lausanne (EPFL), 2004.

119. http://en.wikipedia.org/wiki/Light-emitting_diode, "Light-emitting diode", 2010.

120. C. Liu, V. Kamaev, and Z. V. Vardeny, "Efficiency enhancement of an organic light-emitting diode with a cathode forming two-dimensional periodic hole array," Applied physics letters **86,** 143501 (2005).

121. C. J. Nuese, J. J. Tietjen, J. J. Gannon, and H. F. Gossenberger, "Optimization of Electroluminescent Efficiencies for Vapor Grown GaAsP Diodes," Journal of The Electrochemical Society **116,** 248 (1969).

122. M. R. Krames, G. E. H÷fler, E. I. Chen, I. H. Tan, P. Grillot, N. F. Gardner, H. C. Chui, J. W. Huang, S. A. Stockman, and F. A. Kish, "High power truncated inverted pyramid AlxGa12x. 0.5 In0. 5P/GaP light-emitting diodes exhibiting> 50% external quantum efficiency," Applied physics letters **75,** 2365 (1999).

123. E. F. Schubert, Y. H. Wang, A. Y. Cho, L. W. Tu, and G. J. Zydzik, "Resonant cavity light emitting diode," Applied physics letters **60,** 921 (1992).

124. J. Vuckovic, M. Loncar, and A. Scherer, "Surface plasmon enhanced light-emitting diode," IEEE Journal of Quantum Electronics **36,** 1131-1144 (2000).

125. W. L. Barnes, "Electromagnetic crystals for surface plasmon polaritons and the extraction of light from emissive devices," Journal of Lightwave technology **17,** 2170 (1999).

126. D. M. Koller, A. Hohenau, H. Ditlbacher, N. Galler, F. Reil, F. R. Aussenegg, A. Leitner, E. J. W. List, and J. R. Krenn, "Organic plasmon-emitting diode," Nature Photonics **2,** 684-687 (2008).

127. D. M. Koller, A. Hohenau, H. Ditlbacher, N. Galler, F. R. Aussenegg, A. Leitner, J. R. Krenn, S. Eder, S. Sax, and E. J. W. List, "Surface plasmon coupled electroluminescent emission," Applied physics letters **92,** 103304 (2008).

128. R. Windisch, C. Rooman, S. Meinlschmidt, P. Kiesel, D. Zipperer, G. H. D÷hler, B. Dutta, M. Kuijk, G. Borghs, and P. Heremans, "Impact of texture-enhanced transmission on high-efficiency surface-textured light-emitting diodes," Applied physics letters **79,** 2315 (2001).

129. M. Boroditsky, T. F. Krauss, R. Coccioli, R. Vrijen, R. Bhat, and E. Yablonovitch, "Light extraction from optically pumped light-emitting diode by thin-slab photonic crystals," Applied physics letters **75,** 1036 (1999).

130. A. Drezet, F. Przybilla, E. Laux, O. Mahboub, C. Genet, T. W. Ebbesen, J. S. Bouillard, A. Zayats, I. S. Spevak, and A. V. Zayats, "Opening the light extraction cone of high index substrates with plasmonic gratings: Light emitting diode applications," Applied physics letters **95,** 021101 (2009).

References

131. E. Popov, L. Mashev, and D. Maystre, "Theoretical study of the anomalies of coated dielectric gratings," Journal of Modern Optics **33,** 607-619 (1986).

132. J. Daugman, "How iris recognition works," IEEE Transactions on circuits and systems for video technology **14,** 21-30 (2004).

133. D. Litwiller*, "CCD vs. CMOS: F*acts and Fiction", Photonics Spectra, 154-158, (2001).

134. T. Lule, S. Benthien, H. Keller, F. Mutze, P. Rieve, K. Seibel, M. Sommer, and M. Bohm, "Sensitivity of CMOS based imagers and scaling perspectives," IEEE transactions on electron devices **47,** 2110-2122 (2000).

135. Seitz, P. Solid State Image Sensing. 2009. Doctoral School of Photonics. 2009.

136. http://en.wikipedia.org/wiki/Bayer_filter, 2010.

137. L. B. Wolff, "Applications of polarization camera technology," IEEE Expert: Intelligence Systems Application **10,** 30-38 (1995).

138. S. Makita, Y. Yasuno, T. Endo, M. Itoh, and T. Yatagai, "Polarization contrast imaging of biological tissues by polarization-sensitive Fourier-domain optical coherence tomography," Applied Optics. **45,** 1142-1147 (2006).

139. J. Guo and D. J. Brady, "Fabrication of high-resolution micropolarizer arrays," Optical Engineering **36,** 2268 (1997).

140. G. P. Nordin, J. T. Meier, P. C. Deguzman, and M. W. Jones, "Micropolarizer array for infrared imaging polarimetry," Journal of the Optical Society of America A **16,** 1168-1174 (1999).

141. E. R. Fossum, "Active pixel sensors (APS)-Are CCDs dinosaurs?" Proceedings of SPIE, **1900**, 2-14, (1992).

142. P. F. Ruedi, P. Heim, F. Kaess, E. Grenet, F. Heitger, P. Y. Burgi, S. Gyger, and P. Nussbaum, "A 128/spl times/128 pixel 120-dB dynamic-range vision-sensor chip for image contrast and orientation extraction," IEEE Journal of Solid-State Circuits **38,** 2325-2333 (2003).

143. R. D. R. Bhat, N. C. Panoiu, S. R. J. Brueck, and R. M. Osgood Jr, "Enhancing the signal-to-noise ratio of an infrared photodetector with a circular metal grating," Japanese Journal of Applied Physics **44,** L364-L366 (2005).

144. http://www.ovt.com/technologies/omnibsi.php, 2010.

145. E. Laux, C. Genet, T. Skauli, and T. W. Ebbesen, "Plasmonic photon sorters for spectral and polarimetric imaging," Nature Photonics **2,** 161 (2008).

146. Laux, E. Fundamental aspects of the enhanced transmission phenomenon and its application to photon sorting. 2009. Université Louis Pasteur.

147. http://www.foveon.com/article.php?a=67, 2010.

148. L. Martin-Moreno and F. J. Garcia-Vidal, "Minimal model for optical transmission through holey metal films," Journal of Physics, Condensed Matter **20,** (2008).

Acknowledgements

There are many things I would like to say at the moment I am writing these lines. I unfortunately don't have all the words to express these things, partly because of the lack of sleep due to the long hours sitting at my desk writing this manuscript, but also because of this strange feeling I have, just before printing this manuscript. In simple words, a PhD thesis implies a lot of work that you have to deal with on your own, but I would never have done all this work without the help and support of many people. I would like to thank them here.

First of all, I would like to thank my supervisor Ross Stanley. He first gave me the opportunity to work at CSEM during my master degree. After few months in Neuchâtel, I was convinced that the best place to do my PhD thesis was in his group, because of all what I could learn from him from a scientific point of view, but also because of the person himself. Ross was my mentor over the last 4 years, and I think the way I visualize most of optical effects comes from him.

I would like to express my gratitude to Benoit Deveaud-Plédran, who accepted to be my supervisor at EPFL. It was always a pleasure to meet him, especially because of his positive attitude in any circumstances.

Special thanks to Andrea Dunbar and Rolf Eckert for their availability, their precious advice during this entire thesis and their experience in the field of optics. Thank you also for creating an atmosphere of friendship. I have to mention here our paper meeting and at the same time I take the occasion to thank Mona Klein for her dynamism and her wise advises. Thank you the three of you for the good fight we had altogether during these meetings!

For the nice working environment, I also would like to thank the complete division

"Nanotechnology & Life Sciences", and in particular the sector "MOEMS and Nano-Optics" and the "PhD office". I'm not going to cite everybody in the division as I'm getting tired, but my special thanks go to: Rob Lockhart, alias Ginette, a very funny guy coming from the country of the caribou; Bernard Wenger, for our work on the biosensing part of this thesis, but also because he taught me how to run like a chamois in the Jura; Real Isher, alias Huggy-les-bons-tuyaux, and Nicolas Blondiaux, almost Swiss, ou bien!

I would also like to express my gratitude to Vladislav Spassov and Christian Santschi for the fabrication of sample by FIB. For supplying support with photodetectors, thanks to Edoardo Franzi's group and in particular to Eric Grenet and Pierre-François Ruedi.

I also address my acknowledgment to Luis Martín-Moreno and Francisco J. García-Vidal and their respective group for providing theoretical results which where most of the time in agreement with our experiments. Special thanks go to Alexey Yu. Nikitin for our collaboration regarding the work done on the enhanced light transmission for TE polarization, and Fernando de León-Pérez for discussion on the modal expansion method and for providing theoretical results for the slit and groove structures.

I would like to thank Thomas Ebbesen and his entire group for their hospitality during my stay at ULP Strasbourg. Special acknowledgements go to Eric Laux, Frédéric Przybilla and Aurélien Drezet who trained me on their experimental setup.

Also, I think that a fundamental quality to achieve a PhD thesis is to never give up. As Ross said several times, I'm a "tête de mule" (actually "tête de moules" with his Irish accent...), which I think helped me a lot to be able to write these lines today. I think I should thank my family for that, as it is a quality that I share with most of them.

Thanks also to all my friends, the ones from Switzerland and the others who came to Switzerland to visit me.

Most of all, thank you Agathe. Thank you for providing me love, but also food during these months of writing ;-)

Curriculum Vitae

Mickaël Guillaumée

Date of Birth:	06.06.1983
Place of birth:	Troyes (France)
Nationality:	French
Address:	Chemin de Belleroche 1, CH-2000 Neuchâtel
E-mail:	mickael_guillaumee@hotmail.com

Education

2006-2010   PhD student at the Swiss Centre for Electronics and Microtechnology (CSEM SA), (Neuchâtel, Switzerland) under the supervision of Dr. Ross P. Stanley, head of MOEMS and Nano-Optics group. PhD carried out in collaboration with Prof. Dr. Benoît Deveaud Plédran from the Swiss Federal Institute of Technology Lausanne, Institute of Condensed Matter Physics, Laboratory of Quantum Optoelectronics (EPFL-ICMP-LOEQ).

2005-2006   Master degree in Optics and Nanotechnologies (ONT) at the University of Technology of Troyes (UTT).

2003-2006   Materials engineering degree at the University of Technology of Troyes (UTT).

2001-2003   Student at the University of Technology of Troyes (UTT). Taking a two years Foundation Course in Sciences.

2001   French equivalent to the British A levels in sciences (specialization in mathematics).

Patent

- N. Blondiaux, M. Guillaumée, R. Pugin, R. Stanley, A. Stuck and H. Walter, "Isotropic zero-order diffractive filter", EP1990661-A1, 2008.

Publications

- M. Guillaumée, L. A. Dunbar, and R. P. Stanley, "Analytical description of the symmetric and antisymmetric modes governing the optical transmission through metal gratings", in preparation (2010).

- M. Guillaumée, A. Yu. Nikitin, M. J. K. Klein, L. A. Dunbar, V. Spassov, R. Eckert, L. Martín-Moreno, F. J. García-Vidal and R. P. Stanley, "Observation of enhanced transmission for s-polarized light through a subwavelength slit", *Optics Express*, **18**, 9722 (2010).

- M. J. K. Klein, M. Guillaumée, B. Wenger, L. A. Dunbar, J. Brugger, H. Heinzelmann, and R. Pugin, "Inexpensive and fast wafer-scale fabrication of nanohole arrays in thin gold films for plasmonics", *Nanotechnology*, **21**, 205301 (2010).

- L. A. Dunbar, M.Guillaumée, F. de León-Pérez, C. Santschi, E. Grenet, R. Eckert, F. López-Tejeira, F. J. García-Vidal, L. Martín-Moreno and R.P. Stanley, " Enhanced transmission from a single subwavelength slit aperture surrounded by grooves on a standard detector " *Applied Physics Letters* , **95**, 011113 (2009).

- M. Guillaumée, L. A. Dunbar, Ch. Santschi, E. Grenet, R. Eckert, O. J. F. Martin and R. P. Stanley, "Polarization sensitive silicon photodiodes using nanostructured metallic grids", *Applied Physics Letters*, **94**, 193503 (2009).

- C. Santschi, J. Przybylska, M. Guillaumée, O. Vazquez-Mena, J. Brugger and O. J. F. Martin, "Focused Ion Beam: A Versatile Technique for the Fabrication of Nano-Devices", *Practical Metallography*, **46**, 154 (2009).

- M. Guillaumée, M. Liley, R. Pugin and R. P. Stanley, "Scattering of light by a single layer of randomly packed dielectric microspheres giving colour effects in transmission", *Optics Express*, **16**, 1440 (2008).

Contributions to international conferences

- M. Guillaumée, A. Yu. Nikitin, L. Andrea Dunbar, V. Spassov, M. J. K. Klein, R. Eckert, L. Martin-Moreno, F. J. Garcia-Vidal and R. P. Stanley, "Enhanced transmission of s-polarized light through a metal slit", SPIE Photonics Europe, Brussels (2010).

- M. Guillaumée, L. A. Dunbar, F. de León-Pérez, C. Santschi, E. Grenet, R. Eckert, F. López-Tejeira, F. J. García-Vidal, L. Martín-Moreno and R. P. Stanley, "Metallic nanostructures for photodetection", Summer school on plasmonics, Porquerolles (2009).

- M. Guillaumée, M. J. K. Klein, B. Wenger, S. Pasche, R. Stanley, R. Pugin, G. Voirin, "Nano-slit and -hole arrays for label-free biosensing", Eurosensors XXIII, Lausanne (2009).

- M. Guillaumée, L. A. Dunbar, Ch. Santschi, E. Grenet, R. Eckert and R. P. Stanley, "Design of metallic grating polarizers and application for optical devices", Fourth International Conference on Surface Plasmon Photonics (SPP4), Amsterdam (2009).

- M. J. K. Klein, B. Wenger, M. Guillaumée, J. Brugger, H. Heinzelmann, and R. Pugin, "Large are hole array fabricated by a templating method for refractive index sensing, Fourth International Conference on Surface Plasmon Photonics (SPP4), Amsterdam (2009).

- L. A. Dunbar, M.Guillaumée, F. de León-Pérez, C. Santschi, E. Grenet, R. Eckert, F. López-Tejeira, F. J. García-Vidal, L. Martín-Moreno and R.P. Stanley, "Enhanced Transmission through a subwavelength slit surrounded by surface corrugations on a CMOS fabricated detector", Fourth International Conference on Surface Plasmon Photonics (SPP4), Amsterdam (2009).

- L. A. Dunbar, M. Guillaumée, C. Santschi, R. Eckert, R. Stanley, "Plasmon enhanced photodetectors", Gordon Conference, Tilton School Newhampshire (July 2008).

- M. Guillaumée, M. Liley, R. Pugin and R. P. Stanley, "Scattering of light by a sub-monolayer of randomly packed dielectric microspheres giving color effects in transmission", SPIE Photonics Europe, Strasbourg (2008).

- C. Santschi, J. Przybylska, M. Guillaumée, O. Vasquez-Mena, J. Brugger, and O. J. F. Martin, "Focused Ion Beam a Versatile Technique for the Fabrication of Nano-Devices", FIB workshop "Dreiländertagung SSOM-ASEM-DGE/DGM", Luzern (2008).

- M. J. K. Klein, M. Guillaumée, L. A. Dunbar, R. Eckert, H. Heinzelmann, J. Brugger, R. Pugin, "Optical transmission of hole arrays fabricated by nanobead templating", MNE, Athens (2008).

- R. P. Stanley, R. Eckert, M. Guillaumée, H. Heinzelmann, "Plasmon enhanced photonics", Third International Conference on Surface Plasmon Photonics (SPP3), Dijon (2007).